



Photostability of Perovskite Solar Cells

A dissertation submitted to
The Faculty of Engineering,
University of Duisburg-Essen,
Department of Civil Engineering

for the academic degree of Doctor-Engineer (Dr.-Ing.)

by

Amjad Farooq, M.Sc.

Born in Lahore, Pakistan.

Date of oral examination: 05 October 2021

1st Examiner: Prof. Dr. Doru C. Lupascu

2nd Examiner: Prof. Dr. Bryce S. Richards

Thesis submitted: May 2021, Essen.

DuEPublico

Duisburg-Essen Publications online

UNIVERSITÄT
DUISBURG
ESSEN

Offen im Denken

ub | universitäts
bibliothek

Diese Dissertation wird via DuEPublico, dem Dokumenten- und Publikationsserver der Universität Duisburg-Essen, zur Verfügung gestellt und liegt auch als Print-Version vor.

DOI: 10.17185/duepublico/75369

URN: urn:nbn:de:hbz:465-20220302-101435-0



Dieses Werk kann unter einer Creative Commons Namensnennung - Weitergabe unter gleichen Bedingungen 4.0 Lizenz (CC BY-SA 4.0) genutzt werden.

Declaration

I declare that the contents of this dissertation are original work conducted by myself, except when a particular reference is made to the work of others, including the electronic sources. This work has not been submitted entirely or partially for any other degree or qualification in this, or any other University. This dissertation is the outcome of my original work and the work done in collaboration has been duly acknowledged.

Amjad Farooq

Essen, May 2021.

Acknowledgements

I would like to use these pages as opportunity to express my gratitude to all those who helped me in successfully completing this work. I must say that this work and dissertation would not have been possible without the help, support, and encouragement of many people, including my supervisors, colleagues, friends, and above all, my family.

First of all, I am very thankful to my supervisors Prof. Dr. Bryce Richards, Prof. Dr. Doru C. Lupascu, and Dr. Ulrich Paetzold. It was a privilege to be a part of both the groups, at Karlsruhe Institute of Technology (KIT) under guidance of Prof. Richards, and at Universität Duisburg-Essen (UDE) in close working relationship with Prof. Lupascu. I consider myself very lucky for being a member of Prof. Lupascu's research group, who not only guides the research students but also believes in transforming them into excellent researchers and human beings. I am also grateful to my mentor, Dr. Ulrich Paetzold, who has always been there to guide, help, and encourage me.

I am indebted to the efforts done by Dr. Efthymios Klampaftis by guiding me about each simple task in early days of my PhD. I am also thankful to Ihteaz Hossain for showing me how to fabricate solar cells in the lab, and to Sara Moghadamzadeh for the support during initial experiments. I would also like to express gratitude to Tobias Abzieher who helped me several times in doing various characterizations and Christian Kayser who helped me to work in the cleanroom and maintaining the equipment to make sure a non-stop fabrication of the solar cells. I also acknowledge the help received from Dr. Dmitry Busko for optical characterizations and measurements. I thank my thesis student Shikhar Arvind for helping me in starting the solar cells encapsulation work at KIT, and Malte Langenhorst for the important tips to find a suitable encapsulant material.

I appreciate the help from Dr. Motiur Rahman Khan who agreed to perform thermally stimulated current measurements and guided me to understand and interpret the results. I am thankful to Dr. Mahdi M. Byranvand for the collaborative work done on stability testing and passivation to enhance the stability of the perovskite solar cells. I also acknowledge the help from Dr. Vladimir Shvartsman for the valuable discussions and suggestions. I also express my humble gratitude to Dr.-Ing. Hans-Joachim Keck and Ms. Sabine Kriegel for their help and support over the past years.

I would like to thank Nicole Bartek for her help during write-up and proofreading of this dissertation. I feel blessed to have colleagues like Ihteaz Hossain, Sara Moghadamzadeh, Aiman Roslizar, Jonas Schwenzer, Tobias Abzieher, Raphael Schmager, Fabian Schakmar, Simon Ternes, Ngei Katumo at KIT and Young Un, Nicole Bartek, Andrei Karabanov, Kristina Winkler, Astita Dubey, and Martina Pantaler at UDE. All these people helped me a lot throughout my research work and I am very thankful to them for their help, support, and guidance.

I would also like to acknowledge the financial support from the German Academic Exchange Service (DAAD – Deutscher Akademischer Austauschdienst) for this doctoral research work under the program “Forschungsstipendien – Promotionen in Deutschland, 2016/17 (57214224)” with personal reference number 91604868.

Lastly, I thank my family and friends for their support and encouragement. I express special tribute to my parents, siblings, and my wife for their patience, sacrifice, love, and support over the course of my PhD. I am also very grateful to my dear friends Ali Zaidi, Taimoor Ali, and Mehran Bashir for their valuable advices and push during all this time.

Abstract

Organometal halide perovskite solar cells (PSCs) have emerged as a new disruptive technology in the photovoltaic landscape in recent years. Their power conversion efficiencies (PCE) soared up to over 25% as of now from as little as 3.8% in 2009. Despite the promising device performance, the limited operational stability hampers their commercialization. The instability problem is manifold, mainly due to their vulnerability to thermal decomposition, photo-degradation, and oxidation. The thermal stability is already lifted to the recommended industrial levels by employing compositional engineering. The oxygen and humidity ingress can be controlled by proper encapsulation – as already demonstrated for established PV technologies – leaving behind the problem of photo-instability to be taken care of.

Therefore, in this dissertation, the mechanisms governing the photo-degradation in perovskite solar cells are investigated. Among various spectral regimes in air mass 1.5 global (AM 1.5 G) spectrum, ultraviolet (UV) radiation is identified to contribute most to the photo-degradation, lowering the PCEs by 64% (relative). The most impacted PV parameter is the short-circuit current density (J_{SC}), decreasing by up to ~80% in worst case scenario, with the open-circuit voltage (V_{OC}) being the least affected parameter (20 – 30% decrease). Furthermore, a varying trend of degradation is observed upon exposing the solar cells to spectra belonging to UV-A (315 – 400 nm) and UV-B (280 – 315 nm) radiation, with UV-B being more destructive. In addition to UV triggered instability, investigation of photostability beyond UV radiation revealed that a steady decrease in the degradation exists upon the decreasing energy of the incident photons. This can be observed for wavelengths between 300 nm and 500 nm. The reduction in PCE is noted to be lowest (7%) when exposed to the wavelengths > 500 nm, and highest (43%) for the wavelengths < 400 nm over a period of 250 hours. The spectral selectivity is realized via multiple long-pass and short-pass optical filters. In addition to wavelength-dependent degradation, the intensity dependence of photo-instability is also investigated using neutral density filters and custom-made light intensity moderators. Furthermore, the mechanisms and causes of the photo-degradation are probed by measuring the ideality factors, thermally stimulated currents (TSC), photo spectroscopy, and x-ray crystallography. With TSC measurements it is established that the trap states of different activation energies (265 ± 5 meV and 425 ± 10 meV) are generated upon photo-degradation, stimulating the recombination via trap states thus influencing the device performance.

To counter the severe instability in PSCs towards UV radiation, two protective measures are proposed. These measures include the use of UV-filters to block the troublesome wavelengths. However, this strategy comes at the cost of J_{SC} (up to 1.3 mA/cm^2) since the energy content of the blocked photons is not harnessed. The other method of improving the UV triggered instability involves doping of luminescent downshifting material in the encapsulant or the front covering glass sheet. With this approach, a recovery of J_{SC} in amount of 0.6 mA/cm^2 can be realized in a realistic scenario.

In addition to the role of photon-energy in degradation, bias-dependent photo-instability is also investigated. The worst performance deterioration is found in solar cells maintained at open-circuit condition (77%), while least is observed in the ones held at short-circuit condition (34%). On the other hand, the solar cells maintained at constant voltage near the maximum power point showed a medium degradation of 57% in PCE. Altogether, these findings are important to lay the basis for the improvement of the photo-stability of multi-cation perovskite solar cells.

Keywords: Perovskite solar cells, triple-cation absorber, light-induced degradation, ultraviolet, spectral dependence, long-term stability, luminescent downshifting materials.

Zusammenfassung

Organometall-Halogenid-Perowskit-Solarzellen (PSCs) haben sich in den letzten Jahren als neue disruptive Technologie in der Photovoltaik-Landschaft herauskristallisiert. Ihre Wirkungsgrade (Power Conversion Efficiency, PCE) stiegen auf aktuell über 25% von lediglich 3.8% in 2009. Trotz vielversprechender Bauteil-Leistungen erschwert die begrenzte Betriebsstabilität die Kommerzialisierung. Das Instabilitätsproblem ist vielfältig, hauptsächlich aufgrund der Anfälligkeit für thermische Zersetzung, Photodegradation und Oxidation. Die thermische Stabilität wird durch den Einsatz von Kompositionstechniken bereits auf das empfohlene industrielle Niveau angehoben. Während das Eindringen von Sauerstoff und Feuchtigkeit durch eine geeignete Verkapselung kontrolliert werden kann – wie bereits für etablierte PV-Technologien demonstriert – ist das Problem der Photoinstabilität noch zu lösen.

Daher werden in dieser Dissertation die Mechanismen untersucht, welche die Photo-Degradation in Perowskit-Solarzellen bestimmen. Von den verschiedenen Spektralbereichen im globalen 1,5-Luftmassen-Spektrum (AM 1,5 G) wurde die ultraviolette (UV) Strahlung als größter Beitrag zur Photo-Degradation identifiziert und reduziert die PCEs um 64% (relativ). Der am stärksten betroffene PV-Parameter ist die Kurzschlussstromdichte (J_{SC}), die im schlechtesten Fall um bis zu ~80% sinkt, wobei die Leerlaufspannung (V_{OC}) am wenigsten beeinflusst wird (20 – 30% Abnahme). Die Degradation weist außerdem unterschiedliche Trends auf, wenn die Solarzellen Spektren ausgesetzt werden, die zur UV-A- (315 - 400 nm) und UV-B- (280 - 315 nm) Strahlung gehören, wobei UV-B schädlicher ist. Zusätzlich zu der durch UV-Strahlung ausgelösten Instabilität ergab die Untersuchung der Photostabilität jenseits der UV-Strahlung eine stetige Abnahme der Degradation mit verringerter Energie der einfallenden Photonen. Diese kann für Wellenlängen von 300 nm bis 500 nm beobachtet werden. Die geringste Abnahme im Wirkungsgrad (7%) wird verzeichnet für PSCs, die Wellenlängen von > 500 nm ausgesetzt werden, die stärkste (43%) bei Wellenlängen von < 400 nm, jeweils über einen Zeitraum von 250 Stunden. Die spektrale Selektivität wird über mehrere optische Lang- und Kurzpassfilter realisiert. Neben der wellenlängenabhängigen Degradation wird auch die Intensitätsabhängigkeit der Photoinstabilität mit Hilfe von Neutraldichtefiltern und speziell angefertigten Lichtintensitätsmoderatoren untersucht. Darüber hinaus werden die Mechanismen und Ursachen der Photo-Degradation durch Messung von Idealitätsfaktoren, thermisch stimulierten Strömen

(TSC), Photospektroskopie und Röntgenkristallographie erforscht. Die TSC-Messungen ergeben, dass während der Photodegradation bei unterschiedlichen Aktivierungsenergien (265 ± 5 meV und 425 ± 10 meV) Fallenzustände erzeugt werden, wodurch die Rekombination hierüber und damit die Bauelementleistung beeinflusst werden.

Um der starken Instabilität von PSCs gegenüber UV-Strahlung entgegenzuwirken, werden zwei Schutzmaßnahmen vorgeschlagen. Eine Maßnahme ist der Einsatz von UV-Filtern, um die problematischen Wellenlängen zu blockieren. Diese Strategie geht jedoch zu Lasten des Kurzschlussstroms (bis zu $1,3 \text{ mA/cm}^2$), da der Energiegehalt der herausgefilterten Photonen nicht genutzt wird. Die andere Methode zur Verbesserung der UV-induzierten Instabilität beinhaltet die Dotierung mit lumineszierendem Downshifting-Material im Verkapselungsmaterial oder vorderen Deckglas. Mit diesem Ansatz kann in einem realistischen Szenario eine Rückgewinnung von J_{SC} in Höhe von $0,6 \text{ mA/cm}^2$ realisiert werden.

Zusätzlich zur Rolle der Photonenenergie bei der Degradation wird auch die vorspannungsabhängige Photoinstabilität untersucht. Der größte Leistungsabfall wird bei Solarzellen festgestellt, die im Leerlauf betrieben werden (77%), der geringste bei solchen, die im Kurzschlusszustand gehalten werden (34%). Solarzellen wiederum, die bei konstanter Spannung in der Nähe des Punktes maximaler Leistung betrieben werden, weisen eine mittlere Abnahme von 57% im Wirkungsgrad auf. Insgesamt sind diese Erkenntnisse wichtig, um die Basis für die Verbesserung der Photostabilität von Multi-Kationen-Perowskit-Solarzellen zu legen.

Schlagwörter: Perowskit-Solarzellen, Dreifachkationenabsorber, lichtinduzierter Abbau, ultraviolett, spektrale Abhängigkeit, Langzeitstabilität, lumineszierende Abkonversionsmaterialie.

Table of Contents

Acknowledgements.....	iii
Abstract.....	v
Zusammenfassung.....	vii
1. Introduction	1
1.1 Aims	2
2. Background.....	5
2.1 Discovery of Photovoltaic effect – a Timeline.....	5
2.2 Generations of Solar Cells	8
2.2.1 First Generation Solar Cells	8
2.2.2 Second Generation Solar Cells	8
2.2.3 Third Generation Solar cells.....	9
2.3 Working Principle of Solar Cells	9
2.3.1 Light Absorption and Carrier Generation.....	10
2.3.3 Charge Collection	14
2.3.4 Equivalent Circuit.....	14
2.4 Efficiency Limits.....	16
3. Perovskite Semiconductors and Solar Cells	19
3.1 Characteristic Attributes.....	19
3.1.1 Structural Properties	19
3.1.2 Promises.....	20
3.1.3 Challenges	23
3.2 Performance limiting Mechanisms	25
3.2.1 Intrinsic and Extrinsic Defects	25
3.2.2 Ion Migration and Hysteresis	27
3.2.3 Interfacial Charge Accumulation and Grain Boundaries	27
3.2.4 Trap-assisted Recombination	28
3.2.5 Charge Transport Layers and Extrinsic Ion Infiltration	29
3.3 Stability and Energy Efficiency	32
3.3.1 Levelized Cost of Electricity	32
3.3.2 Stability Test Standards	33
3.4 Approaches to Enhance Stability and Efficiency	35

3.4.1 Incorporation of 2D Perovskites.....	35
3.4.2 Surface Passivation.....	36
3.4.3 Luminescent Downshifting Materials	37
3.5 Device Architectures	40
3.5.1 Standard n-i-p Structure.....	40
3.5.2 Inverted p-i-n Structure	41
3.6 Deposition Methods	41
3.6.1 One-step Recipes	41
3.6.2 Two-step Recipes	42
3.6.3 Solvent-engineering Recipes	43
3.7 Current State of Research.....	43
3.7.1 Thermal Degradation.....	43
3.7.2 Humidity Induced Degradation	44
3.7.3 Light-Induced Degradation.....	45
4. Materials and Characterization	49
4.1 Choice of Materials and Compositions.....	49
4.1.1 Transparent Conductive Oxide.....	49
4.1.2 Electron Transport Layers	50
4.1.3 Hole Transport Layers	52
4.1.4 Perovskite Absorber	53
4.2 Solar Cell Fabrication.....	54
4.2.1 Substrates and Electron Transport layers	54
4.2.2 Perovskite Precursors and Coating.....	55
4.2.3 Hole Transport Layers	56
4.3 Luminescent Downshifting Layers	58
4.4 Analytical Techniques.....	59
4.3.1 Current Density-Voltage (<i>J-V</i>) Measurements	59
4.3.2 Constant Voltage Tracking.....	61
4.3.3 UV-Vis Absorbance Spectroscopy.....	61
4.3.4 X-ray Diffractometry	62
4.3.5 External Quantum Efficiency	63
4.3.6 Thermally Stimulated Current Measurement	64

4.3.7 Ideality Factor Measurements	65
4.3.8 UV Stimulated Degradation Setup	66
4.3.9 Visible Light Degradation Setup	67
5. UV Induced Degradation	71
5.1 Role of Electron Transport Layers	72
5.1.1 Multitude of Employed ETLs	72
5.2 Spectral Distribution of UV Radiation in AM1.5G	74
5.3 UV Stability Test Protocol	75
5.3.1 Standard Protocol	75
5.3.2 Employed Protocol	76
5.4 Role of UV Radiation Spectrum	77
5.5 Role of UV-B Radiation Intensity	82
5.6 Prevention Strategies	83
5.6.1 UV Blocking Coatings	84
5.6.2 Luminescent Downshifting Materials	85
6. Visible Light Induced Degradation	91
6.1 Quality of Solar Cells and PV Parameters	92
6.2 Spectral dependence of Light-Induced Degradation	93
6.2.1 Spectrum Selectivity and its Role	93
6.2.2 Role of Light Intensity	98
6.3 Performance Recovery Investigations	99
6.4 Decomposition of Absorber Material	100
6.4.1 Post-Degradation Compositional Analysis	100
6.4.2 Spectroscopic Analysis	102
6.5 Bulk Defect Formation	105
6.6 Trap Energy Estimation	107
7. Bias Dependent Degradation	113
7.1 Degradation at V_{OC} and J_{SC}	114
7.2 Comparison with Degradation near Maximum Power Point	116
7.3 Performance Recovery	117
7.4 Role of Spectrum Selectivity at Open Circuit	119
Conclusions and Outlook	123

References	127
List of Figures	149
List of Tables.....	153

List of Abbreviations

Abs	Absorbance
ACN	Acetonitril
Au	Gold
AM1.5G	Air mass 1.5 global
AFM	Atomic force microscopy
BCP	Bathocuproine
CB	Chlorobenzene
c-TiO ₂	Compact titanium dioxide
c-SnO ₂	Compact tin oxide
CB	Conduction band
CdTe	Cadmium telluride
CIGS	Copper indium gallium selenide
CPV	Concentrator photovoltaics
Cs	Caesium
CsI	Caesium iodide
C ₆₀	Fullerene molecule consisting of 60 carbon atoms
DMF	N,N-dimethylformamide
DMSO	Dimethylsulphoxide
DSSC	Dye-sensitized solar cells
ETL	Electron Transport layer
e-TiO ₂	Electron beam evaporated titanium dioxide
EQE	External quantum efficiency
Eu	Europium
EVA	Ethylene-vinyl acetate
FAI	Formamidinium iodide
FF	Fill factor
FTO	Fluorine-doped tin oxide

GaAs	Gallium arsenide
GBL	Gamma butyrolactone
HBL	Hole blocking layer
HTL	Hole transport layer
IEC	International electrotechnical commission
ITO	Indium tin oxide
LED	Light-emitting diode
LiTFSI	Bis(trifluoromethane)sulfonimide lithium salt
LUMO	Lowest unoccupied molecular orbital
LP	Long-pass optical filter
MAI	Methylammonium iodide: $\text{CH}_3\text{NH}_3\text{I}_3$
MACl	Methylammonium chloride: MAPbCl_3
MABr	Methylammonium bromide: MAPbBr_3
MAPI	Methylammonium lead triiodide: MAPbI_3
MPP	Maximum power point
m-TiO ₂	Mesoporous-titanium dioxide
NIR	Near infrared
np-SnO ₂	Nanoparticle tin oxide
np-TiO ₂	Nanoparticle titanium dioxide
NREL	National Renewable Energy Laboratory
OSC	Organic solar cell
OPV	Organic photovoltaic
PbBr ₂	Lead bromide
PbI ₂	Lead iodide
PCE	Power conversion efficiency
PSC	Perovskite solar cell
PCBM	Phenyl-C61-butyrac acid methyl ester
PEDOT:PSS	poly(3,4-ethylenedioxythiophene) polystyrene sulfonate

PTAA	Poly(triaryl amine), Poly[bis(4-phenyl)(2,4,6-trimethylphenyl)amine]
PV	Photovoltaic
RH%	Relative humidity
Si	Silicon
Spiro-OMeTAD	2,2',7,7'-Tetrakis[N,N-di(4-methoxyphenyl)amino]-9,9'-spirobifluorene
SP	Short-pass optical filter
4t-BP	4-tert-Butylpyridine
TCO	Transparent conductive oxide
TSC	Thermally stimulated current
UV-Vis	Ultraviolet visible spectroscopy
VB	Valance band
Xe	Xenon
XRD	X-ray diffraction

List of symbols

α	Absorption coefficient (cm^{-1})
d	Lattice spacing (\AA)
e^-	Electron
ε	Extinction coefficient (cm^{-1})
E_g	Band gap energy (eV)
Φ_{ph}	Photon flux density ($\mu\text{mol m}^{-2} \text{s}^{-1}$)
ϕ	Work function (eV)
h	Planck's constant (Js)
h^+	Hole
I_{ph}	Photo-current (mA)
I_D	Dark current (mA)
I_{sh}	Shunt current (mA)
J_{SC}	Short circuit current density (mA cm^{-2})
J_{MPP}	Current density at maximum power point (mA cm^{-2})
k_B	Boltzmann constant (J K^{-1})
λ	Wavelength (nm)
P_{in}	Incident Power (W m^{-2})
P_{MPP}	Power at maximum power point (W m^{-2})
q	Elementary charge (C)
ν	Frequency (Hz)
R_s	Serial resistance (Ω)
R_{sh}	Parallel (shunt) resistance (Ω)
T	Temperature ($^{\circ}\text{C}$)
θ	Diffraction angle ($^{\circ}$)
t	Tolerance Factor
V_{MPP}	Voltage at maximum power point (V)
V_{OC}	Open circuit voltage (V)

1. Introduction

Industrialization and the modern lifestyle have made our energy demand increase continuously, and it is expected to increase by 50% – 60% in 2050.^{1,2} To meet the ever-growing energy needs, major sources that also naturally pollute the environment are coal (38%), gas (23%), nuclear (10%), and oil (3%) respectively.³ The use of these fuels induces a negative impact on the global climate by releasing CO₂ into the atmosphere or due to the dangerous radioactive nature of the nuclear waste. The CO₂ concentration has increased from 393 ppm to 417 ppm within the last decade which, can be directly related to the 0.3 °C rise in global temperature.^{4,5} Despite these alarming facts, ongoing climate action campaigns by the United Nations (UN) and the Paris agreement to cut-short the use of fossil fuels and limit the rise of temperature within 1.5 ° – 2 °C above pre-industrial level, long-term concrete actions are yet awaited.^{6,7} Controlled use of fossil fuels can lead to impactful results. For example, a significant reduction in CO₂ emission is noticed due to mobility restrictions and industry shutdown worldwide during the recent COVID-19 (corona virus disease) pandemic. Overall, 6.4% less CO₂ emission is recorded in 2020 as compared to 2019.⁸

Therefore, it is imperative to use renewable energy resources and maximize the production of clean energy by hydroelectric, wind, and solar power. The scheme of the energy transition is very well reflected in the “*Energiewende*” – the policy devised by Germany to realize the maximum energy production by employing the potential of clean energy sources such as wind, photovoltaics (PV), and hydroelectricity. Among these, solar energy alone has the potential to meet the energy demands of the entire world owing to the fact that in a single hour, the amount of solar power striking the earth is more than the whole world consumes in an entire year.^{9,10}

Total world energy consumption – including all sources like coal, oil, hydroelectric, nuclear, and renewable – in 2018 was recorded to be 14,391 million ton oil equivalent (MTOE).¹¹ This number translates into 167,400 terawatt hour (TWh) or 19.1 terawatts (TW) continuous power throughout the year. This 19.1 TW is equal to sun energy falling on a mere 19,100 km² area of land at noon. It means if we cover the 400×400 km² area of land in the Sahara desert with solar panels of 12.5% efficiency, this would be sufficient to cover the world’s total energy consumption (167,400 TWh).^{11,12} The potential is so enormous that solar power is anticipated to become the world's

largest source of electricity by 2050, with solar photovoltaics and concentrated solar power contributing 16% and 11% to the global overall electricity consumption, respectively.¹³

In pursuit of achieving green and cheap renewable energy, many PV technologies have undergone intensive research, for example, silicon – the market-dominant in the current PV landscape – as well as others like e.g. cadmium telluride (CdTe), copper indium gallium selenide (CIGS), gallium arsenide (GaAs), organic solar cells (OPV), and dye-sensitized solar cells (DSSCs). Despite the existence of numerous leading technologies, perovskite solar cells (PSCs) have attracted the PV research community for bearing many advantages, especially high power conversion efficiencies. For these key features, PSCs have been researched intensively for a decade now with performance looming near to that of silicon solar cells, keeping in mind the difference in areas of both types of solar cells ($\sim 0.1 \text{ cm}^2$ for PSC and $> 100 \text{ cm}^2$ for silicon solar cells).

Despite the promises offered by PSCs, they pose many challenges as well. First, they contain a reasonable content of lead (Pb) which is known for its toxicity.^{14,15} Secondly, the current state of the art stability of PSCs is not up to the mark that can lift a PV product to commercialization. The lifetime of PSCs is merely reaching a year,¹⁶ while silicon holds a guaranteed power production life of 25 years.¹⁷ The short life span of PSCs arises from their sensitivity to environmental parameters like humidity¹⁸ and operational temperature of $> 65 \text{ }^\circ\text{C}$.¹⁹ Most importantly, PSCs are reported to degrade under long-term light exposure.²⁰

In terms of understanding the underlying mechanism of humidity and temperature-induced instability, many disruptive advances have been made by compositional engineering²¹ in addition to applying the moisture-stability enhancement concepts of mature PV technologies like CIGS.²² However, the light-induced instability in PSCs is not very well understood yet. It is then required to identify the underlying mechanisms and highlight the strategies to prolong the photostability in PSCs.

1.1 Aims

The main goal of this thesis is to understand the photo-degradation in PSCs, the underlying mechanism, and propose measures to counter the photo-instability problem. To accomplish this goal, PSCs are fabricated and subjected to light stress and further probed by different techniques

1. Introduction

to unveil the chemical changes in perovskite absorber material and in the solar cells as a whole. The mechanisms identification is then carried over to suggest stability enhancement measures.

This dissertation starts with an overview of the PV effect and timeline of various solar cell technologies followed by the working principle of solar cells in general in Chapter 2 and ends with the efficiency limits posed by different solar cell types depending on the bandgap of the absorber material. Chapter 3 highlights the advantages and disadvantages of PSCs. The stability of PV products is checked according to existing test standards which are explained in this chapter as well. Furthermore, the PSC device structures and various well-known recipes for high-efficiency solar cells are also presented. This chapter ends with an overview of the state-of-the-art stability of PSCs under various stress factors. In Chapter 4, the materials used to fabricate the PSCs, and the fabrication procedure are described. Additionally, the optical and electrical characterization and working of tools used to analyze the performance of as-fabricated and photo-degraded PSCs are explained.

In Chapter 5, ultraviolet (UV) radiation induced degradation is demonstrated for two kinds of UV lamps and different intensities. Here the effect of UV radiation is investigated on the PSC stability. The UV radiation is controlled in terms of wavelength and intensity to observe their impact on solar cells. Further insight on the degradation under visible light is given in Chapter 6. It also highlights the spectral dependence of degradation under light and the underlying mechanisms are investigated using different techniques. In Chapter 7, the bias dependence of photo-degradation is investigated under bias conditions like open circuit, short circuit, and constant voltage tracking near maximum power point.

1. Introduction

2. Background

The photoelectric effect defines the operation of solar cells and is explained in this chapter. A timeline of the progress of solar cells is presented as well. Next, the solar cell working is described in detail and the processes occurring in a solar cell from light absorption to charge generation and collection are given. Lastly, the maximum performance limits of solar cells are described depending on their bandgap.

2.1 Discovery of Photovoltaic effect – a Timeline

The photovoltaic effect – a physical phenomenon allowing the conversion of light to electrical charge – was discovered in 1839.^{23,24} Later, a selenium based solar cell was made with nearly 1% conversion efficiency in 1883.²⁵ After this success, in the first half of the 20th century, the photovoltaic effect was observed in copper-cuprous-oxide junctions.²⁶ Subsequently, the photovoltaic effect was noticed in the naturally grown junctions in silicon (Si) ingots, which proved to be the initial work on Si solar cells and this opened a door towards large scale production.²⁷ Following the discovery of the photovoltaic effect in Si, Bell Labs announced the invention of the first practical silicon solar cell in 1954 with nearly 6% of power conversion efficiency.²⁸ This solar cell helped the researchers to understand the basic working mechanism and then predicting the ideal materials. In the meantime, fabrication of GaAs based photocell was reported in 1954.²⁹ This report was followed by a GaAs solar cell with efficiency of 4% only within a year.³⁰ With this, GaAs emerged as potential candidate in the future PV landscape. A few years later, in 1959, the use of grid contacts was introduced to reduce the resistance of solar cells by Hoffman Electronics, leading manufacturer of silicon solar cells then, creating a 10% efficient solar cell which went up to 14% the next year.

The first real boost for the solar cell industry came when a race started to explore space in the late 1950s and 60s when an off-grid power source was needed. Solar cells were an ideal choice as the power source for the sustainable operation of satellites. The first spacecraft to use solar panels launched by the US in 1958 was the Vanguard-1 satellite, employing silicon solar cells.³¹ Later, the Russian spacecraft Venera-2 launched in 1965 used GaAs solar cells to harvest energy from sunlight. The quest to dominate space motivated the United States and the Soviet Union to pour a

2. Background

lot of resources into the extraterrestrial exploration. Thus, cost was not a hurdle to develop high-efficiency solar cells.

The massive research in terrestrial and domestic applications of solar cells progressed under the effect of the 1970s oil crisis, which proved to be a second push to solar cell research overall. In this phase of extensive research, efforts were made to reduce the price of the solar cells. During this era, focal point was to reduce the amount of material and hence the cost of the solar cell. This approach proved helpful to push further the existing thin-film technologies like cadmium telluride (CdTe), one of the first materials investigated for solar cell applications, or inventing new ones like amorphous silicon (a-Si). However, due to low efficiencies, a-Si solar cells found use in consumer electronics like watches and calculators. Though CuInSe₂ solar cells were already reported in 1976³² with efficiency 4.5% which kept on increasing through continuous research efforts, until incorporation of Ga to make a CuInGaSe₂ (CIGS) composition in 1990 to achieve an efficiency of 12.5%.³³ Further bandgap tuning in this technology resulted in efficiency of 17.7% in 1996³⁴ which currently stands at 23.3% for 1 cm² area of solar cell.³⁵ Regarding silicon solar cells, an alternative technology was developed in 1980 by Solarex that uses multi-crystalline silicon (m-Si). This technology is currently able to supply solar cells with an efficiency of 23.3%.³⁵ However, the market leading technology, crystalline silicon (c-Si) solar cells are still ahead in terms of efficiency with 26.7%. While, for CdTe solar cells, it took researchers nearly three decades to reach encouraging efficiencies around 10% in 1980-1985, and another three decades to reach promising efficiency of 22% in 2016.³⁶ With decades of research efforts, GaAs currently holds the record of best efficiency for single junction, single crystal solar cell, being 29.1% for cell and a 25.1% of module efficiency, followed by crystalline silicon with cell and module efficiency of 26.7% and 24.4%, respectively.³⁵ As compared to other technologies, organic solar cells were thought of as a promising option, however, they are still lacking efficiency to become a real alternative on a large scale. In this context, metal halide perovskite solar cells have emerged as a new technology with a promising class of materials, combining the advantages of both, organic solar cells (easy fabrication, light-weight, and flexible) and silicon solar cells (high-efficiency).

Recently, with the increasing awareness of global warming and drastic climate changes, the third boost for solar cells came in the first decade of the 21st century. This phase spurred a rapid production and installation of solar cells of multiple types. The solar cell efficiency chart by the

2. Background

National Renewable Energy Laboratory (NREL) (Fig. 2.1) gives a good idea of the development of various solar cell technologies over time.

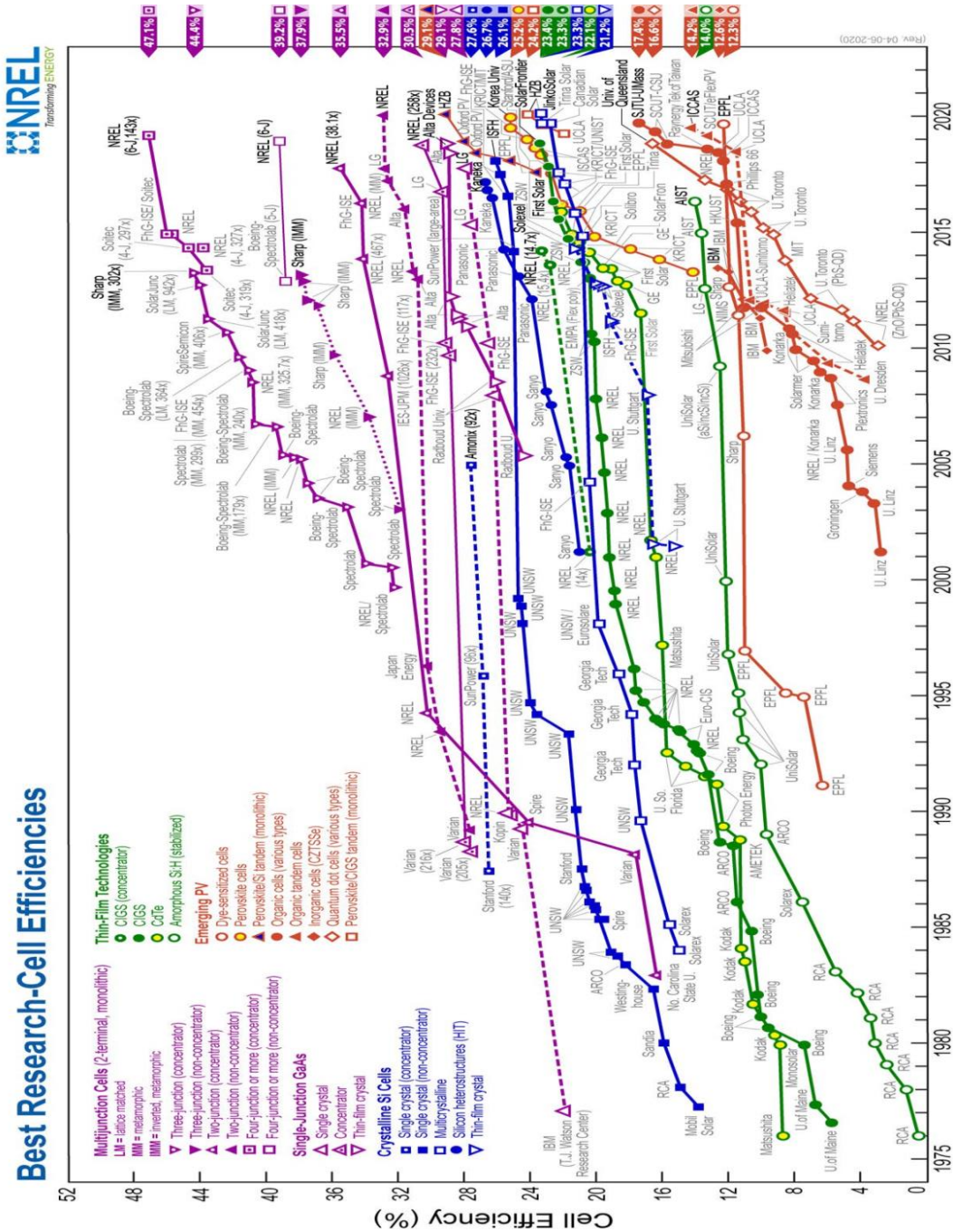


Fig. 2.1: Evolution of solar cell efficiencies for different technologies over time: Crystalline silicon (blue), thin-film (green), and emerging PV (red). Perovskite solar cells are shown as red point circles with yellow filling.

2.2 Generations of Solar Cells

Based on technological carryovers and significant development of material systems, solar cells can be classified into three generations, first introduced in 2000 by an Australian PV expert Professor Martin Green.

2.2.1 First Generation Solar Cells

The conventional or traditional wafer-based solar cells are classified as first generation solar cells, according to the definition given by M. Green.³⁷ These mostly comprise of crystalline silicon material including poly-crystalline and mono-crystalline silicon with a current record cell performance of 23.8% (area 247 cm²) and 26.7% (area 79 cm²), respectively.³⁵ As the technology has matured over several decades of research and development, the cost of this generation of solar cells is dominated by the cost of the starting material, cover sheets, and the encapsulant materials. These cells are commercially predominant, and most of the solar cells on our rooftops belong to this class.

2.2.2 Second Generation Solar Cells

The transition of PV industry from wafer-based PV to thin-film technology is defined as second generation of solar cells. Regardless of the employed material second generation of solar cells offers prospects for major reduction in cost of starting material. Furthermore, thin-film technology also offers the advantage of about 100 times increase in the size of manufacturing unit i.e. silicon wafer (~100 cm²) to that of glass sheet (~1 m²). Second generation includes the amorphous thin-film silicon, CIGS, and CdTe solar cells. Their current cell efficiencies are 10.2% (area ~1 cm²), 23.3% (area ~1 cm²), and 21% (area 1 cm²) respectively,³⁵ less than those of first-generation cells. Additionally, in terms of cost as well, second generation PV is still behind the multi or monocrystalline silicon counter parts. In mid of 2020, the price of modules on average were recorded to be 0.177, 0.200, and 0.221 US dollars per watt peak (USD/W_p) for multicrystalline silicon, monocrystalline silicon, and thin film modules respectively.³⁸ Due to further cost reduction of first generation PV, thin film solar cells face fierce competition in market.³⁹

2.2.3 Third Generation Solar cells

To progress the PV technology further from second to third generation, the performance of solar cells could be improved substantially (2 – 3 times) to exceed the thermodynamic limit of a single junction solar cell by applying different fundamental concepts in their design to realize high-performance and low-cost PV product, according to the definition given by M. Green. Several thin-film technologies belong to third generation solar cells, if applied in tandem with commercially dominant PV products, often described as emerging photovoltaics. Most of these cells are not yet applied commercially. They are still in the research and development phase.⁴⁰ This class of solar cells includes a range of alternatives to the first generation (wafer-based p-n junctions solar cells) and second generation (thin-film solar cells). Common third-generation solar cells include multi-layer (tandem) devices. By definition, the conversion efficiencies of third generation solar cells must be increased substantially to realize much lower overall costs.³⁷

Apart from other possibilities, tandem cell approach can lead the way towards the goal of substantially high conversion efficiencies and lower cost. A promising candidate in this respect is silicon/perovskite tandem technology. PSCs have received tremendous attention with their efficiencies hovering above 25.5% for lab-scale small area ($\sim 0.1 \text{ cm}^2$) solar cells³⁶ and 18% for a module of area 19 cm^2 .³⁵ Silicon solar cells being the most researched and progressed PV technology, and perovskite solar cells offering many advantages become a perfect match for tandem applications to realize third generation PV.

2.3 Working Principle of Solar Cells

A solar cell directly converts the incident light into electricity. Solar radiation reaching the earth is a streams of photons. Thus, photons, falling onto the solar cell surface are converted to electricity, and this conversion takes place in a process mainly involving four steps.

- (i) Absorption of a photon by the active material
- (ii) Generation of an electron-hole pair (exciton)
- (iii) Exciton dissociation into free charge carriers (electrons and holes)
- (iv) Charge transport and extraction of the charge carriers to the respective electrodes.

2.3.1 Light Absorption and Carrier Generation

The photons striking the solar cell's surface carry different energy depending on their wavelength or frequency. Photon absorption by active material is a strictly energy-dependent process in terms of energy of photon and energy level of the absorber material. When the material absorbs a photon of specific energy, a carrier acquires this energy and moves from its relaxed ground state to a higher energy state leaving a vacancy of an electron (hole) behind. To make this process function for electricity production, the excited carrier must be collected before it returns to the ground state. Thus, the lifetime of an excited state must be longer than the time required to extract the charge carrier. Moreover, the photons with energy less than the bandgap energy of the material will transmit through, in case of a perfect semiconductor, without giving rise to any charge excitation. While the ones with energy higher than the bandgap will dissipate their excessive energy in form of heat, giving rise to the loss mechanism called thermalization losses. The photon absorption is explained by a two-level system depicting the cases of photons carrying energies higher and equal to the bandgap energy, as demonstrated in Fig. 2.2 (a).

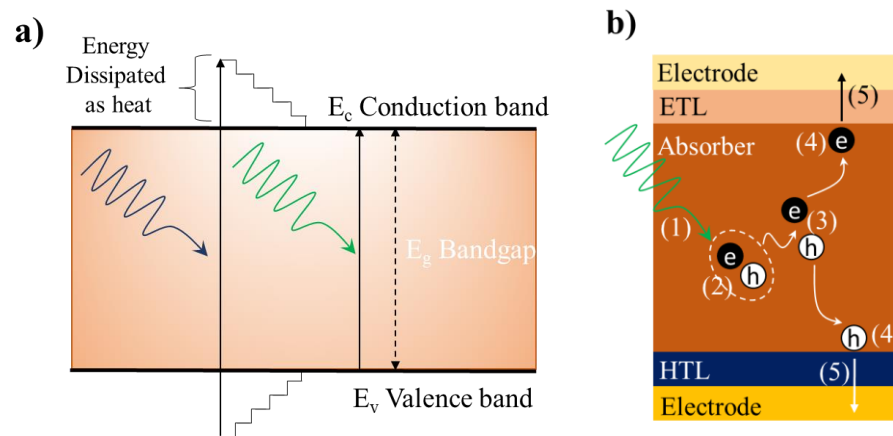


Fig. 2.2: (a) Absorption of a photon with energies (i) more than the bandgap (blue), and (ii) equal to bandgap (green) of the absorber material, (b) Schematic illustration of the physical processes taking place in the solar cell.

The two phenomena shown in blue and green in Fig. 2.2 (a) provide a very important criterion to decide which semiconductor material must be used for a photovoltaic application. If a material with a low bandgap is used, the range of absorbed photons and thus the number of excited charge carriers would be much larger, but a lot of the energy will be dissipated (as shown in blue in Fig.2.2 (a)) because heat is produced during relaxation of the excess energy relaxation. On the other hand,

2. Background

if a semiconductor material with a high bandgap is used, the thermal losses are minimized, but the number of generated charge carriers would also be less due to many sub-bandgap photons which are not absorbed. Considering these losses, black body radiation of a solar cell at room temperature and ideal radiation recombination, the optimum bandgap and maximum solar cell efficiency were calculated by Shockley and Queisser (SQ limit) in 1961 to be 1.4 eV and 33% respectively as discussed later in section 2.4.^{41,42} A solution to exceed the SQ limit is to use multiple absorber materials. Up-conversion or down-shifting of photons can also be used to alter the absorbed photon spectra to better match the employed semiconductor material.⁴³

Photon absorption results in energizing and lifting an electron from the valence band (VB) to the conduction band (CB), leaving behind a hole in the VB. The generated electron-hole pair upon photon absorption is a meta-stable state and will exist only for a time scale equal to the carrier lifetime after which they recombine. In case of recombination, the photo-generated electron-hole pair is lost without giving rise to any current. A few recombination channels existing in the solar cells can be seen in Sec. 2.3.2. The recombination of electron-hole pairs suggests that the efficient collection of the photo-generated charge carriers must happen to generate current.

The spatial separation of electrons and holes is generally carried out using a p-n homojunction (or p-i-n heterojunction in case of perovskite solar cells). Silicon solar cells typically form a p-n junction when the intrinsic layer undergoes a targeted doping to make a junction of the n and p doped materials. In a p-n junction, the difference in the quasi-Fermi energies of the CB electrons (n-doped) and the VB holes (p-doped) provide the driving mechanism for the charge carrier separation. However, in the case of perovskite solar cells, charge carrier separation is carried out by the charge carrier selectivity of the contact layers by making a p-i-n heterojunction instead of targeted doping of the intrinsic material. A p-i-n heterojunction can be realized by sandwiching an intrinsic absorber layer in between a n-type and a p-type conducting layer, acting as electron and hole transport layer, respectively, as shown in Fig. 2.2 (b). As metal halide perovskites show ambipolar charge carrier transport properties, exhibiting very low exciton binding energy, they can act as an ‘intrinsic’ layer in a solar cell. Such a p-i-n heterojunction under dark, in equilibrium is depicted in Fig. 2.3 (a). In this condition, Fermi levels are in equilibrium, termed as E_{F0} . Upon illumination, the concentration of minority carriers (electrons in the p-type and holes in the n-type region) increases strongly to undergo a non-equilibrium condition. Therefore, the Fermi energies

2. Background

in a p-i-n heterojunction split up into quasi-Fermi energies of the electrons (E_{Fn}) and holes (E_{Fp}), as demonstrated in Fig. 2.3 (b). Thus, the separation of the photo-generated charge carriers happens under the influence of the gradient in the electrochemical potential (sum of electrical and chemical potential). The gradients of chemical and electrical potentials lead to charge carrier diffusion and drift, respectively, former being more relevant for PSCs. It is shown in studies that a flat band scenario best describes the PSC working principle. This implies that the carrier separation occurs mostly due to the presence of the gradient in chemical potential, i.e., diffusion of charge carriers. Furthermore, Würfel *et al.* discussed that it is the selectivity of the charge transport layers that plays the most crucial role for an efficient separation of charge carriers, instead of the built-in voltage.⁴⁴ The selectivity is achieved by a large electron conductivity in the n-type and hole conductivity in the p-type layers, allowing electrons and holes to flow easily and blocking the charge carriers of opposite polarity efficiently. Würfel *et al.* used numerical simulations to prove that a p-i-n (or n-i-p) solar cell could be very efficient even if there is no built-in voltage at all or if a small built-in voltage is even opposing the diffusion of charge carries.

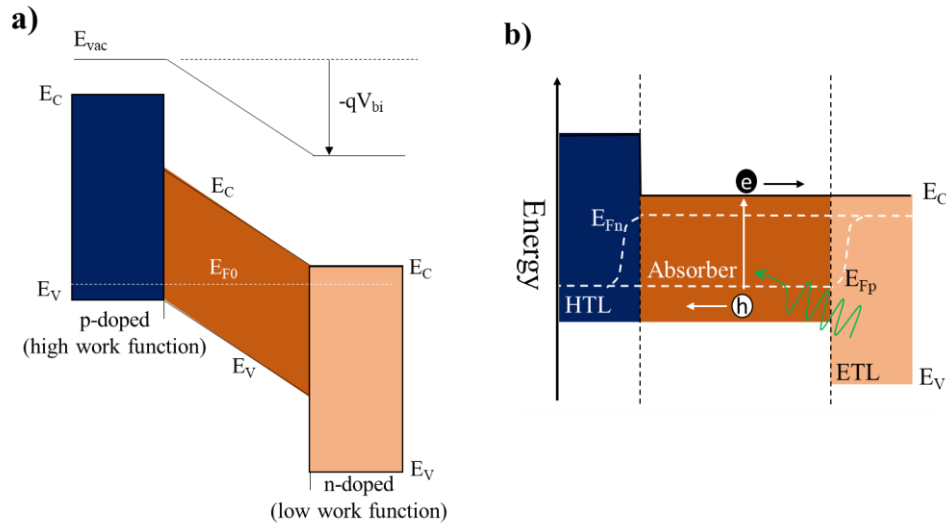


Fig. 2.3: Schematic model of a p-i-n heterojunction solar cell: (a) the system in equilibrium in dark, with Fermi level E_{F0} and a built-in field (V_{bi}) due to work functions difference of the selective contacts (b) illustration of band diagram of a p-i-n solar cell under illumination close to open-circuit conditions.

2.3.2 Recombination

Recombination, a reverse process of charge generation, also exists in solar cells and leads to the decrease of carrier concentration in the materials. Excited electrons can potentially fall back to the

2. Background

electron-hole in the valence band releasing energy radiatively or non-radiatively. If the energy is released in the form of photons, it is termed as radiative recombination. If the energy is released in the form of phonons, it is known as non-radiative recombination. Generally, there are three types of recombination, (i) band-to-band recombination, (ii) trap-assisted recombination, and (iii) Auger recombination as shown in Fig. 2.4.

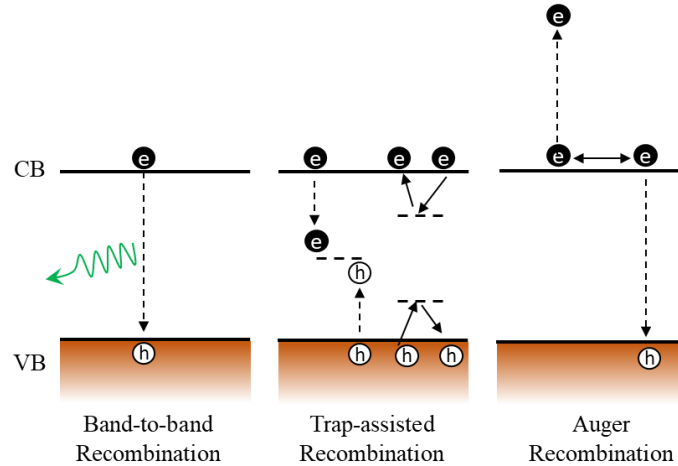


Fig. 2.4: Potential recombination mechanisms in solar cells: (i) band-to-band, (ii) trap-assisted, and (iii) Auger recombination.

Excited charges can recombine through different routes. When they recombine by direct recombination of an electron in the conduction band with a hole in the valence band, this type of recombination is known as band-to-band recombination. This occurs in a radiative manner by releasing a photon. Band-to-band radiative recombination always involves two charge carriers thus termed as bimolecular process. If the defect density inside the bandgap in the solar cell is high, then electrons and holes can also recombine via trap states. This process is known as trap-assisted Shockley-Read-Hall (SRH) recombination. This mechanism is usually non-radiative. For instance, an electron can become trapped at a defect, and subsequently recombine non-radiatively with a hole. Such a single-particle recombination process is thus a monomolecular process. At very high doping concentrations, another form of recombination, called Auger recombination, is also observed. In Auger recombination the released energy is transferred to excite another charge carrier. Auger recombination is negligible at low doping concentrations in solar cells, but both band-to-band and SRH recombination are significant.

2.3.3 Charge Collection

When the charge carriers are efficiently swept to the edge of bulk, the collection of the charges is carried out as a final step to complete the photovoltaic process. As compared to the minimal charge recombination within the perovskite absorber, non-radiative recombination may occur due to mismatched energy levels between the absorber and charge extraction layers. The most effective collection of charge carriers takes place when an ohmic contact is established between the absorber and the charge extraction layers. In the case of non-ohmic contacts, an energy-consuming parasitic resistive effect appears decreasing the device performance by restricting the current. To collect the electrons and block the holes, the CB of the absorber should be higher than that of the electron transport layer (ETL). While to efficiently collect the holes and block the electrons, the VB of the absorber should be lower than that of hole transport layer (HTL), as presented in Fig. 2.5.

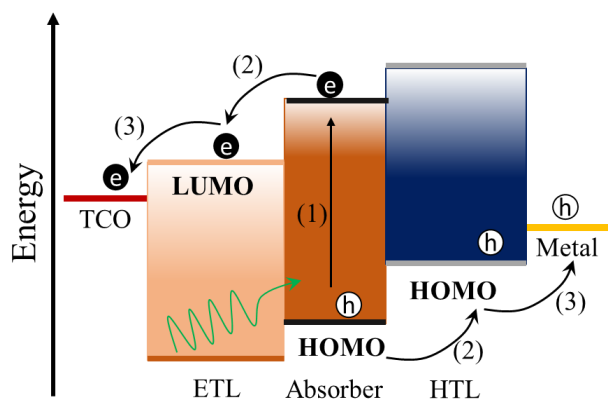


Fig. 2.5: Schematic illustration of energy levels of materials in perovskite solar cell.

2.3.4 Equivalent Circuit

The characteristic current of a solar cell comprises three components, (i) dark current (I_D) (ii) photo-current (I_{ph}), and (iii) shunt current (I_{Sh}). The dark current is determined by the diode properties of a solar cell, photo-current is due to the generation of charge carriers upon illumination, and shunt current arises due to device imperfections. Thus, an equivalent circuit of a solar cell, consisting of a diode and a photocurrent generator, can be devised to depict these currents, as shown in Fig. 2.6.⁴⁵

2. Background

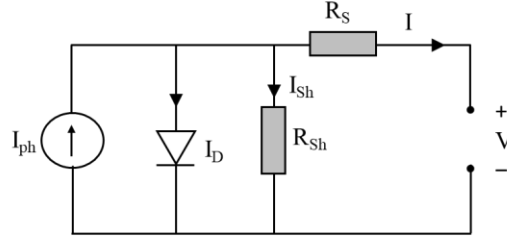


Fig. 2.6: The equivalent circuit of a solar cell, comprising a photocurrent source and a diode. The series (R_s) and shunt (R_{sh}) resistances indicate the loss mechanisms.

The electrical resistance experienced by the photogenerated charge carriers as they are injected in the selected contacts and transported to the electrodes yield series resistance (R_s). The shunt resistance (R_{sh}) is parallel to the semiconductor diode and reflects all shunt current distributions occurring internally. The photocurrent of a solar cell is typically denoted as current density (J) by dividing the current (I) with the solar cell active area (A). Hence, the total current density in a solar cell can be written as:

$$J = J_{ph} - J_D - J_{sh} \quad (2.1)$$

Where J_D is the dark current density, J_{sh} is the shunt current density, and J_{ph} is the photocurrent density. J_D can be described by the Shockley diode equation as:

$$J_D = J_0 \left[\exp \left(\frac{q(V + IR_s)}{nk_B T} \right) - 1 \right] \quad (2.2)$$

Where n is the diode ideality factor, used to describe the diode properties of the solar cell.

J_{sh} can be determined by Ohm's law as:

$$J_{sh} = \frac{V + JR_s}{R_{sh}} \quad (2.3)$$

Thus, the total current density represented in Eq. 2.1 can be rewritten as:

$$J = J_{ph} - J_0 \left[\exp \left(\frac{q(V + IR_s)}{nk_B T} \right) - 1 \right] - \frac{V + JR_s}{R_{sh}} \quad (2.4)$$

Under the assumptions that $R_S \rightarrow 0$ and $R_{sh} \rightarrow \infty$, the open-circuit voltage of the solar cell (no current flowing through it) can be written as:

$$V_{oc} |_{J=0} = \frac{nk_B T}{q} \ln \left(\frac{J_{ph}}{J_0} + 1 \right) \quad (2.5)$$

2.4 Efficiency Limits

The light absorption properties of the solar cell must be optimized according to the illumination source. The spectrum of the sun, being the illumination source for solar cells, can vary according to the location, time, and season. When the light passes through the Earth's atmosphere, a part of the radiations is absorbed and filtered by clouds and other species in the atmosphere. The extent of this filtration and absorption depends on the path length that light rays undergo to reach the Earth's surface which varies throughout the year. Therefore, the field of PV research demands a unified solar spectrum to facilitate the accurate comparison between solar cells measured at different times and locations. Thus, the standard solar spectrum at the earth surface, called air mass 1.5 global (AM1.5G), is used for solar cell characterization and defined as; the irradiance of the sun at 41° above the horizon, which corresponds to an air mass of 1.5 atmospheres, onto a solar cell that is tilted by 37° from the horizontal. This spectrum, as shown in Fig. 2.7, contains an integrated power density of $1,000 \text{ Wm}^{-2}$, which is often termed as the light of 1 sun intensity. The spectrum of the sun just above earth's atmosphere is called air mass zero (AM0) and contains an integrated power density of $1,366 \text{ Wm}^{-2}$ as shown in Fig.2.7. The AM1.5G value of power density is used to calculate the maximum achievable power conversion efficiency for the solar cells with consideration of all loss mechanisms like thermalization, below bandgap radiation, and reflection from the front surface of solar cell. It is known as the Shockley-Queisser (SQ) limit for solar cell efficiency and was determined by Shockley and Queisser in 1961 for a single p-n junction solar cell.⁴¹ SQ limit makes several fundamental assumptions in the original form. The sun and the solar cell are considered as black bodies with temperature 6,000 K and 300 K respectively. Further, it is assumed that all the incident photons with energy above the bandgap energy (E_g) of the absorber are completely absorbed. Moreover, the charge carrier mobility is considered infinite, that allows the charge carrier collection irrespective of their position of generation. Thus, this value gives the upper limit of the achievable efficiency of a solar cell. The result of their work under AM1.5G

2. Background

spectrum is exhibited in Fig. 2.8.⁴⁶ The maximum efficiency strongly depends on the bandgap of employed semiconductor material, which increases with the bandgap and reaches the maximum value of 34% at a bandgap of 1.34 eV, which then decreases with an increase in material's bandgap due to the absorption losses.⁴⁶

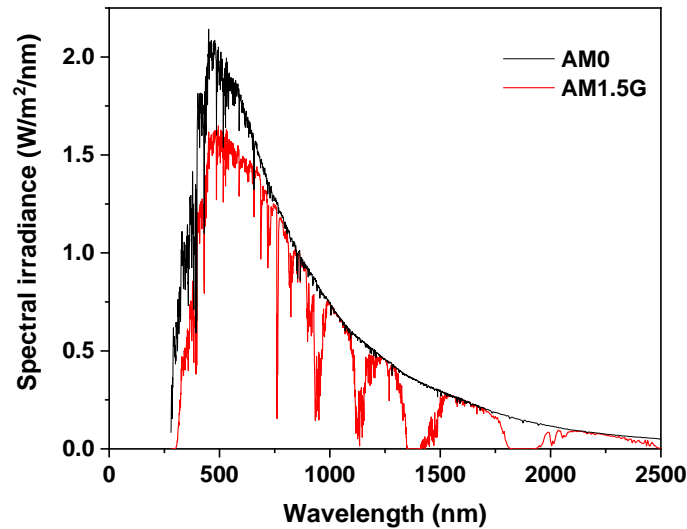


Fig. 2.7: The spectral irradiance from the sun just outside the earth's atmosphere (AM0) and terrestrial solar spectrum (AM1.5G).

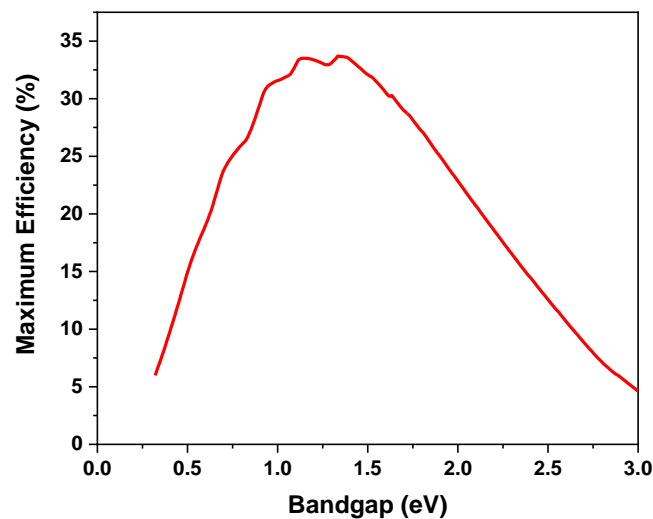


Fig. 2.8: Maximum efficiency of a solar cell with respect to the bandgap for single-junction device under AM1.5G spectrum with absorber temperature 300 K, according to Shockley-Queisser calculations.⁴⁶

2. Background

3. Perovskite Semiconductors and Solar Cells

In this chapter the characteristic properties of halide perovskite semiconductor materials, their advantages and disadvantages in regard to their application in solar cells, and different deposition techniques are discussed. Then the device architectures of existing perovskite solar cells are described in detail. A brief introduction to the current state of the research about the stability of the perovskite solar cells is also provided in the last part of the chapter.

3.1 Characteristic Attributes

3.1.1 Structural Properties

Perovskite semiconductors have a general formula of ABX_3 , where A and B are two cations of different sizes, with A being larger than B, while X is an anion which bonds to both A and B. In the case of halide perovskite A site cation can be an organic or inorganic monovalent ion (Cs^+ , Rb^+ , $CH_3NH_3^+$, $HC(NH_2)_2^+$), site B contains a metal divalent ion (Pb^{+2} , Sn^{+2}), and X is a halide ion (I^- , Cl^- , Br^-). The structural schematic of a perovskite unit cell is presented in Fig. 3.1.

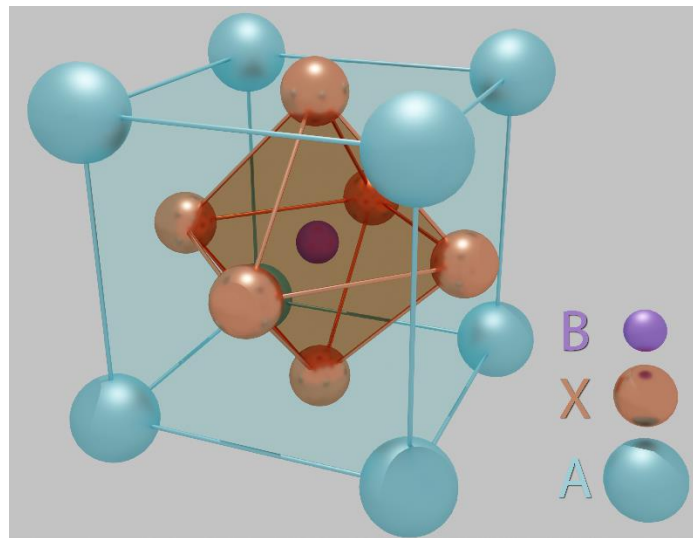


Fig. 3.1 Structural representation of a perovskite unit cell.

To estimate whether the combination of materials (A, B, and X) can make a stable ABX_3 perovskite crystal structure or not, the Goldschmidt tolerance factor t is used, as given in Eq. 3.1.

$$t = \frac{r_A + r_X}{\sqrt{2}(r_B + r_X)} \quad (3.1)$$

Where, r_A , r_B , and r_X are the effective ionic radii of the respective atoms present in the perovskite structure with $r_A > r_B$.

To achieve a stable perovskite structure, the value of the tolerance factor (t) must be in the range of $0.8 < t < 1.0$.⁴⁷ For the narrower range of t ($0.9 < t < 1.0$) a cubic structure is likely to be achieved, and a tetragonal or orthorhombic structure can be expected for smaller t ($0.8 < t < 0.9$).⁴⁸ Non-perovskite structures can be formed when the tolerance factor is higher than 1 or lower than 0.8.⁴⁹ The tolerance factor for MAPbI₃ and FAPbI₃ is 0.911 and 0.986 respectively.⁵⁰

Apart from structural properties, the characteristic electrical and optical properties associated with the perovskite semiconductor materials have some other advantages and disadvantages when they are evaluated from the perspective of their application in solar cells.

3.1.2 Promises

PSCs hold the promise of high efficiency, flexibility of processing routes and conditions, bandgap tunability, defect tolerance, flexibility, and thin film device fabrication. These advantages associated with halide perovskites are associated to their excellent optical and electrical properties which are briefly described herein.

3.1.2.1 Optical and Electronic Properties

First physical process involved in photovoltaic generation is light absorption. Metal-halide perovskites offer a great advantage of high extinction coefficient ($>10^4 \text{ cm}^{-1}$) in this respect.⁵¹ This feature enables absorption of incident light with a very thin layer of perovskite absorber. Thinner absorber layers will lead to shorter paths for charge transport. The shorter the transport paths, the lesser will be the possibilities of recombination. Thus, energetic losses will also be reduced to increase the final device voltage. Another advantage of thin absorber layer is the lesser amount of absorber material incorporated into the solar cell resulting in potentially lowering the price. Another feature of the halide perovskites which further limits the energetic losses is their sharp optical absorption edge. MAPbI₃ displays an Urbach energy of 15 meV.⁵² The Urbach energy is a measure of the energetic disorder in a semiconductor film, as it originates from local states

extending into the bandgap. These localized sub gap states lead to recombination losses. Hence, lower Urbach energy of halide perovskites infers less recombination losses.

Direct bandgap of a semiconductor material offers the advantage that they do not need any phonon i.e. thermal energy to overcome the bandgap and move to the conduction band. Contrary to silicon, organic semiconductors are believed to have a direct optical bandgap, both, experimentally and theoretically.^{53,54} However, recently it has been demonstrated that MAPbI₃ exhibits a weakly indirect bandgap of 60 meV below the direct bandgap.^{55,56} This indirect nature of the bandgap is also believed to explain the apparent contradiction of strong absorption and long charge carrier lifetime in perovskite materials.

Lower values of exciton binding energies in perovskite semiconductors are another advantage of this class of materials which helps in exciton dissociation and creation of free charge carriers at room temperature. The exciton binding energies for MAPbI₃ are estimated to be in the range of 5 – 29 meV, which means that the thermal energy at room temperature (26 meV) is sufficient to efficiently dissociate the excitons.⁵⁷

Another important property of PSCs is their charge carrier lifetime which defines the diffusion length in combination with the charge carrier mobility, and hence determines the probability of a photogenerated charge carrier to reach the respective electrode. The charge carrier lifetime is approaching μs in mixed halide perovskite semiconductors.⁵⁸

Long charge carrier diffusion lengths, among other things, lead to outstanding power conversion efficiency of perovskite solar cells. The charge carrier diffusion lengths are estimated to be 130 nm and 100 nm for electrons and holes, respectively in the case of MAPbI₃⁵⁹ and more than 1 μm in the case of MAPbI_{3-x}Cl_x.⁶⁰ Furthermore, the absorption coefficient for MAPbI₃ is estimated to be $1.5 \times 10^4 \text{ cm}^{-1}$ at 550 nm, representing a penetration depth of 0.66 μm for light of 550 nm. While, at 700 nm, the absorption coefficient is $0.5 \times 10^4 \text{ cm}^{-1}$, which represents a penetration depth of 2 μm .⁵⁹

3.1.2.2 Bandgap Tunability

Another promising quality that perovskite semiconductors possess is the possibility of their bandgap tunability by using a mixture of constituent materials. Upon changing the concentration of halide ion (I⁻, Br⁻, Cl⁻) or metal cation (Pb⁺², Sn⁺²), the bandgap can be tuned according to the

substituent concentration. It was successfully demonstrated by Noh *et al.* that the bandgap of perovskite ($\text{MAPb}(\text{I}_{1-x}\text{Br}_x)_3$) can be tuned between 1.57 eV and 2.29 eV by progressively substituting I⁻ with Br⁻.⁶¹ Similarly, Prasanna *et al.* also demonstrated the bandgap tunability of a perovskite with composition $\text{FA}_{1-x}\text{Cs}_x\text{Pb}_{1-y}\text{Sn}_y\text{I}_3$ between 1.24 eV and 1.56 eV by substituting Pb^{+2} with Sn^{+2} .⁶² This flexibility of bandgap tunability enables to produce solar cells with different bandgaps which can later be used in tandem cells with their other market-dominating counterparts like silicon solar cells. This technique is promising to exceed the SQ limit of a single junction solar cell.

3.1.2.3 Defect Tolerance

Another advantageous feature of halide perovskites is their peculiar defect physics leading to their superior defect tolerance. For a comparison, crystalline silicon absorber layer must exhibit a low defect density ($< 10^{-16} \text{ cm}^{-3}$) for decent semiconducting properties.⁶³ This behavior is termed as defect-tolerance, schematically presented in Fig. 3.2.⁶⁴ For this reason, expensive high temperature purification process is required for Si. On the contrary, the perovskites exhibit a mixture in between these two extremes of defect tolerance and intolerance, hence the optoelectronic properties of perovskite material are impacted only up to a small extent by the high defect density ($\sim 10^{20} \text{ cm}^{-3}$).⁶⁵ A certain density of deep as well as shallow traps (I⁻, MA^+ , Pb^{+2} ions) can also be formed in perovskite material. Even upon having a high defect density, not many of these defects act as trap sites to result in creation of recombination pathways. Yin *et al.* used the DFT calculations to suggest that there are various defects with a low formation energy in MAPbI_3 perovskite, most of which, serve as shallow trap states situated within or close to the MAPbI_3 bands.⁶⁶

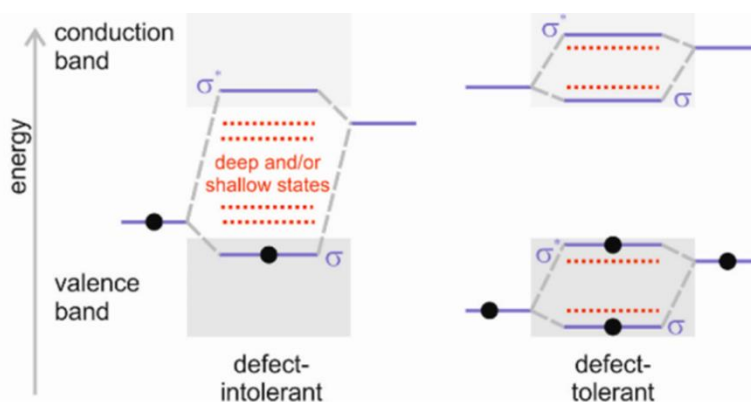


Fig. 3.2: Schematic representation of the intolerant and defect tolerant semiconductor material in terms of comparative trap energies. Reproduced with permission from Ref. 64. Copyright 2017, American Chemical Society.

3.1.2.4 Ease of Processing

The flexibility of processing routes for PSCs, like spin coating, blade coating, drop-casting, inkjet printing, and evaporation, due to high defect tolerance, makes them promising candidates to flourish on the industrial level. The freedom of solution processibility at low temperatures (~ 100 °C) opens the way toward scalable techniques such as printing.⁶⁷ This feature of the PSCs is showcased recently in October, 2020 by the Saule Technologies, a Polish PV start-up, by premiering their flexible perovskite modules embedded solar blinds.⁶⁸

The advantages like large diffusion length, high absorption coefficient, low exciton binding energy, and direct bandgap are the key factors making the PSCs very efficient in power conversion with minimum losses. The currently reported efficiency of small area (~ 0.1 cm²) PSCs is 25.5%, while 18% for minimodule (19 cm² area, 7 serial cells) achieved after a decade of research.³⁵

3.1.3 Challenges

Apart from many advantages, perovskite solar cells are also facing some challenges, like scalability (retaining the high performances with increase in area) and longevity being the most important, which are under intensive research recently. Other problems faced by the PSCs are photo-induced defect formation, ion migration, charge accumulation at the interfaces, and decomposition upon long-term ambient exposures.

3.1.3.1 Scalability

All the reports on high performance PSCs involve lab-scale small area ($\sim 1 \text{ cm}^2$ or smaller) devices. Although, in terms of scalability, recent research efforts give a hope of scalable production of PSCs in addition to retaining the advantage of high efficiency. For example, Panasonic Corporation has recently achieved the highest efficiency of 16.09% for an inkjet-printed perovskite solar module with an aperture area of 802 cm^2 .⁶⁹ However, the performance gap between small area cell (25.5%) and module (16.1%) is much larger (9.5%) than predicted (3 – 4%) based on the common scaling behavior of established PV technologies.⁶⁷ Longevity, on the other hand, still remains as a key challenge for perovskite PV research community.

3.1.3.2 Longevity

Regarding stable long-term performance, the concerned aspects are; thermal instability at elevated temperature, photo-degradation upon prolonged light exposures, and absorber material decomposition when exposed to oxygen or humidity. Regarding thermal degradation, the instability arises from the phase transition of perovskite absorber material from a photo-active to photo-inactive phase at high temperature. The workhorse perovskite absorber, MAPbI_3 , undergoes a phase transition from the tetragonal to cubic phase at $\sim 54 \text{ }^\circ\text{C}$,⁷⁰ a temperature that is of relevance during typical solar cell operation. Therefore, it is imperative to develop perovskites insensitive to composition instabilities under stress conditions for solar cell operation. In addition to the thermal instability, PSCs undergo decomposition when exposed to light. PSCs degrade in three different ways: (i) decomposing back into the constituent materials leaving the by-product $\text{CH}_3\text{NH}_2 + \text{HI}$ behind. This type of degradation is seen to be reversible when the solar cells are kept in dark for certain periods; (ii) formation of $\text{NH}_3 + \text{CH}_3\text{I}$ after the decomposition of precursor materials. This decomposition is considered to be irreversible. And lastly, (iii) a reversible $\text{Pb(0)} + \text{I}_2(\text{g})$ photo-decomposition reaction of the degradation by-product PbI_2 .^{19,20,71,72} In humid environment the perovskite absorber material hydrolyzes and undergoes irreversible degradation and decomposes back into the precursors.^{73,74} In presence of oxygen, it oxidizes, dissociates, and decomposes back into the constituents.^{75,76} The structural deterioration happens upon oxygen incorporation, whether it be interstitial or substitutional, giving rise to an electronic acceptor effect (increase of hole, decrease of access electron concentration).⁷⁵ A detailed current state-of-the-art research on thermal, ambient, and photostability and degradation pathways is presented in Sec. 3.7.

Intensive research, characterization, and stability testing of perovskite solar cells have revealed several mechanisms associated with them which are found responsible for their degradation and temporary or permanent restricted performance upon illumination. All these mechanisms have been seen to exist in the PSCs and they explain the unique materials and device characteristics and instability issues of halide perovskites.

3.2 Performance limiting Mechanisms

Up till now, several mechanisms have been discovered and investigated which hamper the devices performance and cause degradation. An overview of the performance limiting mechanisms to understand their cause and effect on device stability and efficiency is presented in this section.

3.2.1 Intrinsic and Extrinsic Defects

It is known that defects in the light-harvesting layer influence the device performance metrics of the solar cells. The existence of defect states is described in terms of defect density and measured as number of defects per unit volume (cm^{-3}). A defect state can exist in the intrinsic film natively during preparation or can be generated afterwards upon degradation. Such defect states can serve as recombination sites leading to reduction of free charge carriers. Single crystal MAPbI_3 absorbers are reported to have very low defect density ($\sim 10^{11} \text{ cm}^{-3}$)⁷⁷ while the solution processed polycrystalline MAPbI_3 generally have high defect densities ($\sim 10^{16} \text{ cm}^{-3}$)⁷⁷ due to an abundance of crystal defects. The trap states associated with perovskite absorbers are point defects, such as atomic vacancies (atoms missing from the lattice), interstitials (atoms occupying the space between atoms in the lattice), and anti-site substitutions (atoms occupying the wrong site in the lattice), or higher-dimensional defects, such as dislocations, grain boundaries, and precipitates. A schematic illustration of all the possible lattice defects is given in Fig. 3.3.⁷⁷

3. Perovskite Semiconductors and Solar Cells

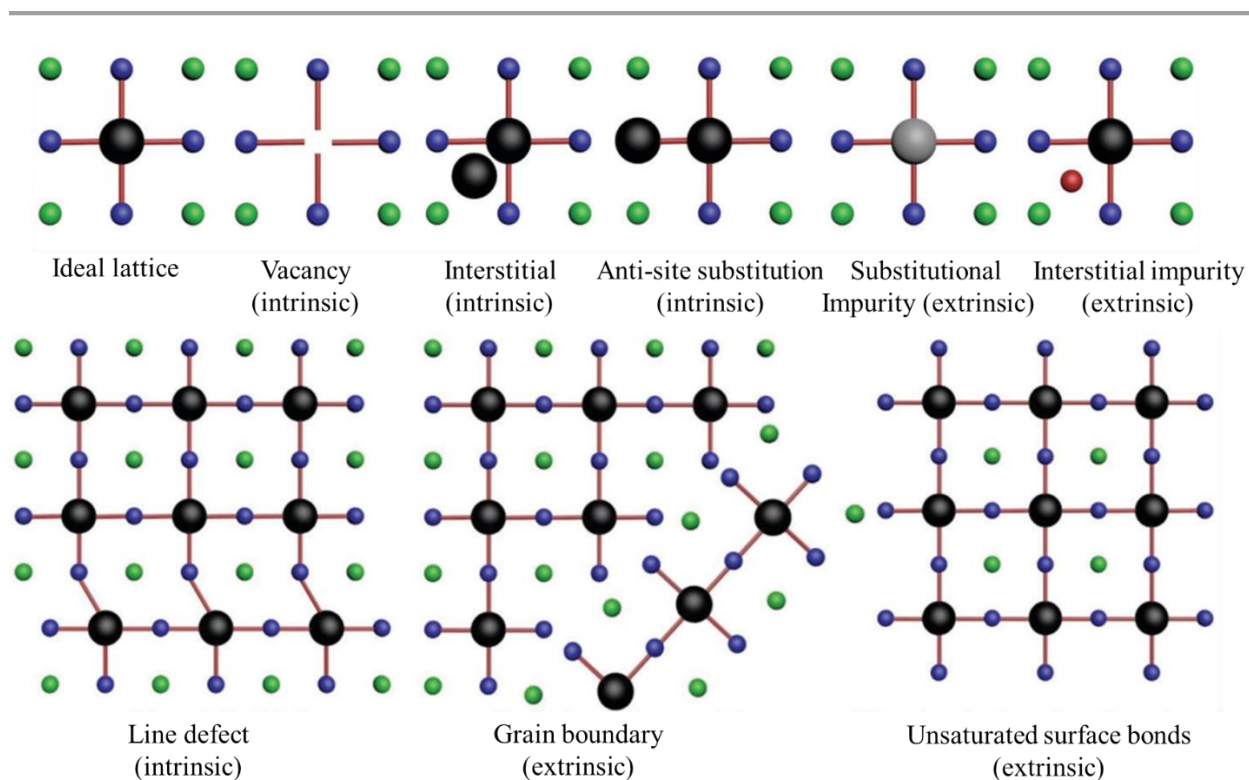


Fig. 3.3: Schematic overview of different intrinsic and extrinsic defect types in halide perovskite layers as compared to an ideal lattice. Reproduced from Ref. 77. Copyright 2020, The Royal Society of Chemistry.

The general defects generated in perovskite absorbers upon degradation are found to be iodine interstitials, lead (Pb^{+2}) vacancies, and methylammonium (MA^+) vacancies with activation energies 0.3 eV, 2.3 eV, and 0.5 eV, respectively, estimated via density functional theory (DFT) calculations.^{78,79} In addition to DFT calculations, thermally stimulated current (TSC) measurements are also employed by many research groups to unveil the nature of trap states formed upon degradation and to estimate their activation energies. Baumann *et al.* used TSC measurements on the MAPbI_3 films to demonstrate the existence of electronic trap states with an activation energy of 0.5 eV and a concentration of $1 \times 10^{21} \text{ cm}^{-3}$.⁸⁰ Hu *et al.* investigated the role of the cation addition (Cs and Rb) to the mixed halide (I and Br, 83% and 17%, respectively) FA/MA perovskites via TSC measurements.⁸¹ It was demonstrated that an FA/MA film which exhibits trap states with activation energy ~ 0.25 eV with a concentration of $7.3 \times 10^{16} \text{ cm}^{-3}$, the activation energy of traps reduced to 0.195 eV and 0.10 eV and concentration of traps to $2.2 \times 10^{16} \text{ cm}^{-3}$ upon addition of 5% Cs. These results are also complemented by another study where the trap states with activation energy ~ 0.19 eV and concentration $1.6 \times 10^{16} \text{ cm}^{-3}$ are found in pristine films with a triple

cation composition.⁸² Moreover, a further addition of 5% Rb reduced the activation energy of traps further to 0.20 eV and 0.07 eV and trap concentration to $1.6 \times 10^{16} \text{ cm}^{-3}$. A depiction of these defects frequently found in perovskite absorbers is presented in Fig. 3.4 (a – c).

3.2.2 Ion Migration and Hysteresis

The ionic species serving as trap states formed upon photo-exposure can also migrate under the influence of applied or built-in electric field (depicted in Fig. 3.4 (d)). The ionic species migrating upon illumination are found to be MA^+ and I^- ions in MAPbI_3 solar cells. Futscher *et al.* estimated the activation energies (via transient ion-drift measurements) for the migration of the mobile ions as 0.29 ± 0.6 eV and $0.39 - 0.90$ eV for I^- and MA^+ , respectively.⁷⁹ Furthermore, the activation energy of I^- mobile ions was found very reproducible, while the activation energy of the mobile MA^+ ions is reported to be strongly device and fabrication conditions dependent.⁷⁹ The high energy for Pb^{+2} cation migration (2.3 eV) suggests their immobile nature in the lattice.⁸³ On the other hand, I^- ions are found to be more mobile, owing to their lower activation energies, with diffusion constants on the order of $\sim 10^{-12} \text{ cm}^2 \text{ s}^{-1}$ being four orders of magnitude higher than MA^+ ions i.e. $10^{-16} \text{ cm}^2 \text{ s}^{-1}$ at 45°C .⁸³ The smaller diffusion coefficient for MA^+ ions as compared to I^- refers that MA^+ species must have a considerable higher activation energy compared to iodine species, which is in agreement with DFT calculations.

The diffusion of ions within the crystal lattice leads to several problems. The ions mobilization in response to an electric field is considered responsible for the commonly known current-voltage hysteresis in solar cells. Since there exists a complex interplay between ionic and electronic response with the application of an electric field, thus the exact causes for hysteresis are not easy to identify. However, recent studies based on experimental and theoretical results propose that a combination of ion migration and interfacial trap states results in hysteresis.

3.2.3 Interfacial Charge Accumulation and Grain Boundaries

The diffusion of charged species within absorber layer leads to their accumulation on the anode or cathode interface depending on their polarity (depicted in Fig. 3.4 (e)). Weber *et al.* used time resolved Kelvin probe force microscopy (tr-KPFM) technique at cross-section of the cleaved devices and concluded that the formation and release of interfacial charges is the dominating factor of hysteresis.⁸⁴ The formation and release times were recorded to be ~ 3 ms and ~ 120 ms,

respectively, after switching on an electrical field, resulting in the stabilization of charges at the interfaces. On the theoretical side, Neukom *et al.* showed that the efficient and hysteresis-free devices are feasible if charge carrier diffusion length of the perovskite absorber layer is long and the surface recombination velocity is low.⁸⁵ On the similar grounds, grain boundaries can also serve as charge accumulation sites (Fig. 3.4 (f)) since they also feature the lattice discontinuity.^{86,87} The exact interplay of grain boundaries and ion migration remains inconclusive. Yun *et al.* used KPFM to show efficient charge carrier separation and collection at the grain boundaries leading to higher current collection than the grain interior.⁸⁸ These results were suggested to be related to ion migration. On the contrary, Baena *et al.* demonstrated a reduction in hysteresis for the devices based on absorber layers with larger grain size (i.e. lesser grain boundary density).⁸⁹ It was concluded from intensity-modulated photocurrent spectroscopy that ionic defect movement is faster for the reduced number of grain boundaries, referring to the ion movement mitigation by the grain boundaries. Furthermore, release of the accumulated charge carriers at the interfaces and grain boundaries is reported to heal or recover the device performance upon storage in dark.⁸⁶

Perovskite solar cells are also known to exhibit so-called light soaking effect, described as the improved device performance upon prolonged light exposure. Mosconi *et al.* observed an increase in photoluminescence lifetime and total intensity, eventually stabilized, for MAPbI₃ films.⁹⁰ It was proposed that this behavior is associated to trap density reduction from $\sim 10^{17} \text{ cm}^{-3}$ to stabilized value of $\sim 10^{16} \text{ cm}^{-3}$ in 10 min. Annihilation of iodine vacancies and interstitials was proposed to be promoted leading to improved crystal environment by eliminating the associated trap centers and resulting in better device efficiency upon illumination. Similar conclusion was also drawn by Cai *et al.* who studied caesium lead iodide (CsPbI₃) based perovskite solar cells and reported that the defect density is reduced due to passivation by the photogenerated charge carriers over short time span upon illumination leading to enhanced device performance.⁹¹

3.2.4 Trap-assisted Recombination

Defects, whether they be intrinsic or extrinsic, in crystal lattice of the semiconductor materials can serve as recombination sites leading to reduction in V_{OC} . The commonly adopted technique to analyze the recombination mechanism is the ideality factor. Tress *et al.* conducted a study by performing ideality factor measurements on planar and mesoporous architectures of triple cation (Cs_{0.05}(MA_{0.17}FA_{0.83})_{0.95}Pb(I_{0.83}Br_{0.17})₃) based PSCs, pristine and aged (for 8 days under white light

1 sun illumination at 65 °C in N₂) to conclude that recombination is not affected severely by the n-type contact in comparison to p-type contact.⁹² The ideality factor values for planar and mesoporous architectures were found identical (~1.6) representing SRH recombination via bulk defects. On the other hand, the aged devices showed ideality factor values of ~2 exhibiting the increase in SRH recombination via bulk defects. Furthermore, Sherkar *et al.* studied the significance of grain boundaries, interface traps, and defect ions in n-i-p as well p-i-n PSCs in terms of recombination via ideality factor.⁹³ It was found that the trap-assisted recombination at the interfaces is the dominant loss mechanism even in presence of traps at grain boundaries.

Moreover, due to the superior quality of ETL/perovskite interface in n-i-p cells, the trap-assisted recombination is suppressed in comparison to the p-i-n devices. Similar conclusion is also drawn by Caprioglio *et al.* via experimental and numerical simulations that the ideality factor of ~1.3 is a consequence of interfacial recombination rather than an interplay between SRH and band-to-band recombination in the absorber layer.⁹⁴ Another complementary study conducted by Stolterfoht *et al.* investigated the role of HTL (PTAA)/perovskite (triple cation) interface for different thicknesses of HTL via ideality factor measurements.⁹⁵ It was found that inefficient charge collection at HTL/perovskite interface causes recombination losses leading to an ideality factor of ~1.5. With these findings, an optimization of HTL is carried out to yield a ~19% efficient device with 1 cm² area.

3.2.5 Charge Transport Layers and Extrinsic Ion Infiltration

Incomplete surface coverage of ETLs can also cause performance decline in PSCs. Similarly, surface cracks or thermally induced structural deformations upon temperature treatment of the ETL can also play a role in overall instability of the solar cells. The dopant ions in HTL are also reported to infiltrate to the absorber layer over longer operational cycles which result in deteriorating the performance. In terms of HTL, most of the laboratory scale n-i-p PSCs use Spiro-OMeTAD as HTL, as done in this dissertation. To increase the hole conductivity of Spiro-OMeTAD, it is doped with, lithiumbis(trifluoromethanesulfonyl)imide (LiTFSI) salt.⁹⁶ Apart from intrinsic ion (MA⁺, Pb²⁺, I⁻) migration in PSCs, extrinsic ions like Li⁺ can also diffuse through the device stack under illumination and hamper the performance. Li *et al.* studied the diffusion of Li⁺ ions in MAPbI₃ and MAPbBr₃ based solar cells (using time-of-flight secondary-ion mass spectrometry) to find that Li⁺ ions diffuse through the device stack to accumulate in the ETL.⁹⁷

This phenomenon can lead to device degradation. Investigating the impact of other layers on perovskite absorber further, Cacovich *et al.* employed scanning transmission electron microscopy in conjunction with energy-dispersive x-ray spectroscopy on PSCs subjected to white light illumination for 100 hours to observe that gold (Au) precipitates at HTL (spiro-OMeTAD)/perovskite interface as well as forms clusters within the perovskite active layer.⁹⁸ This Au infiltration can lead to creation of short circuiting pathways to severely hamper the device performance.

In the following, an overview of these performance limiting mechanisms is given in pictorial form (Fig. 3.4) and a brief description of their nature is provided in tabular form (Table 3.1) as well. The mechanisms depicted in Fig. 3.4 either come into play immediately after the device is illuminated or subjected to applied bias and/or emerge and progress over time as the device continues to perform under test or operational circumstances.

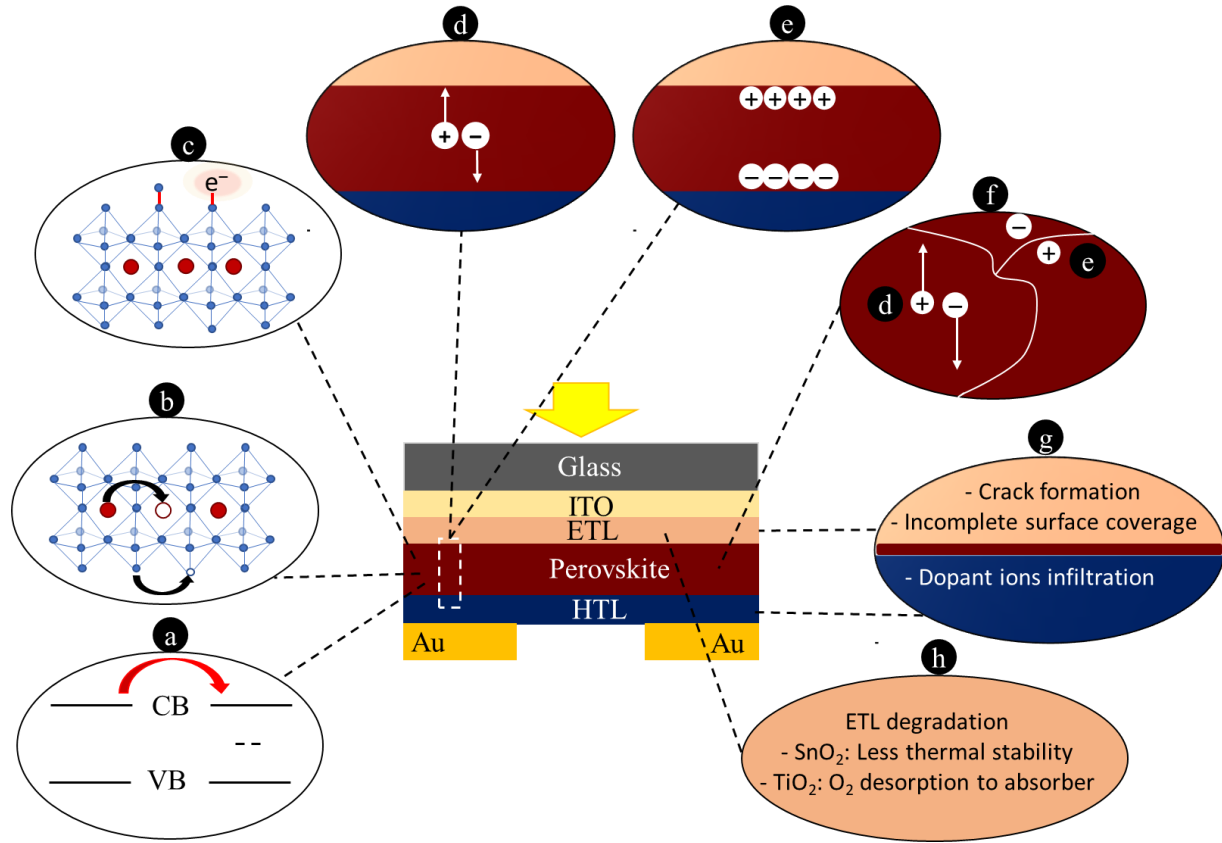


Fig. 3. 4: An overview of the mechanisms present in PSCs, (a) trap state formation, (b) ion movement leading to vacancy creation, (c) ionic and charge trap state formation, (d) ion migration, (e) charge accumulation at interfaces, (f) ion migration within grains and charge accumulation at grain boundaries, (g) defects in charge transport layers, (h) intrinsic instability of ETLs.

Table 3. 1: Description of the mechanisms taking place in halide perovskite solar cells.

Sr. No.	Mechanism	Nature
(a)	Trap state formation	electronic
(b)	Ion movement leading to vacancy creation	ionic
(c)	Ionic and charge trap state formation	ionic + electronic
(d)	Ion migration	ionic
(e)	Charge accumulated at interfaces	electronic
(f)	(d) and (e) at grain boundaries	ionic + electronic
(g)	Defects in charge transport layers	structural
(h)	Degradation of ETLs	chemical

This table and description of the mechanisms known for halide perovskite materials and solar cells will serve as referral point to explain the characterization and analysis of the solar cells. Furthermore, these mechanisms will also be referred to explain the poor device performance and instabilities caused upon prolonged photo exposure in the rest of this dissertation.

3.3 Stability and Energy Efficiency

In finding the balance between cost-effectiveness and high efficiency, the short lifetime of perovskite solar cells is still a challenge for PV research. To measure the usefulness of perovskite solar cells in terms of cost and stability, there are some pre-existing parameters and test standards that can be used to evaluate the effectiveness of PSCs.

3.3.1 Levelized Cost of Electricity

The current market-dominating PV technology is silicon which holds more than 95% of the market share.³⁹ The reason behind this dominance is the cost-effectiveness of silicon PV over its lifetime.. A useful parameter known as the levelized cost of electricity (LCOE), defined as the measure of the average net present cost of electricity generation for a production unit over its lifetime, is used to evaluate the long-term cost of energy of a PV technology. For a specific installation location, the LCOE depends on three factors, (i) cost of the system, (ii) efficiency, and (iii) lifetime.⁹⁹

Validating the cost of silicon and perovskite PV on these parameters, the balance shifts in favor of silicon PV due to the limited lifetime of the perovskite solar cells. The current average cost of silicon PV is 0.28 – 0.40 \$/W,^{100,101} while the minimum modeled cost for perovskite PV is predicted to be 0.53 \$/W in case of a mass production of 1 GW/year, which increases even further to 0.85 \$/W for a production of 10 MW/year.¹⁰² The critical limiting factor arises from the shorter lifetime of the PSCs as compared to silicon which is nowhere near 25 years lifetime yet. The silicon PV module is guaranteed to deliver a minimum of 80 – 90% of the rated power after 25 – 30 years,^{103–106} depending on the technology and type of encapsulation varying among the suppliers, while perovskite solar cells can only reach one year. Considering these factors, there is a lot of room to improve the stability of perovskite solar cells to compete with the industrialized PV technology to give it a respectable market share.^{107,108}

3.3.2 Stability Test Standards

The stability testing of PV modules is conducted according to some existing test protocols. The International electrotechnical commission (IEC) provides the test standards and protocols with necessary requirements. Every PV product must satisfy the IEC test standards before commercialization. The test routines used for silicon and thin-film PV are IEC 61215 and 61646 respectively, which have been combined recently into one norm known as IEC 61215-1:2016. This protocol consists of a series of stress tests to evaluate the performance stability of a PV product. The most important test routines included in IEC 61215-1:2016 are described below along with the stress conditions and duration.

3.3.2.1 UV preconditioning test

During the UV preconditioning test (not to be confused with the outdoor exposure test which is conducted to test preliminary resilience to outdoor conditions), the solar cells are exposed to UV radiation. Overall, the module should be subjected to at least 15 kWh m^{-2} of UV radiation between 280 – 400 nm, with at least 5 kWh m^{-2} between 280 – 320 nm. A minimum threshold on the incident UV radiation is imposed to make sure that a reasonable amount of the UV photons reaches to the solar cell since some of the irradiated UV dose can be absorbed by the front glass covering. This incident UV dose is modeled from the solar irradiation and the spectral transmittance of the laminated material. The UV radiation should not exceed 250 Wm^{-2} between 280 and 400 nm as significantly large amount of high energy UV photons may induce an unrelated damage.¹⁰⁹ The purpose of this test is to identify the materials that are susceptible to UV degradation. The UV exposure duration proposed is sufficient to check the stability of the encapsulant materials which undergo discoloration over extended exposure times.¹¹⁰ However, the vulnerability of the perovskite absorber material to degrade under UV demands a more thorough and decisive test protocol. Further details on the UV preconditioning test are given in Chapter 5 section 5.3.1.

3.3.2.2 Thermal Cycling Test

In the thermal cycling test routine, the modules are subjected to a temperature change from -40 to $85 \text{ }^\circ\text{C}$ for a total of 200 cycles. The minimum time for which the module should stay at the extreme temperatures (-40 or $85 \text{ }^\circ\text{C}$) must not be less than 10 minutes. The maximum temperature ramp

should be 100 °C per hour. This test routine provides insights, whether the solar cells can withstand the field temperatures over extended operational lifetime or not.

3.3.2.3 Damp Heat Test

The humidity stability of a PV module is tested by the damp heat test, where the solar module is held at $85 \pm 5\%$ relative humidity at a temperature of 85 ± 2 °C for 1,000 hours. The purpose of this test is to determine the ability of the module to resist and withstand the long-term exposure to the humidity. The importance of this test can be realized from the fact that it accounts for 17 and 22% of the total failures for crystalline and thin-film PV in the field, respectively.¹¹¹ Delamination, corrosion, and detachment of the module components can take place as a result of humidity ingress.

3.3.2.4 Humidity Freeze Test

In the humidity freeze test, the modules are subjected to 10 cold-heat cycles. During these cycles, the temperature is varied from -40 to 85 ± 2 °C. One complete cycle runs approximately for one day. The temperature of 85 °C is held for at least 20 hours with a relative humidity of $85 \pm 5\%$ and the minimum temperature of -40 °C for at least 30 min. Additionally, the temperature ramp from 0 to -40 °C ($200 - 72$ °C/hour) can be twice as fast as the cooling temperature ramp from 85 to 0 °C ($100 - 72$ °C/hour). The objective of this test is to determine the module's ability to withstand the conjunction of high temperatures and humidity, followed by extremely low temperatures. Low temperatures are generally known to slow down the chemical processes, however, the temperatures reaching the glass transition point can drastically impact the encapsulant polymeric properties. Furthermore, the extreme temperatures are to observe the stability as drastic temperature changes can cause thermo-mechanical stress that can result as delamination of the module. The module failure rate for this test are 10 and 6% for crystalline and thin-film PV, respectively.¹¹¹

These test standards, developed after decades of experience and research, are now widely accepted and agreed to by the suppliers and the buyers. Thus, these must be fulfilled by any PV technology to pave its way to the market. However, for research purposes and uniformity of reported results, the perovskite and organic PV community has devised a set of test protocols suitable for infant technology like perovskite solar cells. An updated version of these test protocols has been released recently.¹¹²

3.4 Approaches to Enhance Stability and Efficiency

Severe instability challenges posed by the perovskite absorber material are taken on by the research community to come up with several routes potentially capable of solving the problem. These approaches involve inclusion of two-dimensional (2D) perovskite in 3D as mixed or layered structure, surface passivation, and use of downshifting materials. These approaches are of particular importance in addition to few others (compositional engineering and interface modification, see Sec. 4.1.2 – 4.1.4). Herein, these approaches are described to view their potential for stability and efficiency enhancement.

3.4.1 Incorporation of 2D Perovskites

2D perovskites, also known as Ruddlesden–Popper perovskites (named after their first reporters in 1957) have the general formula $(\text{RNH}_3)\text{A}_{n-1}\text{B}_n\text{X}_{3n+1}$ where $n = 1, 2, 3, \text{ to } \infty$, and $\text{A}_{n-1}\text{B}_n\text{X}_{3n+1}$ is the common 3D perovskite, as schematically illustrated in Fig. 3.5.¹¹³ Here, the 3D perovskites are separated by the introduction of a long-chain hydrophobic organic cation R-NH_3 . Thus, the 2D/3D perovskite secure the advantage of long-term stability and high efficiency at the same time. A common 2D perovskite employed in PSCs is phenylethyl ammonium (PEA). In mixed 2D/3D multidimensional, Grancini *et al.* employed protonated salt of aminovaleric acid iodide ($\text{HOOC}(\text{CH}_2)_4\text{NH}_3\text{I}$, AVAI) PbI_2 to mix with $\text{CH}_3\text{NH}_3\text{I}_3:\text{PbI}_2$ and reported an exceptionally 1-year stable encapsulated PSC under 1 sun illumination at 55 °C in ambient.⁷⁴ Furthermore, as compared to 2D/3D mixed perovskites, the 2D perovskites can be controllably inserted to mainly exist on the surface or the grain boundaries to take advantage of both 2D and 3D perovskite. This can be done by tuning the stoichiometric composition and concentration of precursor solutions, as demonstrated by Zou *et al.* who prepared a thin layer of 2D perovskite ($(\text{BA})_2\text{PbI}_4$) between the post-treated n-butylamine iodide (BAI) and the residual PbI_2 through chemical reaction on a MAPbI_3 film.¹¹⁴ The resulting PSCs showed PCE >18% and retained 80% of the initial performance after storing in ambient without encapsulation for more than 2,000 hours.

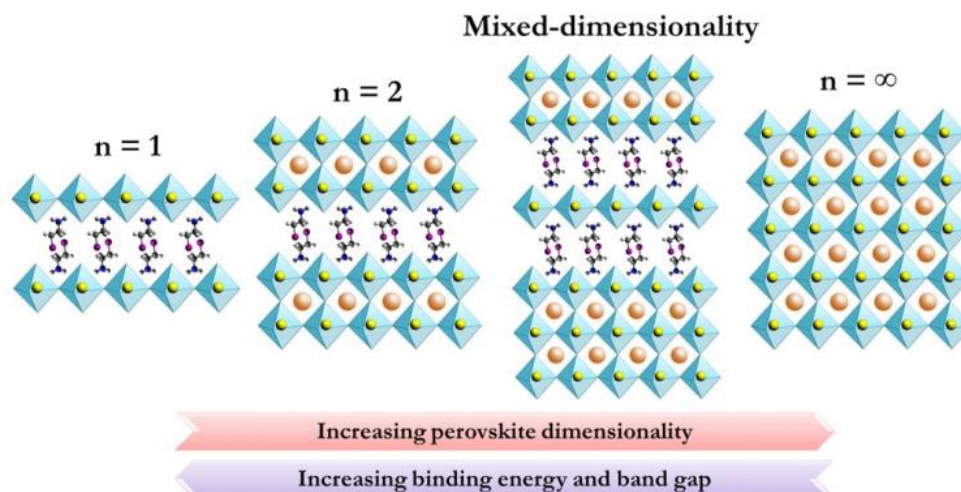


Fig. 3.5: Schematic illustration of the crystalline structure of perovskites with n being the dimensionality ($n = 1, 2, \dots, \infty$). Reproduced with permission from Ref. 113. Copyright 2016, Wiley-VCH.

3.4.2 Surface Passivation

Recently, in addition to using 2D perovskites as passivation layers, few organic materials are also reported to effectively passivate the surface traps and mitigate the negative effects of grain boundaries to enhance the device performance as well as stability. The schematic illustration of the surface passivation is presented in Fig. 3.6 (a). Passivation layers reduce the surface defects by passivating them and leading to less recombination and hence incremental effect in V_{OC} , as exhibited in Fig. 3.6 (b). Jiang *et al.* applied an organic halide salt phenethylammonium iodide (PEAI) to suppress the surface defects and increasing the steady state device performance from 21.3% to 23.2%.¹¹⁵ Moreover, the PEAi is reported to serve as more effective surface passivation additive performing much better in increasing the PCE as compared to the 2D layered PEA_2PbI_4 perovskite. Additionally, in terms of device stability, the PSCs were tested under $1,000 \text{ Wm}^{-2}$ light irradiation in N_2 at 25°C and no performance deterioration was detected after 40 hours. Another such example is demonstrated by Byranvand *et al.* who deposited a finely controlled 1 nm thin homogeneous layer of poly(p-xylylene) (PPX) deposited via chemical vapor deposition.¹¹⁶ It was reported that the 1 nm thin layer passivates the surfaces defects effectively to increase the device PCE from the 19.4% for the control devices to 20.4% for 1 nm PPX coated ones. In terms of stability, the 5 nm thick PPX devices (unencapsulated) retained 60% of their initial PCE after 30

days in ambient (40 – 50% RH) as compared to 1 nm thick PPX which lost 65% of initial PCE and reference devices which were completely dead in 24 days. There are few other insulating polymer layers (PMMA, poly(ethylene oxide) (PEO), Polystyrene, poly(4-vinylpyridine) (PVP); to name a few) which are reported to work equally well for surface passivation to suppress the recombination mechanism.^{117–120}

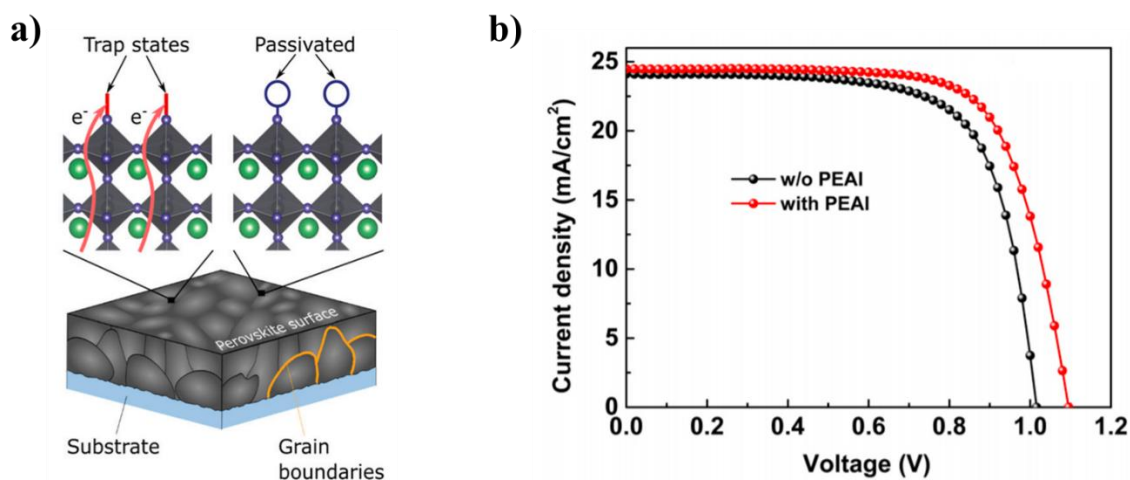


Fig. 3.6: (a) Schematic illustration of polymeric passivation coatings acting to mitigate the surface trap states. Reproduced from Ref. 77. Copyright 2020, The Royal Society of Chemistry. (b) Difference in V_{OC} through J - V scan before and after the surface passivation. Reproduced with permission from Ref. 115. Copyright 2019, Nature Publishing Group.

3.4.3 Luminescent Downshifting Materials

The luminescent downshifting (LDS) materials can be described as the species that involve the conversion of one photon of high energy light – which is inefficiently absorbed by the photovoltaic material – to one photon of lower energy that can be efficiently absorbed by the PV absorber material. LDS materials were first used in PV by Hovel *et al.* to enhance the short wavelength response of solar cells.¹²¹ Since then, there are numerous examples of using different LDS materials to demonstrate a gain in device performance up to some extent. Álvarez *et al.* conducted a comprehensive study on multiple solar devices (CdTe, CIGS, m-Si) with a range of commercially available LDS dyes like, Lumogen (BASF, Germany) violet (V570), yellow (Y083 and Y170), Orange (O240), Red (R300), and Keyplast (United Kingdom) yellow (KPY).¹²² These dyes are embedded in ethylene vinyl acetate (EVA) or poly-methyl methacrylate (PMMA) to apply on the solar cells. It was concluded that the CdTe and CIGS solar cells show significant performance

enhancement since due to the top cadmium sulfide (CdS) buffer layer their short wavelength response is poor (see Fig. 3.7). In CdTe devices the response to wavelengths shorter than 500 nm improved for V570 (maximum 3.5% at 362 nm), KPY (maximum 20% at 408 nm), and Y083 (maximum 16% at 439 nm). In CIGS devices only V570 dye doping yielded a significant gain of 2.2% in short-circuit current density, while in m-Si solar cells only V570 dye offered some gain. Overall, it was concluded that the dyes absorbing at longer wavelengths lead to a reduction in the device performance. Klampaftis *et al.* also reviewed the use of LDS in commercially available PV technologies and concluded that CdS buffer layer based solar cells (CdTe and CIGS) exhibit performance enhancement upon use of LDS materials.¹²³ Other PV technologies (c-Si, a-Si, GaAs) do not seem to benefit largely because of their higher spectral response at short wavelengths.

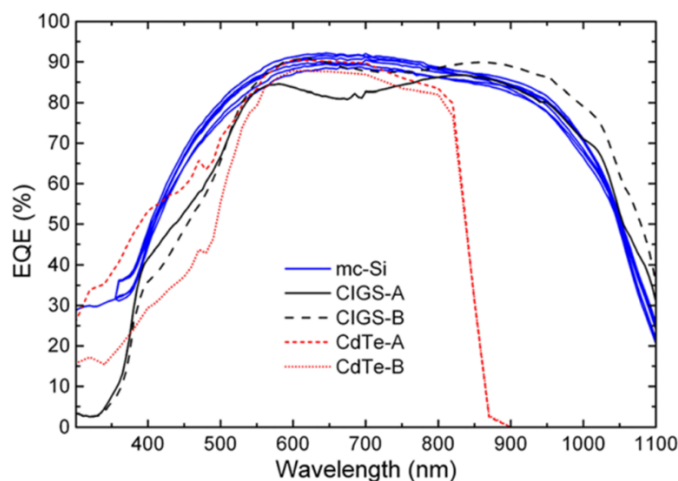


Fig. 3.7: Comparison of the EQEs of the six mc-Si, two CIGS and two CdTe solar cells or mini-modules prior to the addition of any LDS layers. Reproduced with permission from Ref. [122]. Copyright 2015, Wiley VCH.

In PSCs, the LDS materials can be used to downshift the troublesome UV radiation to enhance the device stability. Although, the efficiency enhancement via LDS application seem a challenging task provided the fact that the spectral response of PSCs in short wavelengths is already good, however, there exist few reports in literature where the PCE enhancement is demonstrated successfully. Bella *et al.* were among the first to employ LDS doped fluoropolymer to report a 1.3 mA cm⁻² absolute gain in J_{SC} (and 1.4% absolute gain in PCE) with a 2 wt% loading of V570 in fluorinated coating on front side of MAPbI₃ based PSC.¹²⁴ The EQE spectra revealed that the J_{SC} gain is achieved from the improved short wavelength response (between 300 to 390 nm) of the

PSCs (see Fig. 3.8). Upon UV stability test, these devices exhibited excellent performance by retaining 98% of their initial PCE after 3 months of exposure to a 50 Wm^{-2} of UV radiation in an inert atmosphere. Cui *et al.* used Mn^{4+} doped $\text{Sr}_4\text{Al}_{14}\text{O}_{25}$ inorganic LDS material in PMMA layers on the glass side of MAPbI_3 based PSCs to realize efficiency as well as stability enhancement.¹²⁵ The relative PCE enhancement was reported to be $\sim 7.7\%$, while stability tests conducted in dry cabinet ($<30\%$ RH) under 250 Wm^{-2} illumination showed a 20% drop in initial PCE after 100 hours as compared to the control devices which degraded 95% in 30 hrs. The J_{SC} enhancement was reported to originate from spectral response improvement in 300 – 500 nm wavelength range. Chen *et al.* also reported an enhancement in PCE and UV stability of PSCs upon incorporation of $\text{CeO}_2:\text{Eu}^{3+}$ into the mesoporous layer of n-i-p MAPbI_3 based PSCs.¹²⁶ The reported increase in PCE was 6.9% (relative). While the stability test conducted on devices without encapsulation in ambient under $1,840 \text{ Wm}^{-2}$ illumination showed that the PSCs incorporating $\text{CeO}_2:\text{Eu}^{3+}$ retained 68% of their initial PCE after 50 min, while the control devices degraded to 40% in the same time and conditions. Chander *et al.* used $\text{YVO}_4:\text{Eu}^{3+}$ nano-phosphor layers spray coated on non-conducting side of FTO glass.¹²⁷ The MAPbI_3 based PSCs fabricated on these FTOs yielded 8.1% and 7.7% relative increase in PCE and J_{SC} as compared to the reference solar cells, respectively. The LDS coated PSCs were found 23% more stable when tested in ambient for 12 hours under AM1.5G illumination.

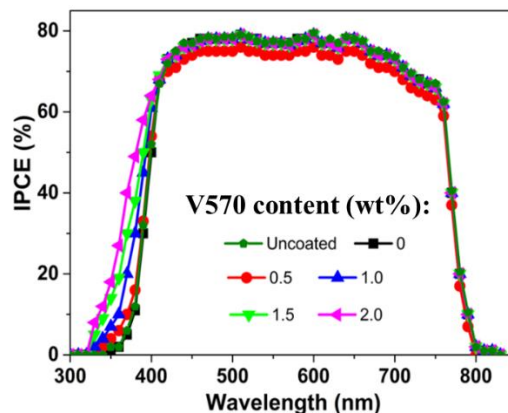


Fig. 3.8: IPCE curves for PSCs coated with the LDS fluoropolymeric layer loaded with different amounts (0 to 2 wt%) of V570. Reproduced with permission from Ref. [124]. Copyright 2016, Science magazine.

3.5 Device Architectures

The quest for enhanced stability, high efficiency, and device architecture simplicity leads researchers to different device architectures with varying power conversion efficiencies. The two frequently employed device architectures are the n-i-p and p-i-n structures.

3.5.1 Standard n-i-p Structure

The regular, most frequently used, and simple architecture is the n-i-p structure which consists of a transparent conductive oxide (TCO), either a fluorine-doped tin oxide (FTO) or indium-doped tin oxide (ITO) coated on glass. This is used as a superstrate. On top of this substrate, an electron transport layer is spin-coated, followed by the perovskite absorber layer and hole transport layer. As the top metal electrode, gold (Au) is used in most cases. The simplified device architecture would be as FTO or ITO/ETL/Perovskite/HTL/Au electrode.¹²⁸ A schematic representation of the n-i-p PSC architecture is given in Fig. 3.9 (a).

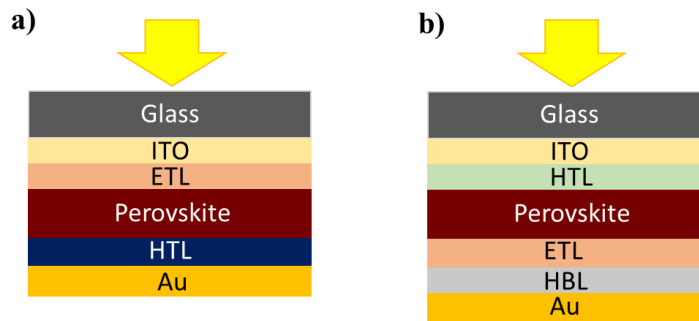


Fig. 3.9: Schematic representation of perovskite device architecture: (a) regular n-i-p architecture (b) inverted p-i-n architecture.

The most frequently used ETLs are tin oxide (SnO_2) and titanium dioxide (TiO_2). The early perovskite solar cells also used to have a mesoporous layer of TiO_2 on top of planar compact TiO_2 . While the common HTL materials are 2,2',7,7'-Tetrakis[N,N-di(4-methoxyphenyl)amino]-9,9'-spirobifluorene ($\text{C}_{81}\text{H}_{68}\text{N}_4\text{O}_8$, or commonly known as spiro-OMeTAD) or the more stable Poly[bis(4-phenyl)(2,4,6-trimethylphenyl)amine (PTAA).^{129,130}

3.5.2 Inverted p-i-n Structure

The inverted architecture for perovskite solar cells is similar to the device architecture adapted from a mature technology of organic solar cells. This architecture comprises an additional hole blocking layer (HBL), while the overall layer structure is: ITO/HTL/perovskite/ETL/HBL/Au as presented in Fig. 3.9 (b). The common materials used as HTL in p-i-n PSCs are NiO_x, PTAA, and PEDOT:PSS.^{131–133} While the ETL materials used in this device architecture are PC₆₀BM and C₆₀.^{134,135} Similar to organic solar cells, in addition to other layers, a hole blocking layer (HBL) is also employed. The common materials used as HBL to minimize recombination at the ETL/metal electrode interface are: bathocuproine (BCP), TiO₂, and poly[(9,9-bis(30-(N,N-dimethylamino)propyl)-2,7-fluorene)-alt-2,7-(9,9-dioctylfluorene)] (PFN).^{136–138}

3.6 Deposition Methods

Since the report of the first solid-state perovskite solar cell, efforts have been made to optimize the routes and recipes to deposit the absorber material. Perovskite absorber materials can easily be deposited via solution processing at low temperatures. This gives the possibility of spin coating, roll-to-roll printing, ink-jet printing, and blade coating. Due to ease of processing and small device area (<0.1 cm²), typically the spin coating technique is used to make most of the PSCs in laboratories worldwide.

In this section, the most common spin-coating recipes to fabricate high quality perovskite layers are discussed.

3.6.1 One-step Recipes

In the so-called one-step recipes, the perovskite precursors are mixed together in a polar solvent, commonly being N,N-dimethylformamide (DMF), dimethyl sulfoxide(DMSO) or gamma-Butyrolactone (GBL). The solution is spin-coated in a single step followed by an annealing step. Further within one-step recipe there are different formulations depending on halide concentration which yield varying surface coverage and defect density.

Lead Iodide Based Recipe

The one-step processes employing a 1:1 molar ratio of methylammonium iodide (MAI) and lead iodide (PbI_2) dissolved in DMF yields needle like structure.¹³⁹ This is due to the fast solvent evaporation during spin-coating. Because of needle like structure this recipe does not give complete surface coverage leading to shunting pathways.

Lead Chloride Based Recipe

The complete surface coverage can be achieved by using a lead chloride (PbCl_2) based recipe.¹⁴⁰ In this recipe, one equivalent of PbCl_2 is mixed with three equivalents of MAI in DMF. Two equivalents of the resultant methylammonium chloride (MACl) slowly evaporate out of the film upon annealing leaving a final film of MAPbI_3 .¹⁴¹

Lead Acetate Based Recipe

Similar to the use of PbCl_2 as lead anion, lead acetate ($\text{Pb}-(\text{CH}_3\text{COO})_2 \cdot 3\text{H}_2\text{O}$) was introduced in the precursor solution by Buin *et al.*¹⁴² It was observed that films grown in iodide poor conditions (using Acetate or Cl as anion) possess much lower trap densities compared to films fabricated with PbI_2 . Due to the achievement of smooth film with low surface roughness through this recipe, it is suitable especially for the inverted architecture. This allows the coating of a thin (~100 nm) and uniform layer of PC_{60}BM with root mean square (RMS) roughness of 10 nm.¹⁴³

3.6.2 Two-step Recipes

Burschka *et al.* first introduced the so-called two step recipe in 2013.¹⁴⁴ In this recipe, first an inorganic layer of PbI_2 (the precursor layer) is coated on a substrate. This is followed by the inorganic film conversion into perovskite by following methods:

- Dipping the PbI_2 coated substrate into a conversion solution containing organic halides (e.g. MAI, MABr, MACl , FAI)
- Spin-coating of a conversion solution on top of the PbI_2 film¹⁴⁵
- Exposing the PbI_2 film to the vapors of organic halide¹⁴⁶

Although these methods typically yield pinhole free films, however, the microstructure and final composition of the films is difficult to control.¹⁴⁷

3.6.3 Solvent-engineering Recipes

The so-called solvent-engineering recipe was introduced by Jeon *et al.* in 2014. This is an extension of one-step recipe, however, it revolutionized the way of producing pinhole free perovskite films.¹⁴⁸ Similar to the one-step methods, all the precursors are mixed in one vial, but a combination of two solvents is employed, either ‘DMF+DMSO’ or ‘GBL+DMSO’. During the spin-coating process, an antisolvent, most commonly Chlorobenzene, is dripped onto the rotating substrate. A subsequent thermal annealing step is executed to form pinhole free APbX₃ perovskite films.¹⁴⁹ This method allows mixing the different perovskite precursors freely and, hence tuning the bandgap. However, the solution chemistry and conversion process critically depend on the precursor composition,¹⁵⁰ the employed antisolvent,¹⁵¹ and the timing of the treatment.¹⁵²

3.7 Current State of Research

After a decade of intensive research efforts, many degradation pathways and mechanisms are found to exist in PSCs. The vast spectrum of the degradation routes and multitude of the stress factors can lead to presence of versatile degradation trends in PSCs. To cover the reported degradation mechanisms, a current state-of-the-art research overview is presented here.

3.7.1 Thermal Degradation

Upon exposure to elevated temperatures, perovskite absorber materials decompose back to the constituent materials. As in real outdoor operational conditions, the solar cell temperature can go up to 85 °C,^{153,154} thus it is necessary to make sure that the solar cells can withstand this thermal stress and keep their performance stable. At temperatures close to the operational temperature for solar cells (~70 C), it is seen that MAPbI₃ based PSCs decompose.¹⁵⁵ The decomposition occurs via two degradation pathways: (i) CH₃NH₂ + HI + PbI₂, and (ii) NH₃ + CH₃I + PbI₂. The gaseous by-products diffuse through the absorber layer to the surrounding. However, when encapsulated devices are subjected to the thermal stress, where the volatile by-products cannot escape the system, the former degradation mechanism is observed to be reversible, while the latter is found irreversible.^{155,156} Kim *et al.* reported that the surface structure of the MAPbI₃ perovskite film changes to an intermediate phase and decomposes to CH₃I, NH₃, and PbI₂ when kept at 100 °C for 20 min or held at 80 °C for over one hour.¹⁵⁷ Taking into account the maximum temperature a

solar cell may need to bear during outdoor operations, thermal degradation poses serious stability challenges.

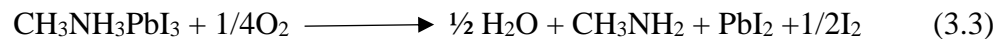
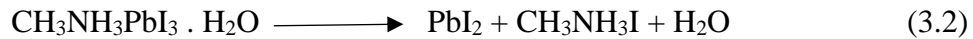
To tackle the thermal decomposition of perovskite absorbers, compositional engineering has been adopted. It has recently been reported that the incorporation of Rb ion into MAPbI₃ perovskite can effectively suppress the decomposition and block the growth of the decomposition by-product PbI₂. The optimized compositional engineering recipe gave an amazing 92% retention of power conversion efficiency during a thermal stress test conducted at 85 °C and 85% relative humidity for 1,000 hours.²¹ This stability protocol is part of the IEC 61215 test routine under title damp heat test. Extending the thermal stability further, Shi *et al.* reported the triple cation (Cs_{0.05}FA_{0.8}MA_{0.15}Pb(I_{0.85}Br_{0.15})₃) based perovskite solar cells to pass two of most critical tests (damp heat test and humidity freeze test) included in the IEC 61215 norm.¹⁵⁸ These results were achieved through proper encapsulation of the devices. Instead of edge sealant, blanket seal (covering the whole device except the aperture area) route was used. Employing the polyisobutylene based polymer as encapsulant enabled the researchers to exceed the requirements set by damp heat test (required 1,000 hours, achieved 1,800 hours) and humidity freeze test (required 10 cycles, achieved 75 cycles) routines of IEC 61215.

Considering these promising results, the imminent commercialization of perovskite PV technology seem plausible, however the field trials report otherwise. Microquanta Semiconductor Co., a China based perovskite PV company whose modules also passed the damp heat and UV preconditioning test of IEC 61215 test norm, however the field trials showed a loss of 80% in their initial performance within 2 years.¹⁵⁹ This fact indicates the need of further research in perovskite material stability and more thorough investigations at device level as well as extensive field trials.

3.7.2 Humidity Induced Degradation

If the perovskite absorber material comes in direct contact with humidity and/or oxygen, it causes degradation. However, in PV industry generally the encapsulation provides sufficient barrier to moisture ingress, especially for moisture susceptible thin-film technology like CIGS.^{22,160} Thus, the existing concepts and encapsulation techniques developed for CIGS solar cells can effectively be used for PSCs as well. However, in case of encapsulation failure, if the moisture or oxygen come in direct contact with perovskite absorber material then it can initiate the degradation. In

presence of moisture, perovskite structure tends to hydrolyze undergoing an irreversible decomposition into the constituents.¹⁶¹ The absorber materials also oxidizes when exposed to oxygen in presence of light.⁷⁵ The chemical reactions can be described as shown below for humidity (eq. 3.1 and 2) and oxygen (eq. 3.3). Moisture induced degradation of the absorber is related to the MAPbI₃ transforming to MAI salt and metal halides.¹⁶² In the presence of moisture, a series of chemical reactions are proposed to happen which are responsible for the degradation.¹⁶³



Provided the fact that excellent encapsulation strategies for commercialized PV technologies are successfully demonstrated already, moisture triggered instability is among least of the concerns for PSCs. Furthermore, PSCs qualifying the IEC 61215's rigorous stability tests like 'damp heat' and 'humidity freeze' essentially results in solution of humidity triggered aspect of instability.^{21,158}

3.7.3 Light-Induced Degradation

Perovskite absorbers are prone to degrade upon prolonged exposure to light. Reports discussing the light-induced degradation of PSCs emphasize different causes of photodegradation. The underlying instability processes are still under investigation. In this regard, the most studied radiation regime is the UV spectrum.¹⁶⁴ Recently, a few studies have been published on visible light degradation of PSCs as well.¹⁶⁵⁻¹⁷⁰

UV instability is proposed to stem from different causes. The electron transport layers are found to degrade when the full solar cell stack is exposed to UV radiation. Ji *et al.* proposed the UV triggered degradation of TiO₂ based PSCs to stem from well-known inherent oxygen vacancies in the TiO₂ layer resulting in Ti³⁺ defects with an unpaired electron ~1 eV below CB minimum.¹⁶⁴ Upon UV induced excitation of TiO₂, VB electron transit to CB leaving back a hole in VB. The unpaired electron at Ti³⁺ site recombines with the hole in VB to make Ti⁴⁺ state and leaving a free electron in CB. The Ti⁴⁺ state captures photo-generated electron from perovskite layer to revert back to Ti³⁺ state. This process leads to a photo-electron accumulation induced by Ti⁴⁺ state causing extra recombination which results in performance decay. With prolonged UV exposure, Ti⁴⁺ state concentration increases leading to a continuous degradation. Leijtens *et al.* proposed that

light-induced desorption of surface-adsorbed oxygen from the mesoporous TiO₂ (meso-TiO₂) transport layer initiates the instability.^{164,171} It was deduced by comparing the instability studies conducted with and without meso-TiO₂ charge transport layers. No instability is observed in solar cells without meso-TiO₂ layer. The instability caused due to the use of TiO₂ as ETL can be explained by the photocatalytic activity of TiO₂.¹⁷² The enhanced chemical reactivity of TiO₂ upon UV irradiation causes the redox reaction at TiO₂/perovskite interface leading to degradation of the absorber material. Li *et al.* demonstrated better UV stability of PSCs by using a ~200 nm thick barrier layer of CsBr on top of TiO₂ which improves the UV stability of TiO₂/CsBr interface as shown by XPS which indicates a negligible change in CsBr as compared to the UV exposed TiO₂/MAPbI₃ interface.¹⁷³ The UV triggered instability is found to be reversible in many reports. Lee *et al.* exposed PSCs to UV radiation of a wavelength 365 nm with intensity 76 Wm⁻² for 1,000 hours in an inert atmosphere. A 26% (relative) loss in short circuit current density was observed.¹⁷⁴ However, when the degraded solar cells are exposed to the full spectrum light of 1 sun intensity, the performance is recovered. On the contrary, there are many studies which report otherwise i.e. only negligible or no performance recovery at all is observed.^{175–182}

However, since the problem of UV stimulated degradation in PSCs persists regardless of the contradictory reports on partial or no performance recovery, many approaches have been suggested to address the UV degradation.^{173,183,184} These approaches include, modification of ETL layer via doping,^{185,186} addition of spacer layer between ETL and absorber material,^{187–189} use of luminescent downshifting materials to absorb the troublesome wavelengths,^{125,183,190} UV filters to block the harmful radiation content,^{191,192} and use of UV stable ETL materials.^{193,194}

The current understanding of the light-induced degradation suggests that if the UV radiation is effectively blocked to reach the solar cells, they should become stable. However, it is seen in literature that this is not the case. Domanski *et al.* exposed the PSCs to UV filtered light and still a photo-induced degradation is observed which suggests that other portions of the light spectrum also contribute to triggering the photo instability in PSCs.¹⁶⁹ Later, a few studies have been published highlighting the visible-light-induced degradation of PSCs. Quitsch *et al.* exposed MAPbI₃ layers to the light of various wavelengths in the ambient environment and discovered that the photons of wavelength below 520 nm are causing degradation while the light above $\lambda = 520$ nm is producing a light-soaking effect.¹⁷⁰ The degradation associated with wavelengths $\lambda < 520$

nm is attributed to the bandgap of PbI_2 which is reported to be 2.4 eV in literature.¹⁹⁵ Similarly, few other studies subjected the MAPbI_3 based solar cells to three different light-emitting diode (LED) sources of blue and red color and noticed that photons of the blue regime are contributing to the degradation of solar cells.^{166–168} Upon exposure to a set of seven blue LEDs (470 nm, $\sim 500 \text{ Wm}^{-2}$),¹⁹⁶ an emergence of the PbI_2 peak was observed referring to the decomposition of the perovskite absorber into the constituents. Under continuous illumination, PbI_2 is reported to decompose into metallic Pb and mobile I_2 , which later diffuses into the perovskite absorber material and probably producing the interstitial defects with activation energies 0.23 eV and 0.57 eV.⁷⁸ Lu *et al.* used two LED sources with irradiance 100 Wm^{-2} each and wavelength ranges in blue and green to study their impact on a double-cation perovskite (CsFAPbI_3) film stability. Via XPS it was found that Cs^+ cations migrate from the surface of the perovskite films into the bulk, with a 50% decrement in its original content within 110 hours.¹⁹⁷ The decrease in the Cs^+ content on the film surface implies the creation of A-site vacancies. This is proposed to happen in result of photo-induced lattice distortion. Furthermore, Travkin *et al.* showed that LED light sources (95 Wm^{-2}) with spectrum lying in blue (440 – 500 nm) and red region (600 – 660 nm), stimulate degradation in MAPbI_3 based perovskite solar cells leading the devices to underperform in a rather brief duration of 90 min.¹⁶⁶ The same is the case for solar cells exposed to the solar simulator for the same duration leaving the devices almost insensitive to light anymore.¹⁶⁶ The root cause for the short-living solar cells under the full spectrum of light is found to be the decomposition of the perovskite absorber into constituent materials.

The up-to-date literature proposes that the UV radiation is harmful for PSC stability. In addition to that, multiple spectral selections within visible light are also found to stimulate the degradation in inert as well as in ambient conditions in time durations spanning over minutes to hours.

4. Materials and Characterization

This chapter includes the materials and precursors used to fabricate the solar cells. Furthermore, it gives insights into the device fabrication procedure and a description of the equipment involved in the fabrication step. Lastly, the tools used to characterize the as-fabricated and degraded solar cells are introduced with their functionality and relevance for the device characterization. The setups used to degrade solar cells under various light stress factors are also discussed in this chapter.

4.1 Choice of Materials and Compositions

This section discusses the possibility of choosing the charge transport materials and absorber compositions among the vast pool of available choices. Furthermore, a variety of top and bottom electrode materials are also described here.

4.1.1 Transparent Conductive Oxide

There is a variety of TCO coated glass superstrates available for the fabrication of PSCs. Among the most utilized TCO thin films are tin doped indium oxide (In_2O_3 , ITO), fluorine doped tin oxide (SnO_2 , FTO), and aluminum doped zinc oxide (ZnO , AZO).¹⁹⁸ The particular characteristics that are taken into account for the selection of a TCO in PV applications are high transmittance and low sheet resistance, apart from its cost effectiveness, long-term stability, and ease of scalability. Among these, ITO is the most widely used TCO due to its high conductivity and transparency in comparison to AZO.¹⁹⁹ This is demonstrated by Baltakesmez *et al.* who compared the performance of PSCs based on ITO and AZO coated substrates and concluded that ITO yields better efficiencies when used as TCO in PSCs over AZO based devices.²⁰⁰ The typical values of resistivity, carrier concentration, carrier mobility, and transmittance for ITO are $\sim 1 \times 10^{-4} \Omega\text{cm}$, $10 - 20 \times 10^{20} \text{cm}^{-3}$, $25 - 40 \text{cm}^2 \text{V}^{-1}\text{s}^{-1}$, and $\sim 85\%$, respectively.²⁰¹ Similarly, the characteristic resistivity, carrier concentration, mobility, and transmittance values for AZO are reported to be $\sim 2.7 \times 10^{-4} \Omega\text{cm}$, $9 \times 10^{20} \text{cm}^{-3}$, $\sim 25 \text{cm}^2 \text{V}^{-1}\text{s}^{-1}$, and $\sim 85\%$, respectively.²⁰² Comparing these values, ITO appear to be a better choice due to low resistivity, high carrier concentration and mobility. Another reason of high efficiency of ITO based PSCs is reported to be the low recombination resistance in them

as compared to FTO and AZO based cells.²⁰³ However, the poor long-term environmental and damp heat stability of AZO makes it less frequently used as compared to ITO. In addition to that, ITO offers high mechanical stability as well which makes it suitable for use in development of flexible devices. A well-known problem encountered while using ITO in PV applications is that the thermal stability of ITO is compromised at elevated temperatures.²⁰⁴ This becomes important when mesoporous architecture is used to fabricate PSCs which needs a 500 °C temperature treatment. The alternative TCO used for high temperature applications is the FTO for its better thermal robustness. In terms of thermal stability, the three TCOs can be prioritized as FTO > AZO > ITO.²⁰² However, FTO is not frequently used in PV application, unless an elevated temperature processing is involved, due to its comparatively high resistivity and less transparency. The typical values of resistivity, carrier concentration, mobility, and transmittance for FTO are reported to be $\sim 4 \times 10^{-4} \Omega\text{cm}$, $5 - 7 \times 10^{20} \text{cm}^{-3}$, $12 - 24 \text{cm}^2 \text{V}^{-1}\text{s}^{-1}$, and $\sim 80\%$, respectively.²⁰⁵ Additionally, both FTO and AZO need high temperature processing and demonstrate poor mechanical stability. FTO is reported to have comparatively high surface roughness and is also found difficult to pattern via wet etching.²⁰² For these reasons, FTO and AZO are yet not an optimum replacement of ITO, hence the frequently used TCO in this work is ITO. However, where thermal annealing of ETL at high temperatures is required (for example in compact-TiO₂ based devices), FTO coated substrates are employed.

4.1.2 Electron Transport Layers

Effective charge collection is of prime importance in a solar device. For this purpose, a careful selection of ETL is critical. The most important characteristic of an ETL is that it must satisfy band alignment with the perovskite absorber. Furthermore, processing conditions and stability of ETLs are yet another parameter that must be favorable for the PSCs. In quest to satisfy these requirements, a multitude of ETLs have been employed in PSCs. These ETLs span over organic and inorganic materials. Among these materials are SnO₂, TiO₂, ZnO, ZrO₂, C₆₀, phenyl-C₆₁-butyric acid methyl ester (PCBM).²⁰⁶⁻²¹⁰ In n-i-p architecture of PSCs where ETL needs to be highly transparent to allow the maximum light reaching to the absorber material, metal oxide based ETL (SnO₂ or TiO₂) are employed for their high transmittance. While organic ETLs cannot be used in n-i-p architectures due to their opacity. Most of the high efficiency solar cells use TiO₂ or SnO₂ as ETL due to their excellent photoelectric properties.²¹¹ However, the high annealing

temperature (~ 500 °C) required to deposit a compact layer of TiO_2 (c- TiO_2) restricts its use to the flexible substrates. Qiu *et al.* employed electron beam induced evaporation of TiO_2 (e- TiO_2) to deposit a thin layer on flexible plastic as well as glass substrates keeping the substrate temperature fairly low (~ 75 °C).²¹² However, thickness of the e- TiO_2 plays a critical role in such process. To avoid pinholes, a sufficiently thick film needs to be deposited which ultimately increases the resistance to impact the device performance. Another route can also be taken to deposit TiO_2 at low temperature. Pre-synthesized nanoparticles of TiO_2 (np- TiO_2) can be dispersed in various type of solvents and a thin film can be obtained via solution-based deposition techniques to circumvent high annealing temperatures.²¹³ However, the use of TiO_2 as ETL material poses a challenge in terms of device hysteresis. The low electron mobility of TiO_2 (anatase = $0.1 \text{ cm}^2 \text{ V}^{-1} \text{ s}^{-1}$, rutile = $2.5 \text{ cm}^2 \text{ V}^{-1} \text{ s}^{-1}$)²¹⁴ lag behind the carrier mobility of workhorse perovskite MAPbI_3 absorber films ($20 \text{ cm}^2 \text{ V}^{-1} \text{ s}^{-1}$).^{215,216} This difference of carrier mobility values leads to charge accumulation at the TiO_2 /perovskite interface resulting in hysteresis. This problem can be avoided by using SnO_2 whose carrier mobility ($240 \text{ cm}^2 \text{ V}^{-1} \text{ s}^{-1}$)²¹⁷ is much higher than TiO_2 . Another aspect that justifies the stability of SnO_2 over TiO_2 as ETL is the photocatalytic activity of TiO_2 .¹⁷² It is well known and reported in literature that TiO_2 is frequently used as photocatalyst in many applications. When TiO_2 is used as ETL in PSCs, its photocatalytic activity causes redox reaction at TiO_2 /perovskite interface upon exposure to UV radiation, leading to irreversible degradation of the absorber material. Again, the deposition of a compact SnO_2 layer (c- SnO_2) needs an annealing step of ~ 250 °C for 30 min which is not suitable for flexible plastic substrates. For a low temperature deposition of SnO_2 , Smith *et al.* used nanoparticle SnO_2 (np- SnO_2) solution diluted in water coated on glass and flexible plastic substrates with a hot air flow (120 °C, 1 min) to demonstrate commercial viability of the process.²¹⁸ Thus, owing to its excellent electron mobility and stability, the current most widely used ETL material is SnO_2 . Due to its high electron mobility, SnO_2 exhibits almost no hysteresis and hence shows improved stability. Furthermore, unlike TiO_2 , SnO_2 does not require high temperature treatment which makes it suitable for mass production. Similar to SnO_2 , ZnO also does not require high temperature process. However, the devices fabricated on ZnO as ETL suffer from severe decomposition due to the $-\text{OH}$ residue on the ZnO surface leading to the absorber degradation.²¹⁷ Due to this reason there is a limited use of ZnO as ETL in PSCs.²⁰⁶

The high efficiency reported till date is for n-i-p architectures of PSCs using either TiO₂ or SnO₂ as ETL. Since aim of this work is to investigate and enhance stability of high efficiency PSCs, the ETL materials used are SnO₂ and TiO₂.

4.1.3 Hole Transport Layers

High efficiency PSCs need hole transport layers to increase charge carrier collection efficiency and reducing the recombination. The variety of HTLs used in PSCs includes spiro-OMeTAD, PTAA, poly(3-hexylthiophene) (P3HT), poly(3,4-ethylenedioxythiophene):polystyrene sulfonate (PEDOT:PSS) are among organic long chain polymeric materials.²¹⁹ While, inorganic HTLs include nickel oxide (NiO_x), copper oxide (CuO_x), Copper thiocyanate (CuSCN).²²⁰ The latter class of charge transport layers is used in p-i-n PSCs for their transparency properties and the former ones are employed in n-i-p architectures. Highly efficient PSCs are based on spiro-OMeTAD as HTL for many reasons, like well-matched energy band with perovskite and high hole mobility value. However, it also bears the challenge of thermal instability and high cost. Furthermore, spiro-OMeTAD is also known to impact the device stability due to high ratio of dopants (Li⁺) to increase its conductivity.²²¹ Upon prolonged photo exposure, the dopant ions infiltrate to the perovskite layer creating shunt paths and reducing the device performance. To improve thermal and photostability of HTL, PTAA is has also been used as HTL.²²² However, due to less affinity of PTAA the wettability of the deposited layer on top of perovskite is bad which make the HTL film processing tricky via solution processing,²²³ which leads to inferior quality of perovskite/HTL interface resulting in recombination losses. Thus, for high performance of devices, Tavakoli *et al.* suggested to employ thermal evaporation of PTAA.²²⁴ P3HT is another HTL material employed in PSCs for being cost effective and strong hydrophobic properties to make a good perovskite/P3HT interface. However, it generally produces devices with lower PCE in spite of its high carrier mobility ($\sim 0.1 \text{ cm}^2 \text{ V}^{-1} \text{ s}^{-1}$)²²⁵ as compared to Spiro-OMeTAD ($\sim 10^{-4} \text{ cm}^2 \text{ V}^{-1} \text{ s}^{-1}$),²²⁶ due to its shallow highest occupied molecular orbital.²²⁷ Madhavan *et al.* gave a direct comparison of CuSCN and Spiro-OMeTAD based PSCs reveal that CuSCN provides better stability but lower values of short-circuit density.²²⁸ Dzikri *et al.* compared PEDOT:PSS and CuSCN as HTL in perovskite solar cells and reported that PEDOT:PSS slightly underperforms in the solar cells as compared to CuSCN due to energy level mismatch between PEDOT:PSS and

perovskite,²²⁰ which suggests that Spiro-OMeTAD gives best device efficiencies among these HTLs.

Another promising inorganic HTL material used in PSCs is NiO_x. It provides high stability and good transparency thus it is widely used in p-i-n architecture based solar cell.²²⁹ Although PSCs employing NiO_x as HTL promise high efficiency and stability, however, they demonstrate low open circuit voltage due to recombination by different oxidation states (Ni³⁺, Ni²⁺) or different phase (Ni₂O₃) are present, influencing the charge extraction and carrier mobility.²³⁰

Considering the n-i-p device architecture and promise of high efficiency, Spiro-OMeTAD is used as HTL throughout this work.

4.1.4 Perovskite Absorber

For many years MAPbI₃ perovskite served as work-horse materials for perovskite solar cells. Since the first report of successful use of MAPbI₃ and MAPbBr₃ as sensitizer materials in solar cells by Kojima *et al.* in 2009,²³¹ and later in all-solid-state devices by Kim *et al.* in 2012.⁵³ However, the bandgap of MAPbI₃ (~1.6 eV)²³² is higher than the single junction optimum. In this regard, formamidinium lead triiodide (FAPbI₃) exhibits more suitable bandgap (~1.4 eV)²³² to reach the maximum efficiency for single junction solar cell. Thus, the trend shifted to the use of FAPbI₃ due to its high thermal stability and promise of high efficiency.^{158,233} Although FAPbI₃ offers high efficiency, however, it is difficult to deposit highly crystalline photoactive pure α -phase of FAPbI₃.²³⁴ Furthermore, the phase instability of FAPbI₃ from photoactive black phase (α -phase) to photoinactive yellow phase (δ -phase) especially in humid environment is limiting its frequent use in PSCs.²³⁵ To attain structural stability, mixed composition (MA/FA) was used and found suitable to realize a stable structure.²³⁶ The stability of mixed MA/FA is achieved likely due to the smaller radius of MA cation which shifts the tolerance factor towards the photoactive α -phase. However, even with this mixed MA/FA composition the absorber material still suffers from incomplete crystallization and traces of photoinactive yellow phase and PbI₂ can be found in the active material. Thus, Saliba *et al.* added further another cation (inorganic Cs) with even smaller ionic radius which helped to achieve fully crystallized and stable photoactive phase of perovskite by shifting the tolerance factor towards a cubic lattice structure.²³⁷ Due to the increased crystallinity, the device performance and stability was increased. Therefore, the absorber material

composition has now evolved and changed from MAPbI₃ to mixed cation-mixed halide composition. Today, the so-called triple-cation composition (MA_xFA_{0.95-x}Cs_{0.05}Pb(I_{1-y}Br_y)₃) is the most widely used perovskite absorber in high efficiency PSCs.²³⁸

Thus, in this dissertation two absorber compositions are used. First is the MAPbI₃ for being the work-horse material in the field of perovskite PV research. Second is the famous so-called triple-cation compositions for its qualities of yielding highly efficient and stable devices.

As top metal electrode, gold (Au) is used for its high conductivity, light reflectivity, and superior stability over other metal electrode materials e.g. silver (Ag).²³⁹

4.2 Solar Cell Fabrication

The performance and quality of perovskite solar cells depend on the environment of the fabrication facility and technique. The easiest deposition technique used for small-area (<1 cm²) perovskite absorber materials is spin-coating which yields smooth and uniform films. As the perovskite materials are sensitive to oxygen and moisture, film preparation is carried out in nitrogen (N₂) filled glove boxes.

The detailed description of the fabrication of the solar cells used throughout this work is explained in the coming section. The details and sources of materials used to fabricate the full stack of solar cells along with the recipes are also presented herein.

4.2.1 Substrates and Electron Transport layers

Solar Cell Substrates

The substrates used to fabricate solar cells are soda-lime glass due to their cost-effectiveness, weatherability, good transparency for visible light, and hardness.^{240,241} The commercially available soda-lime glass coated with two different transparent conducting oxides: (i) ITO (120 nm thick, deposited via sputtering) and (ii) FTO (200 nm thick, deposited via spray pyrolysis) were obtained from Luminescence Technology Corp., Taiwan. The size of the FTO coated glass substrate is 1.6 × 1.6 cm², with a sheet resistance of 20 Ωsq⁻¹. Each substrate has two solar cells with an individual area of 24 mm². The size of the ITO coated glass substrate is 1.6 × 1.6 cm², with a sheet resistance of 15 Ωsq⁻¹. Each substrate has four cells with an individual area of 10.5 mm². The substrates are

first cleaned with liquid soap and rinsed in water to remove dust and glass particles. Later they are ultrasonically cleaned in acetone for 15 min and with isopropanol for 15 min each, respectively. After this, the substrates are dried with an N₂ gun and plasma cleaned in O₃ for another 3 min.

Electron Transport Layers

Solar cells based on five different ETLs according to existing recipes are used in this work overall. The types of ETLs used are: (i) compact tin oxide (c-SnO₂)²⁴² spin-coated for 30 sec at 4,000 rpm and annealed at 250 °C, (ii) nano-particle (np-SnO₂)¹⁹ spin-coated for 30 sec at 4,000 rpm with subsequent annealing at 250 °C for 30 min; plus three kinds made from TiO₂: (iii) deposited via spin coating at 3,000 rpm and post annealed at 500 °C compact (c-TiO₂)²⁴³, (iv) nanoparticles (np-TiO₂) grown via wet-chemical synthesis²⁴⁴ and spin-coated at 6,000 rpm followed by an annealing step of 15 min at 100 °C; (v) TiO₂ deposited via electron-beam evaporation (e-TiO₂) at room temperature with a partial oxygen pressure of 1.7×10^{-4} Torr to maintain the stoichiometry of the film.²⁴⁵ These substrates are then plasma etched in O₃ for 1 min before the deposition of the perovskite absorber material.

4.2.2 Perovskite Precursors and Coating

Methylammonium lead triiodide (MAPbI₃)

MAPbI₃ solution preparation took place in two steps. In the first step 303.4 mg of lead acetate trihydrate (Pb(CH₃CO₂)₂·3H₂O, Sigma-Aldrich) and 381.5 mg of methylammonium iodide (MAI, Dyesol) were dissolved in 760 µl of N,N-dimethylformamide (DMF, Sigma-Aldrich). Then a separate solution is prepared by taking 66.7 mg of lead chloride (PbCl₂, Sigma-Aldrich) and mixed with 114.5 mg of methylammonium iodide (MAI, Dyesol) and then dissolved in 300 µl of DMF. In the second step, 260 µl of the latter solution are mixed into the first one to get a final mixture with a molar ratio of ~20 % PbCl₂.²⁴⁴

Triple Cations Solution

The triple cation solution with final formulation Cs_{0.1}(FA_{0.83}MA_{0.17})_{0.9}Pb(I_{0.83}Br_{0.17})₃ is prepared according to an existing recipe¹⁹ using the chemicals given here. The precursor materials are: methylammonium bromide (MABr, Dyesol), formamidinium iodide (FAI, Dyesol), PbI₂ (Alfa

Aesar), lead bromide (PbBr_2 , Alfa Aesar), and cesium iodide (CsI , Alfa Aesar). The solvents used to dissolve the precursors are: DMSO and DMF.

To obtain the final solution, two separate solutions are prepared and mixed in the proportion as (i) a precursor solution of FAI (1 M), PbI_2 (1.1 M), MABr (0.2 M), and PbBr_2 (0.2 M) in DMF:DMSO in a ratio of 4:1 is prepared; then (ii) a precursor of CsI in DMSO (1.5 M) is prepared. Later, an 88.9 μL aliquot of the second solution is transferred into the first one to prepare the final perovskite solution of formulation $\text{Cs}_{0.1}(\text{FA}_{0.83}\text{MA}_{0.17})_{0.9}\text{Pb}(\text{I}_{0.83}\text{Br}_{0.17})_3$.

Perovskite Spin Coating

The perovskite solution deposition is carried out inside the N_2 filled glovebox (GS glovebox Systemtechnik) with $\text{O}_2 < 10$ ppm and $\text{H}_2\text{O} < 2$ ppm concentration. For the spin coating of the MAPbI_3 solution with spin coater (GS Polos 300), the used coating parameters are: 3,000 rpm for 30 sec with 40 μl amount of solution. The spin coating step is followed by a 6 min drying step in N_2 and then annealing at 115 $^\circ\text{C}$ for 10 min. The final thickness of the films ranges between 300 – 350 nm.

The triple cation solution is spin-coated onto the ETL deposited substrates with a two-step recipe as: step (i) 1,000 rpm for 10 sec; step (ii) 6,000 rpm for 20 sec. 100 μL of chlorobenzene is poured on to the substrate 7 – 10 seconds before the end of the second step. Spin coating is followed by the annealing step at 100 $^\circ\text{C}$ for 1 hour to get films of thickness 300 – 350 nm.

4.2.3 Hole Transport Layers

The material used for the hole transport layer is spiro-OMeTAD. The solution is prepared according to an existing recipe¹⁹ where 79.6 mg of Spiro-OMeTAD are dissolved in 1 ml of chlorobenzene (CB). 27.5 μl 4-tert-Butylpyridine (4tBP) is added to this along with 17.5 μl of bis(trifluoromethane) -sulfonimide lithium salt (Li-TFSI) solution in acetonitrile (ACN). To enhance the conductivity a p-type dopant like Li-TFSI is used to dope the Spiro-OMeTAD. Unlike inorganic systems, the doping process in organic small-molecule systems like Spiro-OMeTAD typically corresponds to chemical oxidation and charge transport involves redox reaction.

HTL Spin Coating and Oxygen Doping

The prepared solution is then spin-coated (employing GS Polos 300 spin-coater) at a spin-coating speed 4,000 rpm for 30 sec on top of the perovskite coated substrates in a N₂ filled glovebox (GS glovebox Systemtechnik) with O₂ < 10 ppm and H₂O < 2 concentration and left in a dry box for oxygen doping for 12 – 16 hours. The purpose of oxygen doping is to increase the conductivity of Spiro-OMeTAD which is not sufficiently high in its pure form.²⁴⁶

Upon leaving the pristine Spiro-OMeTAD film in oxygen environment, Abate *et al.* proposed that Spiro-OMeTAD reacts with O₂ to generate a weakly bound complex in the presence of light as shown below.²⁴⁷ The TFSI anion stabilizes the radical cation while the remaining metal cation forms an oxide complex.



Thus, the radical cation species improves the conductivity of Spiro-OMeTAD.²²¹ This phenomenon reduces the series resistance of HTL, leading to improved charge extraction and hence higher fill factor values for the solar cells.

Metal Electrode Evaporation

To complete the solar cell fabrication, a 60 nm thick layer of Au is thermally evaporated using a bell jar thermal evaporator (Vactec Coat 360) at a rate of 2 Å s⁻¹ after covering the substrates with shadow masks. The final device configuration is: Glass/FTO or ITO/ETL/perovskite/HTL/Au, as shown in pictorial and schematic form in Fig. 4.1.

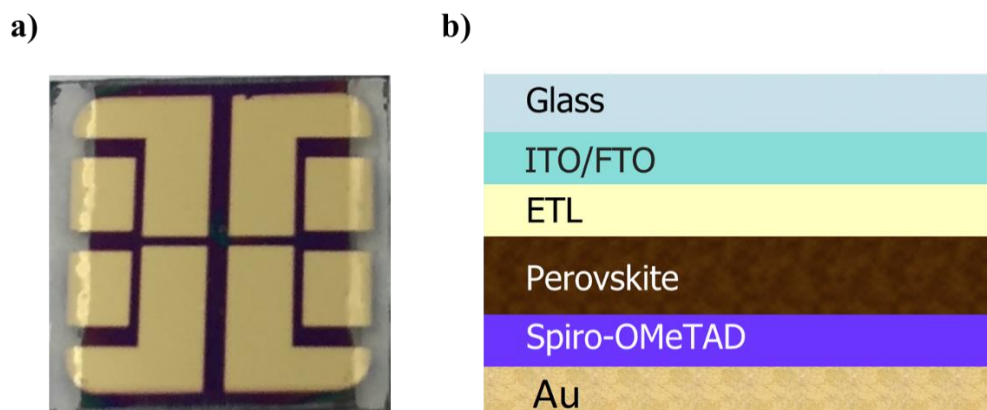


Fig. 4.1: (a) Pictorial view, and (b) schematic illustration of the solar cells.

4.3 Luminescent Downshifting Layers

LDS materials are used and researched among PV community for their capacity to absorb light where device exhibits weak response and to emit where it can be absorbed efficiently. An ideal LDS material for application in PSCs would be the one which absorbs UV radiation only – due to the vulnerability of PSCs to degrade under UV – and exhibit large stokes shift (difference in energy between absorption and emission spectra) to avoid re-absorption. Europium (Eu) complex based LDS offer the advantage of absorption in UV range (300 – 400 nm) and exhibit large stokes shift (> 150 nm).^{248,249} However, Eu^{3+} exhibit low absorption coefficient and require sensitizer to transfer energy across to Eu^{3+} ions to use their luminescence properties effectively. It is demonstrated that bis(2-(diphenylphosphino)phenyl)ether oxide (DPEPO) combined with fluorinated β -diketonates is an excellent choice as sensitizer material.²⁵⁰ The ready-to-use Eu complex doped EVA layers employed in this dissertation were prepared elsewhere.^{249,251} Their preparation method is briefly described herein.

The Eu^{3+} ions and DPEPO combined with fluorinated β -diketonates are used as activator and sensitizer, respectively, to prepare the Eu complex. The Eu complex is dissolved in dichloromethane (DCM) in 2.5 wt%. This mixture is then added to EVA pellets, also diluted in DCM (~25% v/v) and heated to ~90 °C (above the softening point of EVA). The resulting mixture was further stirred for 1 hour on a hotplate to achieve a solution with uniform concentration of LDS complex. The mixture is then poured into an aluminum (Al) mold and placed in a vacuum oven at 60 °C for 3 hours under absolute pressure 0.2 Pa. Later, the solvent residue containing mold is placed between

two polished Al plates and a heated hydraulic press at a plate temperature of 100 °C. The mold was pressed under 2×10^9 Pa pressure for 1 min and was then kept under pressure for another 1 min at the same pressure, while cooling the plates down to 10 °C. The resultant sheets are then peeled starting from the edges to get uniformly thick (1.5 mm) LDS doped EVA layer.

4.4 Analytical Techniques

4.3.1 Current Density-Voltage (*J-V*) Measurements

The electrical performance of a solar cell is determined by the characteristic current density-voltage (*J-V*) measurement. In this characterization, the solar cells are illuminated under a class AAA solar simulator ($\pm 1.25\%$ spectral mismatch to the solar spectrum, $< 2\%$ spatial non-uniformity of irradiance, and a 0.5% short-term temporal instability of irradiance) that can radiate light with a good replication ($\pm 1.25\%$) of sunlight in terms of spectrum and intensity, while a voltage sweep is applied to the terminals of the solar cell.

To measure the *J-V* curve, the solar cell is placed under the illumination of a light source, which is a solar simulator (Newport Oriel Sol3A, 94043A), employing a xenon (Xe) lamp calibrated to give $1,000 \text{ Wm}^{-2}$ light, corresponding to standard illumination at AM1.5G. The spectrum is shown in Fig. 4.2 (a). The calibration is done using a reference solar cell by Newport equipped with an infrared (IR) cut-off filter (KG-5, Schott) at 25 °C. The solar cells are mounted onto a sample holder embedded with gold-plated pins. The data is read out using a Labview coded software. The voltage is applied to the solar cell with a Keithley Source Measure Unit (SMU) model 2400. The scan speed of the *J-V* measurement is kept constant at 600 mV/s which shows a good agreement with the steady-state power output. To eliminate any underestimation of PCE extracted from *J-V* curve due to light-soaking effect, all the solar cells are operated at constant voltage close to the MPP for 5 min before recording a *J-V* curve. The PCE is stabilized within 5 min time after compensating for the light-soaking to get a reproducible and stable *J-V* scan.

The *J-V* characteristic curve for a perovskite solar cell used in this study is given in Fig. 4.2 (b). From the *J-V* characteristic curve, several parameters can be extracted, like short circuit current density (J_{SC}), open-circuit voltage (V_{OC}), fill factor (FF), power conversion efficiency, and the power-voltage curve, as presented in Fig. 4.2 (c).

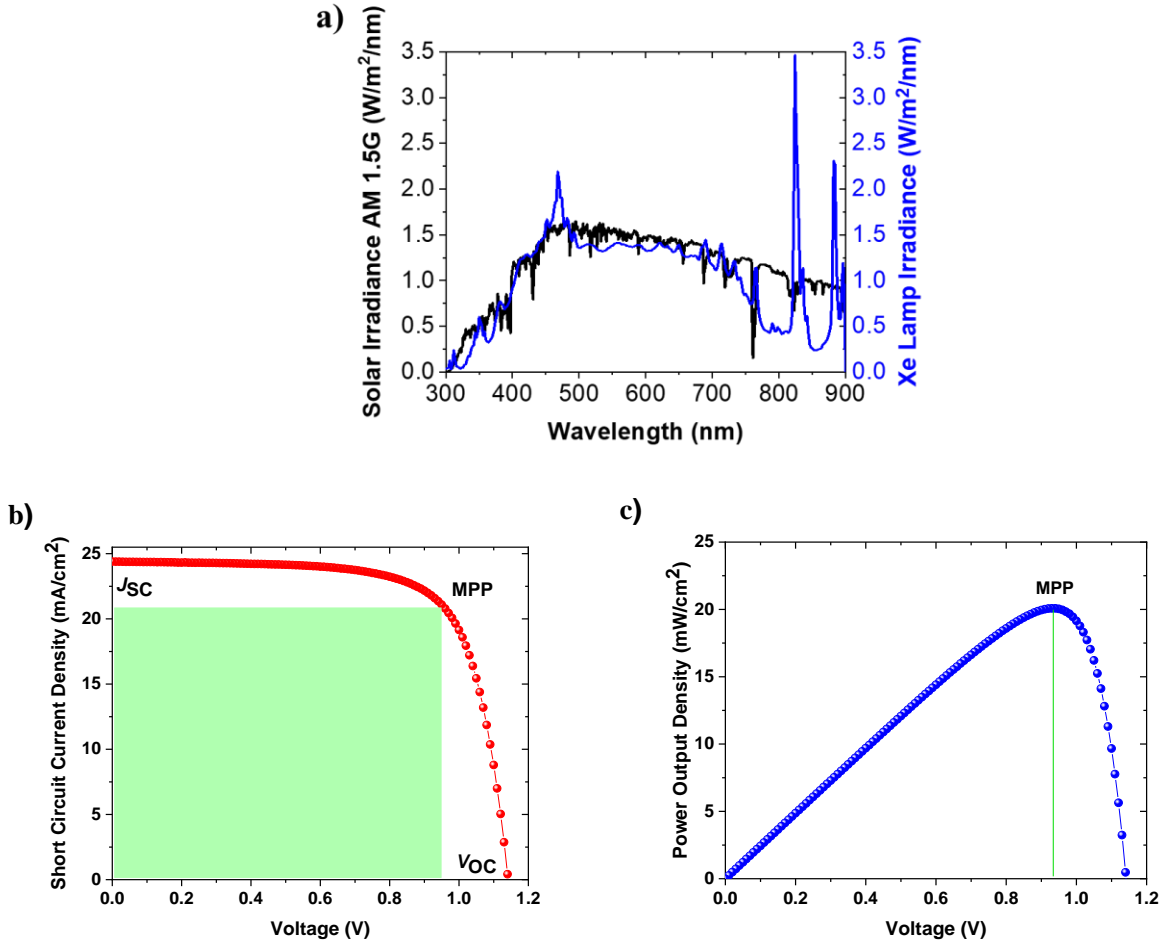


Fig. 4.2: (a) Spectrum of the Xe lamp along with AM1.5G spectrum, (b) J - V characteristic curve, (c) extracted power from solar cell or so-called output power density curve.

The current at zero applied voltage is the maximum and is called short circuit current density, while the voltage being maximum at the zero current value is called open-circuit voltage. The product of voltage and current density values which yields maximum power is called the maximum power point (MPP). The voltage and current density at the maximum power point are known as ‘voltage at maximum power point’ (V_{MPP}) and ‘current density at maximum power point’ (J_{MPP}).

The other important parameters extracted from J - V curves of solar cells are the fill factor, power conversion efficiency, series resistance (R_s), and shunt resistance (R_{sh}).

The fill factor is the showcase parameter to determine the quality of a solar cell. It can be calculated using the following formula (Eq. 4.3) which gives a ratio of the maximum power produced by the solar cell and the maximum power calculated from V_{OC} and J_{SC} .

$$FF = \frac{V_{MPP} * J_{MPP}}{V_{OC} * J_{SC}} \quad (4.3)$$

Where V_{MPP} (V) is the voltage at MMP, J_{MPP} (mA cm⁻²) is the current density at MMP, V_{OC} is the open-circuit voltage (V), and J_{SC} is the short-circuit current density (mA cm⁻²). If the incident light power is known, then the power conversion efficiency of a solar cell can be calculated using the following relation.

$$PCE = \frac{V_{OC} * J_{SC} * FF}{P_{in}} \quad (4.4)$$

Where V_{OC} is the open-circuit voltage (V), J_{SC} is the short-circuit current density (mA cm⁻²), FF is the fill factor and P_{in} is the incident power (Wm⁻²).

4.3.2 Constant Voltage Tracking

The power conversion efficiency of the solar cell might vary as extracted from the J - V curve to those achieved from the field trial where the solar cells are operated at MMP. This difference mostly arises from the hysteresis, a difference in the PCE measured from forward and backward J - V scans, which can lead to an over-estimation of the solar cell PCE. Thus, the long-term performance of the solar cells is monitored by tracking the efficiency at a constant voltage. The constant voltage point for efficiency tracking is taken to be the V_{MPP} , chosen after multiple J - V scans to remove light soaking effect.²⁵²

4.3.3 UV-Vis Absorbance Spectroscopy

Ultraviolet-visible (UV-Vis) absorbance spectroscopy is an important technique to measure the absorption of the active material in different spectral regimes of light, absorption co-efficient, and bandgap of the material. A wavelength range of 250 – 900 nm is used to carry out the measurements, and two kinds of lamps are used to produce light of the mentioned wavelengths, (i) a deuterium lamp for light in the UV range; and (ii) a tungsten lamp for light in visible and near infra-red (NIR) range. The emitted light is passed through a monochromator and guided to the sample under investigation. On interaction with monochromatic light, electronic transitions take place in the material. For transmittance measurements, the test sample is placed in front of the integrating sphere (P1) and for reflectance measurement the test sample is placed at the end of the

integrating sphere (P2) as given in Fig. 4.3. The light transmitted through the sample is recorded and the absorbance of the sample is measured at every wavelength. If the thickness of the sample film is known, the absorption co-efficient (α) can be determined using Lambert-Beer law, as:

$$A = \log\left(\frac{I_o}{I}\right) = \alpha(\lambda)d \quad (4.5)$$

Where A is the measured absorbance, I_o and I are the intensities (W m^{-2}) of the incident and transmitted lights, respectively, α is the absorption coefficient (cm^{-1}) and d is the film thickness (nm).

The spectrophotometer used in this study is a Perkin Elmer Lambda 950 and the measurement is carried out in a step size of 2 nm. All the UV-Vis characterizations of the perovskite absorber films are carried out in air.

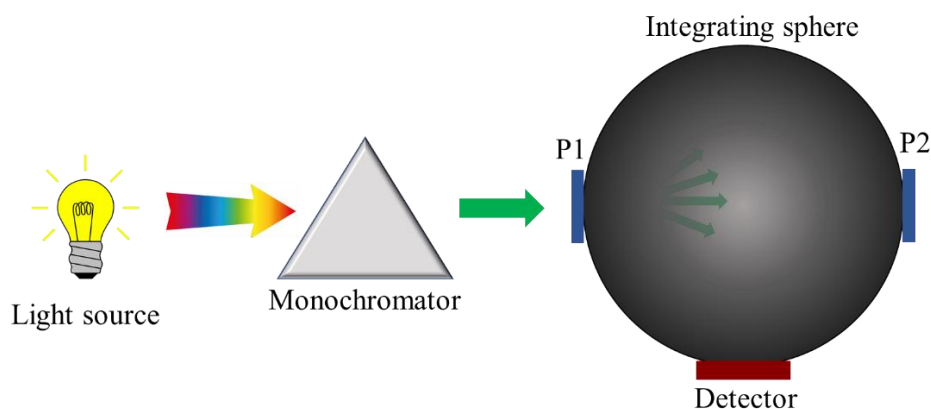


Fig. 4.3: Schematic illustration of a spectrophotometry setup.

4.3.4 X-ray Diffractometry

X-ray diffractometry (XRD) is a technique used to study the atomic and molecular structures of the material. Information about the crystalline structure of a material can be extracted by striking the sample with X-rays and measuring the scattering angle and intensity of the scattered X-rays. When the film is consisting of a crystalline material, the regular distribution of the atoms acts like a grid and diffracts the incident X-rays, as they are of the same order of magnitude. The scattered rays which are in phase will experience constructive interference and those that are out of phase will undergo destructive interference. The intensities of the scattered X-rays are plotted against the scattering angles. The structure of the material under investigation is then determined by the

analysis of the positions (given as a function of angle) and the intensities of the scattered peaks (see Fig. 4.4).

When the incident rays diffract from different lattice points, the diffracted rays interfere constructively at a certain angle of incidence, which can be reinforced according to the Bragg's law,²⁵³ given as:

$$2d_{hkl} \sin \theta = n\lambda \quad (4.6)$$

Where d_{hkl} is the spacing between atomic planes with hkl being the Miller indices, θ is the incident beam angle at which the diffraction peak is measured, n is the diffraction order, and λ is the wavelength of the X-ray. For X-ray diffraction, the condition given in Eq. (4.6) must be fulfilled.

For the X-ray diffraction measurements presented in this dissertation a Bruker D2 phaser, with Cu $K\alpha$ radiation ($\lambda = 1.5405 \text{ \AA}$) was used.

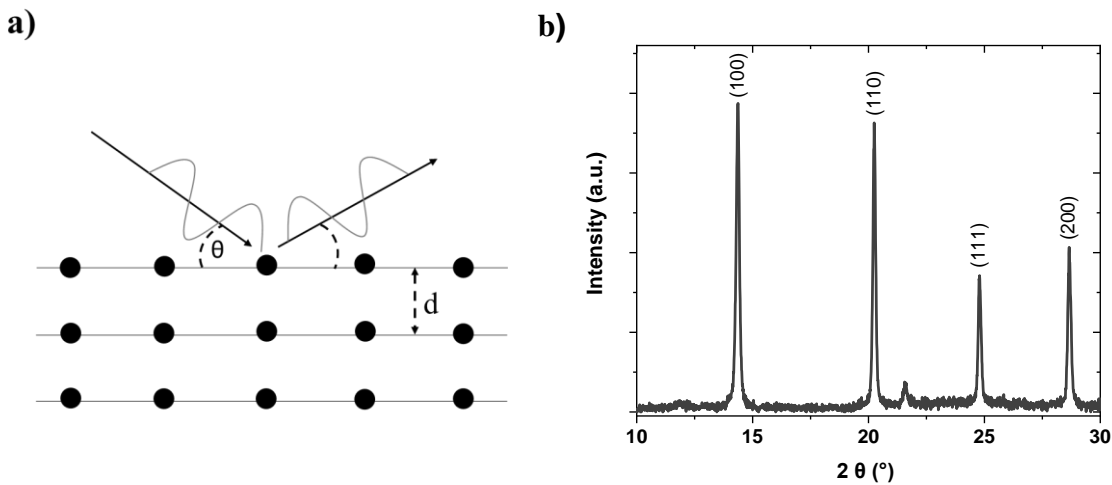


Fig. 4.4: (a) X-ray diffraction (Bragg's law), (b) typical XRD pattern of a perovskite crystal structure.

4.3.5 External Quantum Efficiency

The EQE is a commonly employed technique to estimate spectral dependent performance of a solar cell. It gives the probability of the absorption of an incident photon in the photoactive absorber material that actually contributes to the measured photocurrent. The wavelength dependent EQE measurement allows to extract the precise information about the power generation

of the solar cell as a function of the wavelength of the incident light. For this reason, it is also sometimes termed as incident photon-to-current conversion efficiency (IPCE). The J_{SC} of a solar cell can be calculated by the multiplication with the AM 1.5G spectrum and integrating over the wavelengths of interest:

$$J_{sc} = \frac{q}{hc} \int EQE(\lambda) * AM1.5G(\lambda) * d\lambda \quad (4.7)$$

where q is the elementary charge, h is the Planck constant and c is the speed of light. The EQE data reported in this dissertation is measured via a PVE300 Bentham EQE system. The system consists of two lamps (xenon short arc and quartz halogen), which generate a broad spectrum. The light is passed through a monochromator and then focused on the solar cell. The chopped light is detected with a lock-in amplifier and a silicon solar cell with a known EQE is used as a reference.

4.3.6 Thermally Stimulated Current Measurement

Thermally stimulated current (TSC) measurement is a very useful and powerful technique to investigate electronic trap states and their respective energies in a material.²⁵⁴⁻²⁵⁶ To perform TSC, a full stack of the solar cell is used. First, the solar cell is cooled to a very low temperature (16 K here) which is well below the activation energy of the traps. Then illumination is used to generate the charges filling up the traps. After that, the solar cell is kept at a constant temperature in dark for a few minutes to allow the charge carriers to relax and occupy the potential trap states to complete the thermalization process. The temperature is then increased at a constant rate up to room temperature. Thus, the charge carriers are gradually released from the traps which generate a flow of current in the solar cell.^{81,257-259} During the heating, the TSC signal is recorded in form of current (see Fig. 4.5) using a sub-femtoampere source meter. The source meter used here is the Keithley 6430. The traps already released at low temperatures are shallow traps, whereas charge carriers trapped in deep states require higher thermal energy to release.⁸⁰

The setup used for the TSC measurement consists of a closed-cycle helium cryostat (Janis, CCS-250). The heat transfer medium utilized is helium gas. A white light-emitting diode (LED) array of 1.5 sun intensity – due to uncontrollability over the illumination intensity – is used to fill up the traps while the solar cells are cooled down to 16 K.

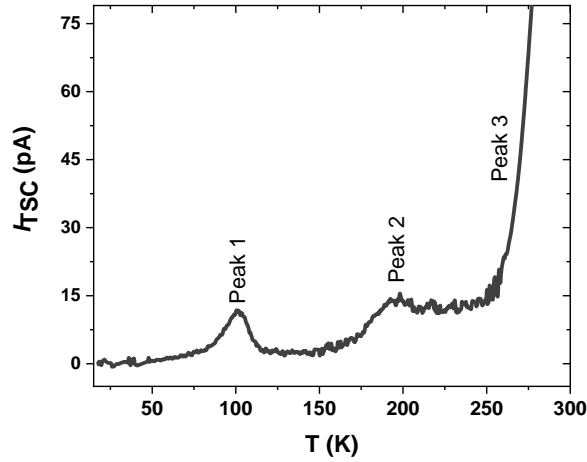


Fig. 4.5: Thermally stimulated current profile of pristine perovskite solar cell.

4.3.7 Ideality Factor Measurements

Ideality factor measurements can give information about the recombination mechanism in a solar cell. There are different methods to measure the ideality factor, however, the best one which can result in an accurate value in the case of perovskite solar cells is the V_{OC} dependence on light intensity (Sun- V_{OC}) technique.^{92,260–263}

The open-circuit voltage depends on the photo-current density in a fashion as described by the following equation 4.8.²⁶⁴

$$V_{OC} = \frac{n_{ID} k_B T}{q} \ln\left(\frac{J_{ph}}{J_0} + 1\right) \quad (4.8)$$

Where, n_{ID} is the ideality factor, k_B is the Boltzmann constant, T is the temperature measured in K, q is the elementary charge, and J_{ph} is the photo-current density, and J_0 is the dark current density.

To measure the ideality factor values, current density-voltage curves are recorded after 2 min of light soaking to get rid of any overestimation caused by the hysteresis. The illumination flux is changed under the solar simulator using multiple neutral density (ND) filters. The ND filters used here are from Thorlabs and having optical densities 0.1, 0.2, 0.3, 0.4, 0.5, 0.6, and 1.0 while the filter models are NE501B, NE502B, NE503B, NE504B, NE505B, NE506B, and NE510B

respectively. The transmittance of these filters and an exemplary graph for ideality factor value is given in Fig. 4.6. The slope of the $\ln I_{sc} - V_{oc}$ graph gives the value of the ideality factor.

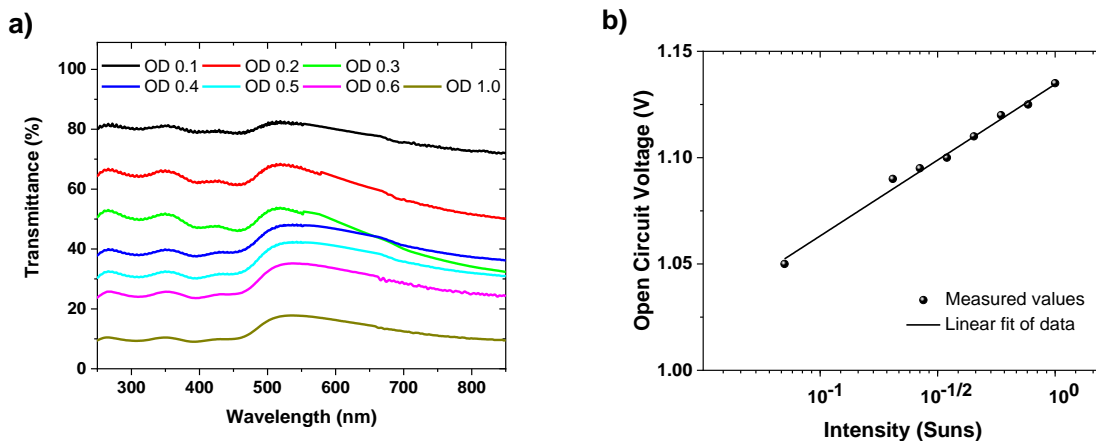


Fig. 4.6: (a) Transmittance of various neutral density filters employed to measure the ideality factor values, (b) exemplary graph of ideality factor value for pristine PSC.

4.3.8 UV Stimulated Degradation Setup

For the UV stability study in this dissertation, a custom-made UV cabinet is used to degrade the perovskite solar cells under multiple regimes of UV radiation. A schematic of the UV cabinet is presented in Fig. 4.7.²⁶⁵

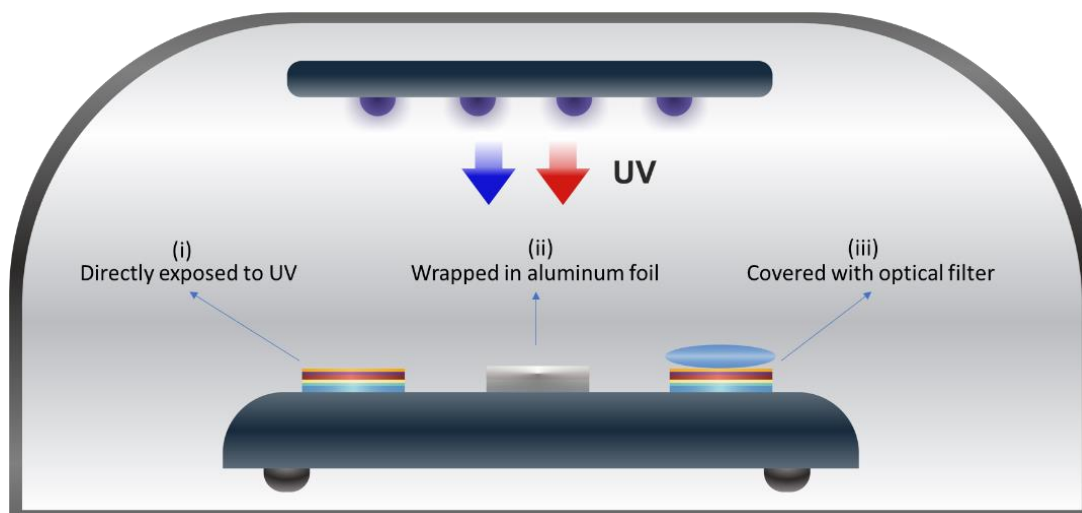


Fig. 4.7: Schematic of the UV degradation setup. Four UV lamps can be installed on the top slots, while the cells are placed on the baseplate. Reproduced with permission from Ref. 265. Copyright 2018, American Chemical Society.

The devices are subjected to UV stress (i) directly, additionally two kind of reference samples are used, as, (ii) the ones wrapped in aluminum foil to see any changes caused by temperature within the UV cabinet, lastly, (iii) the ones covered with long-pass optical filter (400 nm) to observe the role of any other radiation present in the UV cabinet. Two types of UV lamps (Philips, PL-S 9W/01 and PL-S 9W/210) with intensities 211 W m^{-2} and 367 W m^{-2} in the wavelength range 310 – 317 nm and 360 – 380 nm, respectively, can be mounted and dismantled on the ceiling of the UV cabinet. The spectra and intensities of UV lamps are provided in a coming section (5.3.2). The devices subjected to UV stress are taken out and measured under the solar simulator after specific intervals.

4.3.9 Visible Light Degradation Setup

The photo-stability study of the perovskite solar cells is carried out in a climatic chamber (DM 340 C SR Discovery ATT Umweltsimulation). The lamp used to generate the light illumination with an intensity of $1,000 \text{ Wm}^{-2}$ is a metal-halide arc lamp (OSRAM, HMI 1200W/DXS) and replicates the sunlight up to a good approximation ($\pm 2\%$) in the UV and blue region. The spectrum of the employed lamp along with AM1.5G spectrum is presented in Fig. 4.8.²⁶⁶ The spectrum was measured with a CCD (charge coupled device) spectrometer (Avantes AvaSpec-ULS2048x64-TEC). An optical fiber (Thorlabs FP1000URT) is used for the light collection. As intensity of the

lamp is high enough, no other collection optics was used. The spectrometer was irradiance calibrated with the help of a certified halogen lamp (Ocean Optics HL-3 plus).

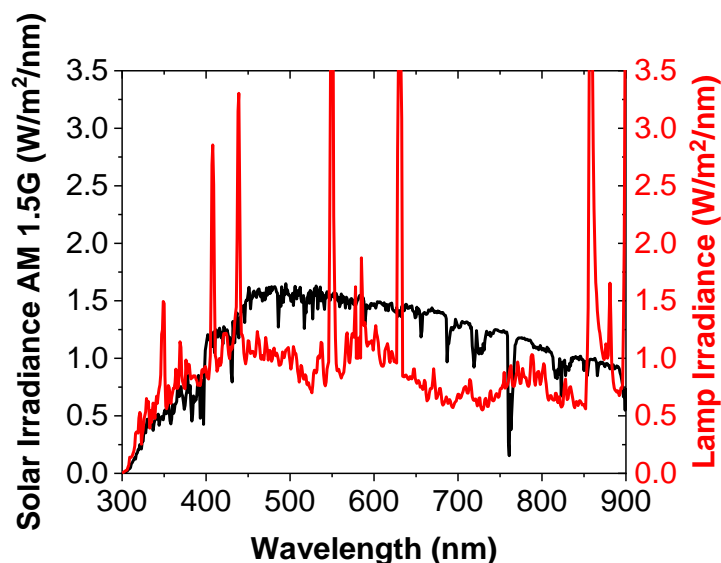


Fig. 4.8: Irradiance of the employed metal-halide arc lamp used in photo-degradation experiments along with AM1.5G spectrum. Reproduced with permission from Ref. 266. Copyright 2021, American Chemical Society.

For tracking the power conversion efficiency inside the climatic chamber, the solar cells are mounted on the sample holder which is placed inside an N_2 filled container with a quartz glass window on top. The purpose of using a quartz glass is to allow the UV radiation to pass through the glass without significant absorption in the glass. Pictorial view of the climatic chamber and sample holder is presented in Fig. 4.9. The contact pins of the sample holder are extended out of the sealed container via airtight connectors (VACOM, SUBD-37).

4. Materials and Characterization

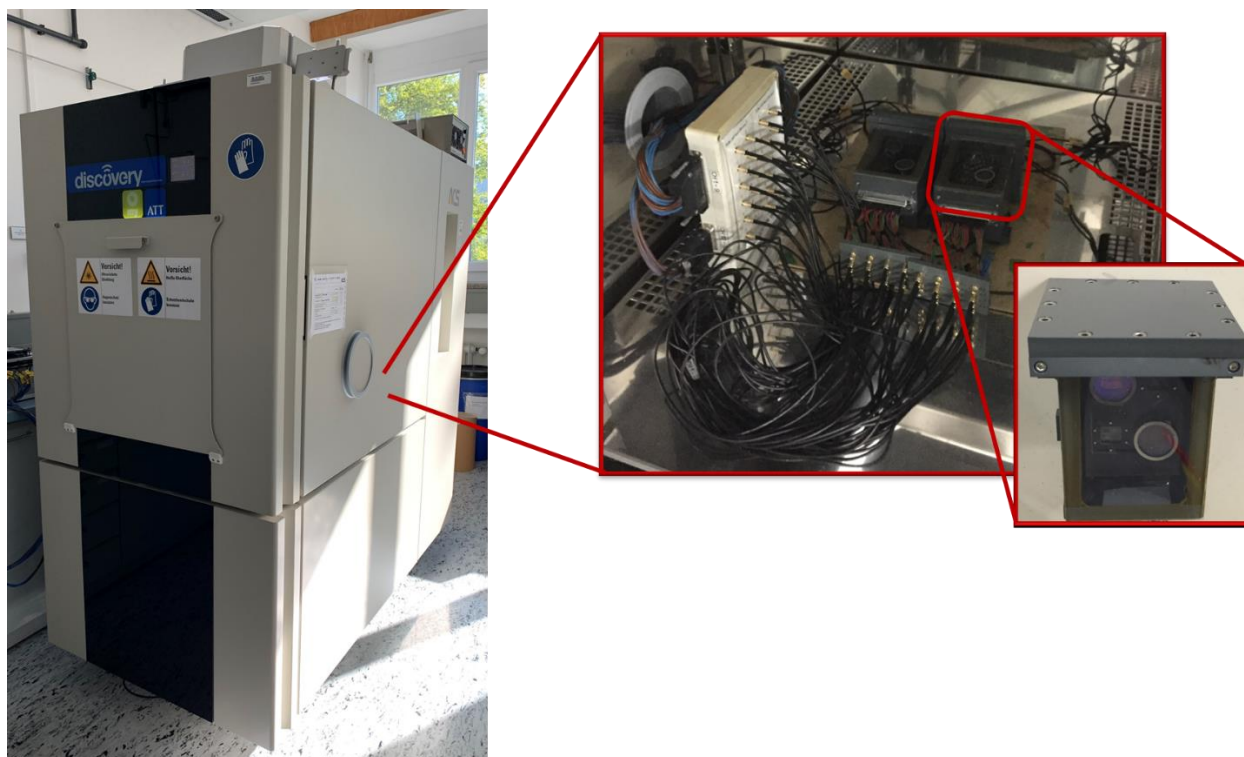


Fig. 4.9: Pictorial view of the climatic chamber and the devices mounted on the sample holder inside the N₂-filled sealed container placed in the chamber. Reproduced with permission from Ref. 266. Copyright 2021, American Chemical Society.

The temperature is set to 25 ± 2 °C on the solar cells throughout the experiments conducted in the climatic chamber. The solar cells exposed to light in the climatic chamber are continuously measured by tracking their stabilized PCE at constant voltage. The stabilized PCE is obtained by measuring the photocurrent at a constant voltage (V_{MPP}), obtained from the MPP of the J - V curve. The solar cells are measured until they are degraded below 80 % of their efficiency or longer.

5. UV Induced Degradation

This chapter is based on the investigation of UV radiation stimulated degradation in MAPbI₃ based PSCs consisting of multiple ETLs. The research question addressed in this chapter is: does the rate of UV triggered degradation change with different UV regimes and intensities, and how it depends on a multitude of ETLs in n-i-p PSCs? The results presented in this chapter are summarized in form of a journal article whose details are as below.

A. Farooq, I. M. Hossain, S. Moghadamzadeh, J. A. Schwenzler, T. Abzieher, B. S. Richards, E. Klampaftis, U. W. Paetzold, “Spectral Dependence of Degradation under Ultraviolet Light in Perovskite Solar Cells”, *ACS Appl. Mater. Interfaces* 2018, 10, 21985–21990.

Acknowledgements and contributions

The following work which summarizes the role of different regimes of UV radiation in triggering degradation of PSCs based on a multitude of ETLs was a result of team effort. In this project, Ihtez M. Hossain prepared the np-TiO₂ solution and optimized its spin coating parameters for development of efficient PSCs. Somayeh (Sara) Moghadamzadeh and Tobias Abzieher together optimized the e-TiO₂ recipe and S. Moghadamzadeh prepared the ETL coated substrates for further use in device fabrication. Jonas A. Schwenzler optimized the MAPbI₃ recipe used in these investigations. Dr. Dmitry Busko provided help in measuring the intensity of the employed UV lamps. Dr. E. Klampaftis provided and proposed the use of LDS doped EVA layers and supervised the related segment of this work.

5.1 Role of Electron Transport Layers

The reports discussing the UV instability in PSCs mostly use two types of ETLs, first TiO₂, second SnO₂. Due to the variation of ETLs, reports conclude different results on UV instability in PSCs. To address this problem thoroughly and for the generality of the results, we fabricate solar cells with four different ETLs to test the impact of UV radiation on them.

The most commonly used ETL in the PSC fabrication and yielding maximum efficiency is TiO₂.²⁶⁷ However, the disadvantage of TiO₂ is that it is known to reduce the solar cell performance due to the photocatalytic effect at the layer surface which starts the decomposition of MAPbI₃ absorber material into PbI₂.^{268–270} Secondly, lower carrier mobility of TiO₂ (2.5 cm² V⁻¹s⁻¹) as compared to MAPbI₃ (20 cm² V⁻¹s⁻¹) leads to charge accumulation at the ETL/perovskite interface resulting in hysteresis.^{214,215} On the other hand, SnO₂ is found to be more robust and stable against UV triggered instability in PSCs as well as leading to minimal hysteresis due to its excellent carrier mobility (240 cm² V⁻¹s⁻¹).^{271,272} Moreover, the hysteresis in SnO₂ based PSCs is found to be negligible as well which also plays a key role in a stable long-term performance of the solar cells.^{273,274}

5.1.1 Multitude of Employed ETLs

The ETLs employed in the solar cell architecture on top of either FTO or ITO, to study the UV-instability in PSCs are:

- (i) Compact SnO₂ (c-SnO₂)
- (ii) Post annealed at 500 °C compact TiO₂ deposited via spin coating (c-TiO₂)
- (iii) Nanoparticle TiO₂ grown via wet-chemical synthesis (np-TiO₂)
- (iv) TiO₂ deposited via electron beam evaporation (e-TiO₂)

The multitude of the employed ETLs will allow us to draw a general conclusion about the dependence of UV instability on the ETLs.

As the bandgap of the used ETLs varies depending on the composition and thickness of the transport layers, thus, to check if the ETLs are transparent for the incident UV radiation or not, their transmittance is measured using UV-Vis spectroscopy as presented in Fig. 5.1.

5. UV Induced Degradation

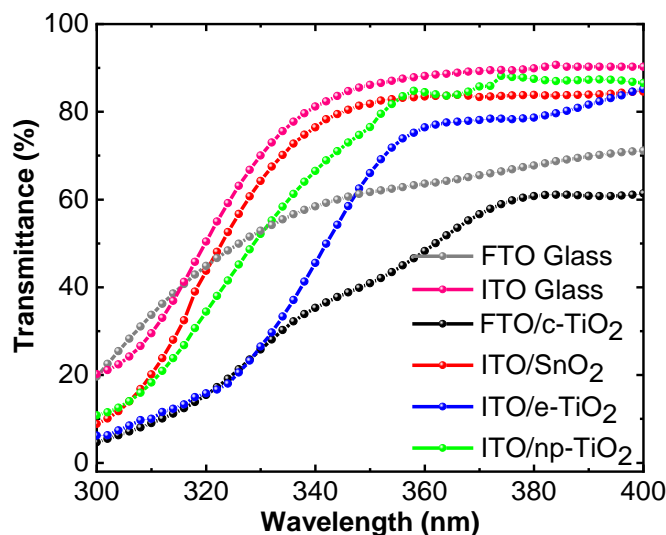


Fig. 5.1: Transmittance of various electron transport layers in the UV range. Reproduced with permission from Ref. 265. Copyright 2018, American Chemical Society.

The transmittance of un-coated ITO glass is higher as compared to FTO glass which arises due to lower thickness of ITO glass (1.1 mm) as compared to the FTO glass (2 mm) which can absorb larger amount of incident light due to higher thickness as well as due to the inherited lower transmittance of FTO layer itself. For the similar reason there exists a significant decrease in transmittance for the c-TiO₂ coated FTO sample as compared to others which are coated on ITO glass. Furthermore, the average transmittance of SnO₂ coated samples is more than the TiO₂ coated ones which is due to the larger bandgap of SnO₂ (3.6 eV) as compared to TiO₂ (3.2 eV). For a comparison of the transmittance through all types of ETLs, weighted average transmittance is presented for the incident spectrum as well as for the UV region in Table 5.1.

Table 5. 1: Weighted average transmittance through different ETLs coated substrates for the incident spectrum.

ETL Type	Weighted average transmittance (%) (300 – 850 nm)	Average transmittance (%) (300 – 400 nm)
SnO ₂	85.0	66
c-TiO ₂	76.6	45
e-TiO ₂	80.5	52.3
np-TiO ₂	83.7	63.9

5.1.2 Employed Solar Cell Architecture

The architecture of the solar cells used for UV stability work is n-i-p, with the MAPbI₃ (350 nm) as the active perovskite absorber material. The hole transport layer used in all the solar cells is Spiro-OMeTAD (300 nm), while the top electrode is 60 nm thick Au deposited via thermal evaporation. The final device architecture is given in Fig. 5.2.²⁶⁵

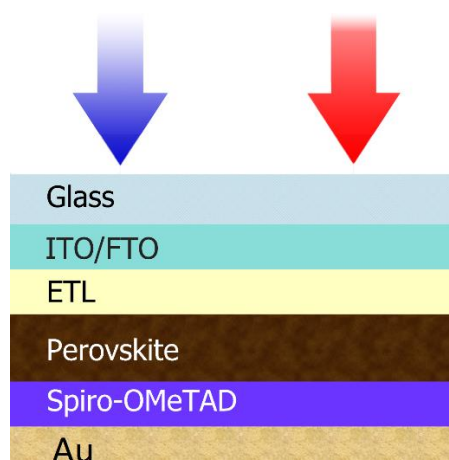


Fig. 5.2: PSC architecture used in UV instability measurement. Reproduced with permission from Ref. 265. Copyright 2018, American Chemical Society.

5.2 Spectral Distribution of UV Radiation in AM1.5G

The UV radiation in the solar spectrum that reaches the earth surface ranges from 280 nm to 400 nm and can be further divided into different classes i.e. UV-A and UV-B. The UV-C (100 – 290 nm) class of radiation is completely absorbed by the ozone layer and the atmosphere. The spectral range of the different classes can be seen in Table 5.2.²⁷⁵

Table 5. 2: Range of the different types of UV radiation in AM1.5G spectrum along with their spectral irradiance.²⁷⁵

UV Type	Wavelength range (nm)	W/m ²
UV-A	320 – 400	45
UV-B	290 – 320	1.6

The content of UV radiation present in AM1.5G spectrum as defined by the American Society for Testing and Materials (ASTM) G-173 standard is displayed in Fig. 5.3.²⁷⁶

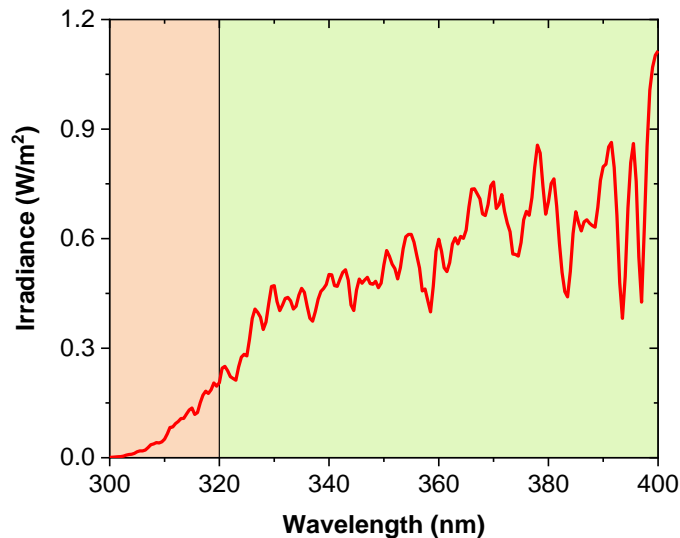


Fig. 5.3: Spectral distribution of various types of the UV radiation present in AM1.5G.

5.3 UV Stability Test Protocol

To check the UV stability of the perovskite devices, UV stability related routine of the already existing test standard, IEC 61215, widely used and trusted by the PV community is used.¹⁰⁹ Herein, we investigate the impact of UV radiation on the stability of PSCs and report the change in PV parameters of the devices over time upon UV illumination.

5.3.1 Standard Protocol

The standard test procedure available to test the UV stability of a solar module before commercialization is the ‘UV preconditioning’ routine present in the IEC-61215 test norm. According to this test routine, the solar modules must be held at 60 ± 5 °C and subjected to a minimum of 15 kWh m^{-2} between 280 – 385 nm with at least 5 kWh m^{-2} between the spectral range 280 – 320 nm.

For comparison, AM1.5G solar spectrum contains 35 and 1.6 Wm^{-2} in the 280 – 385 nm and 280 – 320 nm spectral ranges, respectively. It means that it will take 17.7 days by exposure to sunlight to reach the 5 kWh m^{-2} dose between the wavelengths 280 – 320 nm, and 137 days for the 280 –

385 nm range.¹¹⁰ For comparability purposes, the dose of incident radiation is given in term of kWh m⁻², as proposed by a recent consensus statement released by PV community.¹¹²

5.3.2 Employed Protocol

The UV stability testing protocol used here is rigorous and harsh as compared to the one proposed by IEC-61215. Here, two UV lamps (Philips; PL-S 9W/01, PL-S 9W/210) of intensity 211 Wm⁻² and 367 Wm⁻² with UV radiation in two different spectral ranges are used, (i) UV-A, herein referred as ‘UV-370 nm’ due to its peak emission at this wavelength, and (ii) UV-B, referred as ‘UV-311 nm’ hereafter, as its emission peak lies at the specified wavelength. The spectra of the used UV lamps are given in Fig. 5.4. Furthermore, UV exposure times are also recorded in terms of sun hours. To calculate the equivalent exposure time in sun hours, the intensity of UV radiation is compared directly to the UV content present in the respective spectral regimes of the AM1.5G spectrum. The full-width half maximum (FWHM) spectrum of the lamp is considered here for the sun hours. The irradiance of the UV-311 lamp is 211 Wm⁻² which is directly compared to irradiance in the same spectral range of AM1.5G i.e. 310 – 317 nm which is 1.82 Wm⁻². The direct comparison of 211 Wm⁻² to 1.82 Wm⁻² results in a factor of 116. It means that 1 hour of exposure to the UV-311 is equal to 116 hour of exposure to the same wavelength of AM1.5G. In the case of the UV-370 lamp, the lamp intensity is 367 Wm⁻², which yields a concentration factor of 16 when compared to 23 Wm⁻² of the spectral content in the similar range of AM1.5G solar spectrum.

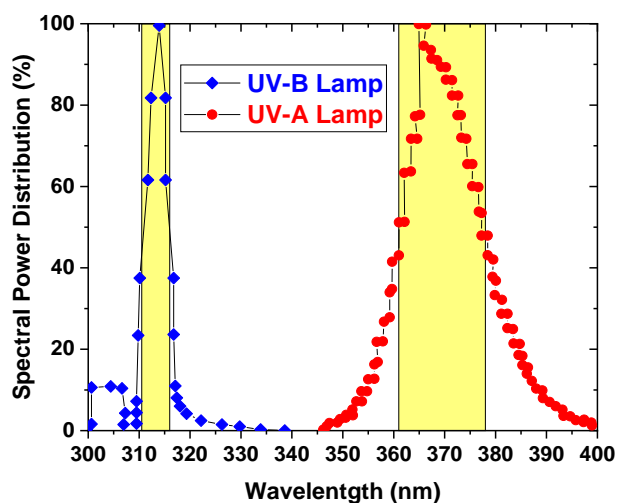


Fig. 5.4: Spectrum of UV-370 and UV-311 lamp employed for UV stability procedure. Reproduced with permission from Ref. 265. Copyright 2018, American Chemical Society.

Four types of devices based on different ETL are used in this experiment, while the number subjected to the illumination of each UV lamp is three, i.e. (i) directly exposed to UV radiation, (ii) exposed to UV after covering with the long-pass optical filter to make sure that any other light present in the UV cabinet is reaching the solar cell except the UV radiation, (iii) solar cells wrapped in aluminum foil to see the change in their performance because of any heat stress in the UV cabinet, and (iv) reference solar cells kept in nitrogen in the glovebox under dark conditions for the same duration of time for which the devices are subjected to UV exposure for a direct comparison in performance deterioration. The current density-voltage curves of the solar cells of all categories mentioned above are traced after regular intervals of time to keep a record of variation in solar cell performance. Before recording the J - V curves, all the solar cells are exposed to the light of 1 sun intensity for 5 min for light soaking and to make sure that the true performance of the solar cells is being recorded.

5.4 Role of UV Radiation Spectrum

When the MAPbI_3 based solar cells are exposed to the UV-370 spectrum (red in Fig. 5.4), a consistency in J_{SC} is observed. The J_{SC} values for all the solar cells employing various ETLs are presented in Fig. 5.5 (a). Eight devices for each category were measured. The error bar for

5. UV Induced Degradation

graphical representation of J_{SC} follows the percentile notation. The mean lines span over the 25th and 75th percentiles and the error bars are determined by the 5th and 95th percentiles. It can be seen (Fig. 5.5 (a)) that the PSCs exposed to UV-370 radiation do not show any prominent degradation in the J_{SC} values within the tested time which is equal to 1750 sun hours. In this case, the quantification of variation in J_{SC} over the 1750 sun hours is 2.9%, 1%, 0.7%, and 2.3% for SnO₂, c-TiO₂, e-TiO₂, and np-TiO₂ based PSCs respectively. However, when the PSCs are exposed to the UV-311 radiation for similar sun-hour duration a noticeable reduction in J_{SC} is observed as presented in Fig. 5.5 (b).

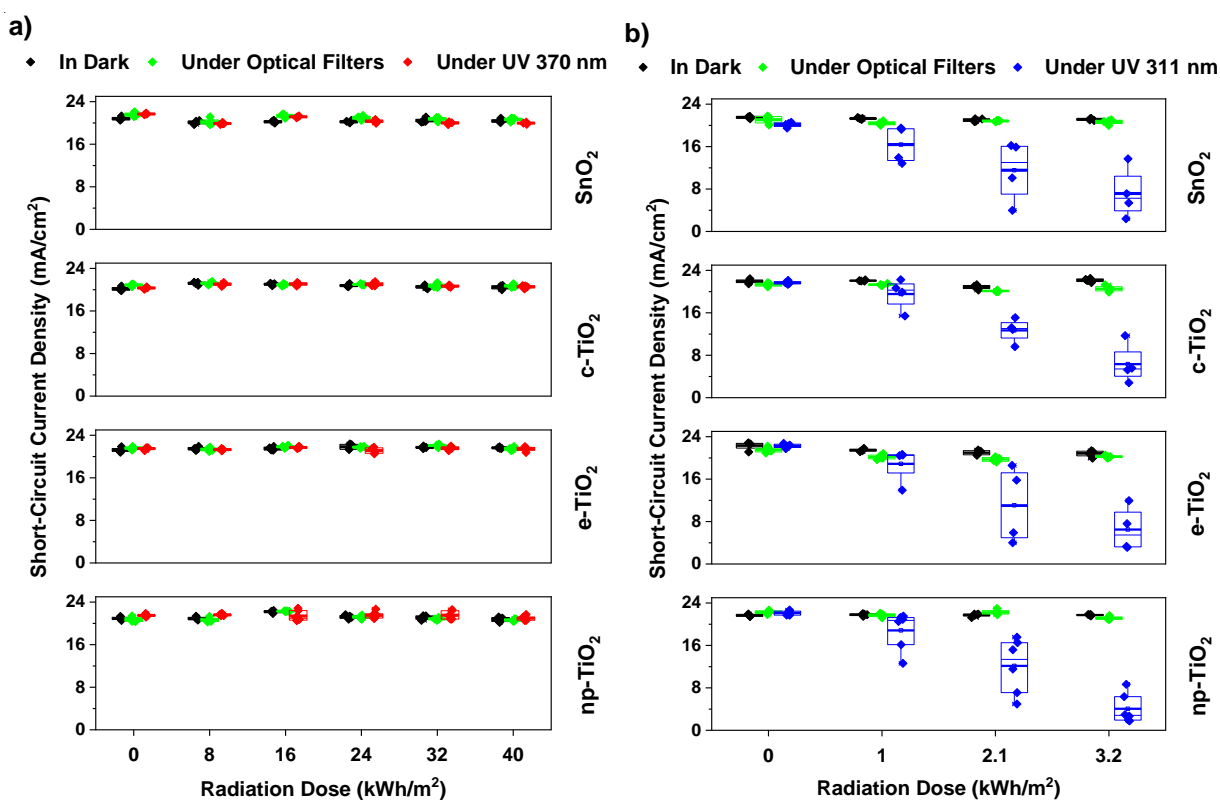


Fig. 5.5: Variation in the J_{SC} of perovskite solar cells based on various electron transport layers and exposed to (a) UV-370 radiation, (b) UV-311 radiation. Reproduced with permission from Ref. 265. Copyright 2018, American Chemical Society.

The decrease in J_{SC} is noted to be 64%, 71%, 72%, and 81% in SnO₂, c-TiO₂, e-TiO₂, and np-TiO₂ based solar cells throughout total UV exposure time, respectively. In contrast, the reference solar cells kept in dark and the solar cells covered with optical filters do not show any noticeable degradation in J_{SC} .

5. UV Induced Degradation

The J_{SC} reduction impacts the overall performance of the solar cells resulting in a decline in the power conversion efficiencies. The trend in change of PCE of the solar cells exposed to both types of UV radiation is exhibited in Fig. 5.6 (a) and 5.6 (b). The devices exposed to UV-370 radiation show a stable behavior within the tested time frame while those exposed to UV-311 radiation exhibit a continuous degradation as compared to the corresponding reference solar cells kept in the dark and under optical filters.

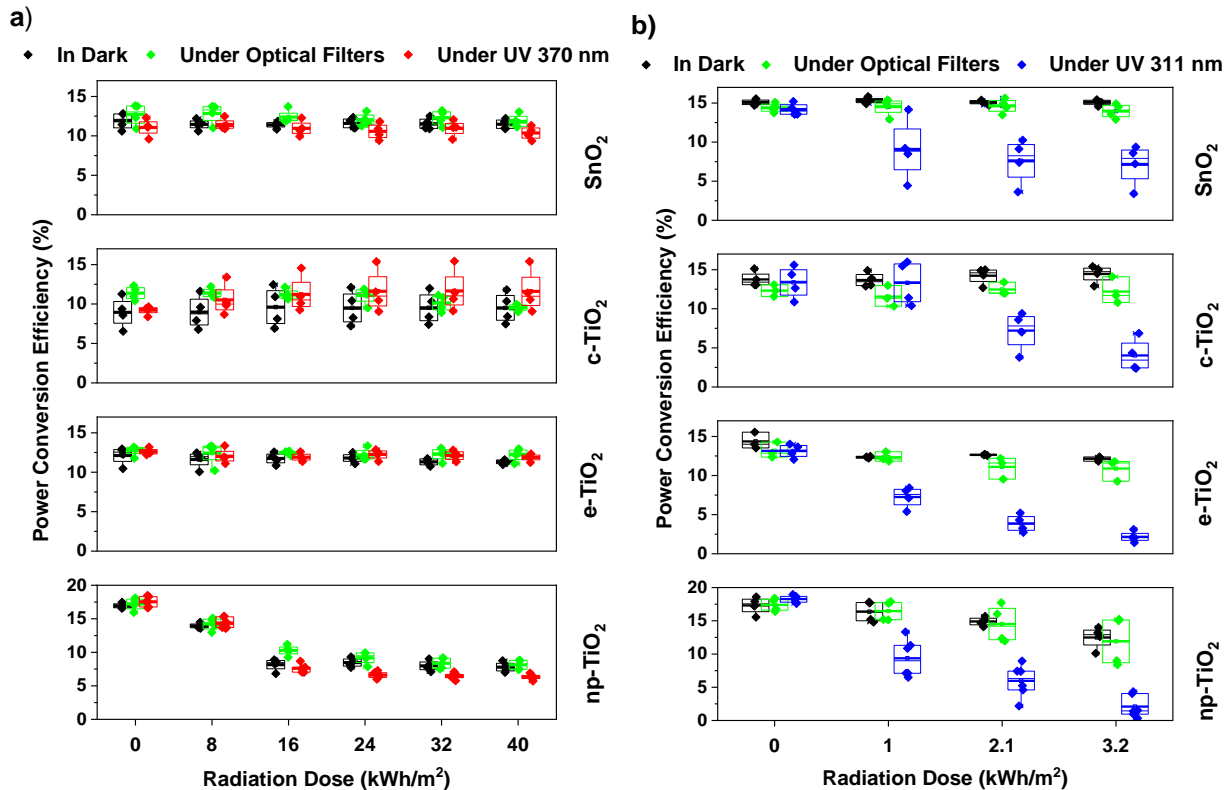


Fig. 5.6: Variation in the power conversion efficiency of solar cells exposed to (a) UV-370 radiation and (b) UV-311 radiation. Reproduced with permission from Ref. 265. Copyright 2018, American Chemical Society.

It is important to point out that the PCEs of the devices employing np-TiO₂ as ETL (bottom row in Fig. 5.6 (a) – show a tendency of gradual decline in performance irrespective of the radiation wavelength they are subjected to. This infers to the poor quality of np-TiO₂ as ETL, that degrades when evaluated over time, or a bad ETL/perovskite interface (Fig. 3.4, mechanism (g), (h)). However, if the PCEs of the devices except based on np-TiO₂ and exposed to UV-370 radiation

5. UV Induced Degradation

and their reference samples are compared, there is no performance deterioration caused due to UV-370 radiation.

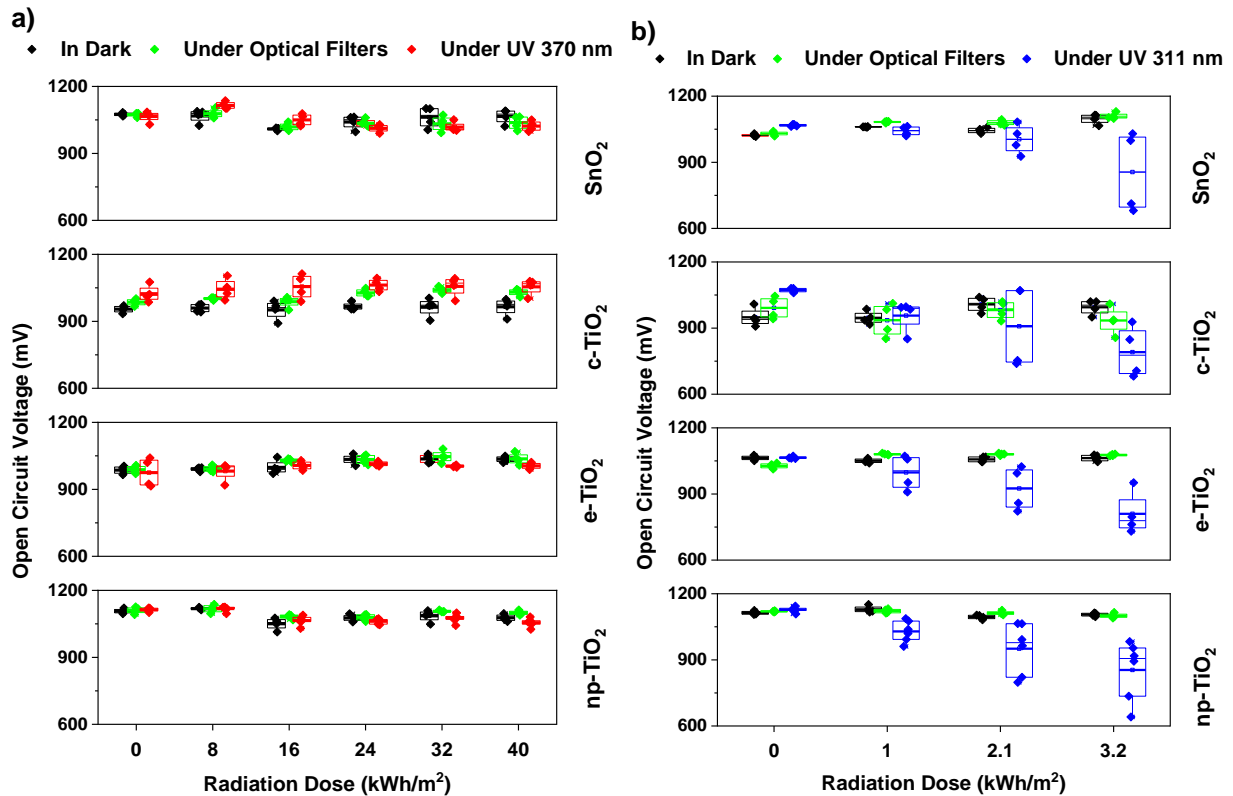


Fig. 5.7: Evolution of V_{OC} in the PSCs based on various ETLs and exposed to (a) UV-370 radiation and (b) UV-311 radiation. Reproduced with permission from Ref. 265. Copyright 2018, American Chemical Society.

If the change in the open-circuit voltage is compared with the change in J_{SC} in the case of the UV-311 radiation, the decrease is not significant. This refers to the decomposition of the perovskite absorber material, while the rest of the device structure remains intact leading to relatively stable V_{OC} values for exposure toward UV-311. However, the V_{OC} of the solar cells exposed to low energy UV-370 radiation does not exhibit any prominent deterioration. The evolution of V_{OC} upon exposure to the UV-370 and UV-311 radiation is presented in Fig. 5.7.

5. UV Induced Degradation

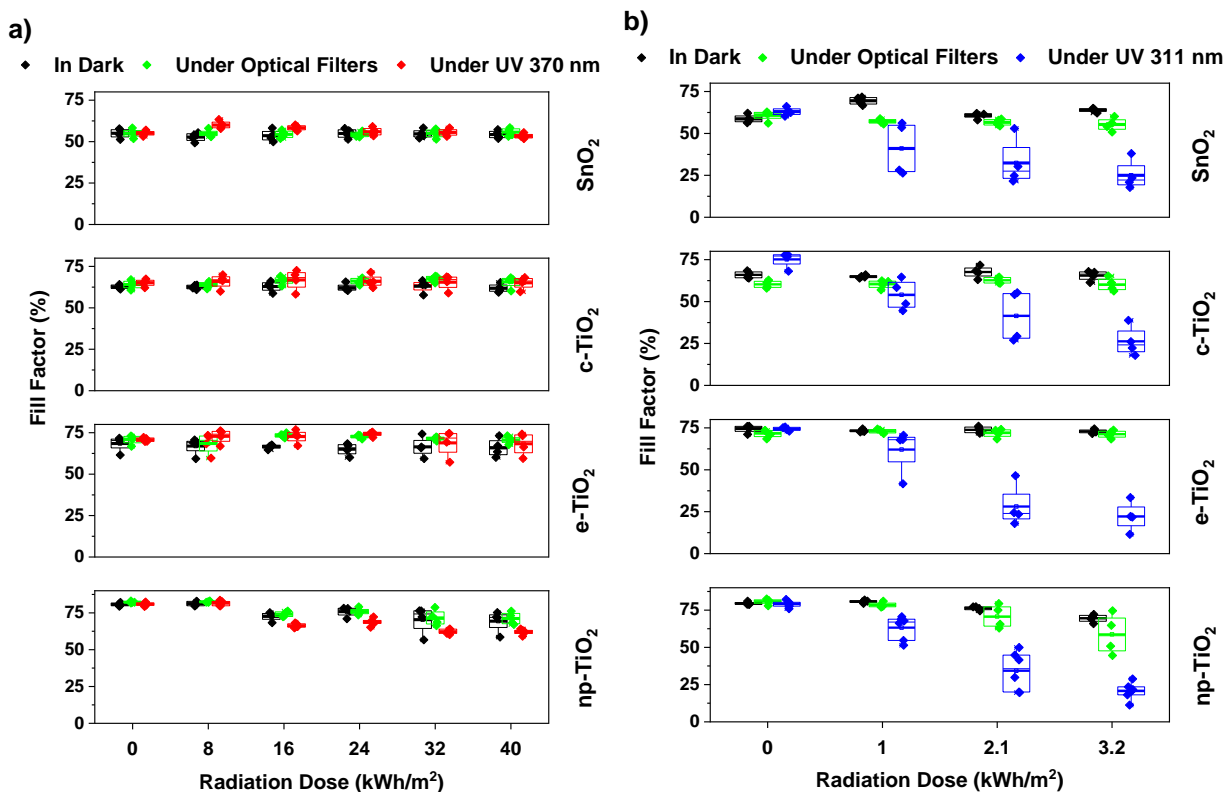


Fig. 5.8: Change in FF values of the PSCs based on various ETLs and exposed to (a) UV-370 radiation and (b) UV-311 radiation. Reproduced with permission from Ref. 265. Copyright 2018, American Chemical Society.

The trend of change in fill factor values as compared to V_{OC} upon exposure to UV-311 radiation is faster (5.8 (b)). This is due to the severe degradation in the J_{SC} of the solar cells. The devices exposed to the 370 nm UV radiation do not show a noticeable decline in FF values over the increasing exposure times (5.8 (a)).

From the presented data in Fig. 5.5 – 5.8, it can be concluded that the high energy UV radiation is more harmful to the stability of the perovskite solar cells within the tested time frame of 1750 sun hours and towards a UV dose of 3.2 kWh m^{-2} . While the less energetic UV-370 radiation does not cause much degradation in comparison within the same sun hour duration but high dose (40 kWh m^{-2}) of the UV radiation. Among all the employed ETLs, SnO_2 based solar cells are found to be relatively more stable showing 38% improved relative stability as compared to the most degraded np-TiO_2 based devices.

5.5 Role of UV-B Radiation Intensity

The intensity of the UV-B (UV-311) radiation, observed to cause degradation in PSC in Sec. 5.4, is 116 times higher (211.6 Wm^{-2}) as compared to that present in AM1.5G spectrum (1.82 Wm^{-2}) in the respective wavelength range. To see whether a less intense light is equally harmful or not, the intensity of incident UV-311 radiation is reduced 90%. Due to unavailability of an electric control over the lamp power, a polymer (cellophane) sheet is employed as UV moderator to reduce the intensity of incident UV-311 radiation. The transmittance of the UV moderator sheet before and after the UV degradation step is presented in Fig. 5.9 to verify that the polymer sheet itself is stable under highly intense UV radiation.

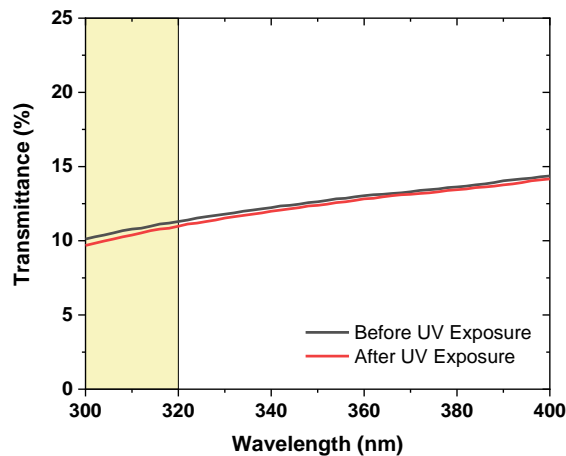


Fig. 5.9: Transmittance through the custom-made UV-B radiation moderator for stability measurements before and after the degradation step.

For the intensity dependence of UV instability, six devices are directly exposed to the UV-311 radiation, six devices are exposed to UV-311 after covering them with UV moderator and six control samples are covered with optical filters to cut-off all the incident UV radiation. The resultant data is presented in Fig. 5.10. The solar cells exposed to UV radiation after covering them with a UV-blocking filter (5.10 (a)) retain their initial performance after an absorbed radiation dose of 3.2 kWh m^{-2} . While the solar cells covered with a moderation filter (5.10 (b) blue) under UV radiation, initially show a light soaking effect but experience a gradual degradation over the increasing exposure time until the 3.2 kWh m^{-2} dose of incident UV radiation. The decrease in PCE in this case is 29% compared to a 3% decrease for the solar cells covered with a UV-blocking

5. UV Induced Degradation

filter and stressed under the same conditions. While the PSCs directly exposed to highly intense UV-311 radiation i.e. 211 Wm^{-2} (5.10 (b) red), exhibit 48% average decrease in PCE. This observation reveals that the UV degradation under intense UV-B radiation is intensity dependent, and the degradation under very intense radiation in short time spans cannot be extrapolated to predict long-term stability of the PSCs.

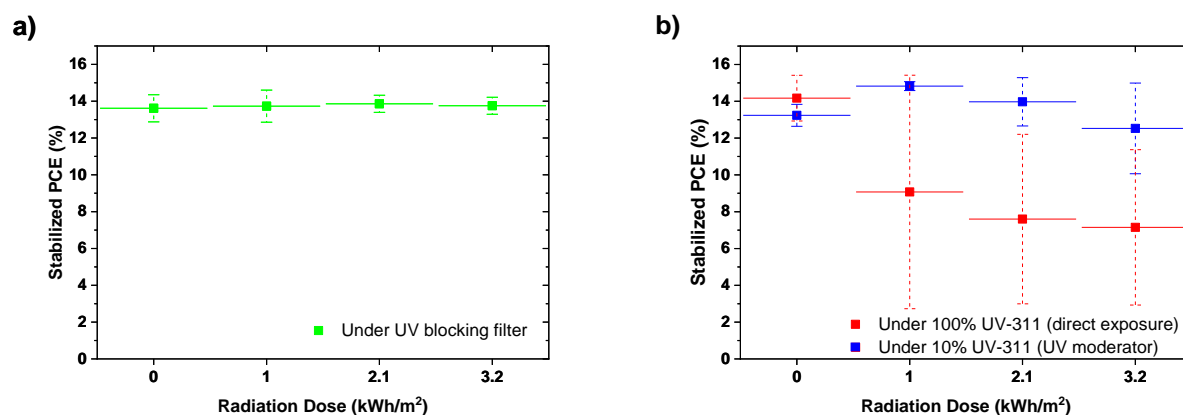


Fig. 5. 10: Variation in PCE of the solar cells exposed to UV-311 radiation (a) by covering them with UV-blocking filter (b) directly exposed (red) and covered with UV moderator that allows only 10% of the incident light to pass through. Adapted with permission from Ref. 265. Copyright 2018, American Chemical Society.

5.6 Prevention Strategies

The UV stimulated degradation in PSCs can be avoided by using many strategies as demonstrated for other counterparts. For example, the extra-terrestrial applications of PV technology suffer performance deterioration due to larger dose of high energy light ($\lambda < 400 \text{ nm}$). In such cases, the front glass of the modules is doped with cerium (Ce^{3+}) ions to minimize the impact of high energy radiation.²⁷⁷ The preference is given to the transparent materials to be used as the front glass covering to allow maximum light to reach the absorber material and be available for charge carrier generation. However, in extra-terrestrial environments where radiation intensity is extremely high, the cover material undergoes discoloration turning into yellow, and eventually lowering the absorbed radiation content. Initially, fused quartz glass was employed as front covering, and later annealed sapphire has also been used in extra-terrestrial PV applications due to its more radiation-resistant qualities as compared to fused quartz.²⁷⁸ Additionally, the cerium doped soda lime glass covering was investigated and used to replace fused quartz glass because of good quality of Ce^{3+}

5. UV Induced Degradation

to resist radiation and for its luminescent properties. In typical low-iron Ce-doped glass, the Ce is present in both (Ce^{3+} and Ce^{4+}) states. However, it is the Ce^{3+} state only that absorbs UV radiation to inhibit radiation induced discoloration.²⁷⁹ Upon exposure to UV radiation, the Ce^{3+} will be oxidized to the Ce^{4+} state, resulting in losing the radiation resistant properties.^{280–282}

In the case of terrestrial applications, initially polydimethyl silicone (PDMS) based encapsulants were used because of their exceptional UV resistance and thermal stability. However, due to higher cost of PDMS, efforts were focused on development of low-cost alternatives which resulted in the development of copolymer encapsulant material which is now commonly employed for sealing the PV modules. However, EVA also suffered a number of notable problems like of turning into yellow, or brownish in some cases, and delamination depending on the illumination intensities and exposure times when exposed to sunlight.²⁸³ The common reason for this discoloration is the high energy UV dose present in the sunlight. In the recent years, stabilized formulations for EVA have been developed, giving more confidence in the long-term stability of encapsulation.^{281,284} Thus, with the availability of more robust and UV stable encapsulant materials, the UV instability of the absorber material can pose a serious challenge to the stable long-term device operation. In case of PSCs, it is well established that they undergo degradation over long-term UV exposures.

Thus, the strategies recommended to circumvent the UV stimulated degradation problem in PSCs are: (i) UV filtering using UV blocking coatings, and (ii) luminescent downshifting (LDS) materials. Both strategies have their own advantages and disadvantages. Their ultimate employment in the PSC technology can only be decided after analyzing them based on cost and enhancement in solar cell lifetime.

5.6.1 UV Blocking Coatings

The simplest solution to get rid of the UV instability in PSCs can be blocking the harmful radiation content by using UV absorber coatings or modified UV absorber protective glass which can prevent the transmission of troublesome radiation towards the absorber material. A few examples of such coatings already exist in literature which can be modified according to the application in PSCs to give more UV stable solar cells.^{285–288}

However, this strategy comes at a price, which is the loss of some amount of current density as a reasonable portion of the light (46 Wm^{-2} between 300 – 400 nm) in the UV range will not be

5. UV Induced Degradation

absorbed. The blocked radiation will eventually reduce the device output current and overall performance. A summary of the loss in short circuit current density upon blocking the UV radiation of different wavelengths with a step of 10 nm is given in Fig. 5. 11.²⁶⁵

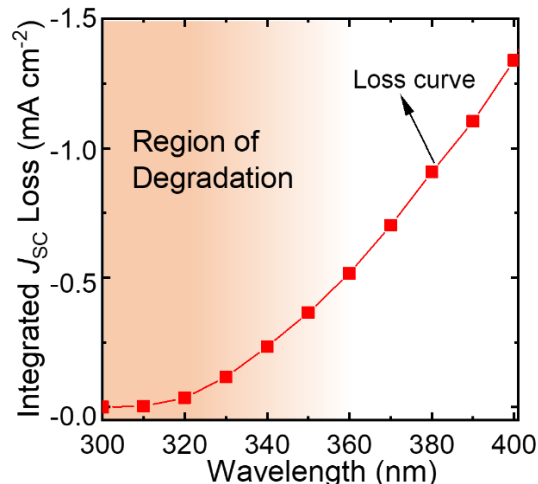


Fig. 5. 11: Loss in J_{sc} of the PSCs upon blocking the UV radiation to 400 nm in AM1.5G spectrum. Adapted with permission from Ref. 265. Copyright 2018, American Chemical Society.

The UV instability problem can also be handled by a simpler solution of using Ce^{+3} doped protective glass. However, the Ce^{+3} undergoes photoionization to become Ce^{+4} , which cannot absorb UV radiation.²⁸⁰ Another potential route can be the use of luminescent downshifting materials which can absorb the high energy photons and re-emit them in the low energy regions.

5.6.2 Luminescent Downshifting Materials

The advantage of using LDS materials instead of UV absorber coatings is that the high energy UV photons can be absorbed by the LDS species and re-emitted in the spectral region which is not harmful to the PSCs. Moreover, the external quantum efficiency is maximum in this range to make the best use of the downshifted photon. The EQE is defined as the ratio of the number of charge carriers collected by the solar cell to the number of incident photons on the solar cell surface. By this means, not only UV instability can be moderated, but enhancement in the current density can also be experienced (ideally, only if the short wavelength EQE response of the devices is poor) instead of the total loss of harmful UV radiation. The EQE spectrum of the under-study PSC and

the absorption and emission spectrum to confirm that there is no overlapping of both spectra, is presented in Fig. 5.12.

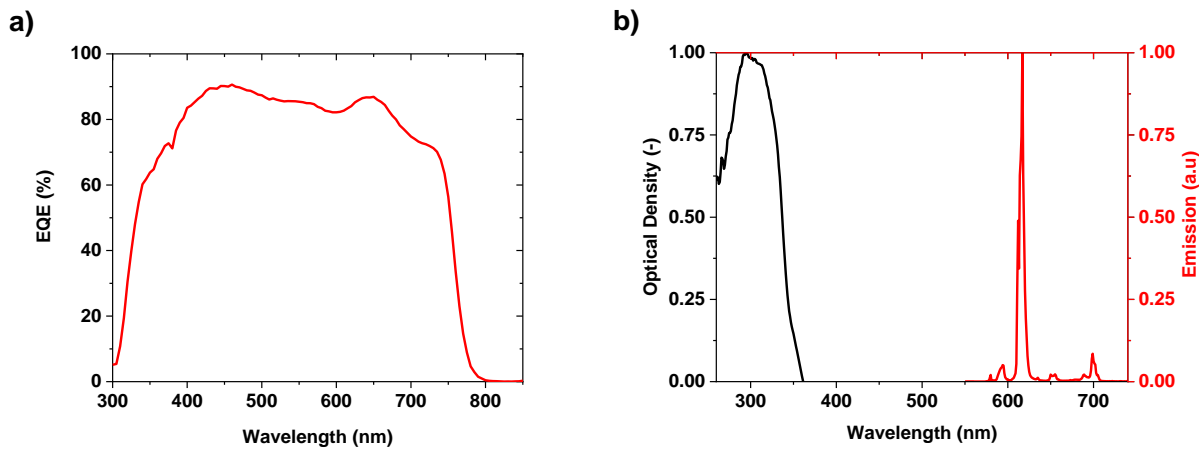


Fig. 5. 12: (a) EQE response of the employed solar cell, (b) emission and absorption spectra of Eu complex doped EVA.

To realize the gain in J_{SC} upon the use of the LDS material, the typical encapsulant material used for Si solar cells, i.e. EVA is doped with 2.5 wt% of Eu^{3+} complex as described in Sec. 4.3. To investigate the gain in UV regime via Eu doped EVA, the estimation presented below is used to evaluate the effectiveness of this strategy in terms of J_{SC} enhancement. First, the ideally recoverable current in the UV region is estimated. For this estimation, it is assumed that all the incident UV radiation is absorbed in the downshifting species the light of longer wavelength is emitted and absorbed by the solar cell as a result. This scenario is exhibited in Fig. 5.13 (green curve). Additionally, there are some other loss mechanisms as well which limit the efficiency of LDS material doped encapsulants, for example, sub-unity photoluminescence quantum yield (PLQY), emission in unwanted directions, increased reflection due to insertion of another layer, overlapping of absorption and emission regimes of downshifting material and others, as shown in Fig. 5.14.¹²³ However, considering the favorable assumptions (all the downshifted light is absorbed by the solar cell, i.e. no side emission or escape from the LDS layer and zero reflection of the incident rays), the calculated results of maximum and realistically recoverable J_{SC} are presented in Fig. 5.13²⁶⁵ (green and blue curves respectively).

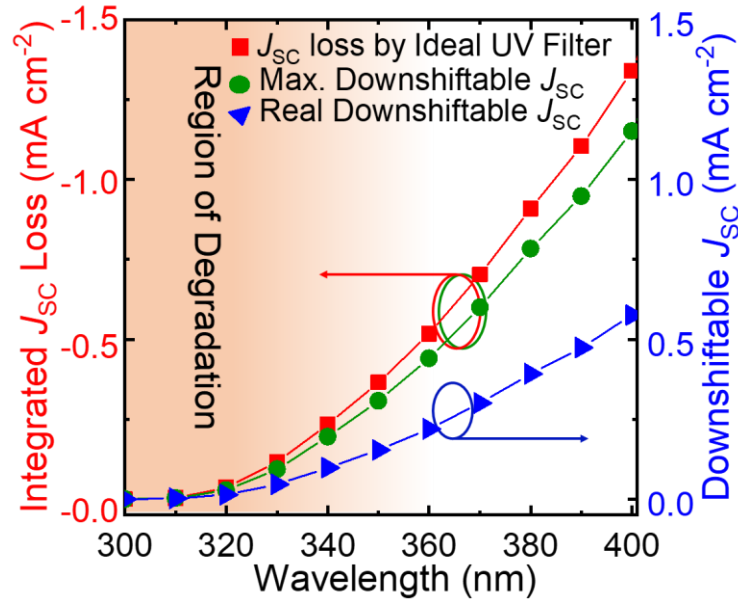


Fig. 5. 13: Maximum and realistically recoverable J_{SC} using the Eu doped EVA sheet. Reproduced with permission from Ref. 265. Copyright 2018, American Chemical Society.

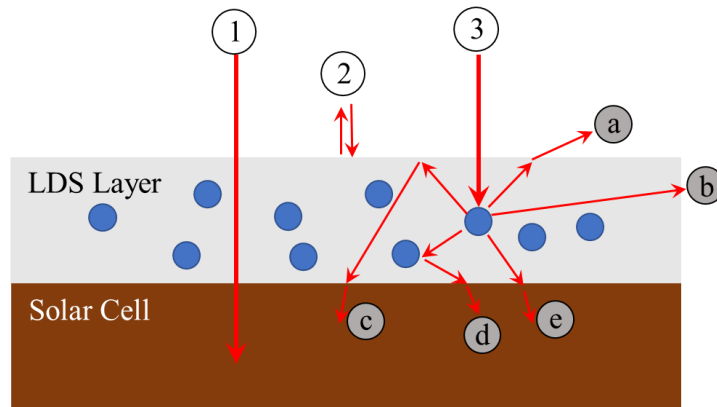


Fig. 5. 14: Schematic illustration of light absorption and loss mechanisms upon insertion of LDS layer on top of a solar cell. Adapted from Ref. 123. Copyright 2009, Elsevier.

Upon employment of LDS layer on top of solar cells, different loss channels are also created as shown in Fig. 5.14. Light that is not absorbed by the luminescent species will be transmitted to the cell, as ①. Some portion of the incident radiation may reflect back from the LDS layer as represented by ②. Radiation absorbed and re-emitted by the luminescent specie, depicted as ③ can undergo different gain or loss channels as: ① emitted out of the solar cell, ② emitted through the side of the LDS layer, ③ absorbed by the device after internal reflection from air-LDS

5. UV Induced Degradation

interface, \textcircled{d} absorbed and re-emitted by another luminescent specie, and \textcircled{e} emitted to the device. Considering the overall gain scenario by using Eu doped EVA, the outcome is not very promising.

To see the real performance of LDS layer practically, the Eu complex doped EVA layer is placed on glass side and stucked with an index matching liquid. The change in J_{SC} and PCE with and without LDS layer on top is shown in Fig. 5.15, which is -11.2% for J_{SC} and PCE each when covered with LDS layer. Due to the insertion of an additional layer on top of the solar cell, it creates extra reflection from the LDS/solar cell interface, as shown in inset of Fig. 5.15 (b). This reflection is accounted for 11.2% loss in J_{SC} and PCE. Since the main purpose of the LDS employment is to investigate its potential whether it can improve the UV stability or not, the position of the LDS layer (whether it is above or below the glass, given that glass also absorbs a portion of UV radiation), does not matter here as long as it can absorb the UV radiation effectively.

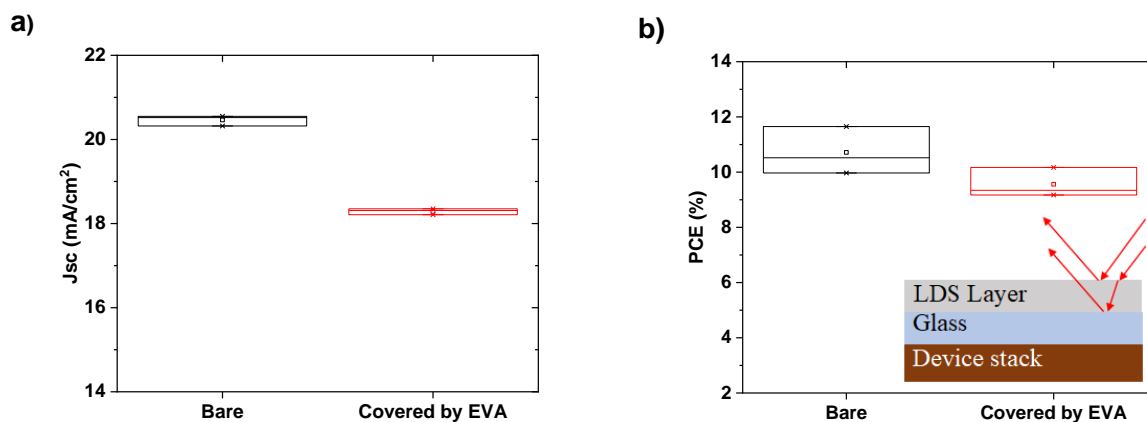


Fig. 5. 15: Decrease in (a) J_{SC} and (b) PCE of the PSCs upon covering with clear EVA.

Another challenge posed by the Eu doped EVA is the self-instability of the Eu complex upon prolonged exposure to the UV radiation. Fig. 5.16 (a) shows the result of the UV stability test of PSCs kept in dark as reference, exposed to UV directly, or covered with Eu doped EVA as well as with optical filters to cut-out the incident UV radiation to see any change in the PCE caused by any other factor except UV in the test cabinet. The devices which are directly exposed to UV show continuous degradation, while those covered with Eu doped EVA remain stable initially and then start to degrade with almost the same rate as the UV exposed devices do. This can be explained by the self-degradation of Eu complex upon exposure to UV radiation and thus losing its downshifting

5. UV Induced Degradation

properties which results in the degradation of the solar cells. This is checked by measuring the transmittance of the fresh and a ~100 hours UV exposed Eu doped EVA layer as presented in Fig. 5.16 (b).

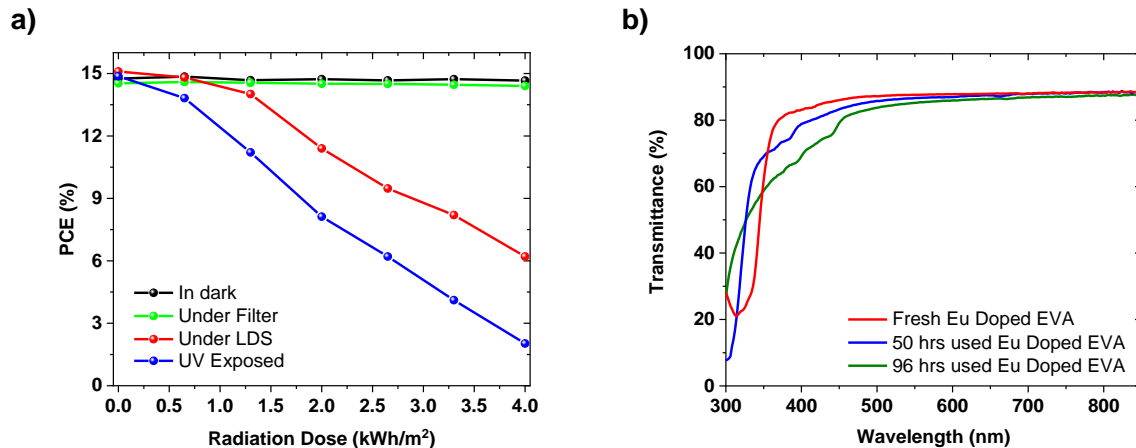


Fig. 5. 16: (a) UV stability of the devices kept in dark and exposed to UV radiation directly or under optical filters and LDS layer, (b) change in transmittance of the Eu doped EVA after different UV exposure times.

It can be noted that the fresh layers are initially absorbing ~80% of the incident UV radiation in 300 – 350 nm range. However, upon increasing UV exposure time it starts to become transparent in the concerned UV range (300 – 350 nm) while become less transparent in the trouble-free spectral range (350 – 450 nm) which can effectively contribute to the J_{SC} . The UV exposure times (50 hours and 96 hours) in Fig. 5.16 (b) represent a radiation dose of ~9 and ~18 kWh m⁻², respectively. However, even if the LDS material is stable, the maximum possible gain (realistically) achieved by using them is 0.22 mA cm⁻² for a wavelength range of 300 – 360 nm. However, incorporation of the LDS material in the device stack or in the cover glass will add further complexity to the manufacturing process. On the other hand, if a UV blocking coating is employed, only a small fraction of the photocurrent (0.53 mA cm⁻²) is sacrificed by blocking the UV radiation of 300 – 360 nm range. Thus, it is advisable that the UV blocking strategy can work better in prolonging the stability of perovskite solar cells. Another potential solution, which can be explored in future, is the use of LED color converter materials.²⁸⁹ They exhibit long-term life and high performance as well. In pursuit of achieving high UV stability for PSCs, the best approach can be the development of such an ETL that has relatively lower bandgap to absorb maximum dose of incident UV radiation and work as efficient charge extraction layer as well.

6. Visible Light Induced Degradation

This chapter presents the results of the visible-light-induced degradation in perovskite solar cells based on a triple cation absorber material. The composition of the triple cation absorber used here is $\text{Cs}_{0.1}(\text{FA}_{0.83}\text{MA}_{0.17})_{0.9}\text{Pb}(\text{I}_{0.83}\text{Br}_{0.17})_3$. The electron transport material employed in these solar cells is SnO_2 , which is found to be most stable, highly efficient, and robust as explained in Chapter 4 and 5. The research question aimed to address in this chapter is: Does visible light degrades the PSC? How different wavelengths within visible light impact the photostability?

The photostability evaluation includes the constant voltage tracking of the solar cells over several hundred hours to see the change in device performance for multiple spectra of the incident light. Later, the exploration to find the causes of the degradation is done by measuring the ideality factor and thermally stimulated currents. The chemical changes are traced using X-ray diffraction measurements. The results presented in this chapter are summarized and published in form a research article with citation details as:

A. Farooq, M. R. Khan, T. Abzieher, A. Voigt, D. C. Lupascu, U. Lemmer, B. S. Richards, U. W. Paetzold, “Photodegradation of Triple-Cation Perovskite Solar Cells: The Role of Spectrum and Bias Conditions”, *ACS Appl. Energy Mater.*, **2021**. doi.org/10.1021/acsaem.0c02813

Acknowledgements and contributions

The following section summarizes the photostability investigations of triple cation perovskite solar cells whose recipe was optimized by S. Moghadamzadeh. Dr. M. R. Khan performed the TSC measurements on the reference and degraded devices as well as calculated the activation energies associated with the trap states. T. Abzieher helped in performing and analyzing the ideality factor measurements and results. F. Schakmar provided the initial design for sealed, air-tight sample container, further modified by A. Farooq. R. Schmager and I. H. Hossain assisted in measuring the EQE response of the devices. The setup used to measure stabilized PCE over 250 hours was designed and programmed to control it remotely by A. Voigt. Dr. D. Busko extended help to measure the spectrum of the lamp employed in the presented work.

6.1 Quality of Solar Cells and PV Parameters

The performance of the solar cells employed in the photostability investigations is up to the mark as shown in Fig. 6.1 and Fig. 6.2 (a) with average PCE > 19%. Stabilized PCE of all the devices is also measured by tracking the PCE at maximum power point for 5 min and found >18% (as given in Fig. 6.2 (b)), before subjecting them to the stability test.

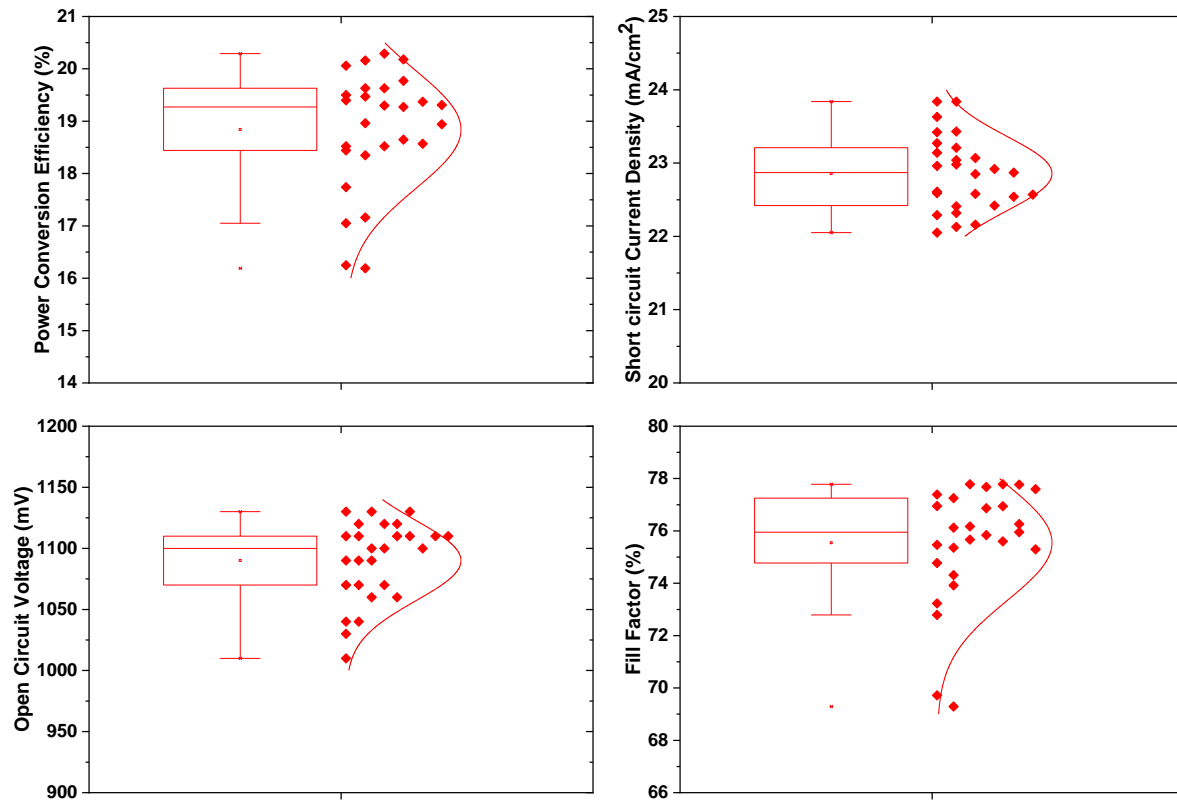


Fig. 6.1: Photovoltaic parameters of the solar cells before subjecting them to light stress.

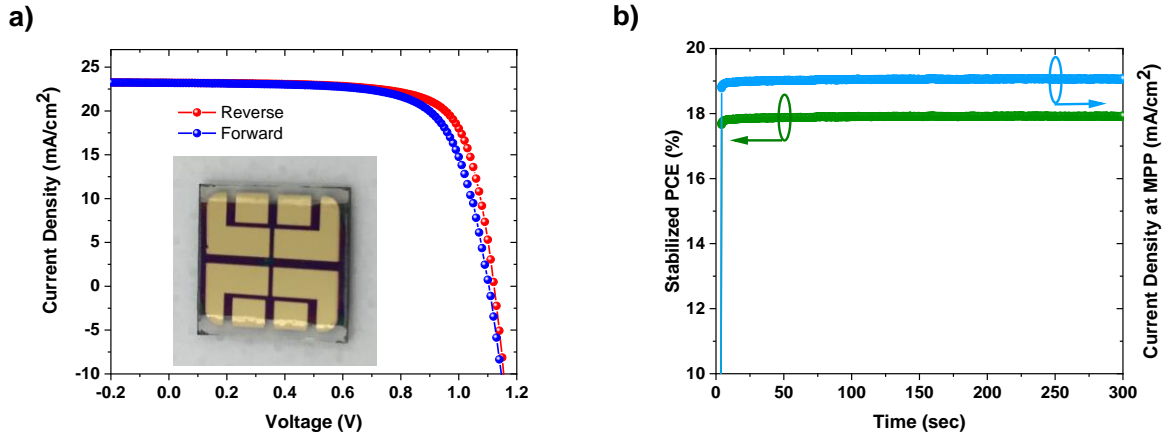


Fig. 6.2: (a) J - V curve of the representative solar cell along with a sample picture of a fabricated solar cell in the inset, and (b) stabilized power conversion efficiency at maximum power point along with current-density.

6.2 Spectral dependence of Light-Induced Degradation

The as-fabricated solar cells are measured to extract their PV parameters (PCE, J_{SC} , V_{OC} , and FF), and the devices with high performance are subjected to light stress. To investigate the role of various spectral regimes, optical filters are used to select light of a certain wavelength.

6.2.1 Spectrum Selectivity and its Role

The spectral dependence of photo-degradation is investigated using multiple optical filters, i.e. short-pass 400 nm (SP-400), long-pass 400 nm (LP-400), long-pass 450 nm (LP-450), long-pass 500 nm (LP-500), and neutral density filter with an optical density of 0.3 (ND-50%) which transmits only 50% of the incident light. All the used optical filters are listed in Table 6.1.

Table 6. 1: List of all the optical filters employed in the visible-light-induced degradation study.

Filter	Cut-off wavelength	Company/make	Role
Short-pass 400	400 nm	Thorlabs/ FGUV11M	To block visible light
Long-pass 400	400 nm	Thorlabs/ FEL0400	To block UV light
Long-pass 450	450 nm	Thorlabs/ FEL0450	To pass light $\lambda > 450$ nm
Long-pass 500	500 nm	Thorlabs/ FEL0500	To pass light $\lambda > 450$ nm
Neutral density	0.3 (optical density)	Thorlabs/ NE203B	To reduce intensity by 50%

6. Visible Light Induced Degradation

The transmittance of the optical filters listed in Table 6.1 can be seen in Fig. 6.3 (a) and the transmitted light intensity towards the solar cells underneath them for the given lamp is presented in Fig. 6.3 (b) and (c).

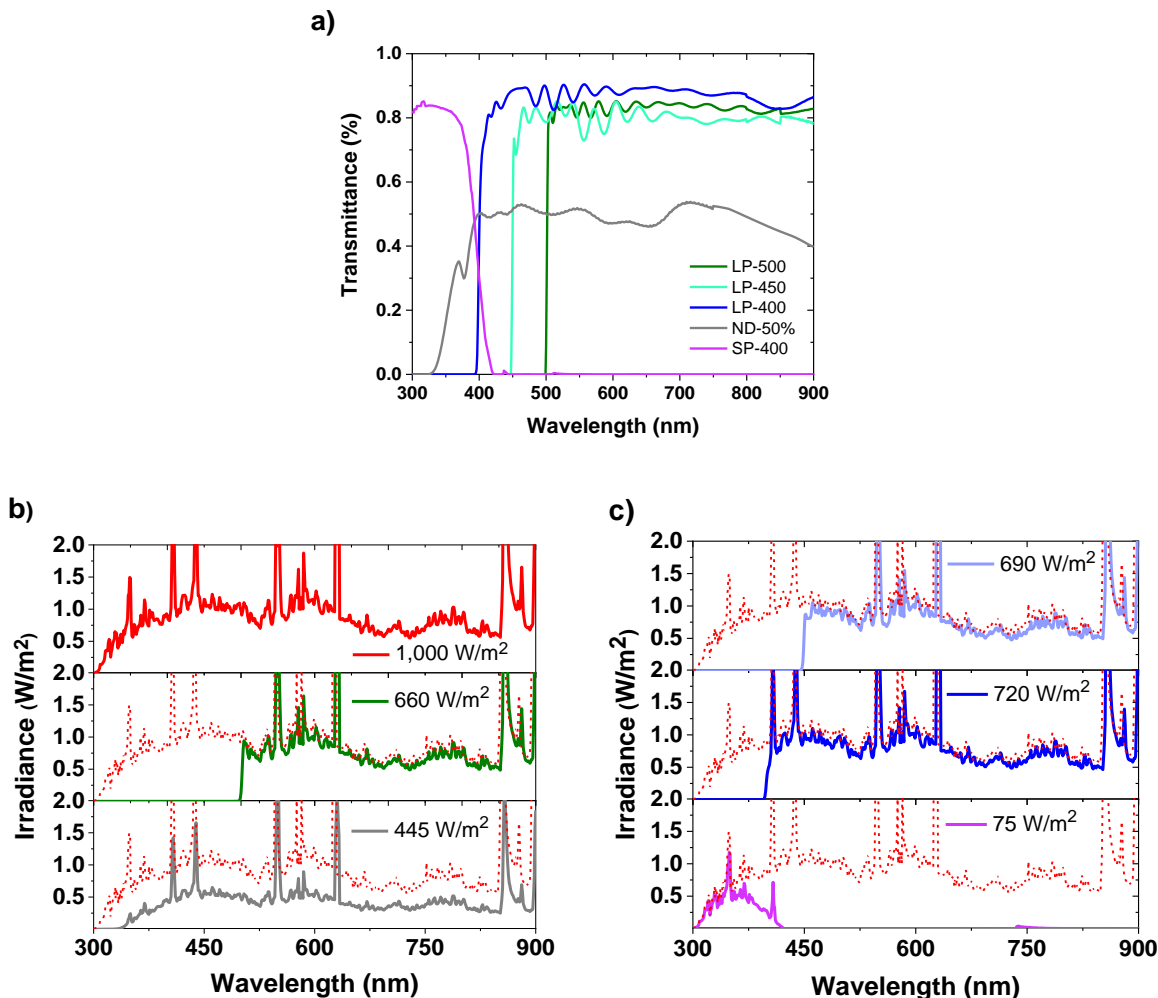


Fig. 6.3: (a) transmittance of the optical filters, (b) light irradiance on the solar cells through filters (a) LP-500, ND-50%, and without filter, (c) SP-400, LP-400, and LP-450. Reproduced with permission from Ref. 266. Copyright 2021, American Chemical Society.

When the solar cells are exposed to multiple light spectra as presented in Fig. 6.3 (b) and (c), the light impacts the devices differently. The phenomenon behind the different effects on the stability of the solar cells exposed to various regimes of light arises from varying energy of the absorbed light. The degradation stems from the absorption of the photons of high energies in the absorber material. Upon photon absorption, the device degradation can occur due to multiple reasons like, ionic movement is triggered in the absorber which leads to multiple effects, deep traps are

6. Visible Light Induced Degradation

generated resulting in decreasing the device performance by capturing the charge carriers, or charges are accumulated at the interfaces to hamper the efficient charge collection as depicted in Chapter 3 (Fig. 3.4). The ultimate result of the light absorption and the ongoing mechanisms is the lower performance of the solar cells which keeps on decreasing with increasing exposure time. Prolonged exposure is found to result in trap state formation and decomposition of the absorber material.

The decrease in the stabilized power conversion efficiencies measured at a constant voltage near the MPP is presented in Fig. 6.4 (a). It is pertinent to note that the solar cells exposed to light after covering them with LP-500 show consistent performance over an exposure time of 250 hours with a comparatively small degradation of 7% in PCE. However, the solar cells directly exposed to the light of 1 sun intensity undergo significant degradation (58%, relative) in the same period of continuous light exposure. This observation highlights that the low energy spectral regime ($\lambda > 500$ nm) causes minimal harm within the tested time frame, while the full spectrum of light impacts heavily on the stability of the investigated PSCs. The considerably stable performance under low energy light with wavelengths $\lambda > 500$ nm, together with the observed degradation under the full spectrum, implies that there is some part of the spectrum ($\lambda < 500$ nm), which stimulates the light-induced degradation. To find the most detrimental portion of the light which decreases the stability severely, the solar cells are covered with more optical filters LP-450, LP-400, and SP-400, and their effect on the stabilized PCEs is exhibited in Fig. 6.4 (b).

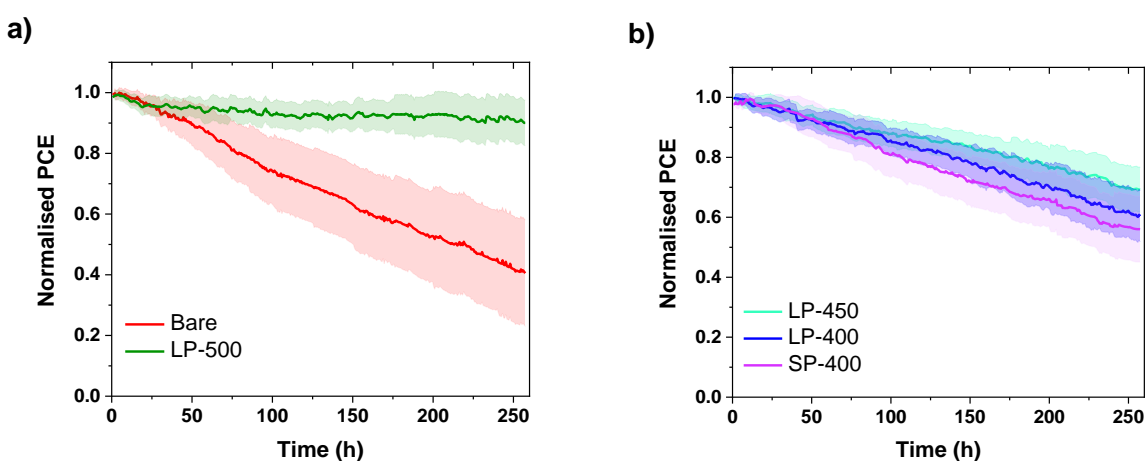


Fig. 6.4: Decline in PCE of the solar cells exposed to the light of 1 sun intensity (a) directly and under LP-500, (b) under filters LP-450, LP-400, and SP-400. Adapted with permission from Ref. 266. Copyright 2021, American Chemical Society.

6. Visible Light Induced Degradation

The SP-400 filter helps in knowing the impact of only UV light on the stability of solar cells and a direct comparison of UV versus visible-light-induced degradation can provide the foundation of the degradation stimulus. Upon covering the solar cells with LP-450, LP-400, and SP-400 filters and exposing them to light, a distinct trend of degradation is observed as presented in Fig. 6.4 (b). This observation shows that as the exposure wavelength range moves toward the high energy photonic regime, the performance deterioration also speeds up accordingly. The degradation speed is less for solar cells exposed to wavelengths $\lambda > 450$ nm (31%, relative) and highest for the solar cells exposed to wavelengths $\lambda < 400$ nm (44%, relative).

The intensity of light going through the optical filters varies according to their cut-off wavelengths. Thus, there is a fair chance that the degradation observed in Fig. 6.4 (a) and (b) is caused by the amount of incident light instead of its energy. The verification of this hypothesis is done by calculating the amount of light going through each type of optical filter and a direct comparison is made on this basis. The amount of absorbed light power by the perovskite solar cells underneath the employed optical filters and kept under the light of 1 sun intensity is presented in Fig. 6.5 (a). Utilizing this data, a relation between the decline in PCE to the absorbed light energy irrespective of the wavelength can be plotted as shown in Fig. 6.5 (b). After undergoing a degradation step of 250 hours under various spectral regimes of light, the solar cells degrade as seen via J - V curves as well as change color visibly. Fig. 6.6 presents the J - V scans before and after the degradation step along with visual condition of the devices in the insets.

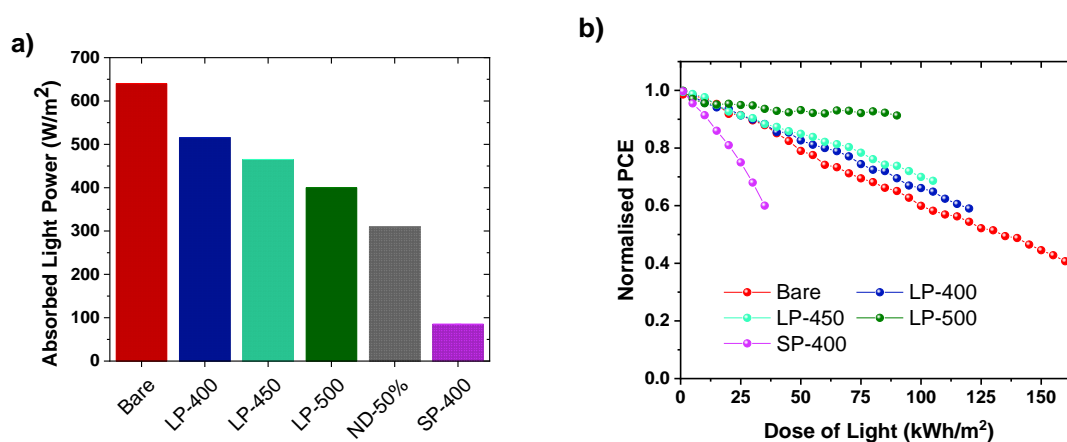


Fig. 6.5: (a) Light power absorbed by the solar cells through optical filters (b) performance deterioration in PSCs against the dose of incident light. Reproduced with permission from Ref. 266. Copyright 2021, American Chemical Society.

6. Visible Light Induced Degradation

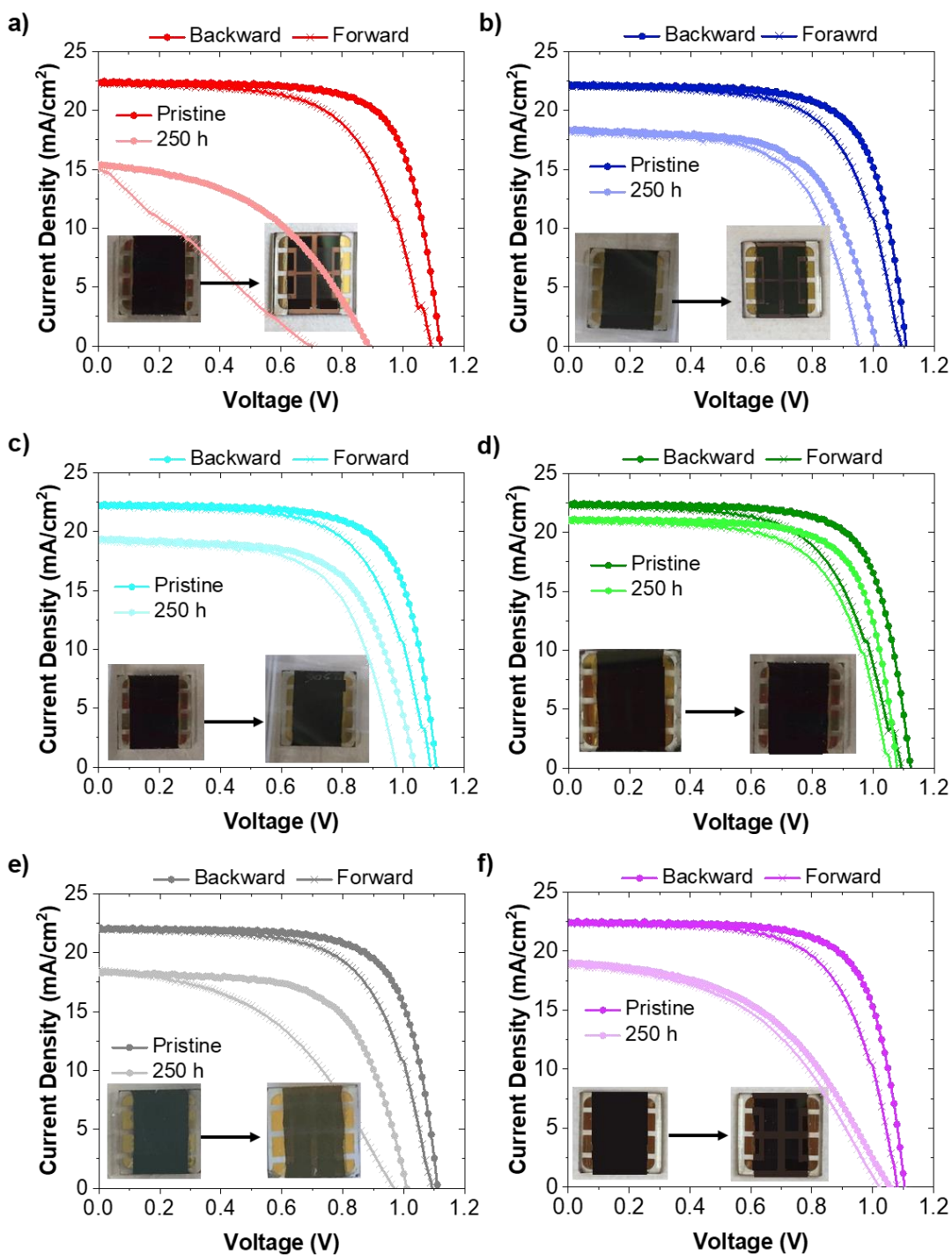


Fig. 6.6: J - V curves of PSCs recorded before and after the degradation step (a) directly exposed to light, covered with optical filters (b) LP-400 (c) LP-450 (d) LP-500 (e) ND-50% and (f) SP-400. Insets exhibit the visual condition of the solar cells before and after degradation to see any discoloration upon photodegradation. Reproduced with permission from Ref. 266. Copyright 2021, American Chemical Society.

Since Fig. 6.5 (b) presents the dose of light energy going through the optical filters and being absorbed in the solar cells underneath independent of the wavelength. Thus, it provides a direct relation between PCE deterioration and absorbed dose of light. The minimum dose of light is absorbed by the solar cells under the SP-400 filter which show maximum degradation. While the solar cells under LP-500 filter absorb almost double dose of light than those under SP-400 but their PCE is degraded significantly less. It infers that the photo-degradation is not a light dose-dependent, rather a wavelength-dependent mechanism.

6.2.2 Role of Light Intensity

The full spectrum of light causes degradation which becomes less pronounced as the energy-rich content of light is cut-off. Another aspect that can influence the photo-degradation is a higher intensity per unit time instead of the energy of the incident light. To investigate the light-intensity dependence of degradation, a neutral density filter of optical density 0.3 is used to cover the solar cells along with some bare devices and their PCE is measured over time. The performance deterioration in such a case is given in Fig. 6.7 (a) along with the spectral content of light going through the ND-50% filter in Fig. 6.7 (b).

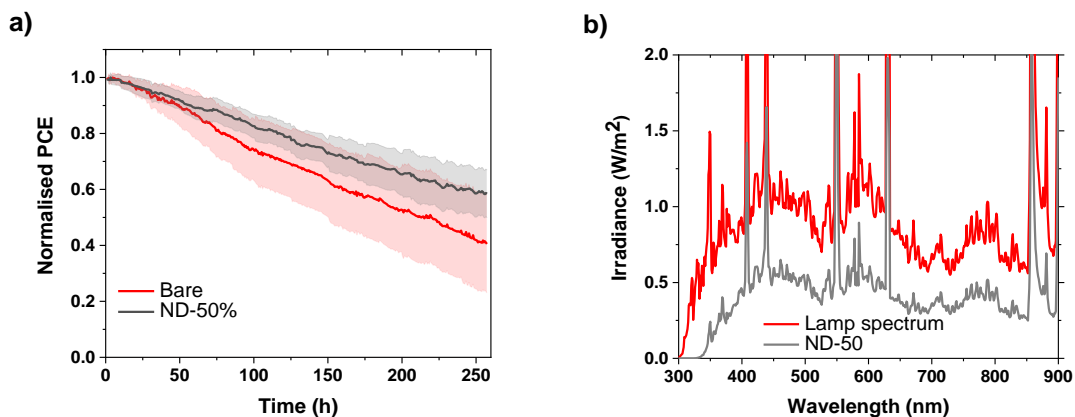


Fig. 6.7: (a) PCE deterioration for solar cells exposed to light directly and under ND-50% optical filter (b) spectra of light incident on solar cells directly or under ND-50% filter. Adapted with permission from Ref. 266. Copyright 2021, American Chemical Society.

This observation confirms that the light-induced degradation of PSCs is a spectral dependent phenomenon rather than being an intensity-dependent mechanism. The light of high energy, even if it is less intense, stimulates degradation in perovskite solar cells. As we reduced the incident

light intensity, the performance degradation is reduced as well, however, the relation is not linear. The solar cells directly exposed to light show a ~60% (relative) degradation in stabilized PCE, while the solar cells kept under 50% of the incident light intensity show a ~40% (relative) decline in performance. This observation infers that an enhanced stability cannot be achieved by decreasing the intensity of the incident light but filtering the energy-rich content of light can be a solution at the cost of a drastic reduction in J_{SC} .

6.3 Performance Recovery Investigations

Another important feature associated with perovskite solar cells is that they can show the property of performance recovery upon storage in the dark overnight.^{290–292} However, according to literary reports the performance recovery is observed only in moderately degraded solar cells.²⁹³ To see if the degraded solar cells show any improvement in deteriorated performance, all of them were kept in dark for 12 hours. The results of the performance recovery (Fig. 6.8 (a) and (b)) show that the solar cells which have undergone an intensive photo-degradation step have changed up to an extent that no performance recovery can be seen in them.

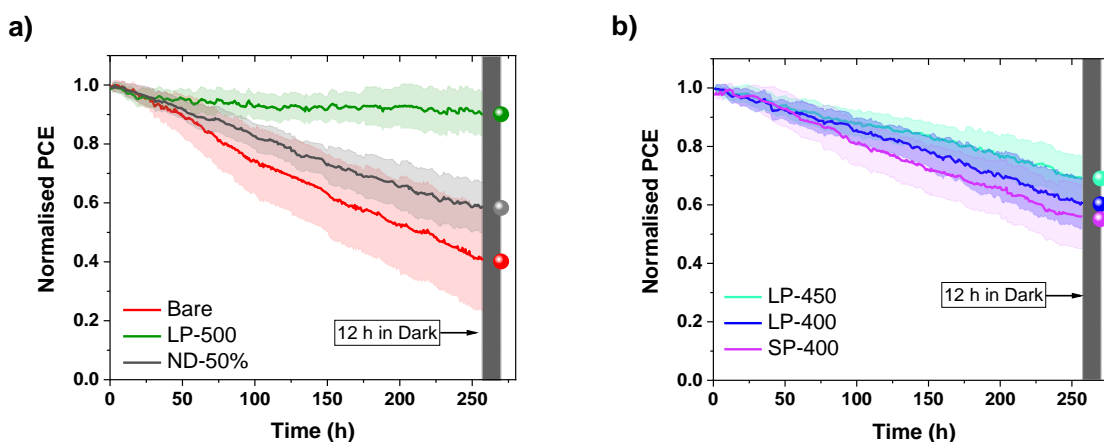


Fig. 6.8: The performance deterioration and subsequent recovery in solar cells (a) exposed directly or under LP-500 and ND-50% filter, (b) covered with LP-450, LP-400, and SP-400 filters. Reproduced with permission from Ref. 266. Copyright 2021, American Chemical Society.

The performance recovery is reported to be a result of trap passivation and the potential neutralization of these traps by the degradation by-product PbI_2 .²⁹⁰ However, as the degradation goes on upon continuous light exposure, the pronounced formation of PbI_2 results in irreversible

performance degradation. This can be explained by an abundance of PbI_2 which is a non-conducting species itself. Hence, at a certain point, the recovery of PCE becomes impossible and the cases presented in Fig. 6.8 are a representative of such an irreversible performance recovery scenario.

6.4 Decomposition of Absorber Material

Upon degradation of any kind, i.e. thermal, light, or humidity, the perovskite absorber material is observed and reported to decompose into its constituents. To verify the chemical decomposition in the degraded perovskite absorber films, XRD and UV-Vis spectroscopy are carried out.

6.4.1 Post-Degradation Compositional Analysis

Having demonstrated that the exposure to multiple spectral regimes induces degradation in perovskite solar cells, an analysis of the degraded absorber films is executed via XRD. In Fig. 6.9 the XRD patterns of the reference layers kept in dark for the same time duration along with the absorber layers subjected to the spectral light stress are presented.

The reference sample which is kept in dark did not show any change in its XRD pattern over time as seen in Fig. 6.9 (a). While other samples, exhibit a noticeable change in the XRD peaks in comparison to the dark reference. The absorber layer directly exposed to light undergoes massive degradation resulting in the appearance of a strong PbI_2 peak at a diffraction angle of 12.6° . In addition to this, the intensity of the first perovskite peak at 14.3° shows a significant reduction which is an indication of the disappearance of the perovskite features of the absorber materials.

6. Visible Light Induced Degradation

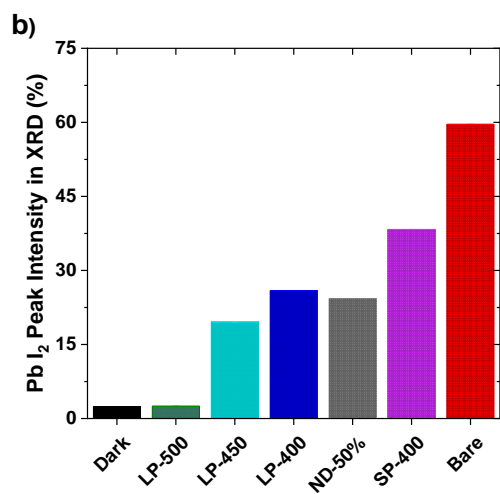
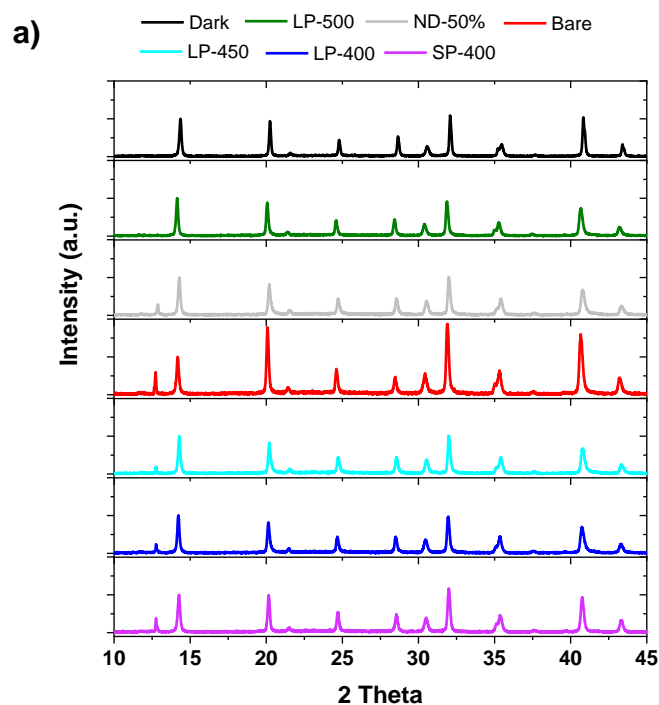


Fig. 6.9: XRD pattern of perovskite absorber layers (a) kept in dark, exposed to light directly or under optical filters LP-500, ND-50%, LP-450, LP-400, and SP-400. (b) PbI₂ peak intensity versus first perovskite peak in XRD patterns. Reproduced with permission from Ref. 266. Copyright 2021, American Chemical Society.

A similar trend of PbI₂ appearance can also be noticed for the absorber layers exposed to light after covering with the SP-400 which shows maximum degradation. This degradation rate is the highest after the samples which are exposed to the light with no filter atop. This observation infers that the

most harmful spectral regime is the UV radiation, although not the only one causing instability. In addition to UV radiation, the high energy blue light of wavelengths $400 \text{ nm} < \lambda < 450 \text{ nm}$ is also responsible for degradation. The spectral regime of the wavelengths $450 \text{ nm} < \lambda < 500 \text{ nm}$ also contributes to the device degradation; however, its harmfulness is the least among all the tested spectral regimes. The increasing content of PbI_2 while shifting the light exposure range toward high-energy light is not astonishing as the decomposition rate is also expected to escalate with progressive degradation. All the observations from XRD patterns can be summed up to conclude that the light with wavelength $\lambda < 500 \text{ nm}$ causes the most degradation in perovskite solar cells. This observation is also important for directly relating the performance deterioration with the increasing extent of decomposition which validates our previous knowledge from the literature that the higher the content of PbI_2 , the poorer is the device performance.

Moreover, the higher extent of decomposition in perovskite absorber films covered with the SP-400 optical filter gives a direct indication that the radiation with wavelength $\lambda < 400 \text{ nm}$ is the most detrimental part for the stability of PSCs. It is also worth pointing out that the photons with energies higher than 2.48 eV ($\lambda < 500 \text{ nm}$) heavily contribute to stimulating the degradation in the PSCs. This unique degradation behavior can be explained by the reported bandgap energy (2.4 eV) of the primary degradation by-product PbI_2 .^{294,295}

To further find a relation between the performance decline to the extent of the perovskite decomposition, the intensities of the PbI_2 versus first perovskite peak at 14.3° for all the solar cells are presented in Fig. 6.9 (b). The higher the value of this ratio, the greater is the decomposition taken place in the absorber material. The intensity of the PbI_2 peak is the highest for the layers directly exposed to light, which is a direct denotation of the highest degradation caused by the unfiltered full spectrum of light, followed by the ones exposed to the light of $\lambda < 400 \text{ nm}$. The chemical composition of the reference in dark and LP-500 covered solar cells remains almost unaltered.

6.4.2 Spectroscopic Analysis

To investigate that the absorber material decomposition takes place in the bulk of the layer or not, ultra-violet visible (UV-Vis) absorbance spectroscopy is carried out. The samples characterized

via UV-Vis spectroscopy are the perovskite films subjected to a degradation step of 250 hours with and without optical filters on top as described in Sec. 6.2.

Upon probing the reference and degraded perovskite absorber layers via UV-Vis spectroscopy a trend in absorbance variation is observed in all the samples. The UV-Vis absorbance spectra of all the samples are presented in Fig. 6.10 (a) and (b).

The reference sample kept in dark exhibits the characteristic absorbance pattern with an absorbance onset at 765 nm. After that, there is a gradual increase in the absorbance up to 500 nm with a strong absorbance in the range of 400 – 500 nm. A similar spectral absorbance pattern is also observed for the perovskite film covered with the LP-500 filter. The likeness of both absorbance patterns agrees with the non-degradation behavior of such samples observed during the *J-V* scanning and XRD characterization. However, the other samples e.g. those which are exposed to light directly or by covering with the ND-50% filter show a prominent reduction in the absorbance throughout the spectral envelope. Furthermore, the absorption peak of the perovskite at 740 nm shows a gradual decrease. In addition to that, severe absorbance reduction is noticed in the spectral range of 650 – 765 nm. This reduction is particularly attributed to the disappearance of the characteristic photoactive perovskite black phase (α -phase) in the bulk of the absorber layer.²⁹⁶ The remaining absorption edge in the wavelength range of 400 – 500 nm is associated with the presence of PbI_2 . In the samples exposed to filtered light by covering them with LP-450, LP-400, and SP-400 optical filters, a similar degradation pattern in the absorbance is observed as presented in Fig. 6.10 (b). Similarly, a reduction in EQE response throughout the spectral envelope is recorded for the devices directly exposed to full spectrum of 1 sun intensity radiation (Fig. 6.11). In comparison to this, the solar cells exposed to light under LP-500 filter or kept in dark did not show significant change in EQE response. These variations in the absorbance and EQE spectra for the degraded devices are an indication of the compositional changes happening in the bulk of the absorber material which give rise to the significant loss in the light absorbance capacity of these layers.

6. Visible Light Induced Degradation

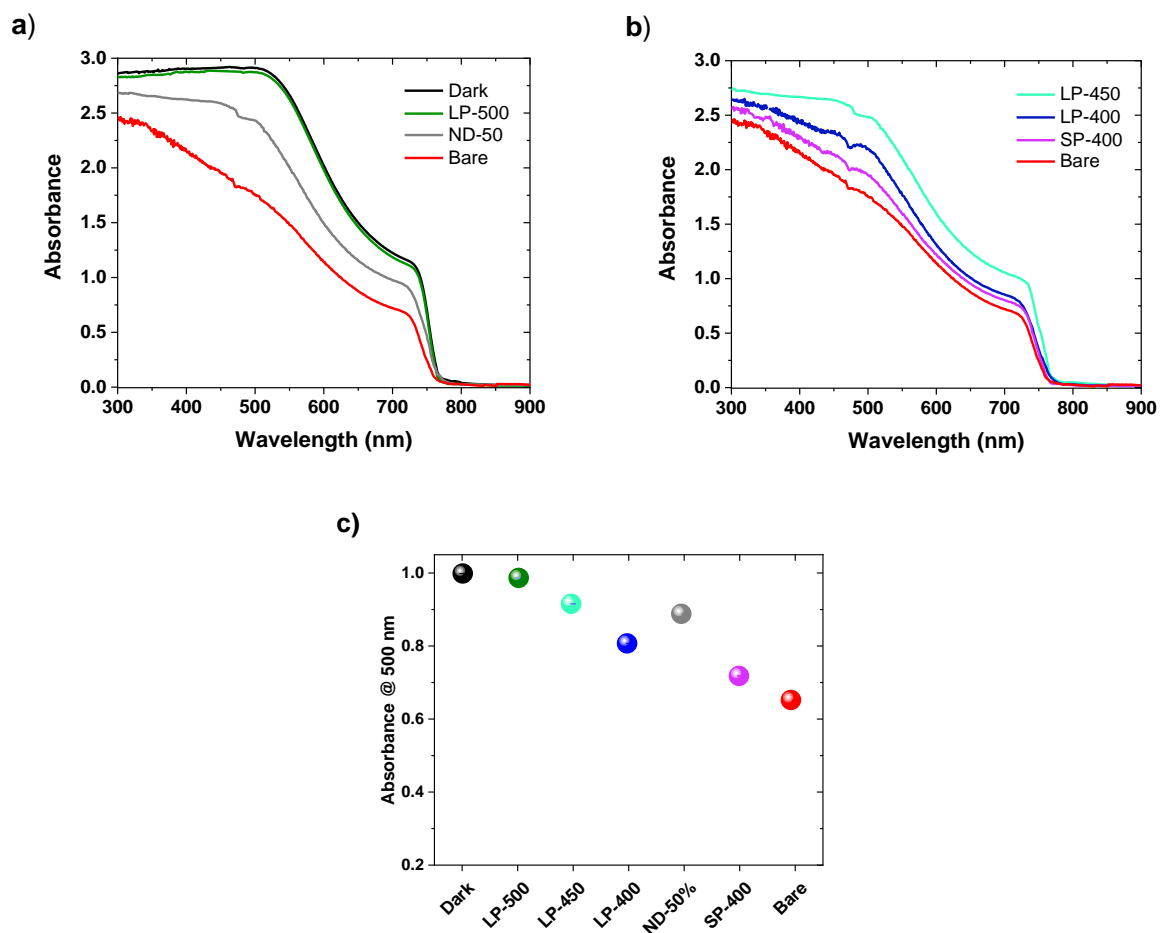


Fig. 6.10: (a) Absorbance spectra of perovskite layers after 250 h kept in dark, degraded under unfiltered and filtered light using LP-500 and ND-50% filter (b) absorbance spectra of perovskite layers degraded under filtered light via LP-450, LP-400, and SP-400 filters (c) absorbance values at 500 nm for all the samples employed in the experiment. Reproduced with permission from Ref. 266. Copyright 2021, American Chemical Society.

For an overall idea of the trend, the absorbance values at 500 nm for all the samples, dark reference, or subjected to the filtered and unfiltered light is presented in Fig. 6.10 (c). The tendency of a decrease in absorbance for the samples exposed to the light of higher energy is in accordance with the XRD measurements and leads to the conclusion that the exposure of perovskite solar cells to the energy-rich light for extended periods must be avoided.

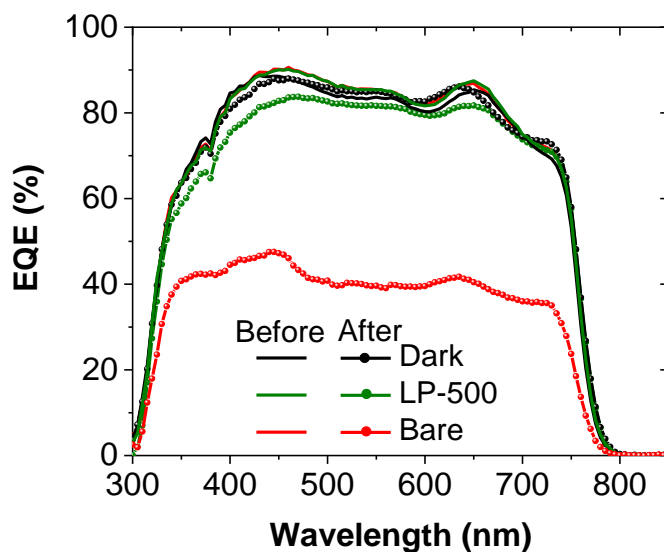


Fig. 6. 11: variation in EQE response of the solar cells kept in dark as reference or exposed to full spectrum of light directly or under LP-500 filter. Adapted with permission from Ref. 266. Copyright 2021, American Chemical Society.

6.5 Bulk Defect Formation

The perovskite degradation leads to compositional alteration in the photo-active absorber material by converting it back to the constituent materials. The chemical alteration and decomposition can result in trap states formation. The generated charge carriers can fall into these trap states and stay there until they recombine. The recombination impacts the device performance and reduces the power conversion efficiency of the solar cells. The ideality factor (n_{id}) measurement is a characterization tool that can provide information about the recombination mechanisms in the solar cells. The value of the ideality factor can be directly linked to the type of recombination process. The procedure of measuring the ideality factor values is described in Sec. 4.3.7. These values are traced from the slope of V_{OC} versus light intensity graphs. The V_{OC} versus light intensity graphs for all the solar cells kept in dark and exposed to light are presented in Fig. 6.12 (a) and (b). While the average values of ideality factors extracted from these graphs along with error bar for all types of the solar cells employed in the experiment are shown in Fig. 6.12 (c).

6. Visible Light Induced Degradation

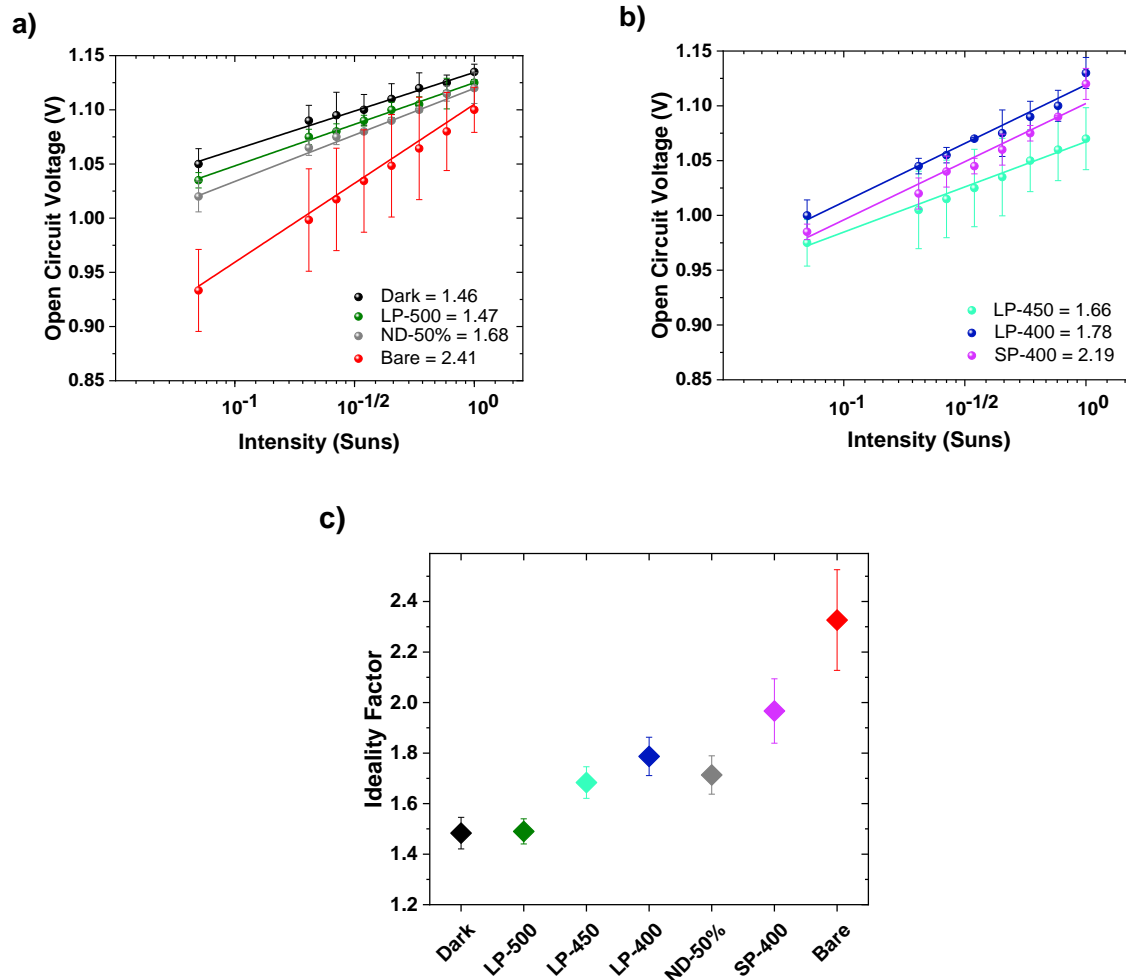


Fig. 6.12: V_{OC} versus light intensity curves for solar cells (a) kept in dark and exposed to light directly or under LP-500 and ND-50% filters (b) exposed to light under LP-450, LP-400, and SP-400 filters, and (c) ideality factor values extracted from all the V_{OC} versus light intensity graphs. Reproduced with permission from Ref. 266. Copyright 2021, American Chemical Society.

The average ideality factor value extracted for the reference solar cells kept in dark is 1.46. This value matches those calculated for PSCs with efficiencies above 20% in literature.⁹² This value indicates the presence of only distributed SRH recombination throughout the absorber layer. The average value extracted for solar cells exposed to light after covering them with the LP-500 filter is 1.47. The matching values of the dark reference and LP-500 covered solar cell indicate their similar performance, referring to a minimal degradation in LP-500 covered devices. The solar cells exposed to light directly as well as after covering them with an ND-50% filter show values of 2.41 and 1.68, respectively. The drastic increase in the n_{id} values for the solar cell directly exposed to

light indicates the formation of trap states in bulk upon the absorber material decomposition leading to SRH recombination via bulk.⁹² The values greater than 2 do not have any physical meaning according to the traditional theory of semiconductor solar cells. Such values have been reported before for PSCs due to the presence of both traps and mobile ions in the perovskite layer.²⁹⁷ The value of 1.68 for the devices covered with ND-50% filter is a denotation of an increase in trap assisted SRH recombination in the bulk. The ideality factor values for the solar cells covered with LP-450, LP-400, and SP-400 are 1.66, 1.78, and 2.19, respectively. The progressive increase in n_{id} indicates a rise in SRH recombination via bulk and in the space charge region as the dominant recombination route in the specified solar cells.⁹² This observation infers that upon degradation, structural defects appear in absorber layer (see Fig. 3.4 (a – c)) leading to the restricted device performance by limiting the number of charge carriers available for the current generation via recombination.

6.6 Trap Energy Estimation

The defect states produced in the perovskite absorber materials upon degradation reduce the solar cell performance by trapping the generated charge carriers. The trap energy of these defect states is estimated via thermally stimulated current measurement. The solar cells characterized by the TSC method are the dark reference sample, directly exposed to light, and the one exposed to filtered light after covering with LP-500 optical filter.

Fig. 6.13 (a) presents the TSC measurement of dark reference, directly exposed to light, and LP-500 covered solar cells. The dark reference devices and the ones kept under the light with LP-500 atop exhibit rather identical TSC profile. These profiles for solar cells of both types show two distinct peaks at around 100 K and 200 K. These peaks are denoted as T1 and T2, respectively. The explanation of the different peaks in a typical TSC signal is that these peaks arise at different temperatures due to the electronic trap states with different energetic depth. The solar cells exposed to light directly show more peaks as well in addition to peak T1 and T2. These peaks appear at temperature values 120 K, 160 K, and 230 K, denoted as T3, T4, and T5 respectively. However, the peak T2 in the TSC signal of the solar cell directly exposed to light could not be seen clearly due to its suppression by the rising part of peak T5.

6. Visible Light Induced Degradation

The emergence of some additional peaks in the solar cells exposed to unfiltered light as compared to dark reference device is an indication of the trap states formation in the perovskite bulk. The activation energies associated with these trap states represented by T4 and T5 in the TSC signal can be estimated from an Arrhenius plot as shown in Fig. 6.13 (b).

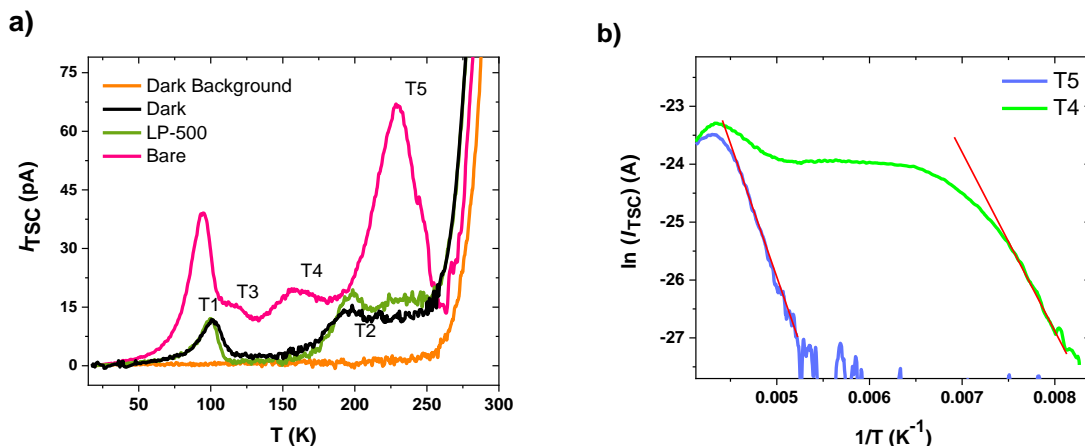


Fig. 6.13: (a) TSC signals of perovskite solar cells kept in dark, directly exposed to light, and under LP-500 filter (b) Arrhenius plot of the TSC signal after thermal cleaning for the peak T4 and T5 (red lines indicate the linear fit). Reproduced with permission from Ref. 266. Copyright 2021, American Chemical Society.

The activation energy of the traps is estimated using the initial rise method using the equation

$$I_{TSC} \propto \exp(-E_A / k_B T) \quad (6.1)$$

where E_A is the activation energy of the traps, k_B is the Boltzmann constant (8.617×10^{-5} eV K^{-1}), and T (K) is the temperature.

The activation energy of peak T3 could not be estimated due to the suppression of its rising part by T1. Moreover, there are fair chances of underestimating the activation energies of peaks T4 and T5 due to the overlap of the rising parts of both with their nearest peaks. This problem is resolved by doing thermal cleaning of the overlapping parts via fractional TSC characterization. This technique is also called the $T_{start-stop}$ method. In this technique, trap filling is carried out in the same way as for normal TSC measurement, but instead of ramping the full temperature range, the device is only heated up to a certain temperature known as T_{stop} (here 132 K for T3 and 212 K for T5). In the subsequent step, the solar cell is cooled down to a low temperature called T_{start} (here 80 K for

T4 and 110 K for T5). Then, the TSC signal is recorded without any further illumination. The thermal cleaning graph of peak T4 and T5 via fractional TSC measurement is shown in Fig. 6.14.

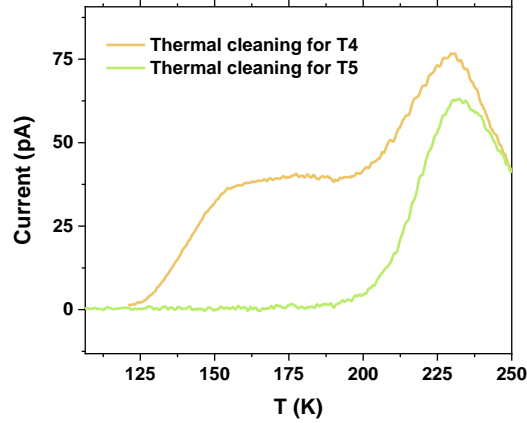


Fig. 6.14: Thermal cleaning of the overlapped peaks T4 and T5 using fractional TSC measurement. Reproduced with permission from Ref. 266. Copyright 2021, American Chemical Society.

The activation energies of the trap states corresponding to T4 and T5 are estimated from the Arrhenius plot as shown in Fig 6.13 (b) and found to be 265 ± 5 meV and 425 ± 10 meV, respectively. The lower limit of trap density is estimated by time integral of TSC signal using equation:

$$\int I_{TSC} dt \leq qN_t d.A \quad (6.2)$$

where N_t is the trap density (cm^{-3}), q is the elementary charge (1.602×10^{-19} C), d (280 nm) and A (0.105 cm^2) are the thickness and active area of the device, respectively. The lower limit of the trap density is estimated to be 3×10^{16} and $5 \times 10^{16} \text{ cm}^{-3}$ for T4 and T5, respectively. It is not possible to determine the activation energy of peak T3 due to the suppression of its rising part by T1.

Furthermore, the TSC measurement on a solar cell without a spiro-OMeTAD layer is also performed, as presented in Fig. 6.15. The rest of the solar cell stack is identical to the ones used in this study. It should be noted that the peak T1 at around 100 K is attributed to the spiro-OMeTAD layer as it is not observed in the TSC signal of the solar cells without HTL, and thus the trap energy for the T1 peak is not calculated.

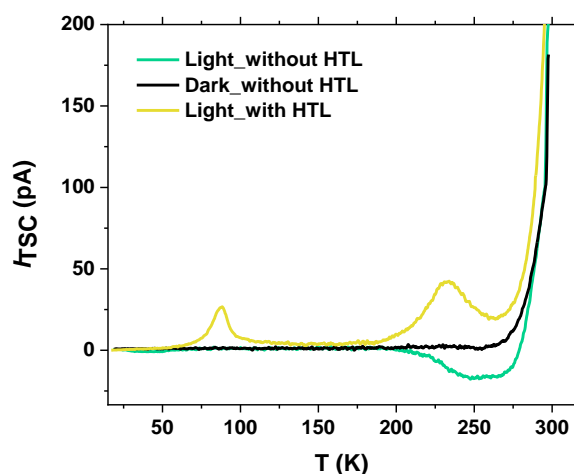


Fig. 6.15: TSC measurement of perovskite solar cell with and without hole transport layer. Reproduced with permission from Ref. 266. Copyright 2021, American Chemical Society.

Altogether, the perovskite solar cells when exposed to filtered and unfiltered light exhibit a tendency of a spectral dependence of photo-degradation. A maximum degradation is experienced to appear in solar cells directly exposed to unfiltered light followed by the ones exposed to UV light only. Photo-degradation can cause the excessive charge accumulation at the interfaces, multiple trap states formation, compositional alteration leading to ions and charge trap formation, dopant ion infiltration from HTL to the perovskite absorber resulting in formation of shunt pathways. For a better visual understanding, it is referred to look at Fig. 3.4 for an overview of all the potential mechanisms resulting in photo-degradation. The decomposition is observed via XRD characterization. The decomposition generated trap states acting as recombination sites to reduce device performance are characterized via ideality factor measurements. Further evaluation of the trap states reveals that they have activation energies of 0.26 and 0.42 eV. These findings are important for further development and optimization of a photo-stable perovskite absorber material.

Although accelerated degradation of the solar cells to extrapolate their estimated lifetime is proved a viable approach for the established PV technologies. However, in case of PSCs, even they passed the rigorous IEC 61215 test routine, yet they lost >80% of their initial performance within 1 – 2 years of field trial, as indicated by Microquanta Semiconductor Co., for their perovskite solar modules.¹⁵⁹ This highlights the need of not only further research efforts in enhancing the photostability of PSCs but also demands testing the stability in real outdoor operational conditions.

6. Visible Light Induced Degradation

Thus, it is advisable for PSCs to conduct extensive field trials and testing their stability in real or operational scenarios. Combination of different stress factors during outdoor operations (light, heat, humidity) can provide trustworthy statistics about the weatherability of perovskite solar cells to gain faith of the market stakeholders and pave their way towards commercialization.

7. Bias Dependent Degradation

This chapter highlights the role of biasing on the light-induced degradation in perovskite solar cells. Although the solar cells are operated at the maximum power point during deployment, a varying trend of degradation might need careful handling in the delivery, installation, and operational stage. For these reasons, the stability of perovskite solar cells towards various bias conditions is investigated in this chapter. The absorber material used for these investigations is based on the triple cation composition ($CS_{0.1}(FA_{0.83}MA_{0.17})_{0.9}Pb(I_{0.83}Br_{0.17})_3$), and the device architecture is: ITO/SnO₂/perovskite/Spiro-OMeTAD/Au. The research question addressed in this chapter is: How the rate of photo-degradation is related to the different bias conditions in PSCs?

The results presented in this and the last chapter were included in the research article which is already mentioned in opening remarks of Chapter 6.

Acknowledgements and contributions

The triple cation recipe used to fabricate the solar cells was optimized by Somayeh Moghadamzadeh. Jonas A. Schwenger provided optical filters to cover the solar cells before exposing them to the light during spectral dependent bias induced degradation step. Initial design of the sealed sample holder container was prepared by Fabian Schakmar and further optimized by A. Farooq to keep the solar cells in nitrogen environment. Bias dependent experiments were conducted by A. Farooq as well the J - V curves measurements of the solar cells after frequent intervals of degradation.

7.1 Degradation at V_{OC} and J_{SC}

The bias conditions can affect the device internal field, current, and accumulation of charge carriers, and hence can potentially lead to a different degradation trend.²⁹⁸ The solar cells left open circuited in the light will have no current flowing through them and a maximum accumulation of photo-generated charge carriers at their terminals occurs. When the light is incident on a solar cell, the creation of photogenerated charge carriers and, by Fermi level splitting, a photovoltage is produced between the contacts.²⁹⁹ This photovoltage is similar to the forward bias voltage as in a conventional p-n-junction diode. This forward bias voltage is always applied to the solar cells as long as it stays under light exposure during its operation. Thus, the photovoltage generated by light exposure is considered to induce an electric field in the perovskite solar cells. While the solar cells left at short circuit conditions under the light will have the highest current density and least accumulation of charge carriers inside the solar cell.

When the as-fabricated perovskite solar cells are exposed to unfiltered light at open circuit and short circuit conditions, their performance degrades heavily as presented in Fig. 7.1. As reference, some devices are kept in dark throughout this experiment which are exhibited in black in Fig. 7.1. The percentage decrease in PCE, J_{SC} , V_{OC} , and fill factor after 250 hours of direct exposure to unfiltered light at the open and short circuit is provided in Table 7.1.

7. Bias dependent Degradation

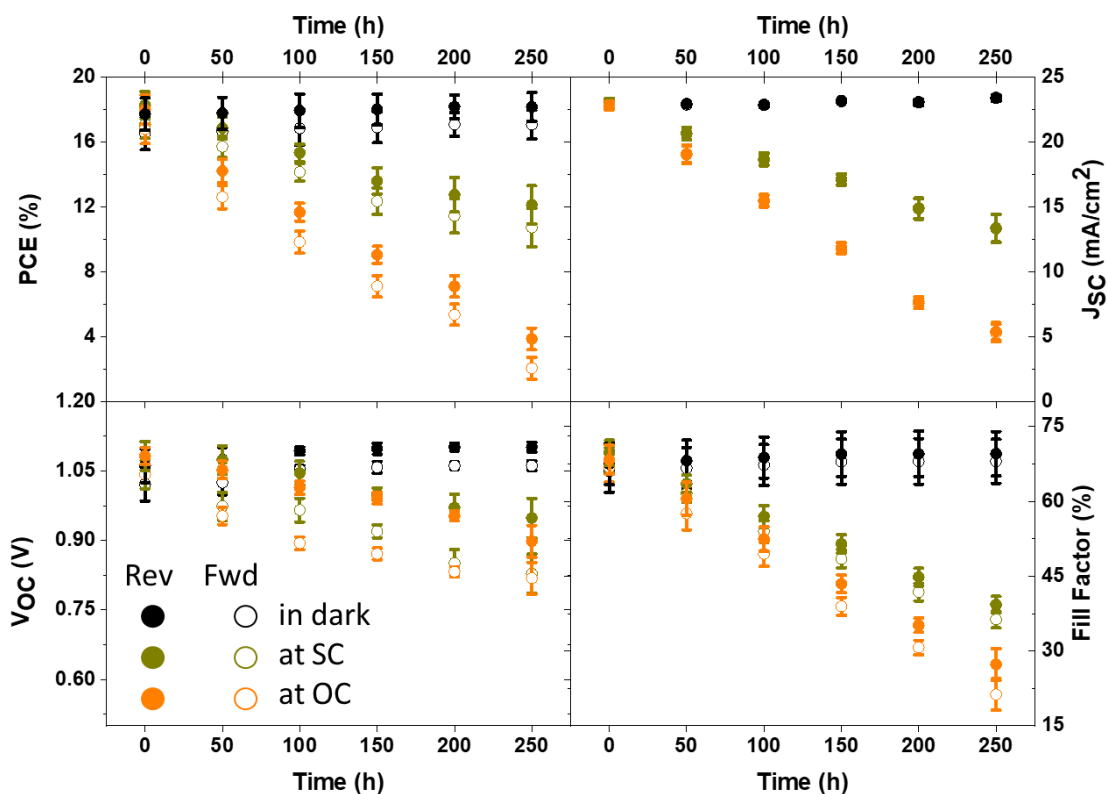


Fig. 7.1: Variations in PV parameters of perovskite solar cells exposed to light at bias conditions (i) open circuit and (ii) short circuit. Reproduced with permission from Ref. 266. Copyright 2021, American Chemical Society.

Table 7.1: Percentage change in all the PV parameters in solar cells left at the open and short circuit under direct exposure to light.

PV parameter	Percentage change (%)	
	At short circuit	At open circuit
PCE	34	78
J_{sc}	41	76
V_{oc}	12	17
FF	43	60

Intrinsic ion migration (occurring only within absorber layer) is speculated to be the reason for bias dependent degradation in perovskite solar cells according to many reports.^{300–302} Ion migration

can take place by a vacancy migration or by interstitial migration. For such kinds of defects, the required formation energy heavily depends on the chemical potential or the Fermi level in the perovskite absorber material. In several cases, these formation energies are low enough that these defects occur at room temperature by the entropy or kinetic driving forces like crystal growth from high temperature and then quenching.

However, in the experiment carried out here, exhibited in Fig. 7.1, a clear difference in degradation rate at OC and SC conditions is found. Particularly, the severe degradation under open-circuit conditions hinders the process of easy installation and demands a careful pre-installation handling of the perovskite solar module to avoid degradation under light without any load applied. The reason behind the drastic degradation in the OC bias scenario is speculated to be charge trapping along with radical formation. This degradation phenomenon could also be assisted by the unfavorable extrinsic ion diffusion which cannot be prevented when internal bias potentials are present. While the slower degradation under SC conditions is attributed to the intrinsic and extrinsic ion migration in response to the internal interfacial potentials.

7.2 Comparison with Degradation near Maximum Power Point

In the real-world outdoor installations, PV modules are supposed to operate at the maximum power point. To investigate the degradation speed for cases close to real bias scenarios, the as-fabricated solar cells are subjected to light exposure by tracking their PCE at constant voltage near the MPP. The deterioration in PCE of the solar cells left at open circuit, short circuit, and at a constant voltage near the MPP is measured for 250 hours and plotted as shown in Fig. 7.2.

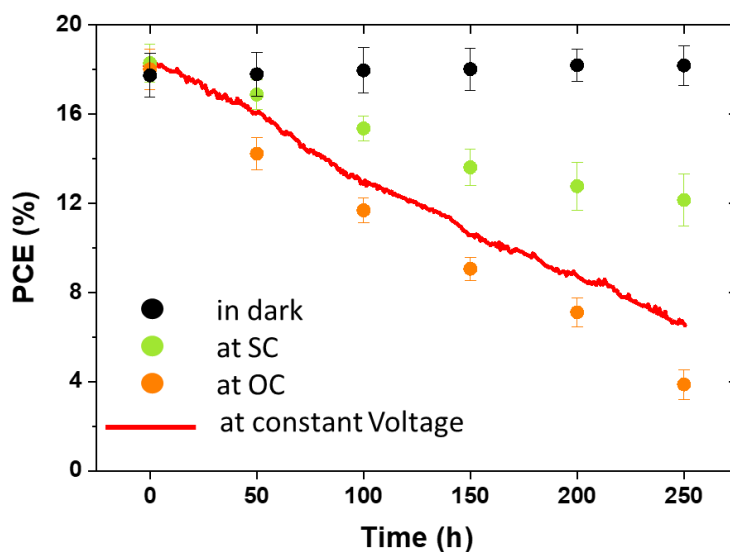


Fig. 7.2: Change in PCE of solar cells subjected to photo-degradation at (i) short circuit, (ii) open circuit, and (iii) constant voltage near MPP. Reproduced with permission from Ref. 266. Copyright 2021, American Chemical Society.

The percentage decrease in PCE at constant voltage is 59% (relative) which is approximately between 34% (relative) in the short circuit and 78% (relative) in the open circuit bias scenarios. There are a few explanations for the decreased rate of degradation at a constant voltage near MPP in literature.^{303,304} The light-induced traps at MPP bias scenario are expected to be partially populated resulting in small charged regions. In this case, the intrinsic ion migration should be small due to the applied bias being close to the built-in potential and opposite in polarity. While the external migration of perovskite ions into the charge selective layers is speculated to be dominant and driven by the reduced interfacial electric fields. As none of these mechanisms in constant voltage tracking near MPP is at its peak, the reduced degradation rate at the MPP compared to the open circuit condition can be justified.^{298,305-307}

7.3 Performance Recovery

The solar cells which undergo moderate degradation are seen to recover some of the lost performance degradation upon a subsequent rest in the dark overnight. A similar approach is applied for the solar cells subjected to the bias-dependent degradation under SC condition, to see

7. Bias dependent Degradation

any potential performance recovery. The PCE data for the solar cells degraded at short circuit condition under light for 250 hours with subsequent storage in dark in a N₂ filled glovebox followed by a measurement step the next day is shown in Fig. 7.3. However, it can be observed that there is no particular performance recovery for all the degraded devices as expected except some improvement in measured values which can also be an artifact of the solar simulator intensity or light soaking effect. Although the reports on performance enhancement by healing the devices in the dark highlight the fact that this phenomenon is only observable in moderately degraded solar cells, no recovery in PCE is noticed here.

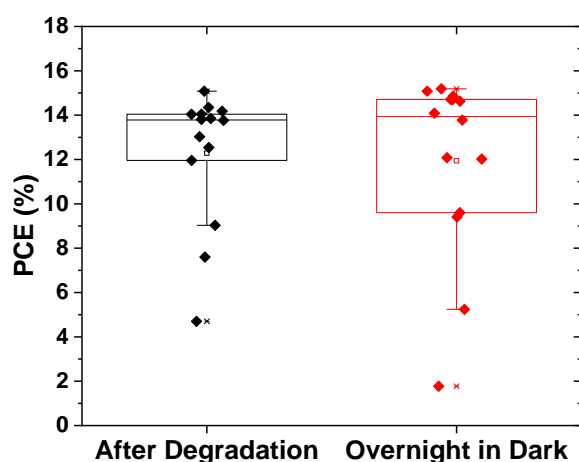


Fig. 7.3: Performance recovery after a degradation step upon dark storage overnight.

The performance recovery is discussed to arise from trap passivation. The passivation and neutralization of these traps occur due to the availability of the degradation by-product PbI₂. However, the irreversible performance degradation of the perovskite solar cells under different test conditions can be supported by a few postulates. Firstly, the accumulation and interaction of holes and cations at the electron transport layer can permanently change the interface reactivity. Secondly, the irreversible interaction between iodide ions and the oxidized form of spiro-OMeTAD could also cause an increase in the solar cell's series resistance owing to the reduced performance and failure in recovery.^{308–310}

7.4 Role of Spectrum Selectivity at Open Circuit

It was demonstrated in Chapter 6 that the various spectral regimes impact the solar cell stability differently when measured at a constant voltage near the MPP. Here it is investigated how the various spectral regimes play a role in performance deterioration of a solar cell under OC condition. Considering the severe degradation caused under OC condition, the following investigation is carried out only under the OC bias scenario. The experiment is conducted for 100 hours to see whether the degradation slows down or speeds up unexpectedly when tested at OC condition under different optical filters. Fig. 7.4 presents the change in PCE of the solar cells exposed to light directly or under optical filters along with some reference devices kept in dark for comparison in performance variation.

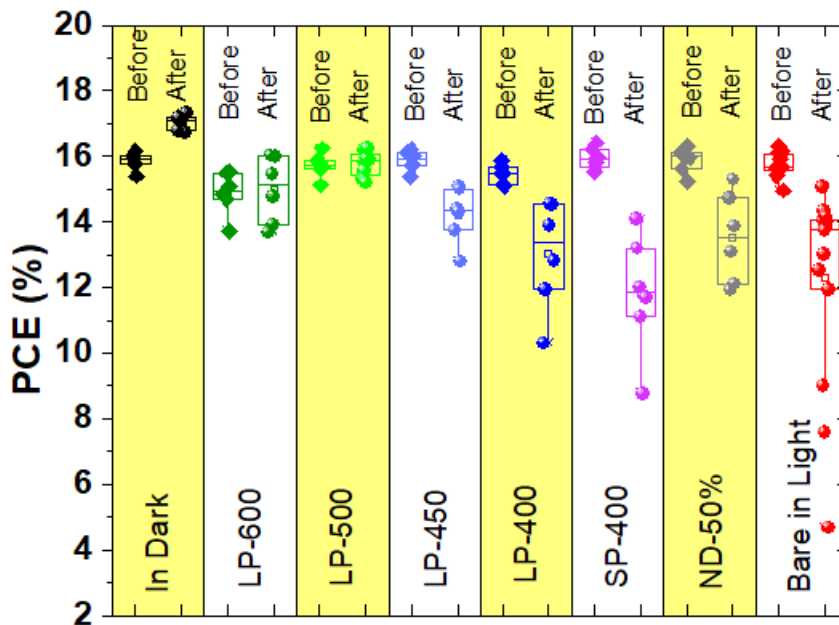


Fig. 7.4: Change in PCE of the solar cells exposed to filtered and unfiltered light for 100 hours under open-circuit conditions.

The experiment is conducted for 100 hours as this duration already degrades the initial performance of the solar cells by more than 20%, except those covered with LP-500. In the stability testing of solar cells, an investigation must be conducted at least until the time when the solar cell

7. Bias dependent Degradation

loses 20% or more of its performance. Due to this fact, probing the degradation trend under OC conditions under filtered and unfiltered light is carried out for 100 hours.

Table 7.2: Absorbed light dose by the solar cells exposed to light directly or under optical filters, along with percentage change in PCE after the degradation step.

Covered with	Absorbed radiation dose (kWh m ⁻²)	Change in PCE (%)
Directly exposed	64	25.5
In dark	-	-6.7
LP-600	30	-0.7
LP-500	40	-0.6
LP-450	45	11.2
LP-400	50	16
SP-400	14	24.8
ND-50%	32	15.5

The light dose absorbed by all the solar cells exposed directly to the light or under filters LP-600, LP-500, LP-450, LP-400, SP-400 and ND-50% are 64, 30, 40, 45, 50, 14, and 32 kWh m⁻², respectively. While the percentage decrease (relative) in PCEs is noted to be 25.5%, -0.7%, -0.6%, 11%, 16%, 25.1%, and 15.5%, respectively, as given in Table 7.2. Here, the negative values (-6.7%, -0.7%, and -0.6%) represent an increase in the PCE which can be attributed to the light soaking effect and the material crystallinity improvement due to strain relaxation, as already reported in literature.³¹¹ The analysis of the change in PCE values of the solar cells subjected to the open circuit biasing stress under filtered and unfiltered light reveals that the performance decline follows a similar pattern as observed earlier in Chapter 6 (Sec. 6.2). This observation indicates the demand of a careful handling of the perovskite solar modules considering their sensitivity to degrade even under the light of considerably less intensity and in open circuit biasing scenario.

The bias-dependent degradation mechanism alone and in conjunction with other stress factors (like light, heat, oxygen, and humidity) can result in various degradation trends and routes. Thus, the bias-dependent degradation may pose different causes under dark and illumination scenarios

7. Bias dependent Degradation

potentially leading to different mechanisms governing the degradation and hence various circumvention possibilities. Furthermore, in the case of tandem application of PSCs with a two-terminal architecture, where the PSC may operate at voltage lower than its own V_{OC} , the bias dependent degradation can pose serious challenges. For such a case, there is a lack of the information about the defect formation, activation energies of the defects and the chemical potential of charged defects in absorber and other layers of the PSCs as a function of the applied bias potential. Thus, further experimentation and research must be conducted to devise and implement the prevention strategies against bias-dependent degradation of perovskite solar cells.

Conclusions and Outlook

The scope of this thesis is to derive a better fundamental understanding of the highly debated problem of photo-instability in the perovskite solar cell (PSC) technology. Two perovskite absorber materials and multiple electron transport layers (ETLs) are investigated to draw a general conclusion. The explored absorbers are the workhorse material methylammonium lead triiodide (MAPbI₃ or CH₃NH₃PbI₃) and the highly efficient and most stable multi-cation composition Cs_{0.1}(FA_{0.83}MA_{0.17})_{0.9}Pb(I_{0.83}Br_{0.17})₃. Since the quality of devices plays a decisive role in determining the lifetime, highly efficient devices (~20% power conversion efficiency) are used to draw a conclusion. Assessment of the multiple ETLs is paramount. With a change in ETL, the mechanism and speed of degradation can vary drastically. This infers that the ETL itself and the interfaces of ETL and perovskite absorber are important parameters that need to be controlled and carefully designed to delay the degradation.

Although, the ultraviolet (UV) radiation regime of the solar spectrum as a whole is considered injurious to the device stability, however, in this work it is found that the higher the energy of the UV radiation, the greater is its impact on the stability. The absorber material under study in this scenario is MAPbI₃. The most harmful UV radiation spans over 310 – 320 nm triggering the instability to leave the devices with 20% (relative) of the initial power conversion efficiency (PCE) after a dose of 3.2 kWh m⁻². Furthermore, when intensity dependence of this degradation is investigated it appears to play a major role in triggering the degradation. Upon reducing the intensity of high energy UV radiation (311 nm) to 10% i.e. from 211 Wm⁻² to 21.1 Wm⁻², the degradation is only 48% for the similar dose of radiation (3.2 kWh m⁻²). The UV degradation trend is also observed to be dependent on the type of ETL employed in the device stack. The most stable ETL is found to be SnO₂ – degrading only 50% for a dose of 3.2 kWh m⁻² of intense UV radiation – as compared to the np-TiO₂ which degraded the most (88%) for the similar radiation dose.

Extending the photo-stability study further, it is also investigated that if the solar cells become stable or not when the UV radiation is cut-out of the incident light spectrum. Still after blocking the UV portion in the light of 1 sun intensity, 42% degradation is noted. Upon cutting-out the different spectral regimes of the incident spectrum via multiple long-pass optical filters with cut-off wavelengths 400 nm, 450 nm, and 500 nm, different patterns of photo-instability are observed

8. Conclusions and Outlook

for a continuous test duration of 250 hours. The observed degree of the degradation for radiation range $\lambda > 400$ nm, $\lambda > 450$ nm, and $\lambda > 500$ nm is found to be 40%, 32%, and 7%, respectively. The minimal performance deterioration of 7% for the wavelengths > 500 nm infers to the least harmfulness of this spectral region. This wavelength threshold can be associated with the bandgap energy of degradation by-product lead iodide (PbI_2) i.e. 2.4 eV. Among these tested spectral regimes, UV region is experienced to be most detrimental, causing a degradation of 43% for the least dose (37 kWh m^{-2}). While in comparison to these, a decrease of 58% in PCE is recorded for the solar cells exposed to unfiltered light of intensity equal to AM1.5G. In the meantime, the solar cells stored in dark in inert atmosphere retained their initial performance for the similar time duration. The stimulus of degradation is the energy-rich content of light which alters the chemical composition of the absorber material converting it to a non-photoactive material (PbI_2) after the evaporation of volatile by-products. This observation is supported by x-ray diffraction measurements (XRD) which reveal a chemical alteration of the precursors, resulting in trap states serving as recombination sites leading to substandard performance.

Upon probing the causes of degradation via XRD, it is discovered that the perovskite absorber layer started to decompose back to the constituent materials. A strong PbI_2 signal is detected for the degraded solar cells, which is a signature of the perovskite decomposition. Furthermore, this decomposition and abundance of photo-insensitive PbI_2 material in the absorber layer is found to reduce the photo-activity of the perovskite by reducing its radiation absorbance properties. The absorber decomposition leads to trap state formation. The trap states are known to serve as charge recombination sites as verified via ideality factor measurements. Further, external quantum efficiency (EQE) measurements of the reference and degraded solar cells revealed that their spectral response is compromised throughout the wavelength range (300 – 800 nm). Upon measuring the ideality factors for solar cells exposed to various light regimes, highest values (2.4) are recorded for the solar cells exposed to full spectrum of 1 sun light intensity. Those which are exposed to wavelengths $\lambda > 400$ nm, $\lambda > 450$ nm, and $\lambda > 500$ nm show values 1.8, 1.7, and 1.5, respectively. With the progressive increase in the energy of the incident photon content, the degradation also increases leading to a higher value of ideality factor which represent the higher degree of recombination mechanism. When explored the nature of trap states further via thermally stimulated current (TSC) measurements, deep trap states are noticed to be formed upon photo-

degradation. Two distinct peaks in the TSC profile are recorded for the most degraded solar cells representing trap states. Upon estimating the activation energies of the trap sites formed upon prolonged photo-exposure, these are found to be 3×10^{16} and $5 \times 10^{16} \text{ cm}^{-3}$, respectively. Moreover, trap density of these trap sites is also measured and estimated to be $265 \pm 5 \text{ meV}$ and $425 \pm 10 \text{ meV}$, respectively.

The UV stimulated instability is proposed to be suppressed via either employing UV filtering layers or luminescent downshifting (LDS) materials. However, the use of UV blocking layers (in range 300 – 400 nm) will come at a cost of a fraction of loss in J_{SC} (1.4 mA cm^{-2}). Thus, LDS materials can be utilized which offer a potential re-absorption of the harmful radiation after moderating their energies. When the potential of the LDS materials (Eu complex doped EVA) in PSCs is investigated it is found that even in ideal case the gain in J_{SC} cannot exceed 0.6 mA cm^{-2} .

A similar degradation behavior is observed under various applied bias conditions, being short-circuit (SC), open-circuit (OC), and constant voltage tracking near maximum power point (MPP), leading to similar degradation pathways. The OC bias scenario is found to be most detrimental leading to a 77% decrease in PCE. The least degradation is observed at SC (34%), while constant voltage tracking near MPP causes a degradation with rate in between those at OC and SC (57%). Open-circuit biasing condition is critical for having a maximum effect on stability.

Given these facts, further research efforts must be directed to completely resolve the instability issue of PSCs. Provided all the potential stability and efficiency enhancement approaches employed, still the field trials based lifetime of perovskite solar modules is not beyond 1 – 2 years. Hence, to gain trust of commercial stakeholders and to lift the stability of PSCs to match the market dominating PV technologies, more absorber compositions should be explored, and further outdoor operational stability tests must be conducted.

8. Conclusions and Outlook

References

- (1) International Energy Outlook 2019 with projections to 2050 <https://www.eia.gov/outlooks/ieo/pdf/ieo2019.pdf>.
- (2) World Energy Scenarios: Composing Energy Futures to 2050. In <http://www.Worldenergy.Org/>; 2013; pp 1–288.
- (3) Nuclear Power Today | Nuclear Energy - World Nuclear Association <https://www.world-nuclear.org/information-library/current-and-future-generation/nuclear-power-in-the-world-today.aspx> (accessed Feb 8, 2021).
- (4) Global Monitoring Laboratory - Carbon Cycle Greenhouse Gases <https://www.esrl.noaa.gov/gmd/ccgg/trends/weekly.html> (accessed May 21, 2020).
- (5) Data.GISS: GISS Surface Temperature Analysis (v4): Analysis Graphs and Plots <https://data.giss.nasa.gov/gistemp/graphs/> (accessed May 21, 2020).
- (6) United Nations - ActNow Climate Action Campaign <https://www.un.org/en/actnow/> (accessed May 21, 2020).
- (7) The Paris Agreement | UNFCCC <https://unfccc.int/process-and-meetings/the-paris-agreement/the-paris-agreement> (accessed May 21, 2020).
- (8) Tollefson, J. COVID Curbed Carbon Emissions in 2020 — but Not by Much. *Nature* **2021**, 589 (7842), 343–343.
- (9) Headley, S. A New Day Dawning. *Youth Stud. Aust.* **2013**, 32 (2), 1–2.
- (10) Lewis, N. S.; Nocera, D. G. Powering the Planet: Chemical Challenges in Solar Energy Utilization. *Proc. Natl. Acad. Sci. U. S. A.* **2006**, 103 (43), 15729–15735.
- (11) Enerdata. World Energy Statistics | Enerdata <https://yearbook.enerdata.net/> (accessed May 22, 2020).
- (12) Ruhe, C. H. W. Statistical Review. *JAMA J. Am. Med. Assoc.* **1973**, 225 (3), 299–306.
- (13) Labouret, A.; Viloz, M. Solar Photovoltaic Energy. *Sol. Photovolt. Energy* **2010**, 1–373.
- (14) Wani, A. L.; Ara, A.; Usmani, J. A. Lead Toxicity: A Review. *Interdisciplinary Toxicology*. Slovak Toxicology Society June 1, 2015, pp 55–64.
- (15) Mason, L. H.; Harp, J. P.; Han, D. Y. Pb Neurotoxicity: Neuropsychological Effects of Lead Toxicity. *BioMed Research International*. **2014**, 840547.
- (16) Grancini, G.; Roldán-Carmona, C.; Zimmermann, I.; Mosconi, E.; Lee, X.; Martineau, D.; Narbey, S.; Oswald, F.; De Angelis, F.; Graetzel, M.; Nazeeruddin M.K. One-Year Stable Perovskite Solar Cells by 2D/3D Interface Engineering. *Nat. Commun.* **2017**, 8, 15684.
- (17) Chowdhury, M. S.; Rahman, K. S.; Chowdhury, T.; Nuthammachot, N.; Techato, K.; Akhtaruzzaman, M.; Tiong, S. K.; Sopian, K.; Amin, N., An Overview of Solar Photovoltaic Panels' End-of-Life Material Recycling. *Energy Strategy Reviews*. 2020, 27, 100431.
- (18) Contreras-Bernal, L.; Aranda, C.; Valles-Pelarda, M.; Ngo, T. T.; Ramos-Terrón, S.; Gallardo, J. J.; Navas, J.; Guerrero, A.; Mora-Seró, I.; Idígoras, J.; Anta J. Homeopathic Perovskite Solar Cells: Effect of Humidity during Fabrication on the Performance and Stability of the Device. *J. Phys. Chem. C* **2018**, 122 (10), 5341–5348.

References

- (19) Schwenzer, J. A.; Rakocevic, L.; Gehlhaar, R.; Abzieher, T.; Gharibzadeh, S.; Moghadamzadeh, S.; Quintilla, A.; Richards, B. S.; Lemmer, U.; Paetzold, U. W. Temperature Variation-Induced Performance Decline of Perovskite Solar Cells. *ACS Appl. Mater. Interfaces* **2018**, *10* (19), 16390–16399.
- (20) Juarez-Perez, E. J.; Ono, L. K.; Maeda, M.; Jiang, Y.; Hawash, Z.; Qi, Y. Photodecomposition and Thermal Decomposition in Methylammonium Halide Lead Perovskites and Inferred Design Principles to Increase Photovoltaic Device Stability. *J. Mater. Chem. A* **2018**, *6* (20), 9604–9612.
- (21) Matsui, T.; Yamamoto, T.; Nishihara, T.; Morisawa, R.; Yokoyama, T.; Sekiguchi, T.; Negami, T. Compositional Engineering for Thermally Stable, Highly Efficient Perovskite Solar Cells Exceeding 20% Power Conversion Efficiency with 85 °C/85% 1000 h Stability. *Adv. Mater.* **2019**, *31* (10), 3–8.
- (22) Carcia, P. F.; McLean, R. S.; Hegedus, S. Encapsulation of Cu(InGa)Se₂ Solar Cell with Al₂O₃ Thin-Film Moisture Barrier Grown by Atomic Layer Deposition. *Sol. Energy Mater. Sol. Cells* **2010**, *94* (12), 2375–2378.
- (23) Comptes rendus hebdomadaires des séances de l'Académie des sciences. Volume 9. 1839 : Académie des sciences (France) <https://archive.org/details/comptes-rendus-hebdomadaires-des-seances-...-academie-des-bpt-6k-2968p> (accessed May 23, 2020).
- (24) Fatet, J. Recreating Edmond Becquerel's Electrochemical Actinometer. *Arch. des Sci.* **2005**, *58* (2), 149–158.
- (25) Fritts, C. E. On a New Form of Selenium Cell, and Some Electrical Discoveries Made by Its Use. *Am. J. Sci.* **1883**, *s3-26* (156), 465–472.
- (26) Grondahl, L. O. The Copper-Cuprous-Oxide Rectifier and Photoelectric Cell. *Rev. Mod. Phys.* **1933**, *5* (2), 141–168.
- (27) Oh, R. S. *Light-Sensitive Electric Device*; 1946.
- (28) Chapin, D. M.; Fuller, C. S.; Pearson, G. L. A New Silicon P-n Junction Photocell for Converting Solar Radiation into Electrical Power [3]. *J. Appl. Phys.* **1954**, *25* (5), 676–677.
- (29) Welker, H. Semiconducting Intermetallic Compounds. *Phys. XX, Amsterdam Conf.* **1954**, 893–909.
- (30) Gremmelmaier, V. R. GaAs-Photoelement. *Z. Naturforsch* **1955**, *10a*, 501–502.
- (31) Easton, R. L.; Votaw, M. J. Vanguard I IGY Satellite (1958 Beta). *Rev. Sci. Instrum.* **1959**, *30* (2), 70–75.
- (32) L. L. Kazmerski, F. R. White, and G. K. M. Thin-Film CuInSe₂ / CdS Heterojunction Solar Cells. *Appl. Phys. Lett.* **1976**, *29* (August), 268–270.
- (33) Devaney, W. E.; Chen, W. S.; Stewart, J. M.; Mickelsen, R. A. Structure and Properties of High Efficiency ZnO/CdZnS/CuInGaSe₂ Solar Cells. *IEEE Trans. Electron Devices* **1990**, *37* (2), 428–433.
- (34) Tuttle, J. R.; Ward, J. S.; Duda, A.; Berens, T. A.; Contreras, M. A.; Ramanathan, K. R.; Tennant, A. L.; Keane, J.; Cole, E. D.; Emery, K.; et al. Performance of Cu(In,Ga)Se₂-Based Solar Cells in Conventional and Concentrator Applications. In *Materials Research Society Symposium - Proceedings*; Materials Research Society, 1996; Vol. 426, pp 143–151.
- (35) Green, M. A.; Dunlop, E. D.; Hohl-Ebinger, J.; Yoshita, M.; Kopidakis, N.; Hao, X. Solar Cell Efficiency Tables (Version 56). *Prog. Photovoltaics Res. Appl.* **2020**, *28* (7), 629–638.

References

- (36) Green, M. A.; Dunlop, E. D.; Hohl-Ebinger, J.; Yoshita, M.; Kopidakis, N.; Ho-Baillie, A. W. Y. Solar Cell Efficiency Tables (Version 55). *Prog. Photovoltaics Res. Appl.* **2020**, *28* (1), 3–15.
- (37) Green, M. A. Third Generation Photovoltaics: Ultra-High Conversion Efficiency at Low Cost. *Prog. Photovoltaics Res. Appl.* **2001**, *9* (2), 123–135.
- (38) Benda, V.; Černá, L. PV Cells and Modules – State of the Art, Limits and Trends. *Heliyon* **2020**, *6* (12).
- (39) *Photovoltaics Report - Fraunhofer ISE*; 2020.
- (40) Conibeer, G. Third-Generation Photovoltaics. *Mater. Today* **2007**, *10* (11), 42–50.
- (41) Shockley, W.; Queisser, H. J. Detailed Balance Limit of Efficiency of P-n Junction Solar Cells. *J. Appl. Phys.* **1961**, *32* (3), 510–519.
- (42) Park, N. G.; Segawa, H. Research Direction toward Theoretical Efficiency in Perovskite Solar Cells. *ACS Photonics* **2018**, *5* (8), 2970–2977.
- (43) Day, J.; Senthilarasu, S.; Mallick, T. K. Improving Spectral Modification for Applications in Solar Cells: A Review. *Renew. Energy* **2019**, *132*, 186–205.
- (44) Würfel, U.; Cuevas, A.; Würfel, P. Charge Carrier Separation in Solar Cells. *IEEE J. Photovoltaics* **2015**, *5* (1), 461–469.
- (45) Bisquert, J. *The Physics of Solar Cells: Perovskites, Organics, and Photovoltaic Fundamentals*; CRC Press, 2017.
- (46) Rühle, S. Tabulated Values of the Shockley-Queisser Limit for Single Junction Solar Cells. *Sol. Energy* **2016**, *130*, 139–147.
- (47) Bartel, C. J.; Sutton, C.; Goldsmith, B. R.; Ouyang, R.; Musgrave, C. B.; Ghiringhelli, L. M.; Scheffler, M. New Tolerance Factor to Predict the Stability of Perovskite Oxides and Halides. *Sci. Adv.* **2019**, *5* (2), eaav0693.
- (48) Green, M. A.; Ho-Baillie, A.; Snaith, H. J. The Emergence of Perovskite Solar Cells. *Nat. Photonics* **2014**, *8* (7), 506–514.
- (49) Li, Z.; Yang, M.; Park, J. S.; Wei, S. H.; Berry, J. J.; Zhu, K. Stabilizing Perovskite Structures by Tuning Tolerance Factor: Formation of Formamidinium and Cesium Lead Iodide Solid-State Alloys. *Chem. Mater.* **2016**, *28* (1), 284–292.
- (50) Kieslich, G.; Sun, S.; Cheetham, A. K. An Extended Tolerance Factor Approach for Organic-Inorganic Perovskites. *Chem. Sci.* **2015**, *6* (6), 3430–3433.
- (51) Yin, W. J.; Shi, T.; Yan, Y. Unique Properties of Halide Perovskites as Possible Origins of the Superior Solar Cell Performance. *Adv. Mater.* **2014**, *26* (27), 4653–4658.
- (52) De Wolf, S.; Holovsky, J.; Moon, S. J.; Löper, P.; Niesen, B.; Ledinsky, M.; Haug, F. J.; Yum, J. H.; Ballif, C. Organometallic Halide Perovskites: Sharp Optical Absorption Edge and Its Relation to Photovoltaic Performance. *J. Phys. Chem. Lett.* **2014**, *5* (6), 1035–1039.
- (53) Kim, H. S.; Lee, C. R.; Im, J. H.; Lee, K. B.; Moehl, T.; Marchioro, A.; Moon, S. J.; Humphry-Baker, R.; Yum, J. H.; Moser, J. E.; Grätzel, M.; Park N.G. Lead Iodide Perovskite Sensitized All-Solid-State Submicron Thin Film Mesoscopic Solar Cell with Efficiency Exceeding 9%. *Sci. Rep.* **2012**, *2*, 591.

References

- (54) Baikie, T.; Fang, Y.; Kadro, J. M.; Schreyer, M.; Wei, F.; Mhaisalkar, S. G.; Graetzel, M.; White, T. J. Synthesis and Crystal Chemistry of the Hybrid Perovskite (CH₃NH₃)PbI₃ for Solid-State Sensitised Solar Cell Applications. *J. Mater. Chem. A* **2013**, *1* (18), 5628–5641.
- (55) Wang, T.; Daiber, B.; Frost, J. M.; Mann, S. A.; Garnett, E. C.; Walsh, A.; Ehrler, B. Indirect to Direct Bandgap Transition in Methylammonium Lead Halide Perovskite. *Energy Environ. Sci.* **2017**, *10* (2), 509–515.
- (56) Sarritzu, V.; Sestu, N.; Marongiu, D.; Chang, X.; Wang, Q.; Masi, S.; Colella, S.; Rizzo, A.; Gocalinska, A.; Pelucchi, E.; Mercuri, M.L.; Quochi F.; Saba, M.; Andrea Mura A.; Bongiovanni, G. Direct or Indirect Bandgap in Hybrid Lead Halide Perovskites? *Adv. Opt. Mater.* **2018**, *6*, 1701254.
- (57) Baranowski, M.; Plochocka, P. Excitons in Metal-Halide Perovskites. *Adv. Energy Mater.* **2020**, *1903659*.
- (58) Kiermasch, D.; Rieder, P.; Tvingstedt, K.; Baumann, A.; Dyakonov, V. Improved Charge Carrier Lifetime in Planar Perovskite Solar Cells by Bromine Doping. *Sci. Rep.* **2016**, *6*, 39333.
- (59) Park, N. G. Perovskite Solar Cells: An Emerging Photovoltaic Technology. *Mater. Today* **2015**, *18* (2), 65–72.
- (60) Alcocer, M. J. P.; Leijtens, T.; Herz, L. M.; Petrozza, A.; Snaith, H. J. Electron-Hole Diffusion Lengths Exceeding 1 micrometer in an organometal Trihalide Perovskite Absorber. *Science*, **2013**, *18*; 342(6156): 341–4.
- (61) Noh, J. H.; Im, S. H.; Heo, J. H.; Mandal, T. N.; Seok, S. II. Chemical Management for Colorful, Efficient, and Stable Inorganic-Organic Hybrid Nanostructured Solar Cells. *Nano Lett.* **2013**, *13* (4), 1764–1769.
- (62) Prasanna, R.; Gold-Parker, A.; Leijtens, T.; Conings, B.; Babayigit, A.; Boyen, H. G.; Toney, M. F.; McGehee, M. D. Band Gap Tuning via Lattice Contraction and Octahedral Tilting in Perovskite Materials for Photovoltaics. *J. Am. Chem. Soc.* **2017**, *139* (32), 11117–11124.
- (63) Coletti, G. Sensitivity of State-of-the-Art and High Efficiency Crystalline Silicon Solar Cells to Metal Impurities. *Prog. Photovoltaics Res. Appl.* **2013**, *21*, 1163–1170.
- (64) Huang, H.; Bodnarchuk, M. I.; Kershaw, S. V.; Kovalenko, M. V.; Rogach, A. L. Lead Halide Perovskite Nanocrystals in the Research Spotlight: Stability and Defect Tolerance. *ACS Energy Lett.* **2017**, *2* (9), 2071–2083.
- (65) Walsh, A.; Scanlon, D. O.; Chen, S.; Gong, X. G.; Wei, S. H. Self-Regulation Mechanism for Charged Point Defects in Hybrid Halide Perovskites. *Angew. Chemie - Int. Ed.* **2015**, *54* (6), 1791–1794.
- (66) Yin, W. J.; Shi, T.; Yan, Y. Unusual Defect Physics in CH₃NH₃PbI₃ Perovskite Solar Cell Absorber. *Appl. Phys. Lett.* **2014**, *104* (6).
- (67) Li, Z.; Klein, T. R.; Kim, D. H.; Yang, M.; Berry, J. J.; Van Hest, M. F. A. M.; Zhu, K. Scalable Fabrication of Perovskite Solar Cells. *Nat. Rev. Mater.* **2018**, *3*, 18017.
- (68) Blinds – Saule Technologies <https://sauletech.com/blinds/> (accessed Feb 16, 2021).
- (69) Japan’s NEDO and Panasonic Achieve the World’s Highest Conversion Efficiency of 16.09% for Largest-area Perovskite Solar Cell Module, Panasonic Newsroom Global <https://news.panasonic.com/global/press/data/2020/02/en200207-2/en200207-2.html> (accessed Feb

References

- 17, 2021).
- (70) Ono, L. K.; Qi, Y. Surface and Interface Aspects of Organometal Halide Perovskite Materials and Solar Cells. *J. Phys. Chem. Lett* **2016**, *7*, 5.
- (71) Nie, W.; Blancon, J. C.; Neukirch, A. J.; Appavoo, K.; Tsai, H.; Chhowalla, M.; Alam, M. A.; Sfeir, M. Y.; Katan, C.; Even, J.; Tretiak S.; Crochet J.J.; Gupta G.; Mohite A.D. Light-Activated Photocurrent Degradation and Self-Healing in Perovskite Solar Cells. *Nat. Commun.* **2016**, *7*, 11574.
- (72) Aitola, K.; Domanski, K.; Correa-Baena, J. P.; Sveinbjörnsson, K.; Saliba, M.; Abate, A.; Grätzel, M.; Kauppinen, E.; Johansson, E. M. J.; Tress, W.; Hagfeldt A.; Boschloo G. High Temperature-Stable Perovskite Solar Cell Based on Low-Cost Carbon Nanotube Hole Contact. *Adv. Mater.* **2017**, *29* (17).
- (73) Bryant, D.; Aristidou, N.; Pont, S.; Sanchez-Molina, I.; Chotchunangatchaval, T.; Wheeler, S.; Durrant, J. R.; Haque, S. A. Light and Oxygen Induced Degradation Limits the Operational Stability of Methylammonium Lead Triiodide Perovskite Solar Cells. *Energy Environ. Sci.* **2016**, *9* (5), 1655–1660.
- (74) Grancini, G.; Roldán-Carmona, C.; Zimmermann, I.; Mosconi, E.; Lee, X.; Martineau, D.; Narbey, S.; Oswald, F.; De Angelis, F.; Graetzel, M.; Nazeeruddin M.K. One-Year Stable Perovskite Solar Cells by 2D/3D Interface Engineering. *Nat. Commun.* **2017**, *8*, 15684.
- (75) Senocrate, A.; Acartürk, T.; Kim, G. Y.; Merkle, R.; Starke, U.; Grätzel, M.; Maier, J. Interaction of Oxygen with Halide Perovskites. *J. Mater. Chem. A* **2018**, *6* (23), 10847–10855.
- (76) Leijtens, T.; Eperon, G. E.; Noel, N. K.; Habisreutinger, S. N.; Petrozza, A.; Snaith, H. J. Stability of Metal Halide Perovskite Solar Cells. *Adv. Energy Mater.* **2015**, *5*, 1500963.
- (77) Jin, H.; Debroye, E.; Keshavarz, M.; Scheblykin, I. G.; Roeffaers, M. B. J.; Hofkens, J.; Steele, J. A. It's a Trap! On the Nature of Localised States and Charge Trapping in Lead Halide Perovskites. *Mater. Horizons* **2020**, *7* (2), 397–410.
- (78) Meggiolaro, D.; Motti, S. G.; Mosconi, E.; Barker, A. J.; Ball, J.; Andrea Riccardo Perini, C.; Deschler, F.; Petrozza, A.; De Angelis, F. Iodine Chemistry Determines the Defect Tolerance of Lead-Halide Perovskites. *Energy Environ. Sci.* **2018**, *11* (3), 702–713.
- (79) Futscher, M. H.; Lee, J. M.; McGovern, L.; Muscarella, L. A.; Wang, T.; Haider, M. I.; Fakhruddin, A.; Schmidt-Mende, L.; Ehrler, B. Quantification of Ion Migration in CH₃NH₃PbI₃ Perovskite Solar Cells by Transient Capacitance Measurements. *Mater. Horizons* **2019**, *6* (7), 1497–1503.
- (80) Baumann, A.; Väh, S.; Rieder, P.; Heiber, M. C.; Tvingstedt, K.; Dyakonov, V. Identification of Trap States in Perovskite Solar Cells. *J. Phys. Chem. Lett.* **2015**, *6* (12), 2350–2354.
- (81) Hu, Y.; Hutter, E. M.; Rieder, P.; Grill, I.; Hanisch, J.; Aygüler, M. F.; Hufnagel, A. G.; Handloser, M.; Bein, T.; Hartschuh, A.; Tvingstedt K.; Dyakonov V.; Baumann A.; Savenije T.J.; Petrus.M.L.; Docampo P. Understanding the Role of Cesium and Rubidium Additives in Perovskite Solar Cells: Trap States, Charge Transport, and Recombination. *Adv. Energy Mater.* **2018**, *1703057*.
- (82) Moghadamzadeh, S.; Hossain, I. M.; Jakoby, M.; Abdollahi Nejand, B.; Rueda-Delgado, D.; Schwenzer, J. A.; Gharibzadeh, S.; Abzieher, T.; Khan, M. R.; Haghhighirad, A. A.; Howard I.A.; Richards B.S.; Lemmer U.; Paetzold U.W. Spontaneous Enhancement of the Stable Power Conversion Efficiency in Perovskite Solar Cells. *J. Mater. Chem. A* **2020**, *8* (2), 670–682.
- (83) Eames, C.; Frost, J. M.; Barnes, P. R. F.; O'Regan, B. C.; Walsh, A.; Islam, M. S. Ionic Transport in Hybrid Lead Iodide Perovskite Solar Cells. *Nat. Commun.* **2015**, *6*, 7497.

References

- (84) Weber, S. A. L.; Hermes, I. M.; Turren-Cruz, S. H.; Gort, C.; Bergmann, V. W.; Gilson, L.; Hagfeldt, A.; Graetzel, M.; Tress, W.; Berger, R. How the Formation of Interfacial Charge Causes Hysteresis in Perovskite Solar Cells. *Energy Environ. Sci.* **2018**, *11* (9), 2404–2413.
- (85) Neukom, M. T.; Züfle, S.; Knapp, E.; Makha, M.; Hany, R.; Ruhstaller, B. Why Perovskite Solar Cells with High Efficiency Show Small IV-Curve Hysteresis. *Sol. Energy Mater. Sol. Cells* **2017**, *169*, 159–166.
- (86) Phung, N.; Al-Ashouri, A.; Meloni, S.; Mattoni, A.; Albrecht, S.; Unger, E. L.; Merdasa, A.; Abate, A. The Role of Grain Boundaries on Ionic Defect Migration in Metal Halide Perovskites. *Adv. Energy Mater.* **2020**, 1903735.
- (87) Ma, Y.; Cheng, Y.; Xu, X.; Li, M.; Zhang, C.; Cheung, S. H.; Zeng, Z.; Shen, D.; Xie, Y. M.; Chiu, K. L.; Shu F.L.; So S.K.; Lee C.S.; Tsang S.W. Suppressing Ion Migration across Perovskite Grain Boundaries by Polymer Additives. *Adv. Funct. Mater.* **2020**, 2006802.
- (88) Yun, J. S.; Ho-Baillie, A.; Huang, S.; Woo, S. H.; Heo, Y.; Seidel, J.; Huang, F.; Cheng, Y. B.; Green, M. A. Benefit of Grain Boundaries in Organic-Inorganic Halide Planar Perovskite Solar Cells. *J. Phys. Chem. Lett.* **2015**, *6* (5), 875–880.
- (89) Correa-Baena, J. P.; Anaya, M.; Lozano, G.; Tress, W.; Domanski, K.; Saliba, M.; Matsui, T.; Jacobsson, T. J.; Calvo, M. E.; Abate, A.; Grätzel M.; Míguez H.; Hagfeldt A. Unbroken Perovskite: Interplay of Morphology, Electro-Optical Properties, and Ionic Movement. *Adv. Mater.* **2016**, *28* (25), 5031–5037.
- (90) Mosconi, E.; Meggiolaro, D.; Snaith, H. J.; Stranks, S. D.; De Angelis, F. Light-Induced Annihilation of Frenkel Defects in Organo-Lead Halide Perovskites. *Energy Environ. Sci.* **2016**, *9* (10), 3180–3187.
- (91) Cai, B.; Yang, X.; Yu, Z.; Liang, Y.; Shan, Y.; Hagfeldt, A.; Sun, L. Unveiling the Light Soaking Effects of the CsPbI₃ Perovskite Solar Cells. *J. Power Sources* **2020**, *472*, 228506.
- (92) Tress, W.; Yavari, M.; Domanski, K.; Yadav, P.; Niesen, B.; Correa Baena, J. P.; Hagfeldt, A.; Graetzel, M. Interpretation and Evolution of Open-Circuit Voltage, Recombination, Ideality Factor and Subgap Defect States during Reversible Light-Soaking and Irreversible Degradation of Perovskite Solar Cells. *Energy Environ. Sci.* **2018**, *11* (1), 151–165.
- (93) Sherkar, T. S.; Momblona, C.; Gil-Escrig, L.; Ávila, J.; Sessolo, M.; Bolink, H. J.; Koster, L. J. A. Recombination in Perovskite Solar Cells: Significance of Grain Boundaries, Interface Traps, and Defect Ions. *ACS Energy Lett.* **2017**, *2* (5), 1214–1222.
- (94) Caprioglio, P.; Wolff, C. M.; Sandberg, O. J.; Armin, A.; Rech, B.; Albrecht, S.; Neher, D.; Stolterfoht, M. On the Origin of the Ideality Factor in Perovskite Solar Cells. *Adv. Energy Mater.* **2020**, *10* (27).
- (95) Stolterfoht, M.; Wolff, C. M.; Amir, Y.; Paulke, A.; Perdigón-Toro, L.; Caprioglio, P.; Neher, D. Approaching the Fill Factor Shockley-Queisser Limit in Stable, Dopant-Free Triple Cation Perovskite Solar Cells. *Energy Environ. Sci.* **2017**, *10* (6), 1530–1539.
- (96) Li, B.; Zhang, S.; Xia, F.; Huang, Y.; Ran, X.; Xia, Y.; Chen, Y.; Huang, W. Insights into the Hole Transport Properties of LiTFSI-Doped Spiro-OMeTAD Films through Impedance Spectroscopy. *J. Appl. Phys.* **2020**, *128* (8).
- (97) Li, Z.; Xiao, C.; Yang, Y.; Harvey, S. P.; Kim, D. H.; Christians, J. A.; Yang, M.; Schulz, P.; Nanayakkara, S. U.; Jiang, C. S.; et al. Extrinsic Ion Migration in Perovskite Solar Cells. *Energy Environ. Sci.* **2017**, *10* (5), 1234–1242.

References

- (98) Cacovich, S.; Ciná, L.; Matteocci, F.; Divitini, G.; Midgley, P. A.; Di Carlo, A.; Ducati, C. Gold and Iodine Diffusion in Large Area Perovskite Solar Cells under Illumination. *Nanoscale* **2017**, *9* (14), 4700–4706.
- (99) Meng, L.; You, J.; Yang, Y. Addressing the Stability Issue of Perovskite Solar Cells for Commercial Applications. *Nat. Commun.* **2018**, *9*, 5265.
- (100) Price Index <https://www.pvxchange.com/en/price-index> (accessed Feb 18, 2021).
- (101) Solar Price | EnergyTrend <https://www.energytrend.com/solar-price.html> (accessed Feb 18, 2021).
- (102) Mathews, I.; Sofia, S.; Ma, E.; Jean, J.; Laine, H. S.; Siah, S. C.; Buonassisi, T.; Peters, I. M. Economically Sustainable Growth of Perovskite Photovoltaics Manufacturing. *Joule* **2020**, *4* (4), 822–839.
- (103) <https://www.firstsolar.com/en-Emea/-/media/First-Solar/Technical-Documents/Series-4-Datasheets/Series-4V3-Module-Datasheet.ashx> (accessed Feb 18, 2021).
- (104) [http://www.jinkosolar.com/uploads/JinkoSolar-Global Limited Warranty-\(Rev061120-LINEAR\)-V3.pdf](http://www.jinkosolar.com/uploads/JinkoSolar-Global Limited Warranty-(Rev061120-LINEAR)-V3.pdf) (accessed Feb 18, 2021).
- (105) <https://us.sunpower.com/sites/default/files/media-library/warranties/wr-sunpower-residential-complete-confidence-warranty-overview.pdf> (accessed Feb 18, 2021).
- (106) https://static.trinasolar.com/sites/default/files/PS-M-0135_O_Standard_Duomax_Warranty_EN_20200601_V1.pdf (accessed Feb 18, 2021).
- (107) Chang, N. L.; Yi Ho-Baillie, A. W.; Basore, P. A.; Young, T. L.; Evans, R.; Egan, R. J. A Manufacturing Cost Estimation Method with Uncertainty Analysis and Its Application to Perovskite on Glass Photovoltaic Modules. *Prog. Photovoltaics Res. Appl.* **2017**, *25* (5), 390–405.
- (108) Song, Z.; McElvany, C. L.; Phillips, A. B.; Celik, I.; Krantz, P. W.; Wathage, S. C.; Liyanage, G. K.; Apul, D.; Heben, M. J. A Technoeconomic Analysis of Perovskite Solar Module Manufacturing with Low-Cost Materials and Techniques. *Energy Environ. Sci.* **2017**, *10* (6), 1297–1305.
- (109) Holzhey, P.; Saliba, M. A Full Overview of International Standards Assessing the Long-Term Stability of Perovskite Solar Cells. *J. Mater. Chem. A* **2018**, *6* (44), 21794–21808.
- (110) Kempe, M. D. Accelerated UV Test Methods and Selection Criteria for Encapsulants of Photovoltaic Modules. *Conf. Rec. IEEE Photovolt. Spec. Conf.* **2008**, 3–8.
- (111) Köntges, M.; Kurtz, S.; Packard, C. E.; Jahn, U.; Berger, K.; Kato, K.; Friesen, T.; Liu, H.; Van Iseghem, M. *Review of Failures of Photovoltaic Modules*; 2014.
- (112) Khenkin, M. V.; Katz, E. A.; Abate, A.; Bardizza, G.; Berry, J. J.; Brabec, C.; Brunetti, F.; Bulović, V.; Burlingame, Q.; Di Carlo, A.; et al. Consensus Statement for Stability Assessment and Reporting for Perovskite Photovoltaics Based on ISOS Procedures. *Nat. Energy* **2020**, *5* (1), 35–49.
- (113) Koh, T. M.; Shanmugam, V.; Schlipf, J.; Oesinghaus, L.; Müller-Buschbaum, P.; Ramakrishnan, N.; Swamy, V.; Mathews, N.; Boix, P. P.; Mhaisalkar, S. G. Nanostructuring Mixed-Dimensional Perovskites: A Route Toward Tunable, Efficient Photovoltaics. *Adv. Mater.* **2016**, *28* (19), 3653–3661.
- (114) Zou, Y.; Cui, Y.; Wang, H. Y.; Cai, Q.; Mu, C.; Zhang, J. P. Highly Efficient and Stable 2D-3D Perovskite Solar Cells Fabricated by Interfacial Modification. *Nanotechnology* **2019**, *30*, 275202.
- (115) Qi Jiang, Yang Zhao, Xingwang Zhang, Xiaolei Yang, Yong Chen, Zema Chu, Q. Y.; Xingxing Li;

References

- Zhigang Yin; Jingbi You. Surface Passivation of Perovskite Film for Efficient Solar Cells. *Nat. Photonics* **2019**, *13*, 460–466.
- (116) Malekshahi Byranvand, M.; Behboodi-Sadabad, F.; Alrhmman Eliwi, A.; Trouillet, V.; Welle, A.; Ternes, S.; Hossain, I. M.; Khan, M. R.; Schwenzer, J. A.; Farooq, A.; et al. Chemical Vapor Deposited Polymer Layer for Efficient Passivation of Planar Perovskite Solar Cells. *J. Mater. Chem. A* **2020**, *8* (38), 20122–20132.
- (117) Kim, M.; Motti, S. G.; Sorrentino, R.; Petrozza, A. Enhanced Solar Cell Stability by Hygroscopic Polymer Passivation of Metal Halide Perovskite Thin Film. *Energy Environ. Sci.* **2018**, *11*, 2609–2619.
- (118) Wang, F.; Shimazaki, A.; Yang, F.; Kanahashi, K.; Matsuki, K.; Miyauchi, Y.; Takenobu, T.; Wakamiya, A.; Murata, Y.; Matsuda, K. Highly Efficient and Stable Perovskite Solar Cells by Interfacial Engineering Using Solution-Processed Polymer Layer. *J. Phys. Chem. C* **2017**, *121* (3), 1562–1568.
- (119) Wang, Q.; Dong, Q.; Li, T.; Gruverman, A.; Huang, J. Thin Insulating Tunneling Contacts for Efficient and Water-Resistant Perovskite Solar Cells. *Adv. Mater.* **2016**, *28* (31), 6734–6739.
- (120) Chaudhary, B.; Kulkarni, A.; Jena, A. K.; Ikegami, M.; Udagawa, Y.; Kunugita, H.; Ema, K.; Miyasaka, T. Poly(4-Vinylpyridine)-Based Interfacial Passivation to Enhance Voltage and Moisture Stability of Lead Halide Perovskite Solar Cells. *ChemSusChem* **2017**, *10* (11), 2473–2479.
- (121) Hovel, H. J.; Hodgson, R. T.; Woodall, J. M. The Effect of Fluorescent Wavelength Shifting on Solar Cell Spectral Response. *Sol. Energy Mater.* **1979**, *2* (1), 19–29.
- (122) Diego Alonso-Álvarez, David Ross, Efthymios Klampaftis, Keith R. McIntosh, S. J.; Paul Storiz; Theodore Stolz; Bryce S. Richards. Luminescent Down-Shifting Experiment and Modelling with Multiple Photovoltaic Technologies. *Prog. Photovoltaics Res. Appl.* **2015**, *23*, 479–497.
- (123) Klampaftis, E.; Ross, D.; McIntosh, K. R.; Richards, B. S. Enhancing the Performance of Solar Cells via Luminescent Down-Shifting of the Incident Spectrum: A Review. *Sol. Energy Mater. Sol. Cells* **2009**, *93* (8), 1182–1194.
- (124) Bella, F.; Griffini, G.; Correa-Baena, J. P.; Saracco, G.; Grätzel, M.; Hagfeldt, A.; Turri, S.; Gerbaldi, C. Improving Efficiency and Stability of Perovskite Solar Cells with Photocurable Fluoropolymers. *Science (80-.)*. **2016**, *354* (6309), 203–206.
- (125) Cui, J.; Li, P.; Chen, Z.; Cao, K.; Li, D.; Han, J.; Shen, Y.; Peng, M.; Qing Fu, Y.; Wang, M. Phosphor Coated NiO-Based Planar Inverted Organometallic Halide Perovskite Solar Cells with Enhanced Efficiency and Stability. *Appl. Phys. Lett.* **2016**, *109*, 171103.
- (126) Chen, W.; Luo, Q.; Zhang, C.; Shi, J.; Deng, X.; Yue, L.; Wang, Z.; Chen, X.; Huang, S. Effects of Down-Conversion CeO₂:Eu³⁺ Nanophosphors in Perovskite Solar Cells. *J. Mater. Sci. Mater. Electron.* **2017**, *28* (15), 11346–11357.
- (127) Chander, N.; Khan, A. F.; Chandrasekhar, P. S.; Thouti, E.; Swami, S. K.; Dutta, V.; Komarala, V. K. Reduced Ultraviolet Light Induced Degradation and Enhanced Light Harvesting Using YVO₄:Eu³⁺ down-Shifting Nano-Phosphor Layer in Organometal Halide Perovskite Solar Cells. *Appl. Phys. Lett.* **2014**, *105*, 033904.
- (128) Manjunath, V.; Krishna, R.; Maniarasu, S.; Ramasamy, E.; Shanmugasundaram, S.; Veerappan, G. Perovskite Solar Cell Architectures. In *Perovskite Photovoltaics: Basic to Advanced Concepts and Implementation*, **2018**, 89–121.

References

- (129) Urieta-Mora, J.; García-Benito, I.; Molina-Ontoria, A.; Martín, N. Hole Transporting Materials for Perovskite Solar Cells: A Chemical Approach. *Chemical Society reviews*, **2018**, 8541–8571.
- (130) Zhao, X.; Wang, M. Organic Hole-Transporting Materials for Efficient Perovskite Solar Cells. *Materials Today Energy*, 2018, 208–220.
- (131) Pitchaiya, S.; Natarajan, M.; Santhanam, A.; Asokan, V.; Yuvapragasam, A.; Madurai Ramakrishnan, V.; Palanisamy, S. E.; Sundaram, S.; Velauthapillai, D. A Review on the Classification of Organic/Inorganic/Carbonaceous Hole Transporting Materials for Perovskite Solar Cell Application. *Arabian Journal of Chemistry*, **2020**, 2526–2557.
- (132) Kung, P.; Li, M.; Lin, P.; Chiang, Y.; Chan, C.; Guo, T.; Chen, P. A Review of Inorganic Hole Transport Materials for Perovskite Solar Cells. *Adv. Mater. Interfaces* **2018**, 5 (22), 1800882.
- (133) Rajeswari, R.; Mrinalini, M.; Prasanthkumar, S.; Giribabu, L. Emerging of Inorganic Hole Transporting Materials For Perovskite Solar Cells. *Chem. Rec.* **2017**, 17 (7), 681–699.
- (134) Liu, C.; Cai, M.; Yang, Y.; Arain, Z.; Ding, Y.; Shi, X.; Shi, P.; Ma, S.; Hayat, T.; Alsaedi, A.; et al. A C60/TiO_x Bilayer for Conformal Growth of Perovskite Films for UV Stable Perovskite Solar Cells. *J. Mater. Chem. A* **2019**, 7 (18), 11086–11094.
- (135) Mali, S. S.; Hong, C. K. P-i-n/n-i-p Type Planar Hybrid Structure of Highly Efficient Perovskite Solar Cells towards Improved Air Stability: Synthetic Strategies and the Role of p-Type Hole Transport Layer (HTL) and n-Type Electron Transport Layer (ETL) Metal Oxides. *Nanoscale*, **2016**, 10528–10540.
- (136) Long, J.; Huang, Z.; Zhang, J.; Hu, X.; Tan, L.; Chen, Y. Flexible Perovskite Solar Cells: Device Design and Perspective. *Flex. Print. Electron.* **2020**, 5 (1), 013002.
- (137) Butscher, J. F.; Sun, Q.; Wu, Y.; Stuck, F.; Hoffmann, M.; Dreuw, A.; Paulus, F.; Hashmi, S. K.; Tessler, N.; Vaynzof, Y. Dipolar Hole-Blocking Layers for Inverted Perovskite Solar Cells: Effects of Aggregation and Electron Transport Levels. *J. Phys. Mater* **2020**, 3, 25002.
- (138) He, C.; Zhang, F.; Zhao, X.; Lin, C.; Ye, M. Interface Engineering of BCP Buffer Layers in Planar Heterojunction Perovskite Solar Cells With NiO_x Hole Transporting Layers. *Front. Phys.* **2018**, 6, 99.
- (139) Petrov, A. A.; Sokolova, I. P.; Belich, N. A.; Peters, G. S.; Dorovatovskii, P. V.; Zubavichus, Y. V.; Khrustalev, V. N.; Petrov, A. V.; Grätzel, M.; Goodilin, E. A.; et al. Crystal Structure of DMF-Intermediate Phases Uncovers the Link between CH₃NH₃PbI₃ Morphology and Precursor Stoichiometry. *J. Phys. Chem. C* **2017**, 121 (38), 20739–20743.
- (140) Michael M. Lee, Joël Teuscher, Tsutomu Miyasaka, T. N. M.; Snaith, H. J. Efficient Hybrid Solar Cells Based on Meso-Superstructured Organometal Halide Perovskites. *Science*. **2012**, 338, 643–648.
- (141) Yu, H.; Wang, F.; Xie, F.; Li, W.; Chen, J.; Zhao, N. The Role of Chlorine in the Formation Process of “CH₃NH₃PbI₃-XCl_x” Perovskite. *Adv. Funct. Mater.* **2014**, 24 (45), 7102–7108.
- (142) Buin, A.; Pietsch, P.; Xu, J.; Voznyy, O.; Ip, A. H.; Comin, R.; Sargent, E. H. Materials Processing Routes to Trap-Free Halide Perovskites. *Nano Lett.* **2014**, 14 (11), 6281–6286.
- (143) Seo, J.; Park, S.; Chan Kim, Y.; Jeon, N. J.; Noh, J. H.; Yoon, S. C.; Seok, S. II. Benefits of Very Thin PCBM and LiF Layers for Solution-Processed p-i-n Perovskite Solar Cells. *Energy Environ. Sci.* **2014**, 7 (8), 2642–2646.

References

- (144) Burschka, J.; Pellet, N.; Moon, S. J.; Humphry-Baker, R.; Gao, P.; Nazeeruddin, M. K.; Grätzel, M. Sequential Deposition as a Route to High-Performance Perovskite-Sensitized Solar Cells. *Nature* **2013**, *499* (7458), 316–319.
- (145) Im, J. H.; Jang, I. H.; Pellet, N.; Grätzel, M.; Park, N. G. Growth of CH₃NH₃PbI₃ Cuboids with Controlled Size for High-Efficiency Perovskite Solar Cells. *Nat. Nanotechnol.* **2014**, *9* (11), 927–932.
- (146) Chen, Q.; Zhou, H.; Hong, Z.; Luo, S.; Duan, H. S.; Wang, H. H.; Liu, Y.; Li, G.; Yang, Y. Planar Heterojunction Perovskite Solar Cells via Vapor-Assisted Solution Process. *J. Am. Chem. Soc.* **2014**, *136* (2), 622–625.
- (147) Chen, H. Two-Step Sequential Deposition of Organometal Halide Perovskite for Photovoltaic Application. *Adv. Funct. Mater.* **2017**, 1605654.
- (148) Jeon, N. J.; Noh, J. H.; Kim, Y. C.; Yang, W. S.; Ryu, S.; Seok, S. I. Solvent Engineering for High-Performance Inorganic-Organic Hybrid Perovskite Solar Cells. *Nat. Mater.* **2014**, *13* (9), 897–903.
- (149) Paek, S.; Schouwink, P.; Athanasopoulou, E. N.; Cho, K. T.; Grancini, G.; Lee, Y.; Zhang, Y.; Stellacci, F.; Nazeeruddin, M. K.; Gao, P. From Nano- to Micrometer Scale: The Role of Antisolvent Treatment on High Performance Perovskite Solar Cells. *Chem. Mater.* **2017**, *29* (8), 3490–3498.
- (150) Gratia, P.; Zimmermann, I.; Schouwink, P.; Yum, J. H.; Audinot, J. N.; Sivula, K.; Wirtz, T.; Nazeeruddin, M. K. The Many Faces of Mixed Ion Perovskites: Unraveling and Understanding the Crystallization Process. *ACS Energy Lett.* **2017**, *2* (12), 2686–2693.
- (151) Konstantakou, M.; Perganti, D.; Falaras, P.; Stergiopoulos, T. Anti-Solvent Crystallization Strategies for Highly Efficient Perovskite Solar Cells. *Crystals* **2017**, *7* (10), 291.
- (152) Bruening, K.; Tassone, C. J. Antisolvent Processing of Lead Halide Perovskite Thin Films Studied by: In Situ X-Ray Diffraction. *J. Mater. Chem. A* **2018**, *6* (39), 18865–18870.
- (153) Benganem, M.; Al-Mashraqi, A. A.; Daffallah, K. O. Performance of Solar Cells Using Thermoelectric Module in Hot Sites. *Renew. Energy* **2016**, *89*, 51–59.
- (154) Nordmann, T.; Clavadetscher, L. Understanding Temperature Effects on PV System Performance. *Proc. 3rd World Conf. Photovolt. Energy Convers.* **2003**, *C*, 2243–2246.
- (155) Juarez-Perez, E. J.; Ono, L. K.; Uriarte, I.; Cocinero, E. J.; Qi, Y. Degradation Mechanism and Relative Stability of Methylammonium Halide Based Perovskites Analyzed on the Basis of Acid-Base Theory. *ACS Appl. Mater. Interfaces* **2019**, *11* (13), 12586–12593.
- (156) Kim, N. K.; Min, Y. H.; Noh, S.; Cho, E.; Jeong, G.; Joo, M.; Ahn, S. W.; Lee, J. S.; Kim, S.; Ihm, K.; et al. Investigation of Thermally Induced Degradation in CH₃NH₃PbI₃ Perovskite Solar Cells Using In-Situ Synchrotron Radiation Analysis. *Sci. Rep.* **2017**, *7*, 4645.
- (157) Kim, N. K.; Min, Y. H.; Noh, S.; Cho, E.; Jeong, G.; Joo, M.; Ahn, S. W.; Lee, J. S.; Kim, S.; Ihm, K.; et al. Investigation of Thermally Induced Degradation in CH₃NH₃PbI₃ Perovskite Solar Cells Using In-Situ Synchrotron Radiation Analysis. *Sci. Rep.* **2017**, *7*, 4645.
- (158) Shi, L.; Bucknall, M. P.; Young, T. L.; Zhang, M.; Hu, L.; Bing, J.; Lee, D. S.; Kim, J.; Wu, T.; Takamura, N.; et al. Gas Chromatography-Mass Spectrometry Analyses of Encapsulated Stable Perovskite Solar Cells. *Science* (80-.). **2020**, *368*, eaba2412.
- (159) Extance, A. The Reality behind Solar Power's next Star Material. *Nature* **2019**, *570* (7762), 429–432.

References

- (160) Olsen, L. . Barrier Coatings for Thin Film Solar Cells Barrier. *Natl. Renew. Energy Lab.* **2010**, No. March, <http://www.nrel.gov/docs/fy10osti/47582.pdf>.
- (161) Zhao, J.; Cai, B.; Luo, Z.; Dong, Y.; Zhang, Y.; Xu, H.; Hong, B.; Yang, Y.; Li, L.; Zhang, W.; et al. Investigation of the Hydrolysis of Perovskite Organometallic Halide $\text{CH}_3\text{NH}_3\text{PbI}_3$ in Humidity Environment. *Sci. Rep.* **2016**, *6*, 21976.
- (162) Fu, Q.; Tang, X.; Huang, B.; Hu, T.; Tan, L.; Chen, L.; Chen, Y. Recent Progress on the Long-Term Stability of Perovskite Solar Cells. *Adv. Sci.* **2018**, *5*, 1700387.
- (163) Ahmad, S.; Kanaujia, P. K.; Niu, W.; Baumberg, J. J.; Prakash, G. V. In Situ Intercalation Dynamics in Inorganic–Organic Layered Perovskite Thin Films. *ACS Appl. Mater. Interfaces* **2014**, *6*, 13, 10238–10247.
- (164) Ji, J.; Liu, X.; Jiang, H.; Duan, M.; Liu, B.; Huang, H.; Wei, D.; Li, Y.; Li, M. Two-Stage Ultraviolet Degradation of Perovskite Solar Cells Induced by the Oxygen Vacancy-Ti⁴⁺ States. *iScience* **2020**, *23* (4), 101013.
- (165) Holovský, J.; Peter Amalathas, A.; Landová, L.; Dzurňák, B.; Conrad, B.; Ledinský, M.; Hájková, Z.; Pop-Georgievski, O.; Svoboda, J.; Yang, T. C. J.; et al. Lead Halide Residue as a Source of Light-Induced Reversible Defects in Hybrid Perovskite Layers and Solar Cells. *ACS Energy Lett.* **2019**, *4* (12), 3011–3017.
- (166) Travkin, V. V.; Yunin, P. A.; Fedoseev, A. N.; Okhapkin, A. I.; Sachkov, Y. I.; Pakhomov, G. L. Wavelength-Selective Degradation of Perovskite-Based Solar Cells. *Solid State Sci.* **2020**, *99*, 106051.
- (167) Xiao, W.; Yang, J.; Xiong, S.; Li, D.; Li, Y.; Tang, J.; Duan, C.; Bao, Q. Exploring Red, Green, and Blue Light-Activated Degradation of Perovskite Films and Solar Cells for Near Space Applications. *Sol. RRL* **2020**, *4* (3), 1–8.
- (168) Merdasa, A.; Kiligaridis, A.; Rehmann, C.; Abdi-Jalebi, M.; Stöber, J.; Louis, B.; Gerhard, M.; Stranks, S. D.; Unger, E. L.; Scheblykin, I. G. Impact of Excess Lead Iodide on the Recombination Kinetics in Metal Halide Perovskites. *ACS Energy Lett.* **2019**, *4* (6), 1370–1378.
- (169) Domanski, K.; Alharbi, E. A.; Hagfeldt, A.; Grätzel, M.; Tress, W. Behaviour of Perovskite Solar Cells. *Nat. Energy* **2018**, *3* (January), 61–67.
- (170) Quitsch, W. A.; Dequillettes, D. W.; Pflingsten, O.; Schmitz, A.; Ognjanovic, S.; Jariwala, S.; Koch, S.; Winterer, M.; Ginger, D. S.; Bacher, G. The Role of Excitation Energy in Photobrightening and Photodegradation of Halide Perovskite Thin Films. *J. Phys. Chem. Lett.* **2018**, *9* (8), 2062–2069.
- (171) Leijtens, T.; Eperon, G. E.; Pathak, S.; Abate, A.; Lee, M. M.; Snaith, H. J. Overcoming Ultraviolet Light Instability of Sensitized TiO₂ with Meso-Superstructured Organometal Tri-Halide Perovskite Solar Cells. *Nat. Commun.* **2013**, *4*, 2885.
- (172) Munusamy, S.; Aparna, R. sai laxmi; Prasad, R. G. S. V. Photocatalytic Effect of TiO₂ and the Effect of Dopants on Degradation of Brilliant Green. *Sustain. Chem. Process.* **2013**, *1*, 4.
- (173) Li, W.; Zhang, W.; Van Reenen, S.; Sutton, R. J.; Fan, J.; Haghighirad, A. A.; Johnston, M. B.; Wang, L.; Snaith, H. J. Enhanced UV-Light Stability of Planar Heterojunction Perovskite Solar Cells with Caesium Bromide Interface Modification. *Energy Environ. Sci.* **2016**, *9* (2), 490–498.
- (174) Lee, S. W.; Kim, S.; Bae, S.; Cho, K.; Chung, T.; Mundt, L. E.; Lee, S.; Park, S.; Park, H.; Schubert, M. C.; et al. UV Degradation and Recovery of Perovskite Solar Cells. *Sci. Rep.* **2016**, *6*, 38150.

References

- (175) Ahn, N.; Kwak, K.; Jang, M. S.; Yoon, H.; Lee, B. Y.; Lee, J. K.; Pikhitsa, P. V.; Byun, J.; Choi, M. Trapped Charge-Driven Degradation of Perovskite Solar Cells. *Nat. Commun.* **2016**, *7*, 13422.
- (176) Khenkin, M. V.; Anoop, K. M.; Visoly-Fisher, I.; Kolusheva, S.; Galagan, Y.; Di Giacomo, F.; Vukovic, O.; Patil, B. R.; Sherafatipour, G.; Turkovic, V.; et al. Dynamics of Photoinduced Degradation of Perovskite Photovoltaics: From Reversible to Irreversible Processes. *ACS Appl. Energy Mater.* **2018**, *1* (2), 799–806.
- (177) Mamun, A. Al; Ava, T. T.; Byun, H. R.; Jeong, H. J.; Jeong, M. S.; Nguyen, L.; Gausin, C.; Namkoong, G. Unveiling the Irreversible Performance Degradation of Organo-Inorganic Halide Perovskite Films and Solar Cells during Heating and Cooling Processes. *Phys. Chem. Chem. Phys.* **2017**, *19* (29), 19487–19495.
- (178) Gomez, A.; Sanchez, S.; Campoy-Quiles, M.; Abate, A. Topological Distribution of Reversible and Non-Reversible Degradation in Perovskite Solar Cells. *Nano Energy* **2018**, *45*, 94–100.
- (179) Kwak, K.; Lim, E.; Ahn, N.; Heo, J.; Bang, K.; Kim, S. K.; Choi, M. An Atomistic Mechanism for the Degradation of Perovskite Solar Cells by Trapped Charge. *Nanoscale* **2019**, *11* (23), 11369–11378.
- (180) Khenkin, M. V.; Anoop, K. M.; Visoly-Fisher, I.; Galagan, Y.; Di Giacomo, F.; Patil, B. R.; Sherafatipour, G.; Turkovic, V.; Rubahn, H. G.; Madsen, M.; et al. Reconsidering Figures of Merit for Performance and Stability of Perovskite Photovoltaics. *Energy Environ. Sci.* **2018**, *11* (4), 739–743.
- (181) Tress, W.; Yavari, M.; Domanski, K.; Yadav, P.; Niesen, B.; Correa Baena, J. P.; Hagfeldt, A.; Graetzel, M. Interpretation and Evolution of Open-Circuit Voltage, Recombination, Ideality Factor and Subgap Defect States during Reversible Light-Soaking and Irreversible Degradation of Perovskite Solar Cells. *Energy Environ. Sci.* **2018**, *11* (1), 151–165.
- (182) Ahn, N.; Kwak, K.; Jang, M. S.; Yoon, H.; Lee, B. Y.; Lee, J. K.; Pikhitsa, P. V.; Byun, J.; Choi, M. Trapped Charge-Driven Degradation of Perovskite Solar Cells. *Nat. Commun.* **2016**, *7*, 13422.
- (183) Bella, F.; Griffini, G.; Correa-Baena, J. P.; Saracco, G.; Grätzel, M.; Hagfeldt, A.; Turri, S.; Gerbaldi, C. Improving Efficiency and Stability of Perovskite Solar Cells with Photocurable Fluoropolymers. *Science (80-.)*. **2016**, *354* (6309), 203–206.
- (184) Chen, T. P.; Lin, C. W.; Li, S. S.; Tsai, Y. H.; Wen, C. Y.; Lin, W. J.; Hsiao, F. M.; Chiu, Y. P.; Tsukagoshi, K.; Osada, M.; et al. Self-Assembly Atomic Stacking Transport Layer of 2D Layered Titania for Perovskite Solar Cells with Extended UV Stability. *Adv. Energy Mater.* **2017**, 1701722.
- (185) Huang, M.; Zhao, Q.; Chen, Z.; Shou, C.; Shen, Q.; Yang, S. A UV-Stable Perovskite Solar Cell Based on Mo-Doped TiO₂ Interlayer. *Chem. Lett.* **2019**, *48* (7), 700–703.
- (186) Roose, B.; Johansen, C. M.; Dupraz, K.; Jaouen, T.; Aebi, P.; Steiner, U.; Abate, A. A Ga-Doped SnO₂ Mesoporous Contact for UV Stable Highly Efficient Perovskite Solar Cells. *J. Mater. Chem. A* **2018**, *6* (4), 1850–1857.
- (187) Liu, C.; Cai, M.; Yang, Y.; Arain, Z.; Ding, Y.; Shi, X.; Shi, P.; Ma, S.; Hayat, T.; Alsaedi, A.; et al. A C60/TiO_x Bilayer for Conformal Growth of Perovskite Films for UV Stable Perovskite Solar Cells. *J. Mater. Chem. A*, **2019**, *7*, 11086–11094.
- (188) Liu, T.; Xiong, Y.; Mei, A.; Hu, Y.; Rong, Y.; Xu, M.; Wang, Z.; Lou, L.; Du, D.; Zheng, S.; et al. Spacer Layer Design for Efficient Fully Printable Mesoscopic Perovskite Solar Cells. *RSC Adv.* **2019**, *9* (51), 29840–29846.

References

- (189) Gong, X.; Sun, Q.; Liu, S.; Liao, P.; Shen, Y.; Grä, C.; Zakeeruddin, S. M.; Grä, M.; Wang, M. Highly Efficient Perovskite Solar Cells with Gradient Bilayer Electron Transport Materials. *Nano Lett.* **2018**, *18*, 6, 3969–3977.
- (190) Chen, W.; Luo, Q.; Zhang, C.; Shi, J.; Deng, X.; Yue, L.; Wang, Z.; Chen, X.; Huang, S. Effects of Down-Conversion CeO₂:Eu³⁺ Nanophosphors in Perovskite Solar Cells. *J. Mater. Sci. Mater. Electron.* **2017**, *28* (15), 11346–11357.
- (191) Aljaioussi, G.; Makableh, Y. F.; Al-Fandi, M. Design and Optimization of Nanostructured UV-Filters for Efficient and Stable Perovskite Solar Cells. *Semicond. Sci. Technol.* **2019**, *34* (12), 125014.
- (192) Sun, Y.; Fang, X.; Ma, Z.; Xu, L.; Lu, Y.; Yu, Q.; Yuan, N.; Ding, J. Enhanced UV-Light Stability of Organometal Halide Perovskite Solar Cells with Interface Modification and a UV Absorption Layer. *J. Mater. Chem. C* **2017**, *5* (34), 8682–8687.
- (193) Shin, S. S.; Yeom, E. J.; Yang, W. S.; Hur, S.; Kim, M. G.; Im, J.; Seo, J.; Noh, J. H.; Seok, S. Il. Colloidally Prepared La-Doped BaSnO₃ Electrodes for Efficient, Photostable Perovskite Solar Cells. *Science (80-.)*. **2017**, *356* (6334), 167–171.
- (194) Pérez-Tomas, A.; Xie, H.; Wang, Z.; Kim, H. S.; Shirley, I.; Turren-Cruz, S. H.; Morales-Melgares, A.; Saliba, B.; Tanenbaum, D.; Saliba, M.; et al. PbZrTiO₃ Ferroelectric Oxide as an Electron Extraction Material for Stable Halide Perovskite Solar Cells. *Sustain. Energy Fuels* **2019**, *3* (2), 382–389.
- (195) da Silva, F.; de Almeida, S.; Ahuja, R.; Arwin, H.; Ferreira da Silva, A.; Persson, C.; Osorio-Guillé, J. M.; Souza de Almeida, J.; Moyses Araujo, C.; Veje, E.; et al. Electronic and Optical Properties of Lead Iodide. *J. Appl. Phys.* **2002**, *92* (12), 7219–7224.
- (196) Holovský, J.; Peter Amalathas, A.; Landová, L.; Dzurňák, B.; Conrad, B.; Ledinský, M.; Hájková, Z.; Pop-Georgievski, O.; Svoboda, J.; Yang, T. C.; et al. Lead Halide Residue as a Source of Light-Induced Reversible Defects in Hybrid Perovskite Layers and Solar Cells. *ACS Energy Lett.* **2019**, 3011–3017.
- (197) Lu, L.; Shen, K. C.; Wang, J.; Su, Z.; Li, Y.; Chen, L.; Luo, Y.; Song, F.; Gao, X.; Tang, J. X. Interaction of the Cation and Vacancy in Hybrid Perovskites Induced by Light Illumination. *ACS Appl. Mater. Interfaces* **2020**, *12* (37), 42369–42377.
- (198) Afre, R. A.; Sharma, N.; Sharon, M.; Sharon, M. Transparent Conducting Oxide Films for Various Applications: A Review. *Rev. Adv. Mater. Sci.* **2018**, *53* (1), 79–89.
- (199) Riza, M. A.; Ibrahim, M. A.; Ahamefula, U. C.; Mat Teridi, M. A.; Ahmad Ludin, N.; Sepeai, S.; Sopian, K. Prospects and Challenges of Perovskite Type Transparent Conductive Oxides in Photovoltaic Applications. Part I – Material Developments. *Sol. Energy* **2016**, *137*, 371–378.
- (200) Baltakesmez, A.; Biber, M.; Tüzemen, S. Inverted Planar Perovskite Solar Cells Based on Al Doped ZnO Substrate. *J. Radiat. Res. Appl. Sci.* **2018**, *11* (2), 124–129.
- (201) Sawada, Y.; Kobayashi, C.; Seki, S.; Funakubo, H. Highly-Conducting Indium-Tin-Oxide Transparent Films Fabricated by Spray CVD Using Ethanol Solution of Indium (III) Chloride and Tin (II) Chloride. *Thin Solid Films* **2002**, *409* (1), 46–50.
- (202) Liu, H.; Avrutin, V.; Izyumskaya, N.; Özgür, Ü.; Morkoç, H. Transparent Conducting Oxides for Electrode Applications in Light Emitting and Absorbing Devices. *Superlattices Microstruct.* **2010**, *48* (5), 458–484.

References

- (203) Wei, Q.; Yang, Z.; Yang, D.; Zi, W.; Ren, X.; Liu, Y.; Liu, X.; Feng, J.; (Frank) Liu, S. The Effect of Transparent Conductive Oxide on the Performance $\text{CH}_3\text{NH}_3\text{PbI}_3$ Perovskite Solar Cell without Electron/Hole Selective Layers. *Sol. Energy* **2016**, *135*, 654–661.
- (204) Zhang, M.; Wilkinson, B.; Liao, Y.; Zheng, J.; Lau, C. F. J.; Kim, J.; Bing, J.; Green, M. A.; Huang, S.; Ho-Baillie, A. W. Y. Electrode Design to Overcome Substrate Transparency Limitations for Highly Efficient 1 Cm² Mesoscopic Perovskite Solar Cells. *Joule* **2018**, *2* (12), 2694–2705.
- (205) Elangovan, E.; Ramamurthi, K. A Study on Low Cost-High Conducting Fluorine and Antimony-Doped Tin Oxide Thin Films. *Appl. Surf. Sci.* **2005**, *249* (1–4), 183–196.
- (206) An, Q.; Fassel, P.; Hofstetter, Y. J.; Becker-Koch, D.; Bausch, A.; Hopkinson, P. E.; Vaynzof, Y. High Performance Planar Perovskite Solar Cells by ZnO Electron Transport Layer Engineering. *Nano Energy* **2017**, *39*, 400–408.
- (207) Syrokostas, G.; Leftheriotis, G.; Yannopoulos, S. N. Double-Layered Zirconia Films for Carbon-Based Mesoscopic Perovskite Solar Cells and Photodetectors. *J. Nanomater.* **2019**, 8348237.
- (208) Mahmood, K.; Sarwar, S.; Mehran, M. T. Current Status of Electron Transport Layers in Perovskite Solar Cells: Materials and Properties. *RSC Adv.* **2017**, *7* (28), 17044–17062.
- (209) Xu, J.; Shi, X.; Chen, J.; Luan, J.; Yao, J. Optimizing Solution-Processed C60 Electron Transport Layer in Planar Perovskite Solar Cells by Interfacial Modification with Solid-State Ionic-Liquids. *J. Solid State Chem.* **2019**, *276*, 302–308.
- (210) Xia, F.; Wu, Q.; Zhou, P.; Li, Y.; Chen, X.; Liu, Q.; Zhu, J.; Dai, S.; Lu, Y.; Yang, S. Efficiency Enhancement of Inverted Structure Perovskite Solar Cells via Oleamide Doping of PCBM Electron Transport Layer. *ACS Appl. Mater. Interfaces* **2015**, *7* (24), 13659–13665.
- (211) Yang, D.; Yang, R.; Wang, K.; Wu, C.; Zhu, X.; Feng, J.; Ren, X.; Fang, G.; Priya, S.; Liu, S. (Frank). High Efficiency Planar-Type Perovskite Solar Cells with Negligible Hysteresis Using EDTA-Complexed SnO_2 . *Nat. Commun.* **2018**, *9*, 3239.
- (212) Qiu, W.; Paetzold, U. W.; Gehlhaar, R.; Smirnov, V.; Boyen, H. G.; Tait, J. G.; Conings, B.; Zhang, W.; Nielsen, C. B.; McCulloch, I.; et al. An Electron Beam Evaporated TiO_2 Layer for High Efficiency Planar Perovskite Solar Cells on Flexible Polyethylene Terephthalate Substrates. *J. Mater. Chem. A* **2015**, *3* (45), 22824–22829.
- (213) Hossain, I. M.; Hudry, D.; Mathies, F.; Abzieher, T.; Moghadamzadeh, S.; Rueda-Delgado, D.; Schackmar, F.; Bruns, M.; Andriessen, R.; Aernouts, T.; et al. Scalable Processing of Low-Temperature TiO_2 Nanoparticles for High-Efficiency Perovskite Solar Cells. *ACS Appl. Energy Mater.* **2019**, *2* (1), 47–58.
- (214) Mi, Y.; Weng, Y. Band Alignment and Controllable Electron Migration between Rutile and Anatase TiO_2 . *Sci. Rep.* **2015**, *5* (January), 1–10.
- (215) Leijtens, T.; Stranks, S. D.; Eperon, G. E.; Lindblad, R.; Johansson, E. M. J.; McPherson, I. J.; Rensmo, H.; Ball, J. M.; Lee, M. M.; Snaith, H. J. Electronic Properties of Meso-Superstructured and Planar Organometal Halide Perovskite Films: Charge Trapping, Photodoping, and Carrier Mobility. *ACS Nano* **2014**, *8* (7), 7147–7155.
- (216) Cho, N.; Li, F.; Turedi, B.; Sinatra, L.; Sarmah, S. P.; Parida, M. R.; Saidaminov, M. I.; Murali, B.; Burlakov, V. M.; Goriely, A.; et al. Pure Crystal Orientation and Anisotropic Charge Transport in Large-Area Hybrid Perovskite Films. *Nat. Commun.* **2016**, *7*, 13407.
- (217) Xiong, L.; Guo, Y.; Wen, J.; Liu, H.; Yang, G.; Qin, P.; Fang, G. Review on the Application of

- SnO₂ in Perovskite Solar Cells. *Adv. Funct. Mater.* **2018**, *28*, 1802757.
- (218) Smith, J. A.; Game, O. S.; Bishop, J. E.; Spooner, E. L. K.; Kilbride, R. C.; Greenland, C.; Jayaprakash, R.; Alanazi, T. I.; Alanazi, T. I.; Cassella, E. J.; et al. Rapid Scalable Processing of Tin Oxide Transport Layers for Perovskite Solar Cells. *ACS Appl. Energy Mater.* **2020**, *3* (6), 5552–5562.
- (219) Pitchaiya, S.; Natarajan, M.; Santhanam, A.; Asokan, V.; Yuvapragasam, A.; Madurai Ramakrishnan, V.; Palanisamy, S. E.; Sundaram, S.; Velauthapillai, D. A Review on the Classification of Organic/Inorganic/Carbonaceous Hole Transporting Materials for Perovskite Solar Cell Application. *Arab. J. Chem.* **2020**, *13* (1), 2526–2557.
- (220) Dzikri, I.; Hariadi, M.; Purnamaningsih, R. W.; Poespawati, N. R. Analysis of the Role of Hole Transport Layer Materials to the Performance of Perovskite Solar Cell. *E3S Web Conf.* **2018**, *67*, 01021.
- (221) Schloemer, T. H.; Christians, J. A.; Luther, J. M.; Sellinger, A. Doping Strategies for Small Molecule Organic Hole-Transport Materials: Impacts on Perovskite Solar Cell Performance and Stability. *Chem. Sci.* **2019**, *10* (7), 1904–1935.
- (222) Gil, B.; Kim, J.; Yun, A. J.; Park, K.; Cho, J.; Park, M.; Park, B. CuCrO₂ Nanoparticles Incorporated into Ptaa as a Hole Transport Layer for 85° c and Light Stabilities in Perovskite Solar Cells. *Nanomaterials* **2020**, *10* (9), 1669.
- (223) Liu, X.; Cheng, Y.; Liu, C.; Zhang, T.; Zhang, N.; Zhang, S.; Chen, J.; Xu, Q.; Ouyang, J.; Gong, H. 20.7% Highly Reproducible Inverted Planar Perovskite Solar Cells With Enhanced Fill Factor and Eliminated Hysteresis. *Energy Environ. Sci.* **2019**, *12* (5), 1622–1633.
- (224) Tavakoli, M. M.; Tavakoli, R. All-Vacuum-Processing for Fabrication of Efficient, Large-Scale, and Flexible Inverted Perovskite Solar Cells. *Phys. Status Solidi - Rapid Res. Lett.* **2021**, *15*, 2000449.
- (225) Yaghoobi Nia, N.; Lamanna, E.; Zendejdel, M.; Palma, A. L.; Zurlo, F.; Castriotta, L. A.; Di Carlo, A. Doping Strategy for Efficient and Stable Triple Cation Hybrid Perovskite Solar Cells and Module Based on Poly(3-Hexylthiophene) Hole Transport Layer. *Small* **2019**, 1904399.
- (226) Weisspfennig, C. T.; Lee, M. M.; Teuscher, J.; Docampo, P.; Stranks, S. D.; Joyce, H. J.; Bergmann, H.; Bruder, I.; Kondratuk, D. V.; Johnston, M. B.; et al. Optimizing the Energy Offset between Dye and Hole-Transporting Material in Solid-State Dye-Sensitized Solar Cells. *J. Phys. Chem. C* **2013**, *117* (39), 19850–19858.
- (227) Jeong, I.; Jo, J. W.; Bae, S.; Son, H. J.; Ko, M. J. A Fluorinated Polythiophene Hole-Transport Material for Efficient and Stable Perovskite Solar Cells. *Dye. Pigment.* **2019**, *164*, 1–6.
- (228) Madhavan, V. E.; Zimmermann, I.; Baloch, A. A. B.; Manekkathodi, A.; Belaidi, A.; Tabet, N.; Nazeeruddin, M. K. CuSCN as Hole Transport Material with 3D/2D Perovskite Solar Cells. *ACS Appl. Energy Mater.* **2020**, *3* (1), 114–121.
- (229) Abzieher, T.; Moghadamzadeh, S.; Schackmar, F.; Eggers, H.; Sutterlützi, F.; Farooq, A.; Kojda, D.; Habicht, K.; Schmager, R.; Mertens, A.; et al. Electron-Beam-Evaporated Nickel Oxide Hole Transport Layers for Perovskite-Based Photovoltaics. *Adv. Energy Mater.* **2019**, *9* (12), 1802995.
- (230) Di Girolamo, D.; Di Giacomo, F.; Matteocci, F.; Marrani, A. G.; Dini, D.; Abate, A.; Di Girolamo, D. Progress, Highlights and Perspectives on NiO in Perovskite Photovoltaics. *Chem. Sci.* **2020**, *11* (30), 7746–7759.

References

- (231) Kojima, A.; Teshima, K.; Shirai, Y.; Miyasaka, T. Organometal Halide Perovskites as Visible-Light Sensitizers for Photovoltaic Cells. *J. Am. Chem. Soc.* **2009**, *131* (17), 6050–6051.
- (232) Targhi, F. F.; Jalili, Y. S.; Kanjouri, F. MAPbI₃ and FAPbI₃ Perovskites as Solar Cells: Case Study on Structural, Electrical and Optical Properties. *Results Phys.* **2018**, *10* (May), 616–627.
- (233) Jeong, M.; Choi, I. W.; Go, E. M.; Cho, Y.; Kim, M.; Lee, B.; Jeong, S.; Jo, Y.; Choi, H. W.; Lee, J.; et al. Stable Perovskite Solar Cells with Efficiency Exceeding 24.8% and 0.3-V Voltage Loss. *Science*. **2020**, *369* (6511), 1615–1620.
- (234) Masi, S.; Gualdrón-Reyes, A. F.; Mora-Seró, I. Stabilization of Black Perovskite Phase in FAPbI₃ and CsPbI₃. *ACS Energy Lett.* **2020**, *5* (6), 1974–1985.
- (235) Koh, T. M.; Fu, K.; Fang, Y.; Chen, S.; Sum, T. C.; Mathews, N.; Mhaisalkar, S. G.; Boix, P. P.; Baikie, T. Formamidinium-Containing Metal-Halide: An Alternative Material for near-IR Absorption Perovskite Solar Cells. *J. Phys. Chem. C* **2014**, *118* (30), 16458–16462.
- (236) Correa Baena, J. P.; Steier, L.; Tress, W.; Saliba, M.; Neutzner, S.; Matsui, T.; Giordano, F.; Jacobsson, T. J.; Srimath Kandada, A. R.; Zakeeruddin, S. M.; et al. Highly Efficient Planar Perovskite Solar Cells through Band Alignment Engineering. *Energy Environ. Sci.* **2015**, *8* (10), 2928–2934.
- (237) Saliba, M.; Matsui, T.; Seo, J. Y.; Domanski, K.; Correa-Baena, J. P.; Nazeeruddin, M. K.; Zakeeruddin, S. M.; Tress, W.; Abate, A.; Hagfeldt, A.; et al. Cesium-Containing Triple Cation Perovskite Solar Cells: Improved Stability, Reproducibility and High Efficiency. *Energy Environ. Sci.* **2016**, *9* (6), 1989–1997.
- (238) Wu, X.; Jiang, Y.; Chen, C.; Guo, J.; Kong, X.; Feng, Y.; Wu, S.; Gao, X.; Lu, X.; Wang, Q.; et al. Stable Triple Cation Perovskite Precursor for Highly Efficient Perovskite Solar Cells Enabled by Interaction with 18C6 Stabilizer. *Adv. Funct. Mater.* **2020**, *30* (6), 1908613.
- (239) Liang, L.; Cai, Y.; Li, X.; Nazeeruddin, M. K.; Gao, P. All That Glitters Is Not Gold: Recent Progress of Alternative Counter Electrodes for Perovskite Solar Cells. *Nano Energy* **2018**, *52*, 211–238.
- (240) Unold, T.; Kaufmann, C. A. *Chalcopyrite Thin-Film Materials and Solar Cells*; Elsevier Ltd., 2012; Vol. 1.
- (241) Bonnet, D. *CdTe Thin-Film PV Modules*, Second Edi.; Elsevier Ltd, 2013.
- (242) Fassel, P.; Lami, V.; Bausch, A.; Wang, Z.; Klug, M. T.; Snaith, H. J.; Vaynzof, Y.; Fassel, P.; Lami, V.; Bausch, A.; et al. Fractional Deviations in Precursor Stoichiometry Dictate the Properties, Performance and Stability of Perovskite Photovoltaic Devices, *Energy Environ. Sci.*, **2018**, *11*, 3380-339.
- (243) Wu J.; Cha H.; Du T.; Dong Y.; Xu W.; Lin ,C.T; Durrant, J. Comparison in Charge Carrier Dynamics in Organic and Perovskite Solar Cells. *Adv. Mater.*, **2021**, 2101833.
- (244) Hossain, I. M.; Hudry, D.; Mathies, F.; Abzieher, T.; Moghadamzadeh, S.; Rueda-Delgado, D.; Schackmar, F.; Bruns, M.; Andriessen, R.; Aernouts, T.; et al. Scalable Processing of Low-Temperature TiO₂ Nanoparticles for High-Efficiency Perovskite Solar Cells. *ACS Appl. Energy Mater.* **2019**, *2* (1), 47–58.
- (245) Qiu, W.; Paetzold, U. W.; Gehlhaar, R.; Smirnov, V.; Boyen, H. G.; Tait, J. G.; Conings, B.; Zhang, W.; Nielsen, C. B.; McCulloch, I.; et al. An Electron Beam Evaporated TiO₂ Layer for High Efficiency Planar Perovskite Solar Cells on Flexible Polyethylene Terephthalate Substrates. *J.*

References

- Mater. Chem. A* **2015**, *3* (45), 22824–22829.
- (246) Wang, Y.; Qu, H.; Zhang, C.; Chen, Q. Rapid Oxidation of the Hole Transport Layer in Perovskite Solar Cells by A Low-Temperature Plasma. *Sci. Rep.* **2019**, *9*, 459.
- (247) Abate, A.; Staff, D. R.; Hollman, D. J.; Snaith, H. J.; Walker, A. B. Influence of Ionizing Dopants on Charge Transport in Organic Semiconductors. *Phys. Chem. Chem. Phys.* **2014**, *16* (3), 1132–1138.
- (248) Kettle, J.; Bristow, N.; Gethin, D. T.; Tehrani, Z.; Moudam, O.; Li, B.; Katz, E. A.; Dos Reis Benatto, G. A.; Krebs, F. C. Printable Luminescent down Shifter for Enhancing Efficiency and Stability of Organic Photovoltaics. *Sol. Energy Mater. Sol. Cells* **2016**, *144*, 481–487.
- (249) Moudam, O.; Rowan, B. C.; Alamiry, M.; Richardson, P.; Richards, B. S.; Jones, A. C.; Robertson, N. Europium Complexes with High Total Photoluminescence Quantum Yields in Solution and in PMMA. *Chem. Commun.* **2009**, No. 43, 6649–6651.
- (250) Xu, H.; Wang, L. H.; Zhu, X. H.; Yin, K.; Zhong, G. Y.; Hou, X. Y.; Huang, W. Application of Chelate Phosphine Oxide Ligand in Eu111 Complex with Mezzo Triplet Energy Level, Highly Efficient Photoluminescent, and Electroluminescent Performances. *J. Phys. Chem. B* **2006**, *110* (7), 3023–3029.
- (251) Klampaftis, E.; Congiu, M.; Robertson, N.; Richards, B. S. Luminescent Ethylene Vinyl Acetate Encapsulation Layers for Enhancing the Short Wavelength Spectral Response and Efficiency of Silicon Photovoltaic Modules. *IEEE J. Photovoltaics* **2011**, *1* (1), 29–36.
- (252) Zhang, T.; Cheung, S. H.; Meng, X.; Zhu, L.; Bai, Y.; Ho, C. H. Y.; Xiao, S.; Xue, Q.; So, S. K.; Yang, S. Pinning Down the Anomalous Light Soaking Effect toward High-Performance and Fast-Response Perovskite Solar Cells: The Ion-Migration-Induced Charge Accumulation. *J. Phys. Chem. Lett.* **2017**, *8* (20), 5069–5076.
- (253) Bragg, W. H.; Bragg Apr, W. L.; H Bragg, B. W.; Professor of Physics, C. The Reflection of X-Rays by Crystals. *Proc. R. Soc. London. Ser. A, Contain. Pap. a Math. Phys. Character* **1913**, *88* (605), 428–438.
- (254) Haering, R. R.; Adams, E. N. Theory and Application of Thermally Stimulated Currents in Photoconductors. *Phys. Rev.* **1960**, *117* (2), 451–454.
- (255) Schmechel, R.; Von Seggern, H. Electronic Traps in Organic Transport Layers. *Phys. Status Solidi Appl. Res.* **2004**, *201* (6), 1215–1235.
- (256) Lewandowski, A. C.; McKeever, S. W. S. Generalized Description of Thermally Stimulated Processes without the Quasiequilibrium Approximation. *Phys. Rev. B* **1991**, *43* (10), 8163–8178.
- (257) Kapil, G.; Bessho, T.; Ng, C. H.; Hamada, K.; Pandey, M.; Kamarudin, M. A.; Hirotsu, D.; Kinoshita, T.; Minemoto, T.; Shen, Q.; et al. Strain Relaxation and Light Management in Tin-Lead Perovskite Solar Cells to Achieve High Efficiencies. *ACS Energy Lett.* **2019**, *4* (8), 1991–1998.
- (258) Schafferhans, J.; Deibel, C.; Dyakonov, V. Electronic Trap States in Methanofullerenes. *Adv. Energy Mater.* **2011**, *1* (4), 655–660.
- (259) Schmechel, R.; Von Seggern, H. Electronic Traps in Organic Transport Layers. *Phys. Status Solidi Appl. Res.* **2004**, *201* (6), 1215–1235.
- (260) Wolff, C. M.; Caprioglio, P.; Stolterfoht, M.; Neher, D. Nonradiative Recombination in Perovskite Solar Cells: The Role of Interfaces. *Adv. Mater.* **2019**, *31*, 1902762.

References

- (261) Wang, Z.; Lin, Q.; Wenger, B.; Christoforo, M. G.; Lin, Y.; Klug, M. T.; Johnston, M. B.; Herz, L. M.; Snaith, H. J. High irradiance performance of metal halide Perovskites for Concentrator Photovoltaics. *Nat. Energy*. **2018**, *3*, 855–861.
- (262) Alsari, M.; Pearson, A. J.; Wang, J. T. W.; Wang, Z.; Montisci, A.; Greenham, N. C.; Snaith, H. J.; Lilliu, S.; Friend, R. H. Degradation Kinetics of Inverted Perovskite Solar Cells. *Sci. Rep.* **2018**, *8*, 5977.
- (263) Lee, H.; Lee, C.; Song, H. J. Influence of Electrical Traps on the Current Density Degradation of Inverted Perovskite Solar Cells. *Materials (Basel)*. **2019**, *12* (10), 1664.
- (264) Correa-Baena, J. P.; Turren-Cruz, S. H.; Tress, W.; Hagfeldt, A.; Aranda, C.; Shooshtari, L.; Bisquert, J.; Guerrero, A. Changes from Bulk to Surface Recombination Mechanisms between Pristine and Cycled Perovskite Solar Cells. *ACS Energy Lett.* **2017**, *2* (3), 681–688.
- (265) Farooq, A.; Hossain, I. M.; Moghadamzadeh, S.; Schwenzler, J. A.; Abzieher, T.; Richards, B. S.; Klampaftis, E.; Paetzold, U. W. Spectral Dependence of Degradation under Ultraviolet Light in Perovskite Solar Cells. *ACS Appl. Mater. Interfaces* **2018**, *10* (26), 21985–21990.
- (266) A. Farooq; M.R. Khan; T. Abzieher; A. Voigt; D.C. Lupascu; U. Lemmer; B.S. Richards; U.W. Paetzold. Photodegradation of Triple-Cation Perovskite Solar Cells : The Role of Spectrum and Bias Conditions. *ACS Appl. Energy Mater.* **2021**, *4*, 4, 3083–3092.
- (267) Jena, A. K.; Kulkarni, A.; Ikegami, M.; Miyasaka, T. Steady State Performance, Photo-Induced Performance Degradation and Their Relation to Transient Hysteresis in Perovskite Solar Cells. *J. Power Sources* **2016**, *309*, 1–10.
- (268) Zhang, P.; Wu, J.; Wang, Y.; Sarvari, H.; Liu, D.; Chen, Z. D.; Li, S. Enhanced Efficiency and Environmental Stability of Planar Perovskite Solar Cells by Suppressing Photocatalytic Decomposition. *J. Mater. Chem. A* **2017**, *5* (33), 17368–17378.
- (269) Lee, S. W.; Kim, S.; Bae, S.; Cho, K.; Chung, T.; Mundt, L. E.; Lee, S.; Park, S.; Park, H.; Schubert, M. C.; et al. UV Degradation and Recovery of Perovskite Solar Cells. *Sci. Rep.* **2016**, *6*, 38150.
- (270) Li, W.; Zhang, W.; Van Reenen, S.; Sutton, R. J.; Fan, J.; Haghighirad, A. A.; Johnston, M. B.; Wang, L.; Snaith, H. J. Enhanced UV-Light Stability of Planar Heterojunction Perovskite Solar Cells with Caesium Bromide Interface Modification. *Energy Environ. Sci.* **2016**, *9* (2), 490–498.
- (271) Xiong, L.; Qin, M.; Chen, C.; Wen, J.; Yang, G.; Guo, Y.; Ma, J.; Zhang, Q.; Qin, P.; Li, S.; et al. Fully High-Temperature-Processed SnO₂ as Blocking Layer and Scaffold for Efficient, Stable, and Hysteresis-Free Mesoporous Perovskite Solar Cells. *Adv. Funct. Mater.* **2018**, *28* (10), 1706276.
- (272) Christians, J. A.; Schulz, P.; Tinkham, J. S.; Schloemer, T. H.; Harvey, S. P.; Tremolet De Villers, B. J.; Sellinger, A.; Berry, J. J.; Luther, J. M. Tailored Interfaces of Unencapsulated Perovskite Solar Cells for >1,000 Hour Operational Stability. *Nat. Energy* **2018**, *3* (1), 68–74.
- (273) Guo, Q.; Wu, J.; Yang, Y.; Liu, X.; Lan, Z.; Lin, J.; Huang, M.; Wei, Y.; Dong, J.; Jia, J.; et al. High-Performance and Hysteresis-Free Perovskite Solar Cells Based on Rare-Earth-Doped SnO₂ Mesoporous Scaffold. *Research* **2019**, *2019*, 1–13.
- (274) Akin, S. Hysteresis-Free Planar Perovskite Solar Cells with a Breakthrough Efficiency of 22% and Superior Operational Stability over 2000 h. *ACS Appl. Mater. Interfaces* **2019**, *11* (43), 39998–40005.
- (275) <https://www.epa.gov/sites/production/files/documents/uvradiation.pdf> (accessed Mar 20, 2021).

References

- (276) Reference Air Mass 1.5 Spectra | Grid Modernization | NREL <https://www.nrel.gov/grid/solar-resource/spectra-am1.5.html> (accessed Mar 20, 2021).
- (277) Kempe, M. D.; Moricone, T.; Kilkenny, M. Effects of Cerium Removal from Glass on Photovoltaic Module Performance and Stability. In *Reliability of Photovoltaic Cells, Modules, Components, and Systems II*; SPIE, 2009; Vol. 7412, 74120Q.
- (278) Glass, S. C.; Haynes, G. A. NASA technical note, effect of radiation on Cerium doped glass December 1970.
- (279) Haynes, G. A. *Effect of Radiation on Cerium Doped Solar Cell Cover Glass*.
- (280) Kempe, M. D.; Moricone, T.; Kilkenny, M. Effects of Cerium Removal from Glass on Photovoltaic Module Performance and Stability. *Reliab. Photovolt. Cells, Modul. Components, Syst. II* **2009**, 7412, 74120Q.
- (281) Allsopp, B. L.; Orman, R.; Johnson, S. R.; Baistow, I.; Sanderson, G.; Sundberg, P.; Stålhandske, C.; Grund, L.; Andersson, A.; Booth, J.; et al. Towards Improved Cover Glasses for Photovoltaic Devices. *Prog. Photovoltaics Res. Appl.* **2020**, 28 (11), 1187–1206.
- (282) Stroud, J. S. Photoionization of Ce 3+ in Glass. *J. Chem. Phys.* **1961**, 35, 844.
- (283) Pern, F. J. Factors That Affect the EVA Encapsulant Discoloration Rate upon Accelerated Exposure. *Sol. Energy Mater. Sol. Cells* **1996**, 41–42, 587–615.
- (284) King, D. L.; Quintana, M. A.; Kratochvil, J. A.; Ellibee, D. E.; Hansen, B. R. Photovoltaic Module Performance and Durability Following Long-Term Field Exposure. *Prog. Photovoltaics Res. Appl.* **2000**, 8 (2), 241–256.
- (285) Aloui, F.; Ahajji, A.; Irmouli, Y.; George, B.; Charrier, B.; Merlin, A. Inorganic UV Absorbers for the Photostabilisation of Wood-Clearcoating Systems: Comparison with Organic UV Absorbers. *Applied Surface Science*, **2007**, 3737–3745.
- (286) Parejo, P. G.; Zayat, M.; Levy, D. Highly Efficient UV-Absorbing Thin-Film Coatings for Protection of Organic Materials against Photodegradation. *J. Mater. Chem.* **2006**, 16 (22), 2165–2169.
- (287) US5061558A - Methacrylate protective coating containing a uv-absorber for polycarbonate - Google Patents <https://patents.google.com/patent/US5061558A/en> (accessed Jul 20, 2020).
- (288) Zayat, M.; Garcia-Parejo, P.; Levy, D. Preventing UV-Light Damage of Light Sensitive Materials Using a Highly Protective UV-Absorbing Coating. *Chem. Soc. Rev.* **2007**, 36 (8), 1270–1281.
- (289) Miller, T. J.; Haase, M. A.; Sun, X.; Hao, B.; Zhang, J.; Smith, T. L.; Ballen, T.; Xie, J.; Barnes, A. S.; Kecman, F.; et al. High Efficiency Green LEDs Using II-VI Color Converters. *Light. Diodes Mater. Devices, Appl. Solid State Light. XIV* **2010**, 76171A.
- (290) Lee, S. W.; Kim, S.; Bae, S.; Cho, K.; Chung, T.; Mundt, L. E.; Lee, S.; Park, S.; Park, H.; Schubert, M. C.; et al. UV Degradation and Recovery of Perovskite Solar Cells. *Sci. Rep.* **2016**, 6, 38150.
- (291) Carolus, J.; Merckx, T.; Purohit, Z.; Tripathi, B.; Boyen, H.-G.; Aernouts, T.; De Ceuninck, W.; Conings, B.; Daenen, M. Potential-Induced Degradation and Recovery of Perovskite Solar Cells. *Sol. RRL* **2019**, 3 (10), 1900226.
- (292) Arabpour Roghabadi, F.; Mansour Rezaei Fumani, N.; Alidaei, M.; Ahmadi, V.; Sadrameli, S. M. High Power UV-Light Irradiation as a New Method for Defect Passivation in Degraded Perovskite Solar Cells to Recover and Enhance the Performance. *Sci. Rep.* **2019**, 9, 9448.

References

- (293) Lee, S. W.; Kim, S.; Bae, S.; Cho, K.; Chung, T.; Mundt, L. E.; Lee, S.; Park, S.; Park, H.; Schubert, M. C.; et al. UV Degradation and Recovery of Perovskite Solar Cells. *Sci. Rep.* **2016**, *6*, 38150.
- (294) Ahlawat, D. S. Study of Band Gap Energy and Thermal Properties of PbI₂ by Photoacoustic Spectroscopy. *Mod. Phys. Lett. B*, **2012**, *26* (16), 1250098.
- (295) Ahuja, R.; Arwin, H.; Ferreira Da Silva, A.; Persson, C.; Osorio-Guillé, J. M.; Souza De Almeida, J.; Araujo, C. M.; Veje, E.; Veissid, N.; An, C. Y.; et al. Electronic and Optical Properties of Lead Iodide, *Journal of Applied Physics*, **2002**, *92*, 7219.
- (296) Chen, Y.; Li, N.; Wang, L.; Li, L.; Xu, Z.; Jiao, H.; Liu, P.; Zhu, C.; Zai, H.; Sun, M.; et al. Impacts of Alkaline on the Defects Property and Crystallization Kinetics in Perovskite Solar Cells. *Nat. Commun.* **2019**, *10*, 1112.
- (297) Wang, Z.; Lin, Q.; Wenger, B.; Christoforo, M. G.; Lin, Y.; Klug, M. T.; Johnston, M. B.; Herz, L. M.; Snaith, H. J. High irradiance performance of metal halide Perovskites for Concentrator Photovoltaics. *Nat. Energy* **2018**, *3*, 855–861.
- (298) Khenkin, M. V.; Anoop, K. M.; Katz, E. A.; Visoly-Fisher, I. Bias-Dependent Degradation of Various Solar Cells: Lessons for Stability of Perovskite Photovoltaics. *Energy Environ. Sci.* **2019**, *12* (2), 550–558.
- (299) Bae, S.; Kim, S.; Lee, S. W.; Cho, K. J.; Park, S.; Lee, S.; Kang, Y.; Lee, H. S.; Kim, D. Electric-Field-Induced Degradation of Methylammonium Lead Iodide Perovskite Solar Cells. *J. Phys. Chem. Lett.* **2016**, *7* (16), 3091–3096.
- (300) Ming, W.; Yang, D.; Li, T.; Zhang, L.; Du, M. H. Formation and Diffusion of Metal Impurities in Perovskite Solar Cell Material CH₃NH₃PbI₃: Implications on Solar Cell Degradation and Choice of Electrode. *Adv. Sci.* **2018**, *5*, 1700662.
- (301) Ran, C.; Xu, J.; Gao, W.; Huang, C.; Dou, S. Defects in Metal Triiodide Perovskite Materials towards High-Performance Solar Cells: Origin, Impact, Characterization, and Engineering. *Chemical Society Reviews*, **2018**, 4581–4610.
- (302) Du, M. H. Efficient Carrier Transport in Halide Perovskites: Theoretical Perspectives. *Journal of Materials Chemistry A*, **2014**, 9091–9098.
- (303) Pearson, A. J.; Eperon, G. E.; Hopkinson, P. E.; Habisreutinger, S. N.; Wang, J. T. W.; Snaith, H. J.; Greenham, N. C. Oxygen Degradation in Mesoporous Al₂O₃/CH₃NH₃PbI_{3-x}Cl_x Perovskite Solar Cells: Kinetics and Mechanisms. *Adv. Energy Mater.* **2016**, *6*, 1600014.
- (304) Bryant, D.; Aristidou, N.; Pont, S.; Sanchez-Molina, I.; Chotchunangatchaval, T.; Wheeler, S.; Durrant, J. R.; Haque, S. A. Light and Oxygen Induced Degradation Limits the Operational Stability of Methylammonium Lead Triiodide Perovskite Solar Cells. *Energy Environ. Sci.* **2016**, *9* (5), 1655–1660.
- (305) Bischak, C. G.; Hetherington, C. L.; Wu, H.; Aloni, S.; Ogletree, D. F.; Limmer, D. T.; Ginsberg, N. S. Origin of Reversible Photoinduced Phase Separation in Hybrid Perovskites. *Nano Lett.* **2017**, *17* (2), 1028–1033.
- (306) K. M., A.; Khenkin, M. V.; Di Giacomo, F.; Galagan, Y.; Rahmany, S.; Etgar, L.; Katz, E. A.; Visoly-Fisher, I. Bias-Dependent Stability of Perovskite Solar Cells Studied Using Natural and Concentrated Sunlight. *Sol. RRL* **2019**, 1900335, 1–11.
- (307) Duong, T.; Mulmudi, H. K.; Wu, Y.; Fu, X.; Shen, H.; Peng, J.; Wu, N.; Nguyen, H. T.; Macdonald, D.; Lockrey, M.; et al. Light and Electrically Induced Phase Segregation and Its Impact on the

References

- Stability of Quadruple Cation High Bandgap Perovskite Solar Cells. *ACS Appl. Mater. Interfaces* **2017**, *9* (32), 26859–26866.
- (308) Kim, H. S.; Seo, J. Y.; Park, N. G. Impact of Selective Contacts on Long-Term Stability of CH₃NH₃PbI₃ Perovskite Solar Cells. *J. Phys. Chem. C* **2016**, *120* (49), 27840–27848.
- (309) Correa-Baena, J. P.; Turren-Cruz, S. H.; Tress, W.; Hagfeldt, A.; Aranda, C.; Shooshtari, L.; Bisquert, J.; Guerrero, A. Changes from Bulk to Surface Recombination Mechanisms between Pristine and Cycled Perovskite Solar Cells. *ACS Energy Lett.* **2017**, *2* (3), 681–688.
- (310) Sanchez, R. S.; Mas-Marza, E. Light-Induced Effects on Spiro-OMeTAD Films and Hybrid Lead Halide Perovskite Solar Cells. *Sol. Energy Mater. Sol. Cells* **2016**, *158*, 189–194.
- (311) Moghadamzadeh, S.; Hossain, I.; Jakoby, M.; Abdollahi Nejand, B.; Rueda-Delgado, D.; Schwenzler, J. A.; Gharibzadeh, S.; Abzieher, T.; Khan, M. R.; Haghighirad, A. A.; et al. Spontaneous Enhancement of the Stable Power Conversion Efficiency in Perovskite Solar Cells. *J. Mater. Chem. A* **2019**, 670–682.

References

List of Figures

Fig. 2.1: Evolution of solar cell efficiencies for different technologies over time: Crystalline silicon (blue), thin-film (green), and emerging PV (red). Perovskite solar cells are shown as red point circles with yellow filling.	7
Fig. 2.2: (a) Absorption of a photon with energies (i) more than the bandgap (blue), and (ii) equal to bandgap (green) of the absorber material, (b) Schematic illustration of the physical processes taking place in the solar cell.....	10
Fig. 2.3: Schematic model of a p-i-n heterojunction solar cell: (a) the system in equilibrium in dark, with Fermi level E_{F0} and a built-in field (V_{bi}) due to work functions difference of the selective contacts (b) illustration of band diagram of a p-i-n solar cell under illumination close to open-circuit conditions.....	12
Fig. 2.4: Potential recombination mechanisms in solar cells: (i) band-to-band, (ii) trap-assisted, and (iii) Auger recombination.....	13
Fig. 2.5: Schematic illustration of energy levels of materials in perovskite solar cell.	14
Fig. 2.6: The equivalent circuit of a solar cell, comprising a photocurrent source and a diode. The series (R_S) and shunt (R_{Sh}) resistances indicate the loss mechanisms.	15
Fig. 2.7: The spectral irradiance from the sun just outside the earth's atmosphere (AM0) and terrestrial solar spectrum (AM1.5G).....	17
Fig. 2.8: Maximum efficiency of a solar cell with respect to the bandgap for single-junction device under AM1.5G spectrum with absorber temperature 300 K, according to Shockley-Queisser calculations.	17
Fig. 3.1 Structural representation of a perovskite unit cell.	19
Fig. 3.2: Schematic representation of the intolerant and defect tolerant semiconductor material in terms of comparative trap energies.	23
Fig. 3.3: Schematic overview of different intrinsic and extrinsic defect types in halide perovskite layers as compared to an ideal lattice.	26
Fig. 3. 4: An overview of the mechanisms present in PSCs, (a) trap state formation, (b) ion movement leading to vacancy creation, (c) ionic and charge trap state formation, (d) ion migration, (e) charge accumulation at interfaces, (f) ion migration within grains and charge accumulation at grain boundaries, (g) defects in charge transport layers, (h) intrinsic instability of ETLs.	31
Fig. 3.5: Schematic illustration of the crystalline structure of perovskites with n being the dimensionality ($n = 1, 2, \dots \infty$).	36
Fig. 3.6: (a) Schematic illustration of polymeric passivation coatings acting to mitigate the surface trap states. Reproduced with permission from Ref. 77. Copyright 2020, The Royal Society of Chemistry. (b) Difference in V_{OC} through J - V scan before and after the surface passivation.	37
Fig. 3.7: Comparison of the EQEs of the six mc-Si, two CIGS and two CdTe solar cells or mini-modules prior to the addition of any LDS layers.	38
Fig. 3.8: IPCE curves for PSCs coated with the LDS fluoropolymeric layer loaded with different amounts (0 to 2 wt%) of V570.....	39
Fig. 3.9: Schematic representation of perovskite device architecture: (a) regular n-i-p architecture (b) inverted p-i-n architecture.	40

Fig. 4.1: (a) Pictorial view, and (b) schematic illustration of the solar cells.	58
Fig. 4.2: (a) Spectrum of the Xe lamp along with AM1.5G spectrum, (b) J - V characteristic curve, (c) extracted power from solar cell or so-called output power density curve.....	60
Fig. 4.3: Schematic illustration of a spectrophotometry setup.....	62
Fig. 4.4: (a) X-ray diffraction (Bragg's law), (b) typical XRD pattern of a perovskite crystal structure.....	63
Fig. 4.5: Thermally stimulated current profile of pristine perovskite solar cell.	65
Fig. 4.6: (a) Transmittance of various neutral density filters employed to measure the ideality factor values, (b) exemplary graph of ideality factor value for pristine PSC.....	66
Fig. 4.7: Schematic of the UV degradation setup. Four UV lamps can be installed on the top slots, while the cells are placed on the baseplate.	67
Fig. 4.8: Irradiance of the employed metal-halide arc lamp used in photo-degradation experiments along with AM1.5G spectrum.....	68
Fig. 4.9: Pictorial view of the climatic chamber and the devices mounted on the sample holder inside the N ₂ -filled sealed container placed in the chamber.	69
Fig. 5.1: Transmittance of various electron transport layers in the UV range.....	73
Fig. 5.2: PSC architecture used in UV instability measurement.....	74
Fig. 5.3: Spectral distribution of various types of the UV radiation present in AM1.5G.	75
Fig. 5.4: Spectrum of UV-370 and UV-311 lamp employed for UV stability procedure.	77
Fig. 5.5: Variation in the J_{SC} of perovskite solar cells based on various electron transport layers and exposed to (a) UV-370 radiation, (b) UV-311 radiation.....	78
Fig. 5.6: Variation in the power conversion efficiency of solar cells exposed to (a) UV-370 radiation and (b) UV-311 radiation.....	79
Fig. 5.7: Evolution of V_{OC} in the PSCs based on various ETLs and exposed to (a) UV-370 radiation and (b) UV-311 radiation.....	80
Fig. 5.8: Change in FF values of the PSCs based on various ETLs and exposed to (a) UV-370 radiation and (b) UV-311 radiation.....	81
Fig. 5.9: Transmittance through the custom-made UV-B radiation moderator for stability measurements before and after the degradation step.	82
Fig. 5.10: Variation in PCE of the solar cells exposed to UV-311 radiation (a) by covering them with UV-blocking filter (b) directly exposed (red) and covered with UV moderator that allows only 10% of the incident light to pass through.	83
Fig. 5.11: Loss in J_{SC} of the PSCs upon blocking the UV radiation to 400 nm in AM1.5G spectrum.	85
Fig. 5.12: (a) EQE response of the employed solar cell, (b) emission and absorption spectra of Eu complex doped EVA.....	86
Fig. 5.13: Maximum and realistically recoverable J_{SC} using the Eu doped EVA sheet.	87
Fig. 5.14: Schematic illustration of light absorption and loss mechanisms upon insertion of LDS layer on top of a solar cell.....	87
Fig. 5.15: Decrease in (a) J_{SC} and (b) PCE of the PSCs upon covering with clear EVA.	88
Fig. 5.16: (a) UV stability of the devices kept in dark and exposed to UV radiation directly or under optical filters and LDS layer, (b) change in transmittance of the Eu doped EVA after different UV exposure times.	89

Fig. 6.1: Photovoltaic parameters of the solar cells before subjecting them to light stress.	92
Fig. 6.2: (a) J - V curve of the representative solar cell along with a sample picture of a fabricated solar cell in the inset, and (b) stabilized power conversion efficiency at maximum power point along with current-density.	93
Fig. 6.3: (a) transmittance of the optical filters, (b) light irradiance on the solar cells through filters (a) LP-500, ND-50%, and without filter, (c) SP-400, LP-400, and LP-450.	94
Fig. 6.4: Decline in PCE of the solar cells exposed to the light of 1 sun intensity (a) directly and under LP-500, (b) under filters LP-450, LP-400, and SP-400.	95
Fig. 6.5: (a) Light power absorbed by the solar cells through optical filters (b) performance deterioration in PSCs against the dose of incident light.	96
Fig. 6.6: J - V curves of PSCs recorded before and after the degradation step (a) directly exposed to light, covered with optical filters (b) LP-400 (c) LP-450 (d) LP-500 (e) ND-50% and (f) SP-400. Insets exhibit the visual condition of the solar cells before and after degradation to see any discoloration upon photodegradation.	97
Fig. 6.7: (a) PCE deterioration for solar cells exposed to light directly and under ND-50% optical filter (b) spectra of light incident on solar cells directly or under ND-50% filter.	98
Fig. 6.8: The performance deterioration and subsequent recovery in solar cells (a) exposed directly or under LP-500 and ND-50% filter, (b) covered with LP-450, LP-400, and SP-400 filters.	99
Fig. 6.9: XRD pattern of perovskite absorber layers (a) kept in dark, exposed to light directly or under optical filters LP-500, ND-50%, LP-450, LP-400, and SP-400. (b) PbI_2 peak intensity versus first perovskite peak in XRD patterns.	101
Fig. 6.10: (a) Absorbance spectra of perovskite layers after 250 h kept in dark, degraded under unfiltered and filtered light using LP-500 and ND-50% filter (b) absorbance spectra of perovskite layers degraded under filtered light via LP-450, LP-400, and SP-400 filters (c) absorbance values at 500 nm for all the samples employed in the experiment.	104
Fig. 6.11: variation in EQE response of the solar cells kept in dark as reference or exposed to full spectrum of light directly or under LP-500 filter.	105
Fig. 6.12: V_{OC} versus light intensity curves for solar cells (a) kept in dark and exposed to light directly or under LP-500 and ND-50% filters (b) exposed to light under LP-450, LP-400, and SP-400 filters, and (c) ideality factor values extracted from all the V_{OC} versus light intensity graphs.	106
Fig. 6.13: (a) TSC signals of perovskite solar cells kept in dark, directly exposed to light, and under LP-500 filter (b) Arrhenius plot of the TSC signal after thermal cleaning for the peak T4 and T5 (red lines indicate the linear fit).	108
Fig. 6.14: Thermal cleaning of the overlapped peaks T4 and T5 using fractional TSC measurement.	109
Fig. 6.15: TSC measurement of perovskite solar cell with and without hole transport layer.	110
Fig. 7.1: Variations in PV parameters of perovskite solar cells exposed to light at bias conditions (i) open circuit and (ii) short circuit.	115
Fig. 7.2: Change in PCE of solar cells subjected to photo-degradation at (i) short circuit, (ii) open circuit, and (iii) constant voltage near MPP.	117
Fig. 7.3: Performance recovery after a degradation step upon dark storage overnight.	118

Fig. 7.4: Change in PCE of the solar cells exposed to filtered and unfiltered light for 100 hours under open-circuit conditions. 119

List of Tables

Table 3. 1: Description of the mechanisms taking place in halide perovskite solar cells.....	31
Table 5. 1: Weighted average transmittance through different ETLs coated substrates for the incident spectrum.	73
Table 5. 2: Range of the different types of UV radiation in AM1.5G spectrum along with their spectral irradiance.	74
Table 6. 1: List of all the optical filters employed in the visible-light-induced degradation study.	93
Table 7.1: Percentage change in all the PV parameters in solar cells left at the open and short circuit under direct exposure to light.	115
Table 7.2: Absorbed light dose by the solar cells exposed to light directly or under optical filters, along with percentage change in PCE after the degradation step.	120

